10-23-2018

Large Eddy Simulations of Vertical Jets in Crossflow

Pranaya Pokharel
Louisiana State University and Agricultural and Mechanical College

LARGE EDDY SIMULATIONS OF VERTICAL JETS IN CROSSFLOW

A Dissertation

Submitted to the Graduate Faculty of the
Louisiana State University and
Agricultural and Mechanical College
in partial fulfillment of the
requirements for the degree of
Doctor of Philosophy

in

The Department of Mechanical and Industrial Engineering

by
Pranaya Pokharel
M.Eng, McNeese State University, 2011
B.E., Tribhuvan University, Nepal, 2008
December 2018

Dedicated to My Family

ACKNOWLEDGEMENTS

I would like to express my sincere thanks to Dr. Sumanta Acharya for providing me guidance and direction for the current work. I immensely thank the Department of Mechanical and Industrial Engineering for providing me funding as a Teaching Assistant during the course of my study. I also like to acknowledge HPC@LSU and LONI for providing computational resources for the work. I express my gratefulness to my committee members Dr. Ram Devireddy and Dr. Shyam Menon for providing me helpful suggestions on the documentation of the work.

I am extremely grateful to my seniors Dr. Somnath Roy and Dr. Prasad Kalghatgi for providing me an expert guidance for conducting and completing this study. I would also thank my colleagues Mr. Susheel Singh and Mr. Yousef Kanani for providing meaningful discussions on the detailed application of the code. I am thankful to all my friends especially Dr. Pratap Rao, Mr. Mohana Gurunadhan, Mr. Manish Patil, Mr. Aniruddha Joshi, Mr. Sukanta Bhattacharjee and Mr. Pramesh Regmi for providing insightful technical discussions during my research.

Finally, I would like to thank my wife and my parents for providing me immense support during my course of study. This work would not have been possible without them.

TABLE OF CONTENTS

ACKNOWLEDGEMENTS iii

ABSTRACT vi

CHAPTER 1. MOTIVATION 1
1.1 Modal analysis 2
1.2 Geometric effects 3
1.3 Effect of inlet turbulence 4
1.4 Objectives 6

CHAPTER 2. INTRODUCTION TO JETS IN A CROSSFLOW 7
2.1 Major features of JICF 8
2.2 Trajectory and scaling of jet 18
2.3 Scalar concentration 20
2.4 Entrainment 22
2.5 Mixing 26
2.6 Stability 28
2.7 Turbulence studies 34
2.8 Rectangular JICF 37
2.9 Conclusions 40

CHAPTER 3. INLET TURBULENCE GENERATION METHODS 42
3.1 Synthesis methods 42
3.2 Recycling methods 58
3.3 Comparisons between various inflow generation methods 69

CHAPTER 4. COMPUTATIONAL METHODS 74
4.1 Governing equations 74
4.2 Preconditioning 79
4.3 Discretization schemes 81
4.4 Parallelization 85
4.5 Large eddy simulation 88

CHAPTER 5. EFFECT OF JET GEOMETRY ON TRANSVERSE JETS 92
5.1 Background 92

5.2 Section 2- Numerical details 92
5.3 Section 3- Validations 101
5.4 Section 4- Flow structures 103
5.5 Section 5- Effect of geometry in flow features 108
5.6 Section 6- Stability 132
5.7 Section 7- Conclusions 154

CHAPTER 6. EFFECT OF JET TURBULENCE ON CYLINDRICAL AND RECTANGULAR TRANSVERSE JETS 158
6.1 Section 1- Background 158
6.2 Section 2- Numerical details 159
6.3 Section 3- Validation studies 162
6.4 Section 4- Qualitative features 169
6.5 Section 5- Comparison of JICF with different intensity at the inlet 176
6.6 Section 6- Comparison of axis switching 202
6.7 Section 7- Conclusions 214

CHAPTER 7. CONCLUSIONS 217

CHAPTER 8. SCOPE OF FUTURE WORK 220

APPENDIX A. DETAILS OF SEM ALGORITHM 221

APPENDIX B. ADDITIONAL RESULTS FROM PIPE-FLOW SIMULATION 223

REFERENCES 226

VITA 234

ABSTRACT

Jets in crossflow (JICF) have applications ranging from oil spill to film cooling of turbine blades. Hence, an understanding of the flow physics is important. The majority of the research has been conducted for low velocity ratios between jet and crossflow with round jets. JICF is demonstrated to behave differently for high velocity ratios and different jet shapes. Circular and rectangular jets are commonly used in aircraft applications. Current study focuses on high velocity ratio JICF issuing from both circular and rectangular exit.

For simulating JICF, an in house code "Chem3D" is used with Large Eddy Simulation (LES) to model turbulence. Initially, a circular jet is simulated and validated. A rectangular jet with the same mass flow rate is simulated for comparison. Dynamic mode decomposition (DMD) is used for modal study of these jets. An inlet turbulence generation algorithm, Synthetic Eddy Method (SEM), is implemented to simulate incoming jets with different turbulence levels. The SEM algorithm is used to study pipe flow and validation with experiment was obtained.

Rectangular JICF exhibits axis switching which is consistent with observations in literature for a rectangular jet without crossflow. Results from different aspect ratio of rectangular jets (0.5, 2.0, and 3.0) are compared. For rectangular JICF with short edge facing the crossflow, axis switching happens earlier if the aspect ratio is decreased. For the same aspect ratio, if the long edge is facing the crossflow, axis switching is delayed. Effect of geometry is seen in trajectory, turbulence and shear layers of the JICF. Overall, rectangular JICF is shown to exhibit dominance of higher frequencies in the shear layer. However, the effect on turbulence is higher for circular JICF.

Additionally, circular and rectangular JICF with different turbulent kinetic energy of jet is simulated. Analysis reveals earlier breakdown of near field shear layer vortices as the turbulence kinetic energy of jet increases. Effect on the trajectory, turbulence and dynamics of the JICF is observed. In rectangular JICF, axis switching is enhanced by the increase of turbulence levels of the jet. This enhancement is related to wall normal vortices which increase with turbulence of the jet.

CHAPTER 1. MOTIVATION

Jets in crossflow (JICF) is one of the physical processes that finds many applications in the engineering world. JICF is found universally, from film cooling to VSTOL aircrafts and oil spills. Figure 1.1 shows two different situations that are JICF systems. Figure 1.1 (Left) shows a smoke coming from a chimney which is considered as a jet, and it is moving by the influence of crosswind. Figure 1.1 (b) shows a gas-turbine combustor where dilution jets are introduced to air-fuel mixture to control the ratio of air to fuel. Hence, a significant amount of research has been done for different aspects of these flows. Previously, simple jets in quiescent flows were studied after which, the focus shifted to jets that are perpendicular to the flow of the surrounding fluid. These types of JICF are called transverse JICF. A detailed review of JICF research done from the past and continuing till the present is found in the review chapter of JICF.

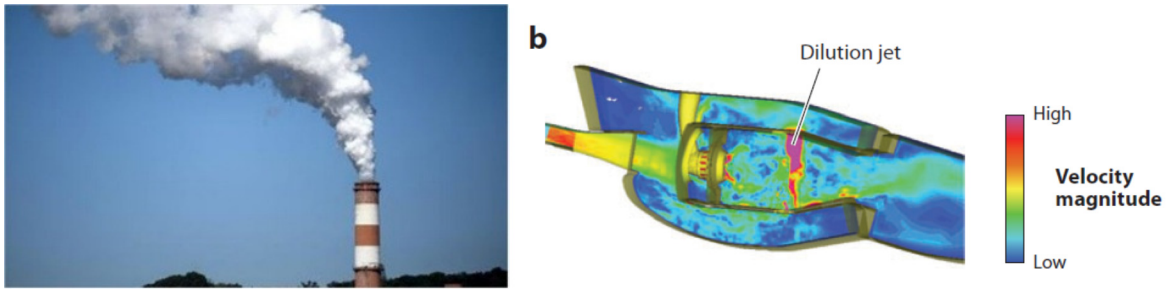

Figure 1.1. (Left) Smoke plume taken from www.transcend.org (Zaid JIlani); (b) Contours of velocity magnitude in a gas-turbine combustor (Mahesh, 2013)

Other specific application of JICF is in active and passive film cooling. Coolant air is injected from an inclined jet on the surface to maintain the surface temperature of turbines relatively cooler. JICF is also used in thrust vector control in rocket engines. Series of JICF injects into the nozzle deflecting the flow. This will allow for the eventual control of direction, thrust etc. for nozzle. More applications of JICF can be found in the review by Karagozian (2010). The motivation is to

push the understanding of JICF further and fill in the gaps that have not been specifically addressed in the past. The main focus of this study on JICF lies in three key areas of the flows-modal analysis, geometric effects, and effect of inlet turbulence.

1.1 Modal analysis

Stability of transverse jets is a field that is being studied recently (Karagozian, 2014). The main necessity of stability studies is in identification of relevant frequencies and excitation of the jet using the knowledge of these frequencies to achieve control of different JICF aspects (penetration, spread, mixing etc.) as desired. Velocity ratio is one of the important parameters to consider in JICF studies. It is defined as the ratio of jet velocity to crossflow velocity. It has been shown that jets with velocity ratio above 3.1, approximately, behaves in a convectively unstable manner and with lower velocity ratios behave in an absolutely unstable manner (Iyer & Mahesh, 2016; Karagozian, 2010; Megerian, et al., 2007). A good study tool to understand this phenomenon of shear layer instability would be Dynamic Mode Decomposition (DMD) (Schmid, 2010). The current study focuses on this aspect of shear layer instability of parabolic profile jet. Apart from study of Iyer and Mahesh (2016), convectively unstable JICF has not been analyzed in detail using DMD. Their work deals with JICF issued from a nozzle. Modal analysis for a velocity ratio 5.7 and JICF issued from a pipe has not been studied yet by DMD. Velocity ratio 5.7 pipe JICF is picked for study because this flow field has been analyzed in great detail with a view-point of turbulence (Muppidi & Mahesh, 2007; Ruiz et al., 2015; Su & Mungal, 2004). Velocity ratio 5.7 JICF falls in convectively unstable regime. Reynolds stresses that are second order flow parameters have been measured in detail for the experimental study of this configuration. Further DNS and LES analysis also revealed important flow features of this JICF. Current studies

are done to understand this configuration. This analysis forms one of the motivations of the current work. Rectangular jets have been studied extensively in quiescent flow. For JICF, only low velocity ratio rectangular jets have been analyzed. In this high velocity ratio regime, different geometries such as rectangular has not been studied especially from stability perspective. Hence the current study is new to simulate and understand these flows using DMD.

1.2 Geometric effects

Rectangular jets were studied in the past owing to its simplicity in experimental set up. Earlier work involving rectangular jets in quiescent flows were reviewed by Gutmark and Grinstein (1999). For low velocity ratios, different aspect ratio jets were studied experimentally and compared (Haven & Kurosaka, 1997). Also, for film cooling flows, inclined JICF with different geometry was simulated using LES and it was concluded that geometry has a significant effect on evolution of jets downstream (Tyagi & Acharya, 2005). The effect of jet geometry on downstream evolution with a focus on turbulence and unstable shear layer modes are not conducted thus far. Maintaining the same mass flow rate of the jet, different rectangular JICF are simulated and compared in detail. Axis switching is a special phenomenon that happens in jets that have unequal lengths on two sides (rectangular, elliptical etc.). As the jet evolves, the smaller side becomes larger and the larger side becomes smaller changing the shape of the jet by 90°. It has been shown that rectangular jets exhibit 90° axis switching (Gutmark & Grinstein, 1999). Earlier studies on rectangular JICF have not touched the aspect of axis switching in detail. Thus, the study of effect of crossflow on axis switching is a new study. Different orientation of aspect ratio 2 rectangular JICF is also simulated and compared. Furthermore, two different aspect ratio rectangular JICF are compared to understand the effects of aspect ratio on the features of

rectangular JICF. As already outlined, this study is new in using DMD to analyze the stability phenomena in all of these rectangular JICF.

1.3 Effect of inlet turbulence

In sensitive processes such as JICF, it is important to get correct conditions at the inlet. This makes it possible to correctly simulate and finally control the downstream processes of the jet such as mixing. Turbulence modeling is at the forefront of numerical studies. Due to advancement in computational power, different approaches for simulating turbulence have been used. It has been concluded that simplified models such as Reynolds averaged Navier Stokes (RANS), k-epsilon and k-omega cannot accurately predict different aspects of complex flows such as Jets in a crossflow (Acharya et al., 2001). More advanced methods such as Direct Numerical Simulations (DNS) and Large Eddy Simulations (LES) are currently used to study complex flows involving turbulence. Even for simple flows such as flows issuing from a pipe, numerically, it would take about 70 d of pipe length to predict correct turbulence (Ruiz et al., 2015). Therefore, some form mimicking turbulence needs to be used as an inlet boundary to predict correct turbulence within a certain length. Consequently, generating appropriate turbulent boundary conditions have itself been a field of research since the last decade. Different algorithms were used for turbulent inlet boundary conditions. Broadly these are classified into recycling methods and synthetic methods. A detailed analysis of these methods are discussed in Chapter 3. For current study, Synthetic Eddy Method (SEM) (Jarrin et al., 2006) was used to generate inlet conditions for turbulent pipe for LES analysis of JICF. The advantage of using synthetic turbulence method is that the input parameters such as length scales and intensity levels can be varied depending on applications.

The turbulence generation method is required for the purpose of understanding the effects of turbulence parameters on the whole flow field.

It was demonstrated that the jet with parabolic velocity profile penetrates deeper compared to a fully turbulent jet at same Reynolds number and velocity ratio (Muppidi & Mahesh, 2005). It is also known that high Reynolds number jet (high turbulence) promote better mixing in the downstream region (Shan & Dimotakis, 2006). The study shows Reynolds number of jets increases the peak of PDF which means that the mixing is more homogenous. The peak of probability distribution function of mixed-fluid concentration is about 17.5% higher when Reynolds number of jet is increased from 10,000 to 20,000 for the same conditions. This is directly correlated to mixing between jet and crossflow fluid. Thus, the study demonstrates that turbulence in the jet affects the flow field significantly. The effect of different intensity of turbulence of jet at same Re has not been studied as per the authors' knowledge. Therefore, one of the objectives of this study is to quantify the effect of jet turbulence intensity on downstream development of turbulence for both circular and rectangular JICF. As per authors' knowledge, effects of jet turbulence on aspects such as axis switching is also first of its kind.

Comparisons in the current study is done for different aspects such as trajectories, mean flow field, and flow dynamics. Flow physics important to the phenomena is also discussed. As the high velocity ratio JICF (>3.1) is currently being studied numerically, this work will also be an overall addition to the understanding of JICF in this regime.

1.4 Objectives

The objectives for this research is to understand the role of jet geometry (circular, rectangular) on the behavior of velocity ratio 5.7 JICF, as well explore the role of incoming jet turbulence levels on the circular and rectangular JICF. Towards this end, the following activities were undertaken:

1) A detailed modal analysis of shear layer instability of the velocity ratio 5.7 jet is performed and comparisons are done to determine whether different geometries of the jet affects this instability.
2) The effects of different aspect ratios for velocity ratio 5.7 rectangular jets in a crossflow are studied.
3) An inlet turbulence generation method (SEM) for LES is implemented in an in-house code 'Chem3D' and applied to JICF which is validated with experiments.
4) The physical process involved in a velocity ratio 5.7 JICF are understood and the effect of turbulence intensity of the jet on the downstream development of the flow field are quantified.
5) The effect of jet turbulence on both cylindrical and rectangular JICF are further analyzed and relevant flow physics are identified.

CHAPTER 2. INTRODUCTION TO JETS IN A CROSSFLOW

Jets and its behavior in flows in different ambient fluids has been a special topic for study of fluid phenomena. Whether to investigate self-similar behavior, heat transfer, entrainment or mixing, jets have been studied to date using analytical, experimental and numerical methods. Different kinds of jets have been studied in the past. Margason (1993) broadly divides them as jet flow including free jets and jet exiting from a plate, jet in a crossflow (JICF) with its variations of jet in hover in ground effect and jet in a crossflow in ground effect. He has extensively reviewed most of the major works done in these fields in the past.

Transverse jets or jets issuing perpendicular in an ambient flow are a good study tool to understand complex fluid phenomena, coherent structures and their interactions, instabilities, etc. Another extensive review is done by Karagozian (2010). She explores studies done in JICF with a strong focus on stability characteristics. Mahesh (2013) has also done a detailed review of JICF with a major focus on latest numerical studies. As noted by Mahesh (2013), due to experimental difficulties more studies have concentrated on sub-sonic jets in a crossflow as compared to supersonic jets in both sub-sonic and supersonic crossflow.

Applications of JICF varies. In air-breathing gas turbine engines, dilution air injection requires the study of JICF. Dilution jets are principally introduced downstream within gas turbine engines to cool the high temperature combustion products before they enter the turbine section. In gas turbine combustors, transversely injected air jets are used as a means of controlling the air-fuel mixture ratio and hence the emissions of nitrogen oxides. JICF are also used in ramjets and scramjet engines. In rocket engines, JICF are used for thrust vector control. Film cooling

applications also use JICF. Both passive and active air injection is used for film cooling. Generally jets are inclined to achieve cooling of turbine blades. Another major study of JICF is required in oil spills. The spilled oil in depths of the ocean behave as high speed jets in the crossflow of ocean currents. To contain and treat the oil on the surface, it is required to predict the exact location of the oil. A slight error in prediction (eg in millimeters) in the depths of ocean will result in error in the order of kilometers at the surface creating problems in containment. Hence, study of JICF is very important in engineering as well as environmental applications. A detailed description of JICF in various fields can be found in review by Karagozian (2010).

2.1 Major features of JICF

Early work on JICF has identified four major features of sub-sonic jets (Fric, 1990; Fric & Roshko, 1988, 1994) in sub-sonic crossflow. This is depicted as a cartoon picture in figure 2.1. The most important structure used to identify jet notably on the far field is the counter-rotating vortex pair (CVP). On the near field, upstream of the jet entering the crossflow there is a vortex structure that wraps around the jet and mixes in the wake region. This vortical structure has been studied as horseshoe vortex owing to its horseshoe like shape. Also upstream of the jet entrance, some vortical structures are seen on the layer where the jet fluid and crossflow fluids contact each other. These structures resulting from the Kelvin-Helmholtz instability, are collectively known as shear layer vortices. The fourth major feature of a typical JICF is the vortical structure in the wake region immediately downstream of the jet exit. These vortices that end on the jet itself on one side and the bottom wall on the other side are collectively known as wake vortices. From their experimental studies Kelso et al. (1996) observed these complex vortical structures and

concluded that they are somehow connected to each other. Fric and Roshko (1994) have depicted the structures in the following cartoon picture.

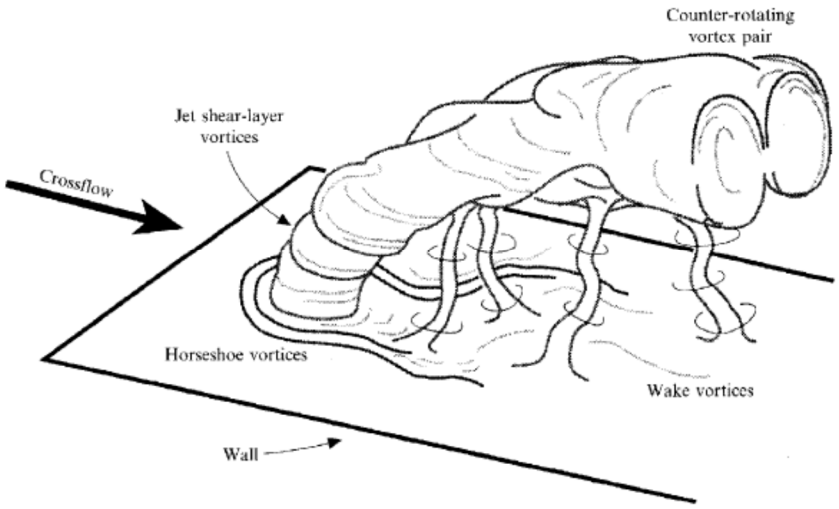

Figure 2.1. Features of JICF taken from Fric and Roshko (1994)

Recent studies that are mostly focused on numerical analysis find evidence of other structures as well. LES by Ruiz et al. (2015) identifies a V-shaped vortex. Experimentally, similar structures are found by Broze and Hussain (1996), and numerically by da Silva and Metais (2002). A variant or a footprint of the structure is reported by Yuan et al. (1999) as 'hanging vortex'. Following sections describe these major components and research done in study of these features.

2.1.1 Counter-rotating vortex pair (CVP)

A wide body of research was done to analyze and confirm the existence of counter-rotating vortex pair. Some earlier work and films such as that by Werle (1968) has been reported by Margason (1993). Many experimental visualization techniques have consistently confirmed the CVP as an important structure of JICF. As described by Muldoon and Acharya (2010), the visualization of CVP is difficult in time instantaneous data (Fig 2.2 (a)) but can clearly be seen in time averaged data (Fig 2.2 (b)). The vortex pair is shaped like kidneys (Acharya et al., 2001). In

instantaneous data, the CVP is not observed as a single vortical structure but as a collection of small vortex structures (Ruiz et al., 2015). Also noted by Muppidi and Mahesh (2007), CVP is displaced downwards on the leeward side of the jet (downstream) compared to the center streamline.

Many studies were devoted to explain the formation of CVP. Karagozian (2010) reviewed different works that explain the formation of CVP in detail. Most of the researchers agree on the conclusion that the near field structures directly affects the formation of these vortex pairs. For example, Yuan et al. (1999) tried to explain the formation of CVP from hanging vortices in the near field. Yuan et al. (1999) say that the hanging vortices rise upward and forward towards the downstream of the jet and upon facing high compressive stress, breaks to form a weak CVP. Similar mechanism have been explained by Ruiz et al. (2015) using the v shaped vortices. V shaped vortices produce couples of small counter-rotating vortex pairs with rotational axis that is parallel to the jet axis. Ruiz et al. (2015) further state that v shaped vortices are primarily responsible for injection of jet fluid into upstream crossflow. An important mechanism about the formation of CVP is stated by Kelso et al. (1996). They suggest that the tilting and folding of shear layer vortices result in the formation of CVP (Figure 2.3). Using their experimental visualization they further conclude that pipe separation, jet shear layer and wall vorticity all contribute to the formation of the CVP. This mechanism was also confirmed by Cortelezzi and Karagozian (2001) in their vortex element simulations. Recently Mahesh (2013) have explained the formation of CVP due to pressure gradients in the near field citing (Muppidi & Mahesh, 2006). The concept is that the pressure difference between the leeward and the windward side of the jet lead to formation of CVP downstream by accumulation of sufficient vorticity (Karagozian, 2010). It is noted in

Mahesh (2013) that there is a general consensus that CVP formation results from modification of the jet vorticity by crossflow and is initiated in the near field. Based on the review by Karagozian (2010), it is noted that the unsteady evolution of shear layer vortices are unnecessary in and of itself to form the CVP. She highlights the work of Muppidi and Mahesh (2006) and Bagheri et al. (2009) where a steady flow was sufficient for the formation of CVP. Overall it is concluded as in Karagozian that even if shear-layer vortices do not form CVP by itself, it has a major role in feeding the evolution of CVP and strengthening it downstream.

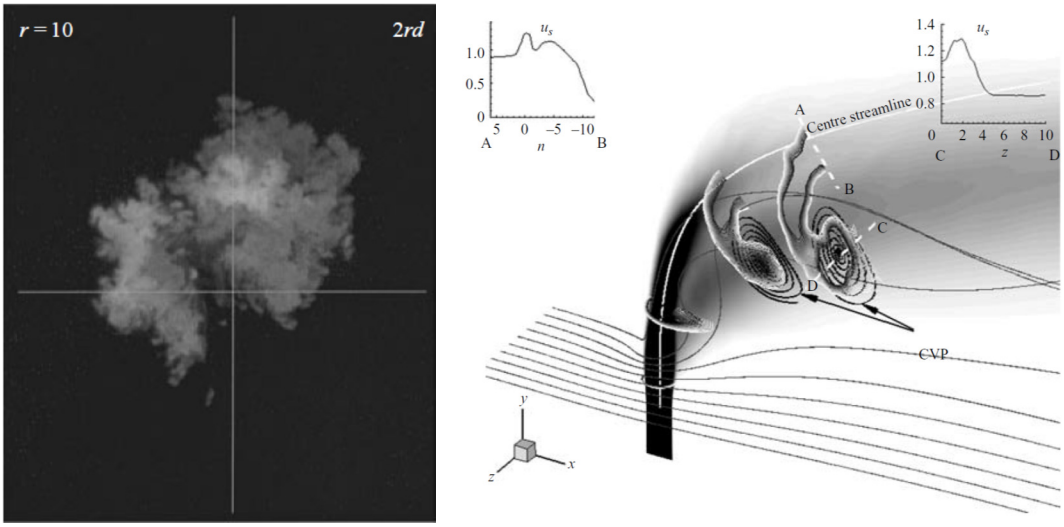

Figure 2.2. (a) Instantaneous CVP taken from Smith and Mungal (1998); (b) Time averaged CVP taken from Muppidi and Mahesh (2007)

CVP is not only important in forming the downstream structure of JICF but also the main mechanism for entrainment of crossflow fluid by the jet in the far field, and hence, mixing of the fluids. The flow when completely dominated by the CVP is classified as far-field.

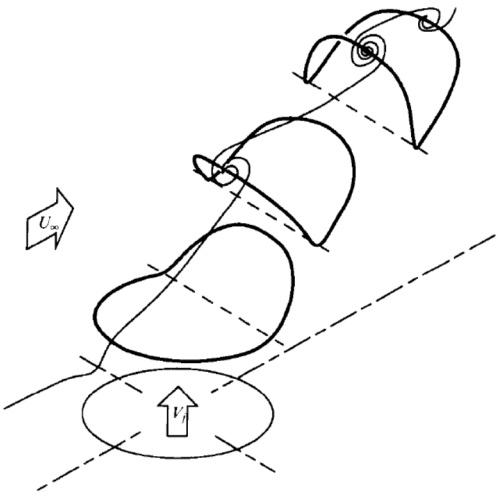

Figure 2.3. Mechanism for formation of CVP by the tilting and folding of shear layer structures taken from Kelso et al. (1996)

2.1.2 Horseshoe vortices

Horseshoe vortices are structures formed upstream of the jet exit. As noted by Mahesh (2013), these vortical structures are formed upstream of the jet owing to the adverse pressure gradient and run around the jet (Figure 2.4 (a) and 2.4 (b)). Kelso et al. (1995) and Krothapalli et al. (1990) have done a detailed study of these vortices. Krothapalli confirms the unsteadiness of this structure upstream and concludes that the frequency of the oscillation of this structure is similar to the frequency of vortex shed around the jet. Kelso also examined the structure consisting of primarily two and three vortices upstream with the same vorticity as that of the boundary layer. For different velocity ratios, they noted that these structures can be either steady with two primary vortices, oscillating with three vortices, and coalescing with three vortices. Furthermore, they also have noted the similarity between the oscillations of the vortices with the vortex shedding in the wake, but do not necessarily confirm the causation of one by the other.

The formation of the horseshoe vortex system is explained on the basis of pressure gradient. Krothapalli et al. (1990) states that the adverse pressure gradient and the deflection of streamlines due to the blockage effect of the jet causes the oncoming boundary layer to be separated and form this complicated vortex pattern. They also explain that this mechanism is necessary for creating tornado like vortices downstream of the jet. However, they conclude that this distinction between primary and secondary separation is less pronounced at low velocity ratios (<1.5) and high velocity ratios (>8). Mahesh (2013) also explains the formation of these vortices using the same line of thought. The formation of horseshoe vortex results because the crossflow boundary layer encounters an adverse pressure gradient upstream of the jet, separates, and forms spanwise vortices that move around the jet. They provide evidence of primary and secondary separation. Other literatures are sparse in explaining the detailed mechanism but almost all of the numerical and experimental studies confirm the existence of these vortices. Some researchers such as Kelso et al. (1996) don't see an important role of horseshoe vortex system for formation of wake vortices. However, Yuan et al. (1999) from their numerical study have found out that horseshoe vortex system is closely related to streamwise vortices found in the wake region. Ruiz et al. (2015) also conclude that it has marginal role on turbulent mixing for their simulation of velocity ratio 5.7 jet.

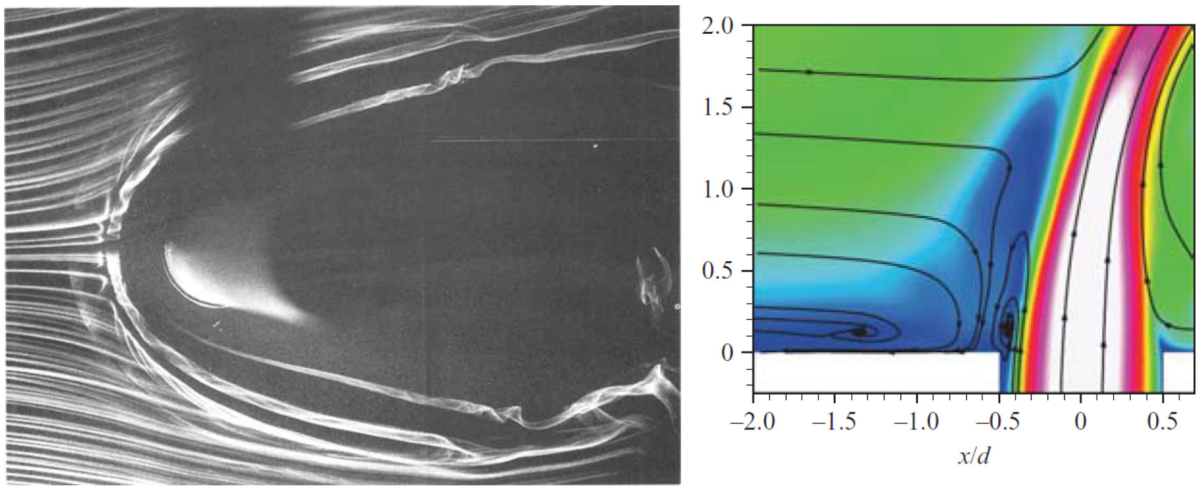

Figure 2.4. (a) Horseshoe vortex taken from Fric and Roshko (1994); (b) Detailed view of nearfield showing Horseshoe vortex taken from Muppidi and Mahesh (2005)

2.1.3 Shear layer vortices

Shear layer vortices are formed in the region where the crossflow fluid meets the jet fluid. Due to the difference between the velocities of the two fluids, Kelvin-Helmholtz instability starts making the interface unstable. This instability in the interface builds up vortices of the faster moving fluid – in this case the jet (Figure 2.5 (a)). These vortices seen in a typical JICF are collectively known as shear layer vortices (Ring vortices shown in 2.5(b)). From experimental studies, Kelso (1996) have concluded that these vortices bend and tilt in a way to contribute to the CVP. Yuan et al. (1999) identify what they call “spanwise rollers” upstream of the jet which defined the upper boundary of the jet. Mahesh (2013) notes that these vortices are present in the instantaneous data field and absent in the time averaged data field. From numerical DNS studies on pulsating jets, Muldoon and Acharya (2010) have found that these vortices are strongly affected by pulsing the jets, producing different vortex merging patterns for different frequencies.

Stability analysis conducted in experiments by (Megerian et al., 2007; Davitian et al., 2010), and numerically by (Bagheri et al., 2009; Iyer & Mahesh, 2016), have concluded that shear layer structures are the most unstable structures and they are the most dominant structures that govern the oscillations of the whole flow domain. For velocity ratios less than about 3.1 (Karagozian, 2010, 2014) has concluded that the flow is absolutely unstable (where shear layer structures become unstable with time) and above that the flow is convectively unstable (where shear layer structures become unstable as they move along). This behavior has been verified numerically by Iyer and Mahesh (2016) using Dynamic Mode Decomposition (DMD) analysis. For inclined JICF, Kalghatgi and Acharya (2014) found that the instability of shear layer structures to be most dominant in the flow. Using DMD analysis, they explain that the formation of hairpin structures in the wake region is due to the effect of these shear layer vortices which are formed from Kelvin-Helmholtz instability.

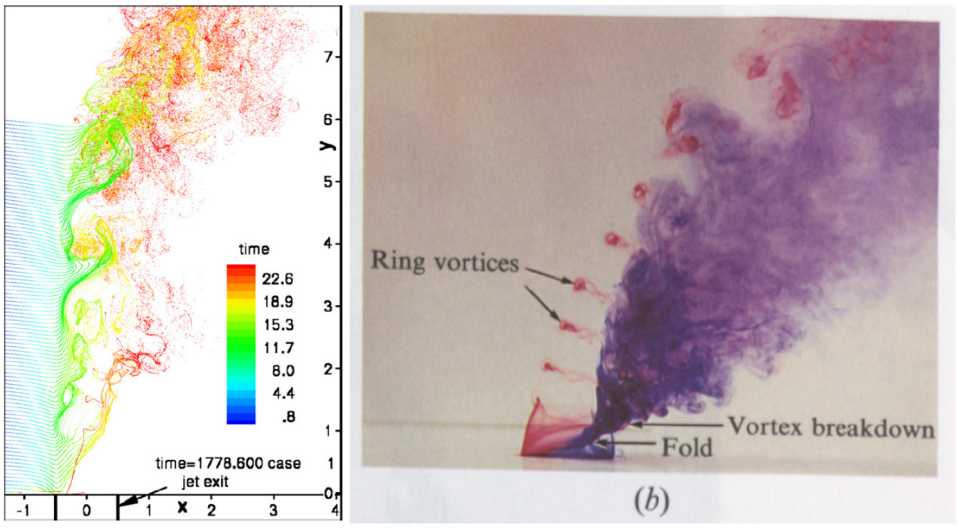

Figure 2.5. (a) Shear layer vortices taken from Muldoon and Acharya (2010); (b) Ring Vortices taken from Kelso et al. (1996)

2.1.4 Wake vortices

The vortical structures in the wake region downstream of the jet are known as wake vortices (Figure 2.6, 2.7). These vortices are “tornado like” and extend from wall region in the downstream of the jet on one side to the jet itself. Earlier researchers have compared this wake to the wake behind a cylinder. However, Fric and Roshko (1994) did a detailed comparison between JICF wake and cylinder wake and conclude they are different and formed by entirely different mechanisms. For high velocity ratios (r>10) there is presence of jet fluid in the wake vortices. This was studied in detail by Smith and Mungal (1998). They found the presence of jet fluid in the wake region for velocity ratios (from r=15 to 20). However, they do not find jet fluid up to velocity ratios of 10. In some instances, at low velocity ratios (r~1), instead of tornado like vortices, there is dominance of hairpin vortices (Figure 2.6). This has been reviewed in detail by Mahesh (2013). Kalghatgi and Acharya (2014) revealed the presence of hairpin structures in the wake region for the inclined JICF. Ruiz et al. (2015) on the other hand, did not find the tornado like structures in the wake (for r=5.7 jet) and suggest that due to high momentum of the jet and low velocity of the crossflow, the jet penetrates deeper and hence no wake vortices are shed from the jet (Figure 2.6). Instead they also observe hairpin structures which do not interact with the main jet. Iyer and Mahesh (2016) also demonstrate wake vortices for moderately low velocity ratios (~2) but no vortices in the wake region for r=4 velocity ratio jet.

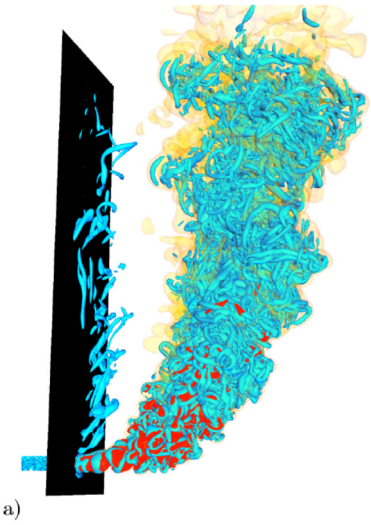

Figure 2.6. Wake structures showing hairpin vortices for R=5.7 JICF taken from Ruiz et al. (2015)

For the formation mechanism of these vortices, Fric and Roshko (1994) conclude that in the wake behind a cylinder the vortices are shed from the cylinder, whereas in jets the vortices are not shed but are formed from the vorticity of the crossflow boundary layer. They also state that the momentum deficit observed is also due to the flat plate boundary layer resulting in vortical structures. Kelso et al. (1996) also have concluded similar mechanism of formation of wake vortices from the flat wall boundary layer. Another DNS study done by Muldoon and Acharya (2010) also explain the formation of wake vortices. They suggest that the wake vortices are formed by the entrainment of jet fluid from behind the jet and then stripping by the crossflow boundary layer. From these conclusions, it is believed that the jet wake vortices are primarily formed from the vorticity in the boundary layer of the crossflow.

Figure 2.7. Wake region taken from Kelso et al. (1996)

2.2 Trajectory and scaling of jet

Much earlier analytical studies have been devoted to find the trajectory of the jet. Trajectories are defined in different ways by researchers. The most common are trajectories based on velocity maxima, scalar maxima, vorticity maxima, or time averaged streamline originating from the center of jet exit (Mahesh, 2013). It is observed by researchers that different definitions give a slightly different path of the jet. Muppidi and Mahesh (2007) have concluded that trajectories based on vorticity is lower than trajectories based on center streamline. In addition, Su and Mungal (2004) observed from their experimental data that flow trajectory based on scalar maxima is lower than that based on center streamline.

To collapse the path of the jet at different conditions, the dimensions are scaled with different length scales. Most researchers agree to the scales based on "rd", where r is the velocity ratio and d is the diameter of the ensuing jet (Figure 2.8). Smith and Mungal (1998) have discussed different length scales used by different authors. According to them, Pratte and Baines (1967) used the rd length scale and the following correlation to collapse the centerline trajectories:

$$\frac{y}{rd} = A\left(\frac{x}{rd}\right)^m$$

Where A=2.05 and m=0.28 for r=5 to r=35, whereas Keffer and Baines (1963) successfully collapsed their trajectories with r^2d. For other profiles used, Margason (1993) listed the various values for constants from different authors. Muppidi and Mahesh (2005) compared the jet trajectories scaled by both rd and r^2d for nine different DNS simulations of different boundary conditions. They observed that although scatter is present in both the cases, the trajectory scaled with rd has less scatter than that scaled with r^2d. Mahesh (2013) points out that Smith and Mungal (1998) suggested the use of r^2d scales, to distinguish near and far fields, where $x/r^2d >$ 0.3 is the far field. They study the concentration decay using different scales and analyze the results using three length scales d, rd, and r^2d. They conclude that d scaling allows analysis of the structural effects that are dependent on r. Trajectory is best scaled using rd and for distinguishing different concentration decay phenomena, it is best to use r^2d scaling. Muppidi and Mahesh (2005) have tried different length scales to see the collapse, and suggest one length scale 'h' which parameterizes the relative inertia of jet and crossflow. Mathematically, h is defined as:

$\frac{h}{d} = \left\{\frac{3}{4}\pi C_m r^2 \frac{\delta^2 d_j^2}{d^4}\right\}^{1/3}$ when $h \leq \delta$ and

$\frac{h}{d} = \frac{2}{3}\frac{\delta}{d} + \frac{\pi}{4} C_m r^2 \frac{d_j^2}{d^2}$ when $h \geq \delta$ where Cm is a proportionality constant, dj is effective diameter and δ is the boundary layer thickness.

They show that the trajectories scaled with this new length scale have a better collapse.

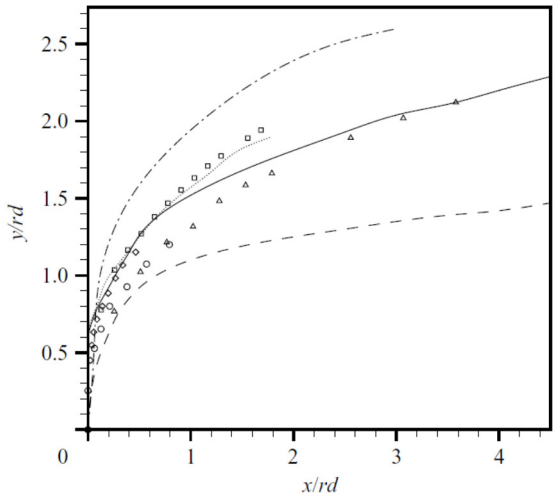

Figure 2.8. Jet trajectories from different authors taken from Muppidi and Mahesh (2005)

2.3 Scalar concentration

Scalar concentration of JICF has been studied by many researchers. For example, Su and Mungal (2004) have included dye in the jet stream to visualize scalar and mixing characteristic of jets in a crossflow. Muppidi and Mahesh (2008) have advected a passive scalar with the jet and analyzed its behavior in their DNS studies. In most cases, scalar is quantified by concentration levels of jet fluid and is a great way of characterizing mixing parameters in JICF. Apart from velocity considerations, scalar measurements provide a good understanding of physical processes involved in JICF and the resultant effects of it.

Scalar field in a JICF is studied numerically by using both DNS and LES formulations. DNS studies such as that done by Muppidi and Mahesh (2008), argue that compared to the velocity field, scalar field convergence is more difficult and they over predict the variance of the field. They further have reported that different approach for solvers will not completely solve the problem. Ruiz et al. (2015) have done their simulations using LES and have under predicted their average scalar concentration and also over predicted variance compared to experiments done by Su and

Mungal (2004). Both of these works have quantified the errors and are bound within twice the maximum value of scalar variance (Muppidi), 10% of scalar concentration in the near field and 15 to 23% in the far field (Ruiz). Figure 2.9 depicts instantaneous scalar concentration from these studies.

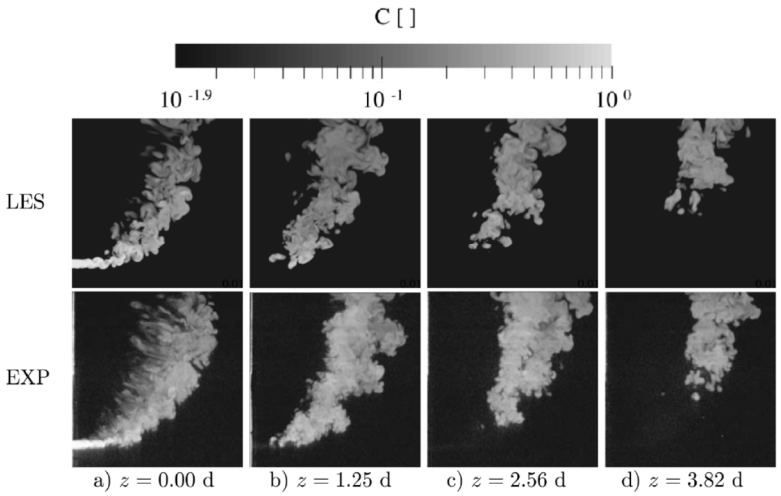

Figure 2.9. Instantaneous scalar concentration using LES taken from Ruiz et al. (2015)

Smith and Mungal (1998) have conducted experiments with PLIF (Planar Laser Induced Fluorescence) using acetone vapor as the dye in the jet. Visualization is shown in Figure 2.10. Shan and Dimotakis (2006) have done their visualizations using rhodamine-6G. They have performed analysis using differently defined concentration measurements. The Reynolds numbers are varied and their effects are discussed in terms of concentration probability density functions (PDFs) and entrainments. They observed intermittency in the concentration levels with a uniform field of concentration followed by a sharp gradient, and then again, another near uniform field. Based on these observations, they arrive at a conclusion that the jet is always anisotropic, even from the smallest scales, and has a preferred orientation along the direction of jet. Their range of analysis included Reynolds Numbers from 1,000 to 20,000 based on jet

diameter. Smith and Mungal (1998) conducted experiments for velocity ratios of jets from 5 to 25. They analyzed the behavior of scalar concentration and found the presence of jet fluid in the wake structures for ratios above 10. They analyzed three different scaling for the jet: d, rd, and r^2d. Based on their analysis, boundary layer separation and vortex roll-up event, scale on jet diameter. The d-scaling allows for the structural effects that are dependent on r. The trajectory and physical dimensions of the jet are scaled with rd. The r^2d-scaling provides a convenient boundary between the regions of higher and slower decay rates. Furthermore, it gives a convenient definition of the far field which is $x=0.2\ r^2d$. Physically, near field is the one where CVP is being formed and far-field is the one where CVP is fully developed.

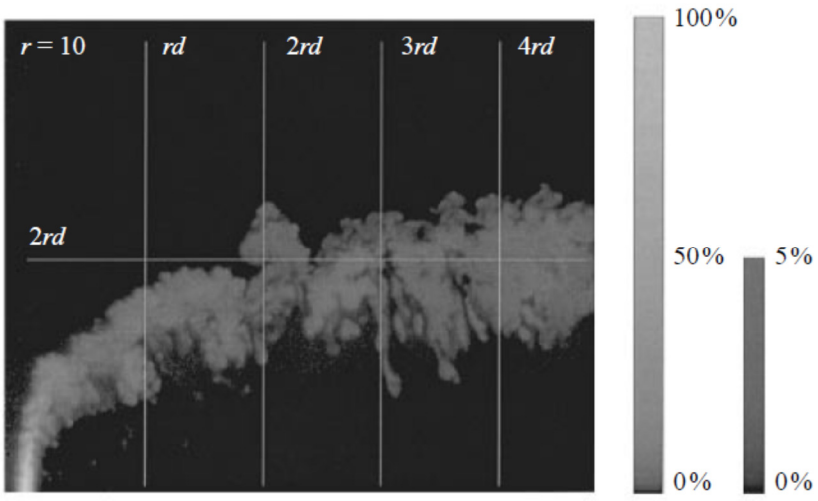

Figure 2.10. Scalar concentration visualization for r=10 taken from Smith and Mungal (1998)

2.4 Entrainment

Entrainment of jet fluid in the mechanism of transverse jets in a crossflow gives a measurement of mixing phenomena. In applications where mixing is to be promoted, JICF is an important way to do so. Researchers such as Muppidi and Mahesh (2008), Shan and Dimotakis (2006), and Smith

and Mungal (1998) etc. all confirm that transverse jets in a crossflow provides better entrainment compared to a free jet in a quiescent liquid.

Mixing and entrainment studies for jets have been done for decades by many researchers. Entrainment rates for free jet had been given by Ricou and Spalding (1961)

$$\frac{\dot{m}}{\dot{m}_0} = 1 + 0.32\frac{s}{d}$$

Where LHS is the mass entrainment ratio, s is the length along jet and d is the jet diameter.

For transverse jets, based on velocity ratio and using momentum transfer argument to turn the jet by crossflow, Hasselbrink and Mungal (2001) proposed

$$\frac{\dot{m}}{\dot{m}_0} = 1 + \frac{r}{AB}\left(\frac{x}{rd}\right)^{1-B}$$

Where r=velocity ratio, A and B are empirical constants given as A=2.1 and B=0.29 approximately.

Using this relation and physical argument Shan and Dimotakis (2006) defined a measurement for mean concentration levels.

For their far field analysis they have compared the entrainment rate to that of free jet by Ricou and Spalding.

It is concluded that transverse jets have higher entrainment rate than free jet in a quiescent liquid. Numerically, DNS studies by Muppidi and Mahesh (2007) also show that transverse jet has higher entrainment compared to free jet. They based their analysis on volume flux of the scalar carrying fluid. They also compared their results with the Ricou-Spalding correlation.

Their simulations also confirm that the transverse jet has more entrainment compared to regular jets.

On their analysis, Muppidi and Mahesh observed that the entrainment on the jet has more contribution from the downstream side compared to upstream side, which is shown on Figure 2.11 (a).

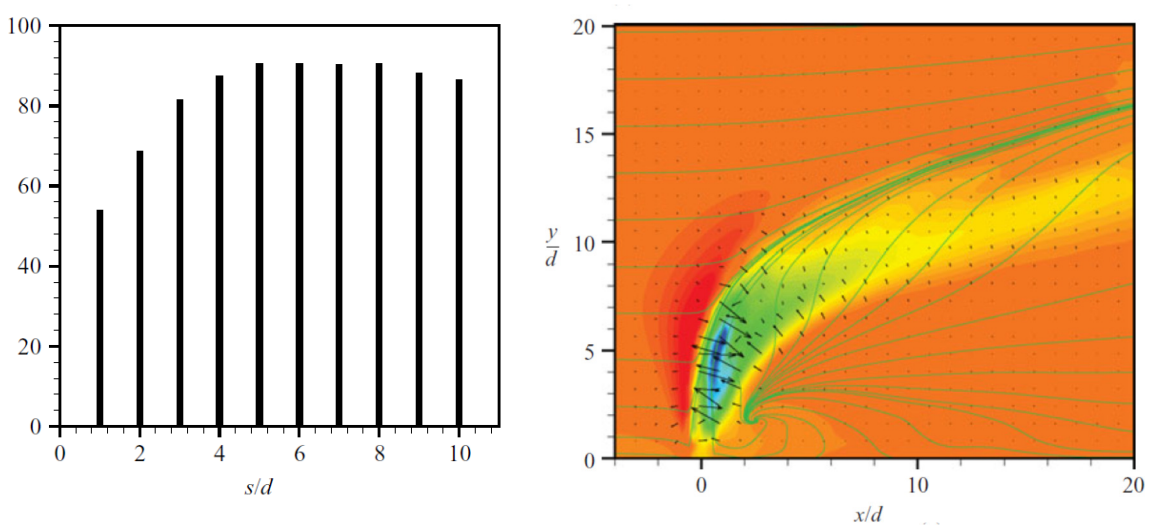

Figure 2.11. (a) Percentage contribution of the downstream side of the jet, to the total entrainment, plotted as a function of the jet length; (b) Contours of pressure on the symmetry plane both taken from Muppidi and Mahesh (2008)

They explain this phenomena on the basis of pressure gradient along the jet (Fig 2.11 (b)). They argue that the crossflow fluid exerts a pressure gradient along the leading edge of the jet and accelerates the jet in the streamwise direction. However, due to presence of pressure gradient near the trailing edge, this acceleration is opposed, which deforms the cross-section. This also decreases the pressure gradient along the trailing edge. The resulting pressure field then drives the downstream crossflow fluid to get entrained in the jet. Hence, more entrainment is observed from the downstream side.

Experimental study of JICF in the Reynolds number ranging from 1,000 to 20,000 was done by Shan and Dimotakis (2006) to analyze the effects of changing Reynolds number on JICF phenomena. They found out that increasing Reynolds number will increase entrainment of the crossflow fluid by the jet.

Entrainment can also be studied by analyzing the decay of scalar concentration of the jet fluid. Entrainment is faster if the decay rate is faster and vice versa. Smith and Mungal (1998) have studied concentration decay for jets in a crossflow with velocity ratios ranging from 5 to 25. From their analysis they have figured out that the centerline concentration remains 100% through the potential core, then decays initially at $s^{-1.3}$ where the trajectory is scaled with rd. This is shown in Figure 2.12. This is higher than that of regular jet where decay is s^{-1}. Broadwell and Breidenthal (1984) had predicted a decay rate of -2/3 for scalar concentration in the far field based on modelling. Smith and Mungal find the possible decay along this rate, after the flow branches from the initial decay discussed above, for the far field. However, for their velocity ratio 5.7 jet, Su and Mungal (2004) found that, initially, concentration decayed faster than 1/s, and beyond s/rd=2.5, the decay rate increased further. They argue that this contrast with Smith and Mungal's data is due to using different jet exit profile (from a pipe) than a nozzle used by them, and conclude that jet exit profile plays a major role in establishing the scaling properties of the mixing field.

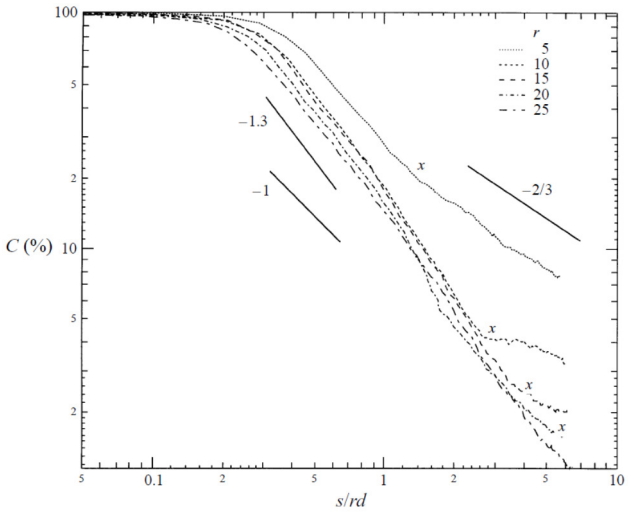

Figure 2.12. Maximum centerline concentration decay plotted with downstream distance s, normalized by rd taken from Smith and Mungal (1998)

2.5 Mixing

Shan and Dimotakis (2006) has described turbulent mixing having three stages: entrainment, stirring, and molecular diffusion. Hence, measure of entrainment is one of the ways to quantify mixing characteristics of jets in a crossflow. Mahesh (2013) provides a physical explanation as how entrainment leads to mixing. Initially, entrainment of the crossflow fluid produces sharp fronts in the concentration. Then turbulent advection increases the surface area of the fronts to a point at which viscosity consumes them. As discussed before, entrainment for transverse jet is higher than that of free jet. Hence, mixing also follows the same rule.

One way to understand and quantify mixing is by measurement of probability density functions of concentration levels. Better peak in PDFs corresponds to more homogenous mixing while shallower peak corresponds to less homogenous mixing. Although researchers have found that jet trajectories, decay of mean concentration, and spatial extent are more sensitive to velocity ratio than jet exit Reynolds number, Shan and Dimotakis (2006) observed that mixing is highly sensitive to Reynolds numbers. Their measurement of PDFs of mixed fluid concentrations for

various Reynolds numbers for same velocity ratio, show this behavior (Figure 2.13). They observed that as the Reynolds number increases, the distribution of mixed fluid develops a peak i.e., -there develops a most-probable concentration in scalar field. Thus, they conclude that scalar field is increasingly stirred and becomes more spatially homogeneous with increasing Reynolds number. Smith and Mungal (1998) also have studied PDFs on the upper edge of the jet for near field to far field. They find out by the behavior of the PDFs that the mixing in near field is different than that of far field. The PDFs behave as non-marching in nature in the near field, whereas in the far-field they behave as tilted in nature. Physically, the preferred value of concentration in a non-marching PDF is invariant across the mixing region; the preferred value in a marching PDF approaches the average layer concentration, merging smoothly at zero concentration and a tilted PDF slants toward the average profile, but the probability of the preferred concentration goes to zero before it merges at zero concentration (Karasso & Mungal, 1996).

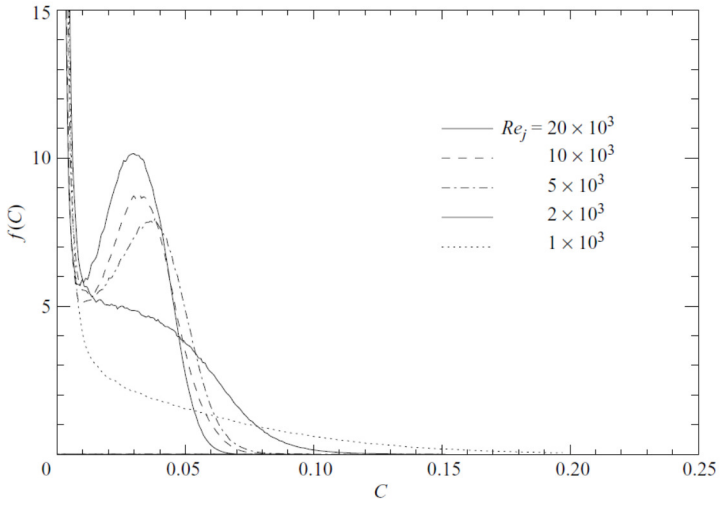

Figure 2.13. Distribution of jet-fluid concentration for varying Reynolds number at r=10 taken from Shan and Dimotakis (2006)

2.6 Stability

Stability analysis for JICF were studied to identify critical Strouhal numbers, velocity ratios, and different flow regimes. Due to advancement of computational power and ability to process large mathematical equations, 3D linear and weakly non-linear stability were performed for jets in a crossflow. Also using various algorithms, most dominant frequency modes have been identified for various aspects of JICF. Notable work on linear stability analysis has been done by Alves et al. (2005), and Karagozian et al. (2010, 2014). Detailed review for stability in transverse jets is done by Karagozian (2010). Important work by Bagheri et al. (2009) deals with decomposition of shear layer frequencies and the most dominant mode of instability is identified. Experiments are done by Megerian et al. (2007) and Davitian et al. (2010), which are also reported in review by Mahesh (2013). Most of the works are done to identify the instability mechanism and its quantification for shear layer instability, which form upstream of the jet as discussed before.

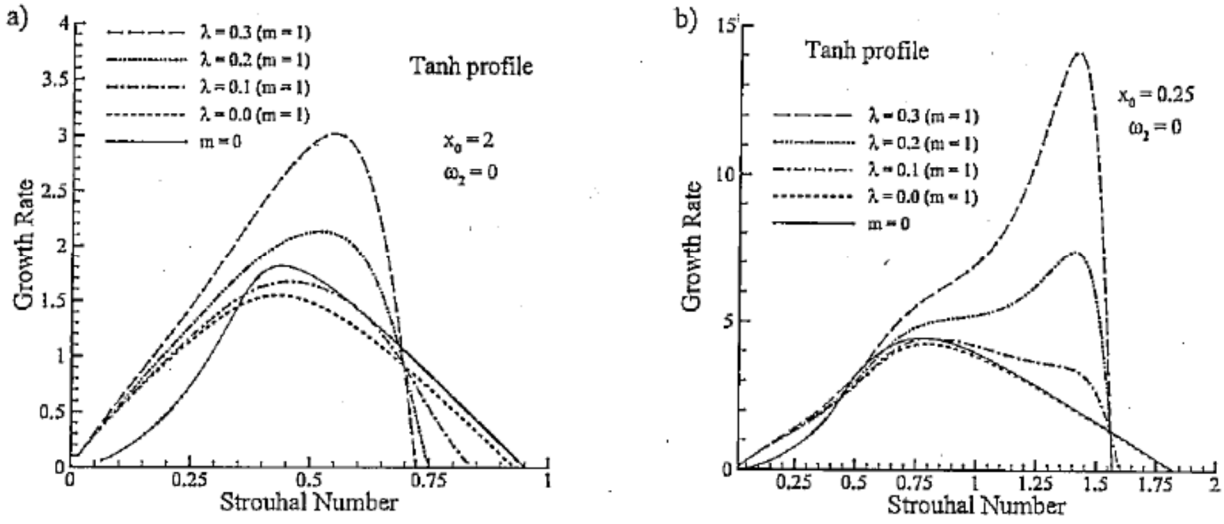

Figure 2.14. Total Growth rate as a function of transverse jet Strouhal Number for several velocity ratios (λ) at streamwise locations of (a) 2 and (b) 0.25 radii beyond jet exit taken from Alves et al. (2005)

Karagozian (2014) identified two kinds of instability regime of shear layer for jets in a crossflow, which depends on the velocity ratio. They have discussed that for iso-density jets, below R≈3.1, the shear layer and jet become absolutely unstable, whereas above that, they are convectively unstable. The spectral behavior of these jets is also different as shown in Figure 2.15 (b), for convectively unstable jets and Figure 2.15(c), for absolutely unstable jets. These are compared to the response as that of free jet (Figure 2.15 (a)). On linear stability analysis, this phenomena is also observed by Alves et al. (2005) (Figure 2.14 (a) and (b)). They explain that absolutely unstable jets mean that the perturbations on the base state grows exponentially with time, i.e. temporally unstable whereas convectively unstable jets mean that the perturbations on the base state grows exponentially as it travels, i.e. spatially unstable. Karagozian (2014) also have identified significant changes in behavior between these jets. For example, the value of Strouhal number associated with the initial instability changes between these regimes. Also, they have observed an insignificant spectral response to sinusoidal flow excitation for absolutely unstable jets, whereas an enhanced response, to such excitations for convectively unstable jets. They further have observed less symmetry for jets with high momentum flux ratio and suggest that the strongest predictor of transverse jet cross-sectional symmetry is in fact the proximity of shear layer roll-up to the jet injection plane, which occurs most commonly for flush jet injection under absolutely unstable shear layer conditions.

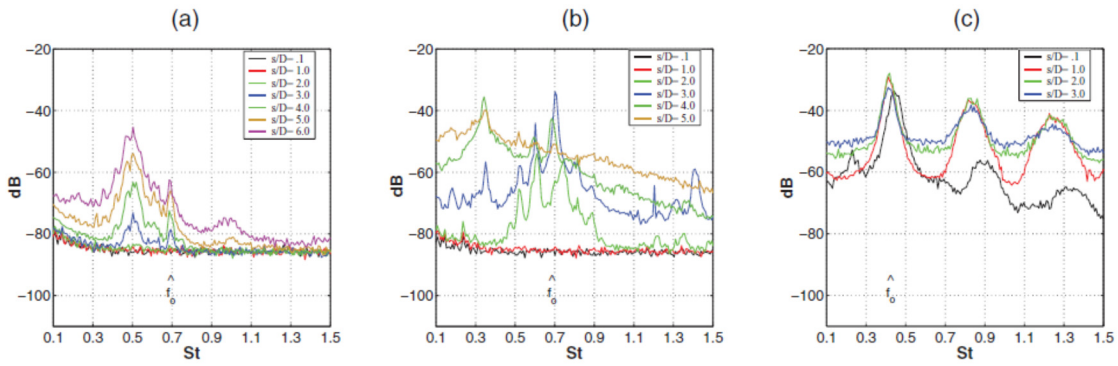

Figure 2.15. Power spectra from hotwire response at various s/D locations along the jet's upstream shear layer (a) free jet; (b) velocity ratio r=6.4 and (c) r=1.15 take from Karagozian (2014)

Mahesh (2013) also reports that at jet-to-crossflow velocity ratios below 3-4, the onset of shear layer instability is driven by mechanisms that may be different from the typical Kelvin-Helmholtz instability. Reporting from Camussi et al. (2002) for this range, he explains that there is a very strong oscillation or waving in the flow, leading to "large scale, periodic" shear-layer rollup. Also citing from the works of Megerian and Davitian, he reports that for velocity ratios greater than 3.2, dominant shear-layer instabilities are observed through measured spectra to be strengthened, to move closer to the jet orifice, and to increase in frequency as the crossflow velocity U∞ increases for a fixed jet Reynolds number. This also compares to the work of Karagozian (2014) of the existence of two different regimes of instability based on velocity ratios.

Numerical modeling studies primarily using modal analysis also suggest this transition of transverse jet from absolutely unstable flow to convectively unstable flow.

Important work on modal analysis of JICF was done by Bagheri et al. (2009). The same configuration was also studied by Rowley et al. (2009). The velocity ratio of jet to that of crossflow was 3.0. The Reynolds number of the crossflow (based on the displacement thickness) was 165 and the ratio between the crossflow displacement thickness to that of jet diameter is 1/3. The

jet was assumed to have a parabolic profile while entering the domain. While Bagheri et al. (2009) extracted the modes using Arnoldi method and a time-stepper approach, Rowley et al. (2009) extracted the modes using Koopman mode analysis (approximated by DMD). The DMD analysis reveals the most dominant mode as the base flow and the second most significant mode corresponding to the shedding of shear layer vortices. Rowley et al. (2009) found that the 6th dominant mode, which has a low frequency, corresponds to large scale positive and negative streamwise velocity near the wall, which can be associated with shedding of the wall vortices. This mode also has structures along the jet trajectory further away from the wall.

Bagheri et al. (2009) reached a similar conclusion. They found the most unstable structures with the highest growth rate occurring on the shear-layer on the CVP. They relate this mode to shear-layer instabilities occurring in a typical JICF. The highest frequency mode also is seen in shear layer, but is symmetric and wraps around the CVP. On the other hand, the low frequency mode has the most pronounced spatial structure at the wall in the wake of the jet.

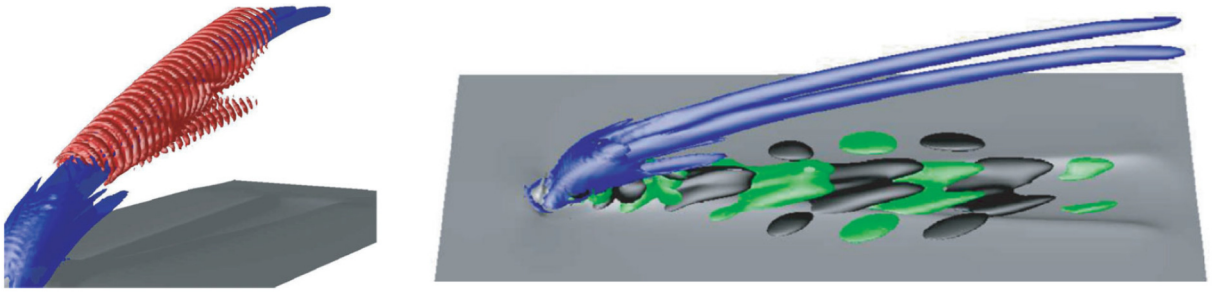

Figure 2.16. (Left) Highest frequency mode shown with red isocontours and (Right) Isocontours of spanwise velocity component pertaining to low-frequency mode shown in green(negative) and black(positive) on the base flow of blue and grey taken from Bagheri et al. (2009)

From their analysis for this configuration of JICF, they find that the unstable wake mode has a smaller growth rate than the shear-layer mode, and conclude that the shear-layer instabilities are the most dominating mechanism.

On the category of low velocity ratio JICF, inclined JICF needs a special mention owing to their wide application in film cooling for turbine blades. Such a JICF was analyzed using DMD by Kalghatgi and Acharya (2014). The velocity ratio was 0.5 and the density ratio of jet to crossflow was 2. Hence, the blowing ratio ($\frac{\rho_j U_j}{\rho_\infty U_\infty}$) is 1. They performed DMD for both velocity and temperature fields. As per the findings, the mode with the strongest growth is the Kelvin-Helmholtz (K-H) mode at a frequency of 3180 Hz (St_θ=0.125). The frequency is found to be consistent with the Fast Fourier Transform (FFT) of the streamwise velocity signal. This mode occurs in the shear layer region.

Through observation, the harmonics of the most dominant mode (star symbols) have considerably lower energy levels. The dominant mode was also analyzed to explain the formation of hairpin vortices downstream after being unstable from K-H instability.

Other lower energy modes are related to the formation of CVP as well. The modal contribution of the temperature fluctuation is shown. The low frequency modes are found to have the largest contribution toward the wall temperature fluctuation and also represent the energetic modes over the entire DMD domain.

All of the above JICF studies are limited to low velocity ratios (<3.1). Hence, they are able to capture a single dominant mode on the domain affecting the dynamics of the flow. Based on studies of JICF by (Karagozian, 2014; Megerian et al., 2007; Davitian et al., 2010) it is now known that JICF exhibits absolute instability below a critical velocity ratio (about 3.1) and exhibits convective instability above that. All the JICF studied above fall under the regime of absolute instability, and that explains the existence of one highly dominant mode and its harmonics in the

whole domain. For velocity ratios in the regime of convective instability, there would exist multiple dominant frequencies along the shear layer. The higher velocity ratio (VR=4) has been analyzed using DMD, by Iyer and Mahesh (2016). In fact, they have compared both the lower velocity ratio (VR=2) JICF and higher velocity ratio (4) JICF to prove the existence of these regimes. Both of these jets are issued from a nozzle.

Iyer and Mahesh (2016) found that for both velocity ratios tested, the dominant DMD modes are the structures in the shear layer. They found the most dominant mode for velocity ratio 2 JICF, is oscillating at a frequency with Strouhal number of 0.65. Another significant mode is a harmonic of the first which has a Strouhal number of 1.3. On the other hand, for velocity ratio 4 JICF most dominant mode has Strouhal number of 0.39 and second most dominant has a Strouhal number of 0.78, which may be suggestive of a harmonic. Iso-contours of Q obtained from the modes of DMD indicate that for absolute instability both the modes of velocity ratio 2 JICF start at the base of the plate, whereas for velocity ratio 4 JICF, 0.78 mode is dominant initially along the shear layer and 0.39 mode becomes dominant along the shear layer after that. This phenomena indicates convective instability where the initial instability at a certain frequency becomes more unstable as it moves along the shear layer. It was also noted that the modes start later in the domain and gets converted to smaller scales faster in the latter case than former case, where both the modes start at the base of the plate and continues to be coherent until some distance. The modes also include the structures near the wall region, which finally gets converted into smaller scales. Thus, they make a distinction between these regimes of instability for JICF using DMD analysis, and validate with the experimental analysis.

Furthermore, to see the effect of the jet inlet profile on stability characteristics, they have tested two cases with pipe like velocity profile with velocity ratio of 2 based on the mean (Rm) and peak (Rp) velocities. DMD was performed for these cases and compared with the nozzle flow DMD. Since all these cases fall in the absolute instability regime, the key comparisons are done in Strouhal number of the unstable mode. For the Rp case, they find the Strouhal number of most dominant mode as 0.15 and second dominant mode as 0.22. For the Rm case, the dominant Strouhal number is 0.075. The Rp case was compared with ratio 3 parabolic inlet of Rowley et al. (2009) where dominant Strouhal number was 0.15.

Furthermore, the modes were different for these cases and were compared to each other. The spanwise isocontours showed most unstable mode as symmetric for nozzle, whereas antisymmetric for both pipe inlet profiles. They compared this with the work of Bagheri et al. (2009) where unstable modes were symmetric for a velocity ratio 3 jet and explain this difference is caused by lower momentum of jet. In conclusion, the jet inlet profiles have a significant effect on the stability characteristics of the jet.

2.7 Turbulence studies

Downstream turbulence of JICF have been studied and measured in detail. In an experiment by Su and Mungal (2004), the second order Reynolds stresses at different stations along the jet for a velocity ratio 5.7 jet was measured. They were able to show how the turbulent stresses change along the jet, i.e. where the turbulence is high in the jet domain along the path of the jet. Furthermore, they provided evidence that the JICF is inherently three-dimensional in nature. It was concluded that the mean scalar concentration decays along the jet trajectory (‘s’). Furthermore, in the near field the concentration levels are higher near the jet symmetry plane

and lesser outwards. However, the decay rates are little different along the spanwise planes. Hence, JICF is a three-dimensional flow field and cannot be predicted correctly using 2D simulations.

The stresses along at different distances from the jet exit in the near field show that initially, turbulence is concentrated more in the shear layer around the jet, which eventually propagates to the central region of the jet. This is evident by two peaks of the stresses as the jet enters the domain and one peak downstream. This apparent breakdown of turbulence from the shear layers to the main jet is sometimes referred to as turbulence breakdown point (TBP).

Same configuration were studied by Muppidi and Mahesh (2007, 2008) numerically using DNS. They were able to obtain validation with the experimental work described above. Furthermore, they studied turbulent kinetic energy along the jet path and also studied budgets of the kinetic energy. They located the points along the domain where the production of turbulence dominates and where the dissipation is significant.

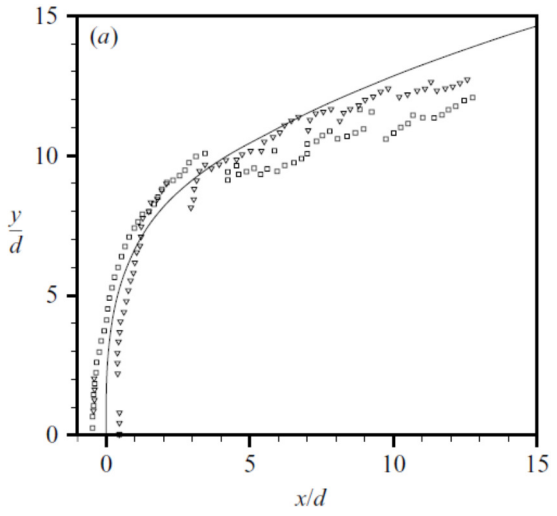

Figure 2.17. Production (square) and Dissipation (triangles) of turbulence kinetic energy along jet trajectory taken from Muppidi and Mahesh (2007)

It is seen from Figure 2.17 that production dominates in the windward side in the near field, whereas dissipation is dominant in the leeward side. Also, after the turbulence is propagated to the main jet, dissipation is seen more on the windward side, whereas production is more in the leeward side. This adds to the above observation that the nature of production and dissipation also changes as the turbulence breakdown happens. They further studied different time scales in the flow field. Using LES, Yuan et al. (1999) also studied the turbulent kinetic energy in their simulation. It is observed by their TKE plots that higher TKE is in the windward side rather than the leeward side.

Also, Ruiz et al. (2015) have studied the flow field described above using fine simulation of LES. They identified the point where the turbulence along the jet transfers from the edges to the central region, and called it Turbulence Breakdown Point (TBP).

They focused on identifying different length scales of turbulence such as integral length scale, Taylor micro scales, and etc., and show their presence in different parts along the domain.

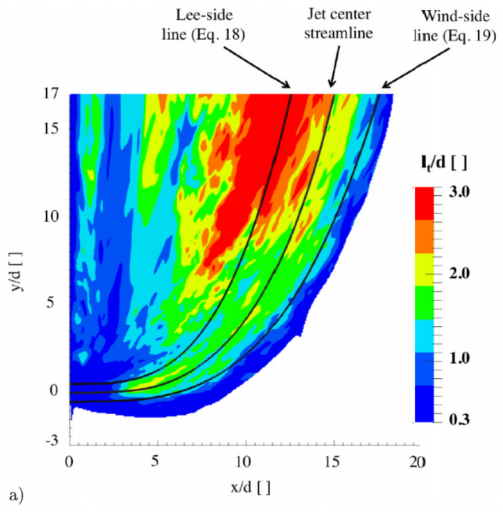

Figure 2.18. Contours of integral length scales of turbulence taken from Ruiz et al. (2015)

It is seen from Figure 2.18, that in the near field smaller length scales dominate, whereas larger length scales are seen in the far field of the jet. These turbulent studies are insightful and they show a way to improve the mixing and entrainment processes of the JICF. It has been understood that turbulence of jet plays a significant role in entrainment of crossflow fluid by the jet (Shan & Dimotakis, 2006).

Comparison studies were conducted for different profiles of jet mean velocity that enters the domain (Muppidi & Mahesh, 2007).

They show that the jet with higher peak velocity (parabolic profile) penetrated deeper into the chamber than with lower peak velocity (mean turbulent velocity). However, detailed comparison of turbulence as described above has not been conducted. Furthermore, as per the authors' knowledge, comparison of turbulence of the JICF for different jet turbulent intensity has not been conducted. Hence, it is an objective to compare and quantify the evolution of different turbulence energies of the jet.

2.8 Rectangular JICF

Different shapes of jets in were studied by researchers. Most popular are cylindrical, rectangular, and elliptical jets. Initially, these jets were studied both experimentally and numerically in a quiescent flow. Different aspect ratios were studied for jets such as rectangular and elliptical jets. Detailed experimental measurements were also conducted for rectangular jets (Quinn, 1991). Extensive review on these jets were done by Gutmark and Grinstein (1999).

Axis switching is a special phenomenon found in jets, which has different lengths in different axes. Most common are rectangular and elliptical jets. As the jet evolves the shorter length becomes larger and the longer edge becomes shorter. After a certain point, the length of the two

axes switch, and hence, the orientation of the jet geometry changes. Furthermore, as the jet travels downstream, another axis switch occurs. The rectangular jets and elliptical jets exhibit 90° axis switching. Even square jets have been shown to exhibit 45° switching. Detailed research were conducted to investigate the physics behind the phenomenon of axis switching. The axis switching was seen to proceed from the deformation of vortex rings by Grinstein (2001). It was further found out that the rib-like, or braid-like, vortices also interacted with the vortex ring and brought about the bifurcations resulting in an axis switch. It was also discussed by Gutmark and Grinstein (1999) that as the aspect ratio of these jets increased, axis switching progressively happened further downstream in the domain. Push and pull by the vorticity surrounding the axis was shown to increase the distance between two longer edges and decrease the distance between two shorter edges by Zaman (1996). Later numerical simulations done by Yu and Girimaji (2005, 2008) and Chen and Yu (2014) using Lattice Boltzman method (LBM) have also explored this axis switching phenomena in detail (Fig 2.19). They have shown axis switching for both laminar and turbulent rectangular jets. For turbulent jets, they have found evidence of saddle back points in the velocity field and explained the mechanism for it as well. They also explained in detail the mechanism of push and pull that happens azimuthally to create axis switching.

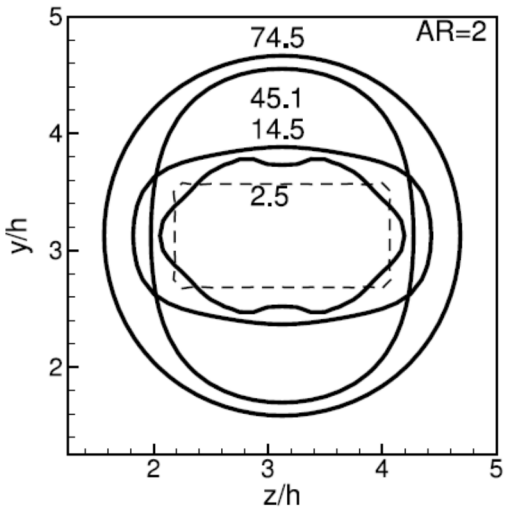

Figure 2.19. Axis switching in aspect ratio 2 jet taken from Chen and Yu (2014)

Jets in a crossflow involving rectangular jets were carried out. Earlier work as such by Krothapalli et al. (1990) has used rectangular jets but only to explain the formation of horseshoe vortex systems. Haven and Kurosaka (1997) studied the lift-off behavior of differently shaped jets using experiments. The conclusion obtained was that the jet trajectory was affected by the vortices formed along the streamwise edge of the jet. As the distances between these vortices increased, it was seen that the jet lift was decreased, making the jet penetration shallower (Fig 2.20).

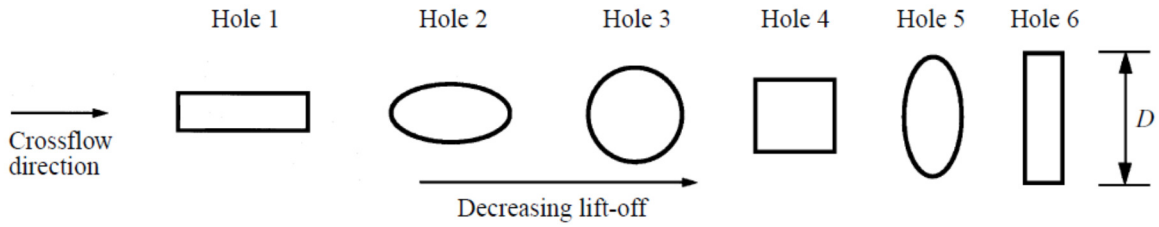

Figure 2.20. Lift off for different geometries taken from Haven and Kurosaka (1997)

Further work by Haven and Kurosaka (1997) analyzed primary and secondary vortices having kidney and anti-kidney for differently shaped jets (rectangular, circular, and elliptical) and explained the physics behind it. However, these studies were limited, to low jet to crossflow

velocity ratio. Different aspect ratios for rectangular jets in crossflow and small blowing ratio was further analyzed by Tyagi (2003) numerically using LES. The work validated some of the conclusions found by Haven and Kurosaka (1997). Furthermore, the effect of different aspect ratio was studied in heat transfer for film cooling applications. It was concluded that low aspect ratio provided better film coverage which helps to enhance film cooling.

2.9 Conclusions

From this review of subsonic transverse jets (JICF) the following conclusions were obtained:

1) Transverse jets are varied in applications from smoke stacks to air injection in turbine blades. However, all of them have some common features and are characterized by some universal coherent structures. These structures are horseshoe vortices, shear layer vortices, counter-rotating vortex pair (CVP), wake vortices, v-shaped vortices and hanging vortices.
2) Scaling the jet by d allows for the study of structural effects dependent on r, 'rd' scaling allows for best fit of trajectory, and 'r^2d' scaling allows to distinguish near field and far field quantitatively. $x/r^2d > 0.2$ is distinguished as far field.
3) Mixing in JICF is primarily affected by entrainment of crossflow fluid by the jet. Entrainment in near field is accomplished by the coherent structures of the shear layer, whereas in the far field is due to CVP. Entrainment is more in downstream region compared to upstream region.
4) Concentration of jet fluid and mixing increases as the jet Reynolds number increases.
5) For velocity ratio less than 3.1, the jet has absolute instability of shear layer structures (where the instability grows with time). For velocity ratio more than 3.1, the jet has

convective instability in shear layer region (where the instability grows as it moves along the shear layer).

6) Numerical stability analysis using DMD concludes that most unstable modes that govern the oscillation of the jet are along the shear layer of JICF.
7) Turbulence analysis reveals the existence of breakdown of turbulence on JICF. Kinetic energies and production also support the above revelation.
8) Different geometries of jet has a significant effect on jets in a crossflow beginning from the jet trajectory itself.
9) Research on rectangular jets reveals that they exhibit 90° axis switching. Furthermore, as the aspect ratio of the jet increases, axis switching happens further downstream.

CHAPTER 3. INLET TURBULENCE GENERATION METHODS

Large Eddy Simulations (LES) are highly sensitive to boundary conditions. Especially the fluctuations of turbulence changes significantly based on the inlet conditions of the simulation, which has a significant influence on the physics downstream of the flow. Hence, a lot of study were conducted on the topic of inlet turbulence for Large Eddy Simulations. Researchers focused on getting correct turbulent conditions at the inlet to use in simulations. One efficient way to study these approaches is to classify them broadly into two methods as done by reviewers (Tabor et al., 2010; Dhamankar et al., 2015; Wu, 2017). First method is characterized as turbulence generation methods, which employ techniques to generate the inlet turbulence using some form of operation on random numbers. This kind of method is known as synthetic turbulence generation methods. The second method is classified as recycling method, which employ techniques to rescale and recycle turbulent flow data from a separate auxiliary simulation or a plane somewhere downstream of the main simulation. As discussed by Wu, the recycling done using an auxiliary simulation can be called strong recycling methods and the recycling done from a plane downstream can be called weak recycling methods.

3.1 Synthesis methods

3.1.1 Spectra

On the synthetic method, notable earlier work was that of Kraichnan et al. (1970). Later researchers such as Smirnov et al. (2001) and Davidson (2007) built upon the original work by Kraichnan. The Random Flow Generation technique (RFG) developed by Smirnov et al. is included in the commercial code ANSYS Fluent. Other later researchers such as Huang et al. (2010) have built upon the earlier work by Smirnov and demonstrated improved results. As reviewed by

Tabor, all these work are based on representation of turbulent fluctuations by a linear sum of sine and cosine functions, with coefficients representing the energy contained in each mode. For example, Smirnov uses

$$u_i(\vec{x},t) = \sqrt{\frac{2}{N}}\sum_{n=1}^{N}\left[p_i^n cos\left(\tilde{k}_j^n \tilde{x}_j + \omega_n \tilde{t}\right) + \left[q_i^n sin\left(\tilde{k}_j^n \tilde{x}_j + \omega_n \tilde{t}\right)\right]\right]$$

Where the first term inside the cosine and sine are normalized with turbulent length scale, the second term with turbulent time scale, and other terms are generated as random numbers. On Smirnov's approach the wave number (k) and frequency (ω) represent a sample of n wave-number and frequencies of the modeled turbulence spectrum.

$$E(k) = 16\left(\frac{2}{\pi}\right)^{1/2} k^4 \exp(-2k^2)$$

In a same manner Davidson uses a cosine term superposition for velocity fluctuations without the use of turbulent time scale.

$$u_i'(x_j) = 2\sum_{n=1}^{N} \hat{u}^n \, cos\left(k_j^n x_j + \Psi^n\right)\sigma_i^n$$

Where

$$\hat{u}^n = \left(E\left(\left|k_j^n\right|\right)\Delta k\right)^{1/2}$$

Furthermore, he samples frequencies and wave numbers from a slightly modified spectrum which is

$$E(k) = \alpha \frac{u_{rms}^2}{k_e} \frac{(k/k_e)^4}{[1+(k/k_e)^2]^{17/6}} e^{\left[-2(k/k_\eta)^2\right]}$$

Where

$k = (k_i k_i)^{1/2}, k_\eta = \epsilon^{1/4}\nu^{-3/4}$, $k_e = \alpha \times 9\pi/L_t$ and L_t is the length scale of the inlet turbulence.

For including the effects of the time scale, he uses an asymmetric time filter for successive realizations of the velocity field.

$$(\mathcal{U}')^m = a(\mathcal{U}')^{m-1} + b(u')^m$$

Where, m is the current time step and $a = \exp(\Delta t/\tau)$, $b = (1-a^2)^{0.5} and\ \tau$ is the inlet turbulent time scale.

Improving on the work of Smirnov, Huang et al. (2010) developed a method called DSRFG (Discretizing and Synthesizing Random Flow generation).In this, he uses a complex energy spectrum defined as

$$E(k) = (3/2)v_0^2\delta(k-k_0)$$

Where v_0 is the rms of velocity in any direction and wave number k is distributed isotropically on the surface of the sphere of radius k_0.

Recent work of Batten et al. (2015) also uses a modification of Smirnov's work in using Cholesky decomposition of stress tensor to replace tensor scaling, and incorporation of the effects of inhomogeneous turbulence and anisotropic length scale effects on the local eddy shapes. They call their method Large Eddy Stimulation (LEST).

Other works in this class of methods are discussed by Wu (2017) in his review as Synthetic Random Fourier Methods (SRFM).

For isotropic turbulence, it is relatively simple to generate signals with physically correct spatial correlations. In this case there is no need of specifying any ad hoc parameters but only an energy spectrum and length scales, and correct probability density functions (PDFs) for random numbers are sufficient. However, the signals generated by this approach lacks correct temporal correlations. So different authors, as discussed above have come up with different physical arguments to generate temporally correlated signals. In an overall sense, this type of method is physically sound in generating correct spatial correlations based on an Energy Spectrum but lacks the inclusion of correct temporal correlations, unless it is modified by using ad hoc parameters.

3.1.2 Synthetic eddy method

Another special method among synthesis methods is known as Synthetic Eddy method (SEM) or sometimes Coherent Eddy Method (CEM). Developed by Jarrin et al. (2006), this method is conceptually simple that it directly injects eddies in the fluid stream, mimicking the turbulent behavior. Eddies are injected randomly in the flow field but their intensities are defined by taking in the effect of Reynolds Stress Tensor. In this method, turbulence is seen as superimposition of coherent structures or "spots". These spots are defined by a shape function (f_σ) which has a compact support $[-\sigma, \sigma]$ considering turbulent length scale (σ) and also satisfies the normalization condition.

$$\frac{1}{\Delta}\int_{-\frac{\Delta}{2}}^{\frac{\Delta}{2}} f_\sigma^2(x)dx = 1$$

Where $\Delta = b - a + 2\sigma$ where a and b are the intervals in which the spots are generated.

Each spot is further assigned a random step value and sign. This spot is then added within a pre-defined volume. Using Taylor's frozen turbulence hypothesis, these spots are advected with the velocity field in the local region. For achieving correct statistics, information about the Reynolds Stress Tensor can be included to match the signal with the statistics. Final form of the signal generated at point x at time t is:

$$u_j'(x,t) = \frac{1}{\sqrt{N}} \sum_{i=1}^{N} \varepsilon_{ij} f_j\big(x - x_i(t)\big)$$

Where ε_{ij} is the sign of vortex i on component j and the independent random steps of values +1 or -1 and N is the number of turbulent spots on the inlet plane.

The final form of reconstructed velocity field from the vortex field generated above is:

$$u_i = \bar{u}_i + a_{ij} u_j'$$

Where a_{ij} is obtained by Cholesky decomposition from the prescribed Reynolds stress tensor and reads

$$\begin{pmatrix} \sqrt{R_{11}} & 0 & 0 \\ R_{21}/a_{11} & \sqrt{R_{22} - a_{21}^2} & 0 \\ R_{31}/a_{11} & (R_{32} - a_{21}a_{31})/a_{22} & \sqrt{R_{33} - a_{31}^2 - a_{32}^2} \end{pmatrix}$$

This inclusion helps in simulating wall bounded flows which has a great variation of statistics at the wall region. Different shapes can be used to construct the eddy and most popular are tent and Gaussian functions. Since these structures have compact support, different length scales can be prescribed at different locations.

Wu (2017) discusses the latest work by different authors using this class of methods for turbulence generation.

3.1.3 Synthetic digital filtering methods

Another class of methods used by researchers to develop synthetic turbulence is known as digital filtering methods. Earlier notable work done in this field is by Klein et al. (2003). Their method is based on digital filtering of random data and is able to reproduce a prescribed second order (one point) statistic as well as autocorrelation function. The process is accomplished by taking a convolution of the random data by the filter. For one dimension, the mathematics underlying this method is given below. If r_m be a series of random data with $\overline{r_m} = 0, \overline{r_m r_m} = 1$, then the velocity signal is generated using

$$u_m = \sum_{n=-N}^{N} b_n r_{m+n}$$

Where b_n are the filter coefficients and N is connected to the support the filter. Since $\overline{r_m r_n} = 0 \; for \; m \neq n$ we can write the autocorrelation as

$$\frac{\overline{u_m u_{m+k}}}{\overline{u_m u_m}} = \sum_{j=-N+k}^{N} b_j b_{j-k} \Big/ \sum_{j=-N}^{N} b_j^2$$

To generate spatially correlated data, an assumption of a special shape of autocorrelation function of velocity is used. For this purpose, Klein et al. (2003) used a form of autocorrelation function which is generally used in case of homogenous turbulence in late stages.

$$R_{uu}(r,0,0) = exp\left(-\frac{\pi r^2}{4L^2}\right) \left(with \; L = L(t) = \sqrt{2\pi\nu(t-t_0)}\right)$$

Where L(t) is the length scale that can be specified. This length scale is specified according to grid spacing as $L = n\Delta x$

The final form of filter coefficient in one dimension that is used is

$$b_k \approx \overline{b_k} \Big/ \left(\sum_{j=-N}^{N} \overline{b_j^2} \right)^{\frac{1}{2}} \; and \; \overline{b_k} \coloneqq exp\left(-\frac{\pi k^2}{2n^2} \right)$$

Finally extending to three dimensions, a three-dimensional filter can be obtained by the convolution of three one-dimensional filters.

$$b_{ijk} = b_i . b_j . b_k$$

Hence, we see this approach is easily adaptable to experimental data since the length scale can be defined locally for each coordinate direction.

As mentioned by Wu (2017), Dietzel et al. (2014) performed a comparative study on 3D homogenous isotropic turbulence by random Fourier method and digital filtering method. He concluded that the decay characteristics are well captured by random Fourier method compared to the filtering method. Ruiz et al. (2015) also used this method to generate turbulent pipe flow for their JICF simulations.

3.1.4 Synthetic volume forcing method

Other novel approaches include addition of synthetic body force terms to Navier-Stokes equations to enhance the triggering of turbulence downstream, or in some cases to maintain turbulence without letting the flow re-laminarize again. Constraints in such methods are discussed by Wu (2017) that the forcing terms should be strong enough to produce rapid

transition, but at the same time be sufficiently weak to avoid leaving notable footprints in the downstream turbulent region. Authors have worked to minimize the difference between the computed and targeted Reynolds stress profiles by dynamically adjusting the forcing terms. This work has been done using wall-normal dynamic forcing in their LES of ZPGSFPBPL by Spille-Kohloff and Kaltenbach (2001) as noted by Wu. Recent work by Alder et al. (2015) have also extended the use of this method to supersonic flows. They first specify a compressible laminar boundary layer of suitable properties at the upstream boundary of the domain. At some distance downstream, they subject the flow to a sharp but localized steady retarding force of sufficient size to induce a small separated region. The resulting shear layer then displays generalized inflection points. Finally, depending on the parameters chosen, the reattaching boundary layer then transitions to turbulence.

3.1.5 Proper orthogonal decomposition based method

Reviews by Dhamankar et al. (2015) and Tabor et al. (2010) give special mention to POD based methods, whereas Wu (2017) includes it in general methods using experiments to generate inlet turbulence data. The concept is explained in detail by Dhamankar et al. (2015). Proper orthogonal decomposition of possibly correlated variables to linearly uncorrelated variables, while preserving the variance as much as possible, gives information about the energy content of the flow. First, POD mode characterizes the largest energy contained in the flow which makes it useful as a representative mode and also the most important in stability analysis. Next, few modes represent next levels of energy content in a cascading process as that of turbulent flow. Hence, only a few modes can describe the major energy processes in the flow. This makes the construction of turbulence based on POD method attractive. Using hot-wire data, Druault et al.

(2004) reconstructed spatial coherent fields and temporal fields and used random signals for incoherent signals. They applied the method to DNS and LES of spatially-evolving mixing layers with encouraging results. However, all researchers point out the limitations of spatial placement of hot-wire probes, which limits the spatial resolutions and temporal resolution limitation of PIV (Particle Image Velocimetry) method. Therefore, as more spatially and temporally correct resolutions are achieved in experiments, these methods will fare better.

3.1.6 Tests and validations

For validations, all of these studies have compared their approach with experiments and/or DNS data. Although a development length is needed for all these approaches, turbulence is eventually triggered and then a turbulent flow is established. Smirnov et al. (2001) have compared their data from flat plate boundary layer with that of experiments, and obtain a good match as shown in the following figure.

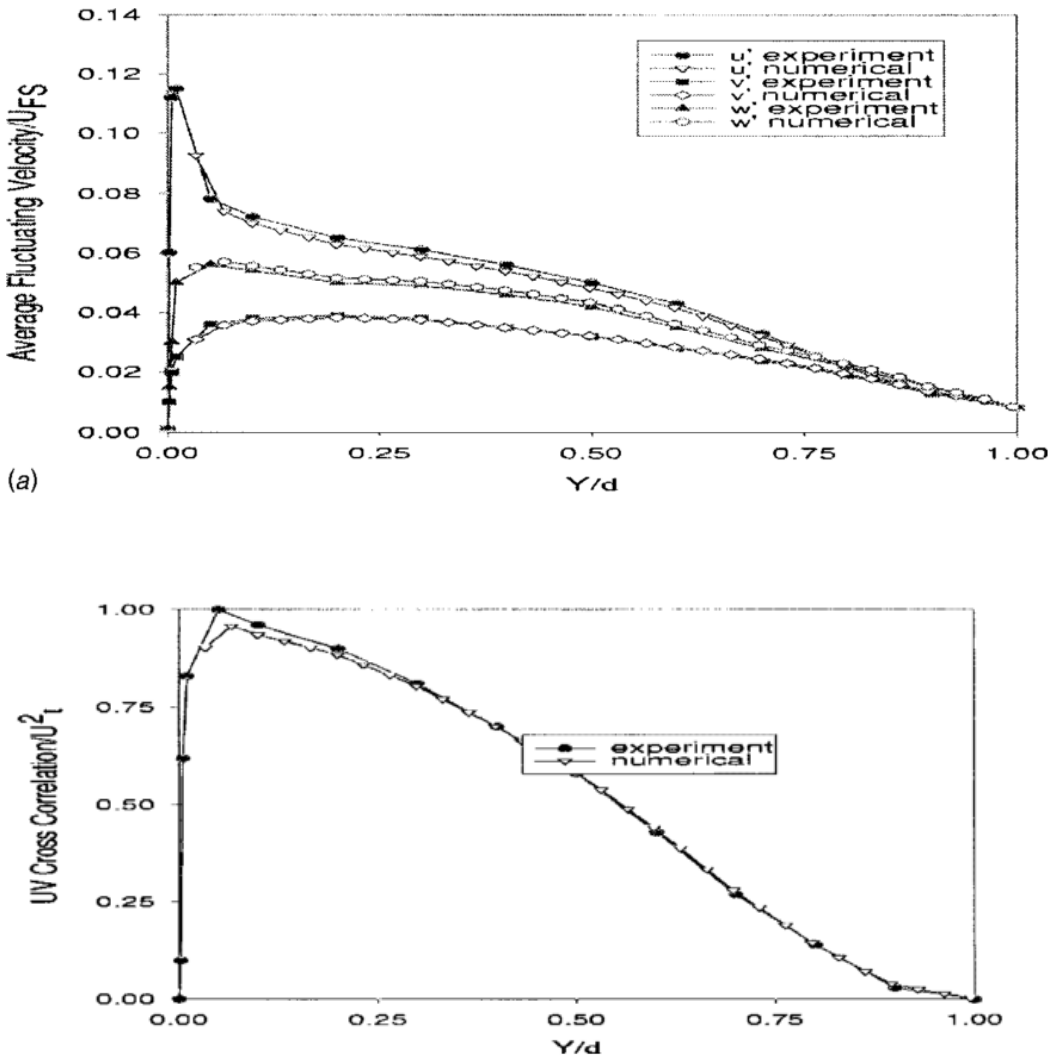

Figure 3.1. Comparison of flat plate boundary layer by Smirnov et al. (2001) with experiments (a) rms velocities; (b) Cross correlations

They have also validated their procedure with flat plate wake flow showing a good match for the rms velocities.

Davidson (2007) also validated their technique with DNS of channel flow (Fig 3.2). They reached within one percent of target friction velocity at 10 boundary layers 'delta' downstream of the flow.

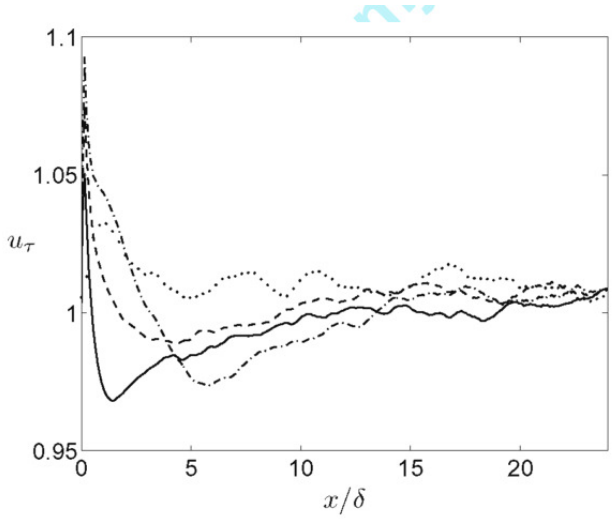

Figure 3.2. Comparison of friction velocity (-,--,-.-) with DNS (...) taken from Davidson (2007)

Huang et al. (2010) on the other hand had compared the DSRFG method with that of turbulent von karman spectrum and shown a good match.

For Fourier's synthesis methods Tabor et al. (2010) has studied the case of channel flow with different techniques and have validated their work with DNS of channel flow data. They have compared mean velocity and shear stress with DNS data and show a good match for different techniques (Fig 3.3). They also compared the same data in terms of wall coordinates as well and show a good validation.

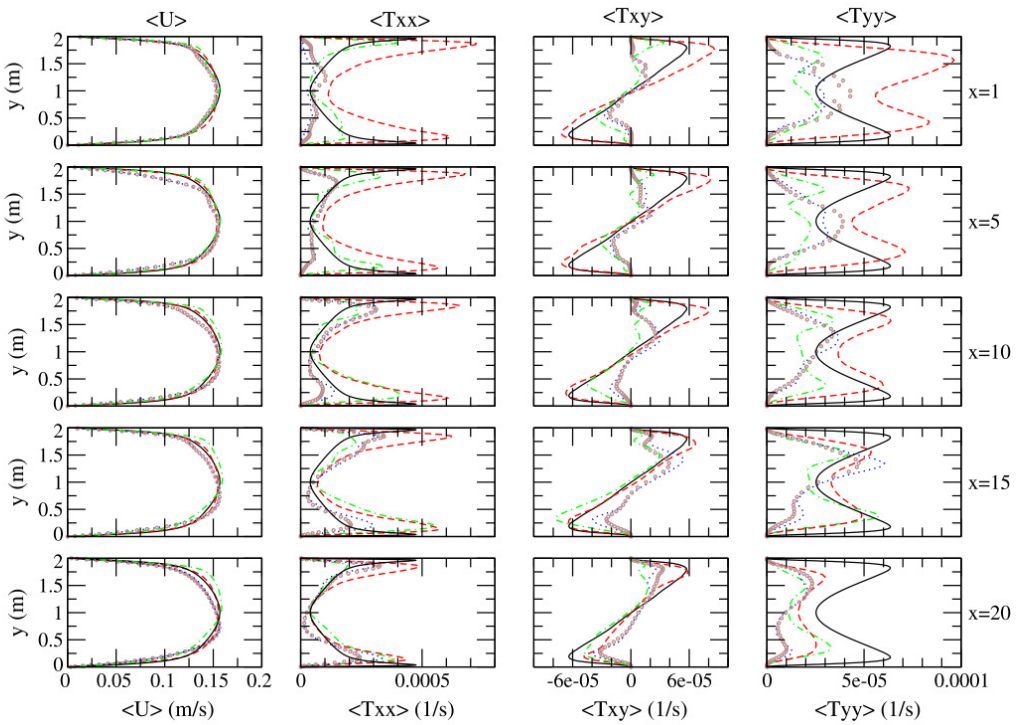

Figure 3.3. Profiles of mean velocity and stress components across the channel. Full line = DNS; dashed line=mapping method; dot-dash line= library look up; dotted line=wavelet synthesis, circle symbols = Fourier series taken from Tabor et al. (2010)

Tabor et al. (2010) also reported the energy spectra shown by different methods at different stations along the channel. They have concluded that the synthesis methods give a good temporal behavior which nearly follows a standard power law with slope of -5/3.

Batten et al. (2015) have used their model to validate decay of isotropic turbulence and the skin friction predictions in a channel bump using their method of Large Eddy Stimulation (LEST).

For validation using Synthetic Eddy Method (SEM), Jarrin et al. (2006) captured the spatial decay of isotropic turbulence.

Jarrin et al. (2006) simulated channel flow using LES and SEM and predicted near correct friction levels and second order correlations within 12 boundary layer thicknesses downstream of the flow (Fig 3.4). The friction Reynolds number in the flow was Re*=395.

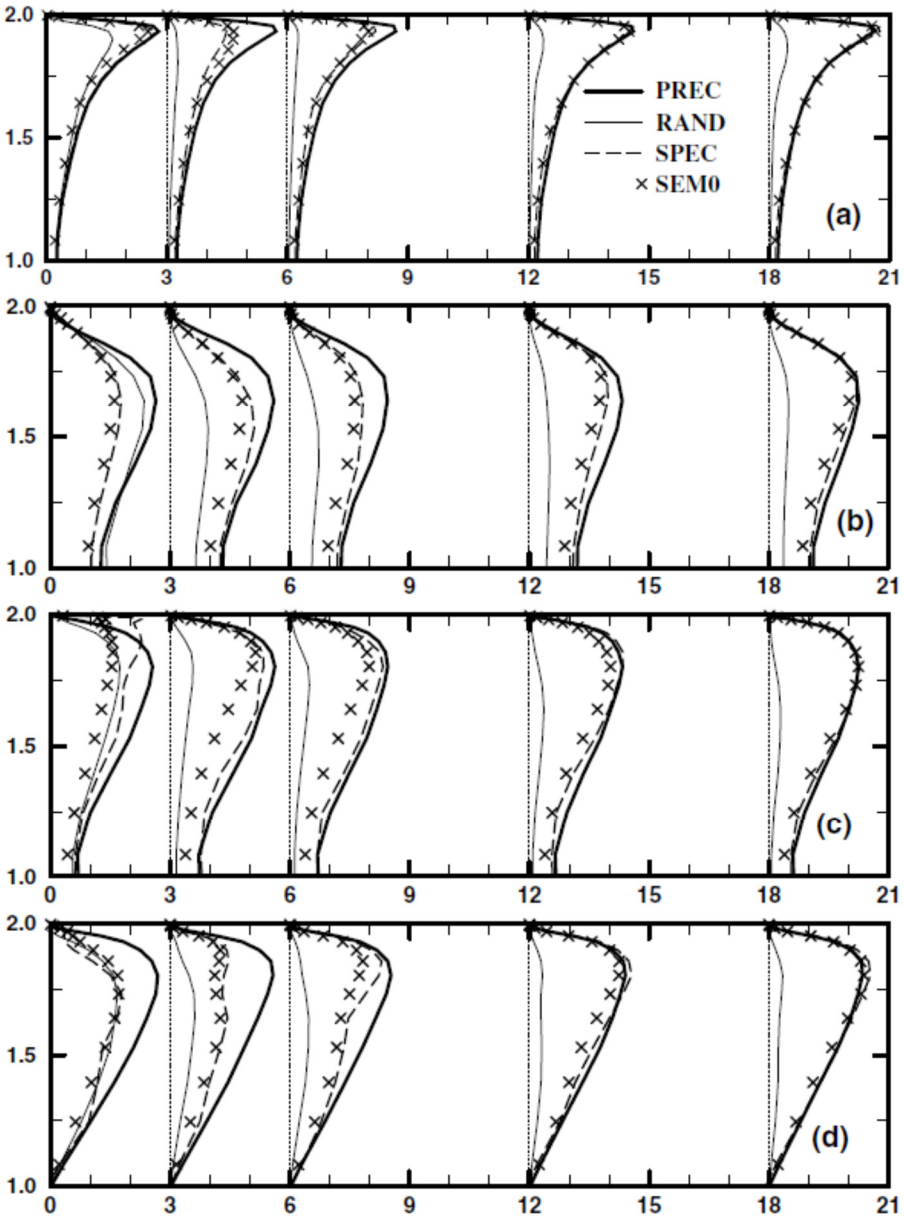

Figure 3.4. Downstream development of the Reynolds stress profiles (a) scaled uu; (b) scaled vv; (c) scaled ww (d) scaled shear stress taken from Jarrin et al. (2006)

SDFM was used by Klein et al. (2003) to validate a plane channel flow compared to DNS data.

Klein et al. (2003) also tested the case of planar turbulent jets in the Reynolds number range from 1000 to 6000. They also studied the two-dimensional DNS of primary breakup of a liquid jet.

Using external body force to trigger turbulence was demonstrated by Alder et al. (2015) to trigger turbulence downstream for supersonic force. The forcing term is implemented in a triangular force field region. The method has been applied to generate the desired profile at several Mach and Reynolds numbers. Figures show validation of boundary layer of a Mach 2.3 flow at a Reynolds number of approximately 17,520.

3.1.7 Sensitivity analysis

One main advantage of synthetic turbulent generation method is that the turbulent length scales, sometimes time scales, and other physical processes can be specified as required in the inlet. This enables the algorithms to have a greater amount of control on input turbulent kinetic energy. Changes in length scales and time scales change the behavior of turbulence, especially in the transition region. All the researchers have agreed on this point and most of them have performed a sensitivity analysis based on these scales and their behavior in the flow domain.

Smirnov et al. (2001) has simulated a flat plate boundary layer based on small and large length scales and compared the results. He compared vorticity contours with that of standard LES solution and showed a similar behavior for both small and large length-scales.

Davidson (2007) in his approach also compared different length scales and concluded that larger length scales are more effective in triggering the momentum equations for turbulence. Sensitivity analysis revealed that the generated turbulence is not much affected by time scales compared to length scales and amplitude of fluctuations. Using smaller and larger length scales up to 1.5 times of the original, and amplitudes also, up to 1.5 times the original, he concluded that the inlet

fluctuations using large length scale and large amplitude are efficient in triggering the momentum equations to resolve turbulence. Davidson also argues that the choice of length scale and time scale should be more dependent on the grid used rather than flow physics, only.

For DSRFG using different length scales, Huang et al. (2010) compared the spatial correlation factor with standard target data. He concluded that best results were obtained using larger length scales about 1.5 times the integral length scale of turbulence. This compared to Davidson's approach also corroborates the fact that larger length scales are better in triggering turbulence.

Tabor et al. (2010) in their review have not analyzed the sensitivity issues of the inlet length and time scales for synthesis methods.

SEM also has the flexibility to specify turbulent length scales as an input. To test the effect of various length scales on simulation, Jarrin et al. (2006) used three different length scales (corresponding to eddy sizes) in the domain. They concluded that length scales corresponding to structures in the central region of channel are large but eventually able to trigger turbulence and predict correct friction velocity downstream. Length scales corresponding to small structures near the wall of the channel seem too small to trigger turbulence downstream and die down. On the other hand, optimum length scales corresponding to structures between the two are able to trigger turbulence and predict friction velocity earlier. They conclude that energy at low wavenumbers is more easily cascaded into higher wavenumbers than the opposite.

Klein et al. (2003) also did some sensitivity analysis on prescribed length scale for plane turbulent jets. Klein concluded that as the jet spreading rate increases, the more kinetic energy is put into

the larger scales. Also, for study of primary breakup of 2D jets, they find from their sensitivity analysis that larger time and length scales lead to a stronger excitation of the jet interface.

3.1.8 Anisotropy

Another important aspect that researchers have addressed for synthetic generation of turbulence is the modeling of anisotropy. Although Kraichnan's method was originally introduced for isotropic turbulence, all researchers have made some modifications for inclusion of anisotropic effects. Most widely used method of generating anisotropic signals is the one used by Lund et al. (1998) where the signal generated u' is added to the mean velocity using the following transformation

$$u_i = \bar{u}_i + a_{ij} u_j'$$

Where a_{ij} is obtained by Cholesky decomposition from the prescribed Reynolds stress tensor and reads

$$\begin{pmatrix} \sqrt{R_{11}} & 0 & 0 \\ R_{21}/a_{11} & \sqrt{R_{22} - a_{21}^2} & 0 \\ R_{31}/a_{11} & (R_{32} - a_{21}a_{31})/a_{22} & \sqrt{R_{33} - a_{31}^2 - a_{32}^2} \end{pmatrix}$$

Although the above transformation divergence-free condition is not guaranteed, researchers still use it and try to get divergence-free condition by some modifications. Other ways also have been used to introduce anisotropy, especially for wall-bounded flows.

Smirnov et al. (2001) selected the length-scale of fluctuations differently in differing spatial directions to generate anisotropy of the fluctuations. Davidson (2007), in his work, only reported generation of isotropic fluctuations, but in work with Billson has used a scaling factor for anisotropy which is taken as the normalized Reynolds stress tensor. This scaling is used to scale the wavenumber and direction, as required for respective directions, and hence anisotropic effects are generated. The DSRFG procedure developed by Huang et al. (2010) was successfully extended to simulate inhomogeneous and anisotropic inflow turbulent flows by incorporating the aligning and remapping procedures. They first aligned the components with the energy spectrum, then scaled the components independently in each direction, and finally, remapped the wavenumber on the surface of the sphere based on the scaled components. In essence, they conserve the total value of the components upon summation and conserve the general energy spectrum used. Batten et al. (2015) has discussed about getting anisotropic behavior by replacing the Reynolds stress tensor scaling of Smirnov by Cholesky decomposition of the tensor.

SEM and SDFM implementation both force the Lund's transformation to generate velocity signals at the inlet.

3.2 Recycling methods

This group is a broad set of methods that use the velocity fluctuations from a separate simulation, or from a library of data, or from the current simulation downstream, to feed at the inlet. The main advantages of these set of methods are that genuine turbulent data can be introduced at the inlet, hence, require little to no additional domain for the flow to develop into turbulence. However, in some of these methods, separate simulations are required, which will increase the computational overhead. For simple flows such as boundary layers, channel flows, and pipe

flows, these methods work efficiently, but for difficult geometries they are difficult to implement. Tabor et al. (2010) and Dhamankar et al. (2015) also discuss about these methods under same classification. However, Wu (2017) also divides this class of methods into two: Strong Recycling Methods and Weak Recycling Methods.

3.2.1 Strong recycling methods

In this method, temporal information of velocity u(x,t) is stored at a plane of an auxiliary simulation and then fed as input to the main simulation. The velocity information may or may not be re-scaled before using as an inlet condition. Cyclic domains to be used as an auxiliary simulation has gained a lot of popularity, especially for simple flows such as channels and pipes. Other ways to generate inflow data is to take temporal velocity information of a pre-prepared library or datasets from experiments. Sometimes, a concurrent simulation was used to generate real-time data to feed as an input to the main simulations. All these methods are discussed in the reviews of Tabor et al. (2010), Dhamankar et al. (2015), and Wu (2017). This type of method is demonstrated effectively in the Fig 3.5 by Dhamankar et al. (2015).

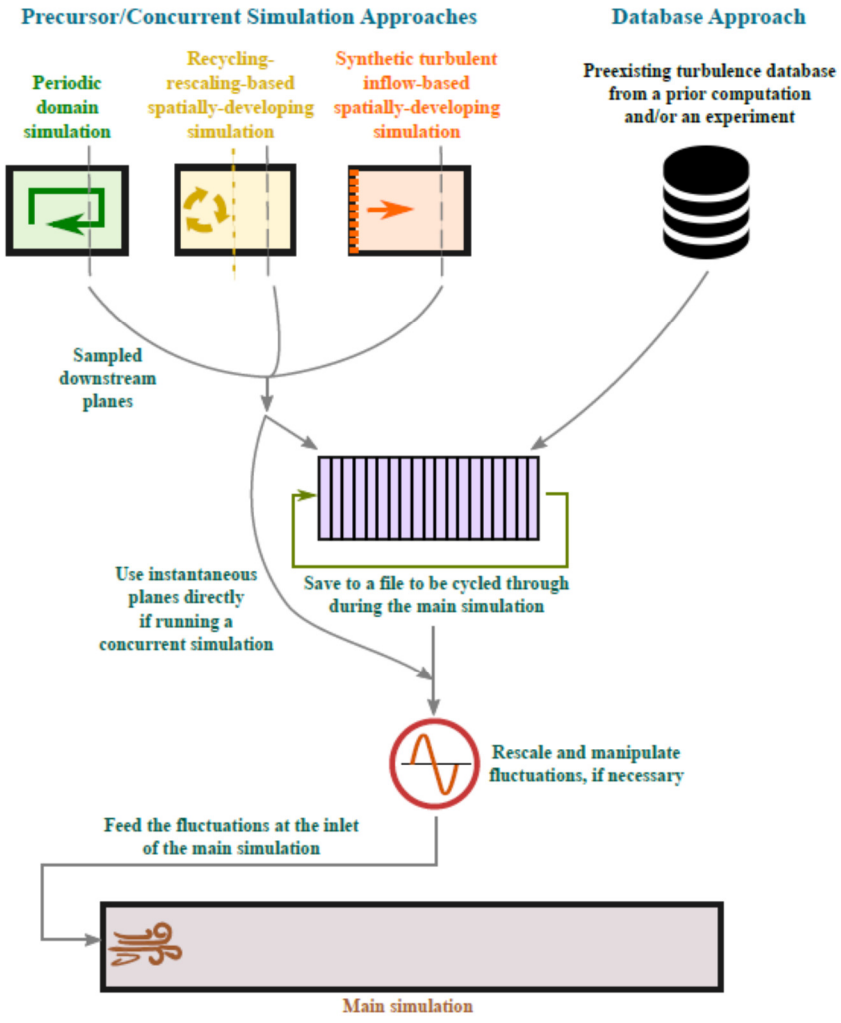

Figure 3.5. Schematic of strong recycling method taken from Dhamankar et al. (2015)

Wu (2017) did extensive research on these methods and highlights some modifications and challenges in utilization for turbulent flows. A primary modification is to sweep along the streamwise direction of the auxiliary periodic simulation domain, at one or multiple selected instants, by invoking Taylor's frozen turbulence hypothesis to acquire the inflow temporal sequence. When adding the information of two or more independent realizations, the sequence may not necessarily maintain two point correlations. Researchers such as Xiong et al. (2004) used a blending zone between two realizations as a remedy, whose linear combination is used to

construct the velocity fields in the blending zone. Major shortcomings, inherent to strong recycling method as highlighted by Wu (2017), is the spurious periodicity that can arise spontaneously in the main spatial simulation, through mechanisms other than the direct reuse and downstream convection of the periodic database fields. He bases this on the evidence provided by Nikitin (2007).

One special variant, of the above discussed method, is using cyclic domains to simulate fully developed flows such as in channels and pipes, and then use the data from one plane of the simulation in the main simulation. The advantage of these methods is that spatially correlated and temporally correlated turbulence data is available, which when used at an inlet in the main simulation does not require any additional length for turbulence to develop. The disadvantages are that they can be used for only simple fully developed flows and require some form of data storage. All the reviewers agree that there is some periodicity involved in extraction of data, since only a limited length is used and requires some time to have fully developed flow variables and correlations. Muppidi and Mahesh (2007) has used this method to generate fully developed turbulent pipe flow for their Jets in a Crossflow (JICF) simulations.

Other methods use the advantage of prepared databases for canonical flows (flat plate boundary layers, channels, pipes etc.). These databases can be prepared by both simulations and experiments. Data storage is an issue but once the database is available, it can be used for the main simulation. However, some challenges are to rescale the data if the database is prepared for some other variations such as Reynolds numbers and geometry etc. Also, if experimental data is used, there is a need of some assumptions to maintain temporally correlated data. This issue is highlighted by Wu (2017) in his review. This method has been used and validated by Schluter

et al. (2004) for swirling flow. They get good results even if they use database of same required flow scenario as the main simulation, or if a different scenario as the main simulation.

3.2.2 Weak recycling method or recycling data from downstream

Although Tabor et al. (2010) and Dhamankar et al. (2015) have included this within precursor simulation and general recycling methods, Wu (2017) has discussed this separately as weak recycling methods. Compared to just simple flows, such as channels and pipes, spatially developing flows pose a considerable challenge to use turbulence parameters at the inlet. Hence, the need was identified to rescale and recycle the flow from downstream of the flow itself. Earlier versions of these methods were used by Wu et al. (1995) for inflow turbulence generation of the Zero Pressure Gradient Smooth Flat Plate Boundary Layer (ZPGSFPBL), by assuming that the flow scales with wall units in the inner region and with boundary layer thickness in the outer region. This method was improved by Lund et al. (1998) building on the work of Spalart et al. (1988). They called this method a modified Spalart method, but currently this method is also styled as Lund, Wu and Squires (LWS) method. Originally Spalart et al. (1988) had devised a method to simulate flows using periodic domains. For spatially developing flows they had to include some "growth terms" in the main Navier-Stokes equations and hence have a complicated set of equations to solve. Modifying this, Lund et al. (1998) recycled sets of data from an auxiliary simulation and reintroduced it at the inlet, after appropriate scaling. Hence, they avoid the complication to have a separate flow solver for the system. Their method can be added to any working flow solver and thus, include turbulence at the inlet. For quantities such as streamwise velocity field, they divide the region as inner and outer and have separate parameters for scaling in both regions. For inner region they scale based on the law of the wall and for the outer region

they scale based on the velocity defect law. Mathematically, the concept as formulated in LWS is discussed below.

$$U_{inlt}^{inner} = \gamma U_{recy}(y_{inlt}^{+})$$

And

$$U_{inlt}^{outer} = \gamma U_{recy}(\eta_{inlt}) + (1-\gamma)U_{\infty}$$

For the fluctuations they scale as:

$$(u_i')_{inlt}^{inner} = \gamma(u_i')_{recy}(y_{inlt}^{+}, z, t)$$

And

$$(u_i')_{inlt}^{outer} = \gamma(u_i')_{recy}(\eta_{inlt}, z, t)$$

The entire scaled field at the inlet is:

$$(u_i)_{inlt} = \left[(U_i)_{inlt}^{innner} + (u_i')_{inlt}^{inner}\right][1 - W(\eta_{inlt})] + [(U_i)_{inlt}^{outer} + (u_i')_{inlt}^{outer}][W(\eta_{inlt})]$$

The weighing function to divide the scales between the two regions is empirically determined and used by Lund.

$$W(\eta) = \frac{1}{2}\left\{1 + tanh\left[\frac{\alpha(\eta - b)}{(1-2b)\eta + b}\right] / tanh(\alpha)\right\}$$

Where $\alpha = 4$ and $b = 0.2$.

For the actual scaling parameter, they decided to take the ratio of friction velocities at the recycle plane and inlet, which is further evaluated from appropriate ratio of momentum thickness at two planes.

$$\gamma = \left(\frac{u_{\tau,inlt}}{u_{\tau,recy}}\right)$$

And

$$u_{\tau,inlt} = u_{\tau,recy}\left(\frac{\theta_{recy}}{\theta_{inlt}}\right)^{1/[2(n-1)]}, n = 5$$

For validations, Lund et al. (1998) have simulated a flat plate boundary layer and used the data extracted from it to feed as an input to a spatially evolving boundary layer. They have validated boundary layer thickness, displacement thickness, and momentum thickness with estimates from momentum integral (Fig 3.6).

Furthermore, they have also validated wall boundary layer profile for channel flows and plotted velocity fluctuations and shear stresses as well, on boundary layer flows. They had also compared simulation data with random fluctuations inflow, as well as parallel flow inflow generation, and concluded that modified Spalart method produces more realistic flows compared to other two.

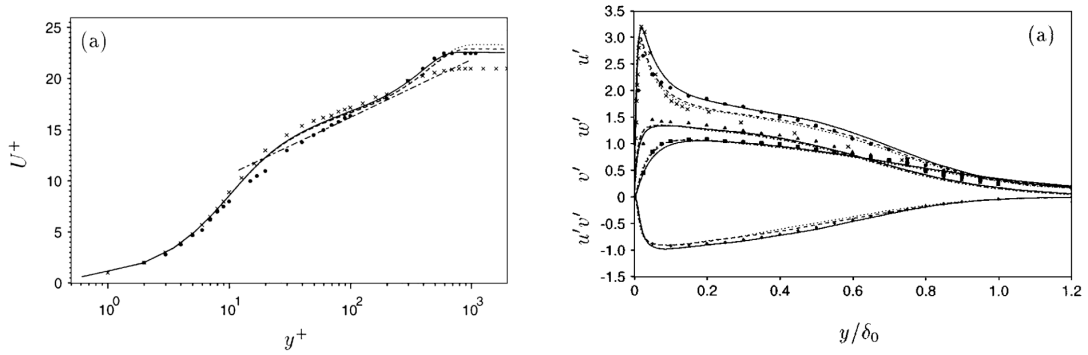

Figure 3.6. Validation of mean flow and rms using modified Spalart method with experiments (symbols) taken from Lund et al. (1998)

They concluded that the method would not require additional domain at the inlet to let the turbulence develop. Although this method was originally using a separate simulation to recycle data, they have further proposed that the method can be used to extract data from the downstream of the same simulation. Since this, a lot of work has been done to improve and resolve issues with the recycling formulation. The challenge of spurious periodicity, as discussed in strong recycling methods, also persists in these methods. Since recycling is done from a plane downstream, abrupt changes in geometry can have effect on the simulation. Hence, researchers such as Spalart (2006) have placed the recycling plane close to the inflow plane and used scaling in the outer only region. To reduce the periodicity, shifting techniques such as constant spanwise shift have been used by authors such as Spalart et al., Jewkes et al. (2011), Arolla and Durbin (2014) etc. to disrupt the coherence between recycling station and inlet plane.

Other researchers such as Araya et al. (2011) have generalized this method to calculate the rescaling parameters dynamically before feeding at the inlet. They have used an additional plane called test plane, somewhere between inlet and recycling planes, to extract the information for rescaling. Mathematically,

$$\frac{(u_\tau/U_\infty)_{inl}}{(u_\tau/U_\infty)_{rec}} = \left(\frac{Re_{\delta inl}}{Re_{\delta rec}}\right)^{\gamma}$$

$$\gamma = \frac{ln[(u_\tau/U_\infty)_{test}/(u_\tau/U_\infty)_{rec}]}{ln[Re_{\delta test}/Re_{\delta rec}]}$$

They have further extended these methods to favorable pressure gradient and weakly adverse pressure gradient flat plate boundary layers successfully. Some of their validations are demonstrated in Fig 3.7.

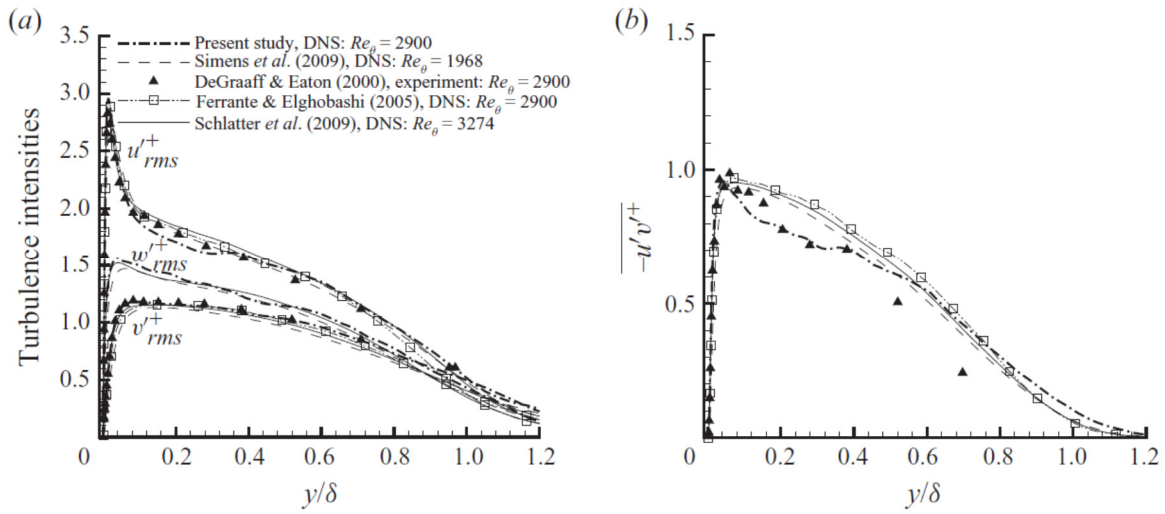

Figure 3.7. Validation of simulation with experiments and DNS; (left) velocity rms; (right) shear stress for Zero Pressure Gradient taken from Araya et al. (2011)

Wu (2017) has done extensive review on use of weak recycling to various applications. Some will be discussed here.

Recycling methods have also been extended to compressible ZPGSFPBL. The main issue in this regard, as highlighted by Wu (2017), is the treatment of thermodynamic variables at the inlet. Works are done by researchers such as Urbin and Knight (2001) for LES of an adiabatic ZPGSFPBL, where the inlet static pressure gradient was assumed to be constant, and mean temperature and

temperature fluctuations are scaled in the same way as mean-wall normal velocity. Other issues, such as spurious periodicity, which is also found in compressible variants of ZPGSFPBL, were tackled by spanwise shifting by authors such as Morgan et al. (2011). Wu (2017) also highlights another issue involving the appearance and gradual amplification, with time, of initially small-amplitude acoustic fluctuations in the free stream. Various authors have worked on the remedy sometimes by using filter to damp out fluctuations (Priebe & Martin, 2010), or by using an additional body force term to silence the waves (Morgan et al., 2014).

Problems using turbulent ZPFSFPBL as a model are required in areas such as marine, wind, aeronautical, and turbomachinery applications. For flow over turbine blades, which have been degraded by combustion products or by cavitation, roughness is an issue. For using this procedure in surfaces which are inherently rough, surface roughness has to be taken into account. When the roughness is small, the modification on the LWS method is done by Nozawa and Tamura (2002). They kept the viscous scaling unchanged but incorporated the equivalent sand-grain roughness height k_s into the correlation between $\frac{\theta_{in}}{\theta_{rec}}$ and $\frac{u_{\tau in}}{u_{\tau rec}}$ with the following sand-grain flat-plate correlation.

$$\frac{\theta_{re}}{\theta_{in}} - 1 = \frac{C'_f}{2}\left(\frac{x_{in}}{\theta_{in}}\right)\frac{1}{1-r}\left[\left(\frac{u_{\tau,in}}{u_{\tau,re}}\right)^{2r-\frac{2}{r}} - 1\right]$$

Where $r = \frac{3.95}{2.87+1.58\log(x_{in}/k_{s)}}$

Where x_{in} is the distance from the leading edge of the plate to the inlet station estimated based on its correlation with θ_{in}. $C'_f(x_{in})$ is the local skin friction coefficient, and $\frac{\theta_{in}}{\theta_{rec}}$ is computed directly from the simulation.

To include the effects of large roughness factor in fully rough boundary layers, Wu (2017) suggests the necessity to include an additional penetration length characterizing the effect of rough elements.

As discussed by Wu, the weak recycling method is a necessary tool in spatially developing LES of many environmental flows, including thermally stratified rough surface boundary layers with pollutant dispersion and microscale urban canopy flow, coupled with mesoscale wind predicted from numerical weather prediction (NWP) codes (see works by Mayor et al. (2002), Kataoka (2008), Tamura (2008), Nakayama et al. (2012)).

3.3 Comparisons between various inflow generation methods

All of the methods as discussed here have been used successfully in more than one application, and each one has its own advantages and disadvantages. Although literature is sparse comparing all of these methods, some comparative studies have been done. This has been discussed by Tabor et al. (2010) in detail. Keating et al. (2004) has worked in comparing the four following methods:

a) a precursor database,

b) a Fourier synthesis method

c) rescaling fluctuations from a lower Reynolds calculation

d) synthetic turbulence generation, with controlled body forces applied at discrete points

They concluded that Fourier synthesis method was able to generate fluctuations with a realistic spectrum, but required a significant length downstream of the inlet for true turbulence to develop. This was ascribed to the reasoning that wall normal fluctuations died down early and hence, they used a forcing term (case d) for wall normal fluctuations, which reduced the development length. Also for precursor database, storage was an issue but still using it also required some development length for turbulence to establish itself. This is due to limitation storage of time series where a larger interval was used. Also with the recycling method, the issue discussed was rescaling for the Reynolds number. It also had a development length somewhere between case b and d.

Tabor et al. (2010) also have compared four methods for a channel flow:

a) Precursor simulation technique

b) Fourier series technique

c) Wavelet synthesis technique

d) Internal mapping (recycling) technique

Based on their simulations using OpenFOAM, they have concluded that synthesis methods (Fourier and Wavelet) are less successful at reproducing the higher order statistics, as they merely mimic the effect of turbulence rather than recreate it. Comparing shear stress, they find out that recycling and precursor simulation methods fare better. However, in wall normal stresses, precursor simulation results are not as good as others illustrating the complications related to maintaining data size. Comparing power law from their spectral analysis, they arrive at a conclusion that the clearest power law spectra are given by the synthesis methods; particularly the wavelet method. The mapping method produces considerable fluctuation in the power law spectrum, whilst the precursor simulation method shows spikes in this region. They ascribe this behavior to repetition of data while generating database for precursor simulations. Overall, they conclude that both approaches have benefits to them. In practice, most methods require the provision of an inlet section in which the non-turbulent inlet fluctuations decay out, but in doing so trigger the development of genuine turbulence within the domain. They also affirm that in terms of accuracy, recycling methods would be better, but may have issues if the flow has to be scaled from a database or if the database size is a problem and may not produce accurate turbulence. On synthesis methods, they conclude that since fluctuations are synthesized somehow, the turbulence is not completely genuine but can only trigger true turbulence downstream. Hence, efficacy of these methods should be judged by the distance it requires to

generate true turbulence. Also, they highlight that synthesis methods have the advantage that they are more easily manipulated to specify the desired turbulent properties, for instance turbulence length scales or energy levels.

Dhamankar et al. (2015) also conclude that each method has its own pros and cons. A method that is suitable for certain flows may not be suitable for other flow scenarios. Citing an example of nozzle simulation in jet noise studies, they highlight that recycling methods (both strong and weak) although more accurate, are a poor choice due to inherent periodicity and also since the size of database to be maintained is very large. Recycling from downstream would be a challenge to implement for parallelized runs, as well as scaling would be a challenge in nozzle simulations. Hence, they pick easily-parallelizable synthetic turbulence generation methods; among those they pick digital filtering method, due to ease of implementation in the structured grid.

Wu (2017) also concluded that strong recycling method, although certainly superior compared to synthetic methods, is still less accurate than extracting inflow turbulence from an accurate spatial transition simulation. He also cites work by Dietzel et al. (2014) who tested synthetic random Fourier method and synthetic digital filtering method and concluded that synthetic random Fourier method captures the decay characteristics as well as velocity correlations better, compared to synthetic digital filtering method.

Based on current research studies, it can be said that all the methods reviewed have their own advantages and disadvantages, which are listed below. All of them have been successfully tested and applied in different flow scenarios.

Advantages of Recycling (Strong and Weak) Methods:

a) These methods use real turbulence data. Therefore, they are highly accurate in producing correct spatial and temporal length scales of turbulence.

b) Ideally require no extra length to trigger turbulence. In reality, this is not always possible, and thus, may require a very short length to generate turbulence.

c) Well suited for simple flows such as channel flows, pipe flows, and flat plate turbulent boundary layers.

Disadvantages of Recycling methods are:

a) For strong recycling methods, the size of the database to store time series poses a challenge.

b) May not get accurate correlations if the data has to be scaled to match the inlet conditions, which destroys the accurate correlations.

c) Due to using repeated data for recycling, periodicity comes in the picture which is difficult to control and avoid.

d) Difficult to implement in parallel computing (weak recycling).

e) Difficult to use recycling for complex geometries, which has abrupt changes downstream.

Advantages of Synthetic turbulent generation methods:

a) Has full flexibility and control for inlet parameters such as length scales, time scales, correlations and intensity levels.

b) Can be easier to implement, even for parallel computing.

c) Can be used in any type of geometry and is not dependent on geometric changes downstream.

Disadvantages of synthetic turbulence methods:

a) Only mimics turbulence but is not actually turbulent; may not have correct spatial and temporal correlations.

b) Requires some development length to trigger correct turbulence.

c) Requires a lot of variables at input (sometimes ad hoc), which in all cases may not be determinable and has to be guessed (Reynolds Tensor, correlations etc.) based on the problem.

It can be concluded that the choice of method to use for inlet turbulence generation is dependent on the simulation requirements.

CHAPTER 4. COMPUTATIONAL METHODS

The compressible flow solver known as Chem3D is used to solve the governing equations for a given geometry. The generated geometry is a block-structured curvilinear mesh with the actual dimensions body fitted to the actual geometry. The mesh is structured and is of hexahedral type. In each hexahedral cell, the primitive variables such as velocity, pressure, temperature etc. are solved in the cell centers whereas the fluxes are solved on the respective face centers of the cell. Since the mesh is block structured, the governing equations are solved for each block which takes the boundary conditions from adjacent blocks via data transfer.

4.1 Governing equations

Generalized conservation principle for any dependent variable is given by:

$$\frac{\partial}{\partial t}(\rho\phi) + \nabla.(\rho \mathrm{u}\phi) = \nabla.(\Gamma\nabla\phi) + S$$

In Cartesian coordinate system the conservation equation can be written as:

$$\frac{\partial}{\partial t}(\rho\phi) + \frac{\partial}{\partial x}(\rho u\phi) + \frac{\partial}{\partial v}(\rho v\phi) + \frac{\partial}{\partial z}(\rho w\phi) = \frac{\partial}{\partial x}\left(\Gamma\frac{\partial\phi}{\partial x}\right) + \frac{\partial}{\partial y}\left(\Gamma\frac{\partial\phi}{\partial y}\right) + \frac{\partial}{\partial z}\left(\Gamma\frac{\partial\phi}{\partial z}\right) + S$$

In more compact form the terms in the RHS can be combined with LHS terms. This form is called the conservative form.

$$\frac{\partial}{\partial t}(\rho\phi) + \frac{\partial}{\partial x}\left(\rho u\phi - \Gamma\frac{\partial\phi}{\partial x}\right) + \frac{\partial}{\partial v}\left(\rho v\phi - \Gamma\frac{\partial\phi}{\partial y}\right) + \frac{\partial}{\partial z}\left(\rho w\phi - \Gamma\frac{\partial\phi}{\partial z}\right) = S$$

In indicial notation it can be written as:

$$\frac{\partial}{\partial t}(\rho\phi) + \frac{\partial}{\partial x_j}\left(\rho u_j\phi - \Gamma\frac{\partial\phi}{\partial x_j}\right) = S$$

The dependent variables can be written in flux terms as a vector. The conservation equation then becomes:

$$\frac{\partial}{\partial t}(Q) + \frac{\partial}{\partial x}(E - \mathrm{E}_v) + \frac{\partial}{\partial v}(F - F_v) + \frac{\partial}{\partial z}(G - G_v) = S$$

And in indicial notation it is:

$$\frac{\partial}{\partial t}(Q) + \frac{\partial}{\partial x_j}(E - E_v)_j = S$$

The variables Q, E, F, G are vectors of inviscid fluxes. The terms E_v, F_v, G_v are the viscous fluxes and S is the vector for body force terms. The vectors of fluxes are given in the following sections.

In 'Chem3D' the Favre-averaged Navier Stokes equations are solved. For curvilinear geometry, the equations need to be transformed in three directions (ξ, η, ζ) from regular coordinates (x,y,z). To transform the equations, the derivatives of the direction (called metric terms) and Jacobian are used to multiply the dependent variables. The final governing equation applicable for curvilinear system (Fig 4.1) is given below.

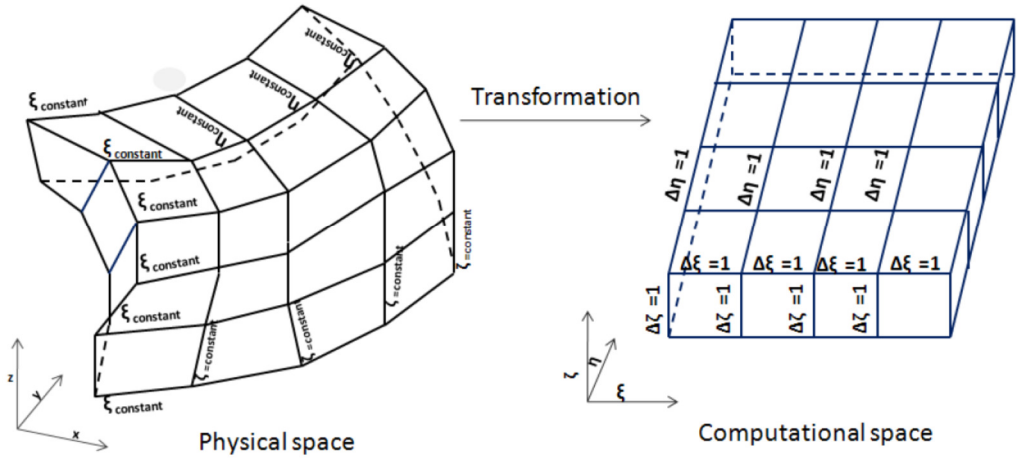

Figure 4.1. Transformation from physical to computational space taken from Roy (2010)

Denoting the differentials as $\partial_t = \frac{\partial}{\partial_t}$, we can write the governing equations in a compact form as:

$$\partial_t \hat{Q} + \partial_{\xi}\left(\hat{E} - \hat{E}_v\right) + \partial_{\eta}\left(\hat{F} - \hat{F}_v\right) + \partial_{\zeta}\left(\hat{G} - \hat{G}_v\right) = \hat{H}$$

The 'i' th species partial pressure, density, mass fraction, molecular weight and enthalpy is $p_i, \rho_i, Y_i, W_i, h_i$ and the thermodynamic pressure, mixture density, velocity components and temperature are given by $p, \rho, u, v, w, and\ T$ respectively. Furthermore, all species are assumed to obey an equation of state $p_i = \rho_i RT/W$. The terms involved in the above equations are described below:

The flux terms are:

$$\hat{Q} = \frac{1}{J} Q$$

$$\hat{E} = \frac{1}{J}\left(\xi_x E + \xi_y F + \xi_z G\right)$$

$$\hat{F} = \frac{1}{J}\left(\eta_x E + \eta_y F + \eta_z G\right)$$

$$\hat{G} = \frac{1}{J}\left(\zeta_x E + \zeta_y F + \zeta_z G\right)$$

$$\hat{E}_v = \frac{1}{J}\left(\xi_x E_v + \xi_y F_v + \xi_z G_v\right)$$

$$\hat{F}_v = \frac{1}{J}\left(\eta_x E_v + \eta_y F_v + \eta_z G_v\right)$$

$$\hat{G}_v = \frac{1}{J}\left(\zeta_x E_v + \zeta_y F_v + \zeta_z G_v\right)$$

$$\hat{H}_g = \frac{1}{J} H_g$$

The term J is the Jacobian of the transformation.

The inviscid flux vectors are:

$$Q = [\rho Y_1, \ldots, \rho Y_N, \rho u, \rho v, \rho w, E_t]^T$$

$$E = [\rho u Y_1, \ldots, \rho u Y_N, \rho u^2 + p, \rho uv, \rho uw, (E_t + p)u]^T$$

$$F = [\rho v Y_1, \ldots, \rho v Y_N, \rho uv, \rho v^2 + p, \rho vw, (E_t + p)v]^T$$

$$G = [\rho w Y_1, \ldots, \rho w Y_N, \rho uw, \rho vw, \rho w^2 + p, (E_t + p)w]^T$$

The viscous fluxes are:

$$E_v = \left[q_{x1}, \ldots, q_{xN}, \tau_{xx}, \tau_{xy}, \tau_{xz}, u\tau_{xx} + v\tau_{xy} + w\tau_{xz} + q_{x_e}\right]^T$$

$$F_v = \left[q_{y1}, \ldots, q_{yN}, \tau_{yx}, \tau_{yy}, \tau_{yz}, u\tau_{yx} + v\tau_{yy} + w\tau_{yz} + q_{y_e}\right]^T$$

$$G_v = \left[q_{z1}, \ldots, q_{zN}, \tau_{zx}, \tau_{zy}, \tau_{zz}, u\tau_{zx} + v\tau_{zy} + w\tau_{zz} + q_{z_e}\right]^T$$

Total energy in the above terms is given by:

$$E_t = \rho\left[e + \tfrac{1}{2}(u^2 + v^2 + w^2)\right]$$

Stress components are determined as:

$$\tau_{xx} = 2\mu_e\partial_x u - \frac{2}{3}\mu_e\left(\partial_x u + \partial_y v + \partial_z w\right)$$

$$\tau_{yy} = 2\mu_e\partial_y v - \frac{2}{3}\mu_e\left(\partial_x u + \partial_y v + \partial_z w\right)$$

$$\tau_{zz} = 2\mu_e\partial_z w - \frac{2}{3}\mu_e\left(\partial_x u + \partial_y v + \partial_z w\right)$$

$$\tau_{xy} = \tau_{yx} = \mu_e\left(\partial_x u + \partial_y v\right)$$

$$\tau_{xz} = \tau_{zx} = \mu_e(\partial_z u + \partial_x w)$$

$$\tau_{yz} = \tau_{zy} = \mu_e\left(\partial_z v + \partial_y w\right)$$

Energy fluxes used in viscous flux terms are

$$q_{x_e} = k_e\partial_x T + \rho\sum_{s=1}^{N} h_s D_{sm}\partial_x Y_s$$

$$q_{y_e} = k_e\partial_y T + \rho\sum_{s=1}^{N} h_s D_{sm}\partial_y Y_s$$

$$q_{z_e} = k_e \partial_z T + \rho \sum_{s=1}^{N} h_s D_{sm} \partial_z Y_s$$

Where T is the temperature and $k_e = k_l + C_{pm}\, \mu_t / Pr_t$

The vectors represented by H are the source terms.

4.2 Preconditioning

To re-scale the acoustic scales to match the convective scales, a low Mach number preconditioning was used (Weiss & Smith, 1995). For this, a pseudo time derivative of the dependent variable vector is added to the above transport equations. This allows for the equations to be stable at different Reynolds numbers and to converge in a stable manner.

$$\Gamma\, \partial_\tau \hat{U} + \partial_t \hat{Q} + \partial_\xi \left(\hat{E} - \hat{E}_v\right) + \partial_\eta \left(\hat{F} - \hat{F}_v\right) + \partial_\zeta \left(\hat{G} - \hat{G}_v\right) = \hat{H}$$

The dependent variable vector is given as:

$$\hat{U} = \frac{1}{J} [p_1, p_2, \dots, p_N, u, v, w, T]^T$$

The pre-conditioning matrix is defined as:

$$\Gamma = \begin{bmatrix} \frac{W_1}{RT}+\Theta Y_1 & \Theta Y_1 & \cdots & \Theta Y_1 & 0 & 0 & 0 & -\frac{\rho_1}{T} \\ \Theta Y_2 & \frac{W_2}{RT}+\Theta Y_2 & \cdots & \Theta Y_2 & 0 & 0 & 0 & -\frac{\rho_2}{T} \\ \vdots & \vdots & \ddots & \vdots & \vdots & \vdots & \vdots & \vdots \\ \Theta Y_N & \Theta Y_N & \cdots & \frac{W_N}{RT}+\Theta Y_N & 0 & 0 & 0 & -\frac{\rho_N}{T} \\ u\left(\Theta+\frac{W_1}{RT}\right) & u\left(\Theta+\frac{W_2}{RT}\right) & \cdots & u\left(\Theta+\frac{W_N}{RT}\right) & \rho & 0 & 0 & -\frac{\rho u}{T} \\ v\left(\Theta+\frac{W_1}{RT}\right) & v\left(\Theta+\frac{W_2}{RT}\right) & \cdots & v\left(\Theta+\frac{W_N}{RT}\right) & 0 & \rho & 0 & -\frac{\rho v}{T} \\ w\left(\Theta+\frac{W_1}{RT}\right) & w\left(\Theta+\frac{W_2}{RT}\right) & \cdots & w\left(\Theta+\frac{W_N}{RT}\right) & 0 & 0 & \rho & -\frac{\rho w}{T} \\ \alpha_1 & \alpha_2 & \cdots & \alpha_N & \rho u & \rho v & \rho w & \rho\left(C_{pm}-\frac{H}{T}\right) \end{bmatrix}$$

where

$$U_{ref} = min\left[a^2, \max\left(\left|\vec{V}\right|^2, K\left|\vec{V}_\infty\right|^2\right)\right]$$

$$\Theta = \frac{1}{U_{ref}^2} - \frac{1}{a^2}$$

$$a_s = H\left(\Theta + \frac{W_s}{RT}\right) - 1$$

Where H is the enthalpy per unit mass, V is the velocity, Uref is the reference velocity, a is the sound speed and K is a constant.

4.3 Discretization schemes

The computational directions (ξ, η, ζ) are denoted by (j, k, and l) respectively. For the following equations, 'n' is used to denote physical time step, and 'p' is used to denote pseudo time step. 'i' denotes a general variable which can be either j, k, or l.

The physical time step is discretized with second order backward 3 –point differencing.

$$\frac{\partial \hat{Q}_i}{\partial t} = \frac{3\hat{Q}_i^{n+1} - 4\hat{Q}_i^{n} + \hat{Q}_i^{n-1}}{2\Delta t}$$

On the other hand, the pseudo time is discretized using Euler differencing method.

$$\frac{\partial \hat{U}_i^{n,p+1}}{\partial \tau} = \frac{\hat{U}_i^{n,p} - \hat{U}_i^{n,p-1}}{\Delta \tau}$$

The convective terms are discretized using 5th order accurate WENO (Weighted Essentially Non-Oscillating) scheme. Second order accurate central differencing is used for viscous fluxes. The discretized version of the governing equations become:

$$\frac{\Gamma}{\Delta \tau}\left(\hat{U}_i^{p+1,n+1} - \hat{U}_i^{p,n+1}\right) + \frac{1}{2\Delta t}\left[3\hat{Q}_i^{p+1,n+1} - 4Q_i^{n} + Q_i^{n-1}\right]$$

$$+\left[\hat{E} - \hat{E}_v\right]_{j+1}^{p+1,n+1} - \left[\hat{E} - \hat{E}_v\right]_{j-1}^{p+1,n+1}$$

$$+\left[\hat{F} - \hat{F}_v\right]_{k+1}^{p+1,n+1} - \left[\hat{F} - \hat{F}_v\right]_{k-1}^{p+1,n+1}$$

$$+\left[\hat{G} - \hat{G}_v\right]_{l+1}^{p+1,n+1} - \left[\hat{G} - \hat{G}_v\right]_{l-1}^{p+1,n+1} = \hat{H}_i^{p+1,n+1}$$

Solution is in the form of change of the dependent variable vector. It is denoted as:

$$\delta U_i^{p+1} = \hat{U}_i^{p+1} - \hat{U}_i^{p}$$

Let vector $\hat{P}$ denote the fluxes $\hat{E}, \hat{F}\ and\ \hat{G}$. The linearization for the inviscid flux terms, viscous flux terms, conserved variable vector and source terms are given by:

$$\hat{P}_{i+\frac{1}{2}}^{p+1,n+1} = \hat{P}_{i\pm\frac{1}{2}}^{p,n+1} + \partial_{\hat{U}}\hat{P}_{i\pm\frac{1}{2}}\delta U_{i\pm\frac{1}{2}}^{p+1,n+1}$$

$$\hat{P}_{v(i+\frac{1}{2})}^{p+1,n+1} = \hat{P}_{v(i\pm\frac{1}{2})}^{p,n+1} + \partial_{\hat{U}}\hat{P}_{v(i\pm\frac{1}{2})}\delta U_{i\pm\frac{1}{2}}^{p+1,n+1}$$

$$\hat{Q}_i^{p+1,n+1} = \hat{Q}_i^{p,n+1} + \partial_{\hat{U}}\hat{Q}_i\delta U_i^{p+1,n+1}$$

$$\hat{H}_i^{p+1,n+1} = \hat{H}_i^{p,n+1} + \partial_{\hat{U}}\hat{H}_i\delta U_i^{p+1,n+1}$$

The Jacobian terms for inviscid flux terms, viscous flux terms, conserved variable terms and source terms are given respectively.

$$\partial_{\hat{U}}\hat{P} = \begin{bmatrix} \frac{UW_1}{RT} & 0 & \cdots & 0 & \rho_1\kappa_x & \rho_1\kappa_y & \rho_1\kappa_z & -\frac{\rho_1 U}{T} \\ 0 & \frac{UW_2}{RT} & \cdots & 0 & \rho_2\kappa_x & \rho_2\kappa_y & \rho_2\kappa_z & -\frac{\rho_2 U}{T} \\ \vdots & \vdots & \ddots & \vdots & \vdots & \vdots & \vdots & \vdots \\ 0 & 0 & \cdots & \frac{UW_N}{RT} & \rho_N\kappa_x & \rho_N\kappa_y & \rho_N\kappa_z & -\frac{\rho_N U}{T} \\ Uu\frac{W_1}{RT}+\kappa_x & Uu\frac{W_2}{RT}+\kappa_x & \cdots & Uu\frac{W_N}{RT}+\kappa_x & \rho(U+u\kappa_x) & \rho u\kappa_y & \rho u\kappa_z & -\frac{\rho Uu}{T} \\ Uv\frac{W_1}{RT}+\kappa_y & Uv\frac{W_2}{RT}+\kappa_y & \cdots & Uv\frac{W_N}{RT}+\kappa_y & \rho v\kappa_x & \rho(U+v\kappa_y) & \rho v\kappa_z & -\frac{\rho Uv}{T} \\ Uw\frac{W_1}{RT}+\kappa_z & Uw\frac{W_3}{RT}+\kappa_z & \cdots & Uw\frac{W_N}{RT}+\kappa_z & \rho w\kappa_x & \rho w\kappa_y & \rho(U+w\kappa_z) & -\frac{\rho Uw}{T} \\ Uh_{t1}\frac{W_1}{RT} & Uh_{t2}\frac{W_2}{RT} & \cdots & Uh_{tN}\frac{W_N}{RT} & \rho(uU+H\kappa_x) & \rho(vU+H\kappa_y) & \rho(wU+H\kappa_z) & \rho U\left(C_{pm}-\frac{H}{T}\right) \end{bmatrix}$$

where $U = \kappa_x u + \kappa_y v + \kappa_z w$ is the contravariant velocity. The generic metric terms $\kappa = \xi\ for\ \hat{P} = \hat{E}$,

$\kappa = \eta\ for\ \hat{P} = \hat{F}$, and $\kappa = \zeta\ for\ \hat{P} = \hat{G}$.

$$\partial_{\hat{U}}\hat{P}_v = \begin{bmatrix} \Lambda D_{im}\beta_1(1-Y_1) & \Lambda D_{im}\beta_2 Y_1 & \cdots & \Lambda D_{im}\beta_N Y_1 & 0 & 0 & 0 & 0 \\ \Lambda D_{im}\beta_1 Y_2 & \Lambda D_{im}\beta_2(1-Y_2) & \cdots & \Lambda D_{im}\beta_N Y_2 & 0 & 0 & 0 & 0 \\ \vdots & \vdots & \ddots & \vdots & \vdots & \vdots & \vdots & \vdots \\ \Lambda D_{im}\beta_1 Y_N & \Lambda D_{im}\beta_2 Y_N & \cdots & \Lambda D_{im}\beta_N(1-Y_N) & 0 & 0 & 0 & 0 \\ 0 & 0 & \cdots & 0 & \mu_e\left(\Lambda+\frac{\kappa_x^2}{3}\right) & \mu_e\frac{\kappa_x\kappa_y}{3} & \mu_e\frac{\kappa_x\kappa_z}{3} & 0 \\ 0 & 0 & \cdots & 0 & \mu_e\frac{\kappa_y\kappa_x}{3} & \mu_e\left(\Lambda+\frac{\kappa_y^2}{3}\right) & \mu_e\frac{\kappa_y\kappa_z}{3} & 0 \\ 0 & 0 & \cdots & 0 & \mu_e\frac{\kappa_z\kappa_x}{3} & \mu_e\frac{\kappa_z\kappa_y}{3} & \mu_e\left(\Lambda+\frac{\kappa_z^2}{3}\right) & 0 \\ \Lambda\beta_1(h_1-h_m) & \Lambda\beta_2(h_2-h_m) & \cdots & \Lambda\beta_N(h_N-h_m) & \pi_u & \pi_v & \pi_w & k_e\Lambda C_{pm} \end{bmatrix}$$

The generic metric terms $\kappa = \xi \; for \; \hat{P} = \hat{E}, \kappa = \eta \; for \; \hat{P} = \hat{F}$, and $\kappa = \zeta \; for \; \hat{P} = \hat{G}$.

$$\Lambda = \kappa_x^2 + \kappa_y^2 + \kappa_z^2$$

$$\beta_i = \frac{W_i}{\rho RT}$$

$$\pi_u = \mu_e\left[\left(\Lambda+\frac{\kappa_x^2}{3}\right)u + \frac{\kappa_x\kappa_y}{3}v + \frac{\kappa_x\kappa_z}{3}w\right]$$

$$\pi_v = \mu_e\left[\frac{\kappa_y\kappa_z}{3}u + \left(\Lambda+\frac{\kappa_y^2}{3}\right)v + \frac{\kappa_y\kappa_z}{3}w\right]$$

$$\pi_w = \mu_e\left[\frac{\kappa_z\kappa_x}{3}u + \frac{\kappa_z\kappa_y}{3}v + \left(\Lambda+\frac{\kappa_z^2}{3}\right)w\right]$$

$$\partial_{\hat{U}}\hat{Q}=\begin{bmatrix} \frac{W_1}{RT} & 0 & \cdots & 0 & 0 & 0 & 0 & -\frac{\rho_1}{T} \\ 0 & \frac{W_2}{RT} & \cdots & 0 & 0 & 0 & 0 & -\frac{\rho_2}{T} \\ \vdots & \vdots & \ddots & \vdots & \vdots & \vdots & \vdots & \vdots \\ 0 & 0 & \cdots & \frac{W_N}{RT} & 0 & 0 & 0 & -\frac{\rho_N}{T} \\ u\frac{W_1}{RT} & u\frac{W_2}{RT} & \cdots & u\frac{W_N}{RT} & \rho & 0 & 0 & -\frac{\rho u}{T} \\ v\frac{W_1}{RT} & v\frac{W_2}{RT} & \cdots & v\frac{W_N}{RT} & 0 & \rho & 0 & -\frac{\rho v}{T} \\ w\frac{W_1}{RT} & w\frac{W_2}{RT} & \cdots & w\frac{W_N}{RT} & 0 & 0 & \rho & -\frac{\rho w}{T} \\ \Lambda_1 & \Lambda_2 & \cdots & \Lambda_N & \rho u & \rho v & \rho w & \partial_t E_t \end{bmatrix}$$

Where $\Lambda_i = \frac{1}{\gamma-1} + \frac{W_i}{RT}\frac{1}{2}(u^2+v^2+w^2)$

$$E_t = \rho\left[e + \frac{1}{2}(u^2+v^2+w^2)\right]$$

$$\partial_T E_t = \frac{\rho R}{\gamma-1} - \frac{\rho}{T}\left[e + \frac{1}{2}(u^2+v^2+w^2)\right]$$

$$\partial_{\hat{U}}\hat{H}=\begin{bmatrix} \partial_{p1}S_1 & \partial_{p2}S_1 & \cdots & \partial_{pN}S_1 & 0 & 0 & 0 & \partial_T S_1 \\ \partial_{p1}S_2 & \partial_{p2}S_2 & \cdots & \partial_{pN}S_2 & 0 & 0 & 0 & \partial_T S_2 \\ \vdots & \vdots & \ddots & \vdots & \vdots & \vdots & \vdots & \vdots \\ \partial_{p1}S_N & \partial_{p2}S_N & \cdots & \partial_{pN}S_N & 0 & 0 & 0 & \partial_T S_N \\ \frac{W_1 g_x}{RT} & \frac{W_2 g_x}{RT} & \cdots & \frac{W_N g_x}{RT} & 0 & 0 & 0 & -\frac{\rho g_x}{T} \\ \frac{W_1 g_y}{RT} & \frac{W_2 g_y}{RT} & \cdots & \frac{W_N g_y}{RT} & 0 & 0 & 0 & -\frac{\rho g_y}{T} \\ \frac{W_1 g_z}{RT} & \frac{W_2 g_z}{RT} & \cdots & \frac{W_N g_z}{RT} & 0 & 0 & 0 & -\frac{\rho g_z}{T} \\ \frac{W_1 \gamma}{RT} & \frac{W_2 \gamma}{RT} & \cdots & \frac{W_N \gamma}{RT} & \Delta\rho g_x & \Delta\rho g_y & \Delta\rho g_z & -\frac{\rho\gamma}{T} \end{bmatrix}$$

Where $\gamma = ug_x + vg_y + wg_z$ and Sj is the total change of mass concentration

$\partial_{pi}S_j = \frac{1}{RT}\partial_p S_j$

The final discretized equation to be solved is:

$$\left(\frac{\Gamma}{\Delta\tau}+\partial_{\hat{U}}\hat{H}_i+\frac{1.5}{\Delta t}\partial_{\hat{U}}\hat{Q}_i\right)\delta\hat{U}_i^{p+1,n+1}$$

$$+\left[\partial_{\hat{U}}\hat{E}-\partial_{\hat{U}}\hat{E}_v\right]_{j+1}\delta\hat{U}_{j+1}^{p+1,n+1}-\left[\partial_{\hat{U}}\hat{E}-\partial_{\hat{U}}\hat{E}_v\right]_{j-1}\delta\hat{U}_{j-1}^{p+1,n+1}$$

$$+\left[\partial_{\hat{U}}\hat{F}-\partial_{\hat{U}}\hat{F}_v\right]_{k+1}\delta\hat{U}_{k+1}^{p+1,n+1}-\left[\partial_{\hat{U}}\hat{F}-\partial_{\hat{U}}\hat{F}_v\right]_{k-1}\delta\hat{U}_{k-1}^{p+1,n+1}$$

$$+\left[\partial_{\hat{U}}\hat{G}-\partial_{\hat{U}}\hat{G}_v\right]_{l+1}\delta\hat{U}_{l+1}^{p+1,n+1}-\left[\partial_{\hat{U}}\hat{G}-\partial_{\hat{U}}\hat{G}_v\right]_{l-1}\delta\hat{U}_{l-1}^{p+1,n+1}=RHS^{p,n+1}$$

Where

$$RHS^{p,n+1}=-\{\left[1.5\hat{Q}_i^{p,n+1}-2\hat{Q}_i^{n}+0.5\hat{Q}_i^{n-1}\right]/\Delta t$$

$$+\left[\hat{E}-\hat{E}_v\right]_{j+1}^{p,n+1}-\left[\hat{E}-\hat{E}_v\right]_{j-1}^{p,n+1}$$

$$+\left[\hat{F}-\hat{F}_v\right]_{k+1}^{p,n+1}-\left[\hat{F}-\hat{F}_v\right]_{k-1}^{p,n+1}$$

$$+\left[\hat{G}-\hat{G}_v\right]_{l+1}^{p,n+1}-\left[\hat{G}-\hat{G}_v\right]_{l-1}^{p,n+1}+\hat{H}_i^{p,n+1}\}$$

The above equation is solved by using Incomplete LU decomposition in Chem3D. This code was originally developed by Dow Chemical. Modifications have been added to it by various researchers. More detailed description of the code is found in Roy (2010).

4.4 Parallelization

To obtain efficient solution, the computational domain is created with a block structured curvilinear mesh. The advantage of dividing the total geometry to different blocks is that the separate blocks can be solved in separate processors at the same time. This parallel simulation

reduces the total computational time significantly. In Chem3D the blocks are known as zones. These zones are distributed among different processors. Each processor is then responsible to simulate the zones assigned to it and obtain solution. As a rule, the number of processors requested cannot exceed the number of zones to be simulated.

Each zone has a boundary, which may be an internal boundary or a physical boundary. If it is an internal boundary, then the boundary conditions are provided by the connected zones to the appropriate face. If the connected zones are in the same processor then this is accomplished via inter processor memory transfer. However, in most cases, when the connected zones are in different processors, the data transfer as boundary conditions is accomplished via MPI algorithm (Gropp et al., 1996). Since the data is to be transferred during every iteration of solution, careful management of communication is required for efficiency. To perform this in a more efficient pattern, a communication matrix is set up during initialization. The matrix comprises a set number of values to be transferred. Hence, after each iteration, only the values of the matrix are updated.

The strategy for efficient simulation is to create uniform sized blocks during mesh generation. In most cases the number of blocks exceed the number of processors requested. If the numbers are chosen carefully, each processor can have a similar number of zones associated with them. However, the sizes of the blocks should not be too small, because it is not desired that the communication transfer takes more computational overhead than actual computation. The number of zones to be distributed among various processors is accomplished by using standard METIS division (Karypis & Kumar, 1998).

Scalability tests have been performed for simulation in Chem3D in multiple platforms.

Experiences of using this code up to 800 processors on quadcore Xeon clusters (of QueenBee, LONI), using infiband communications, confirm the scalability of this code up to a large number of processors. Table 1 shows the computational time required for simulation in QueenBee super computer at LONI. It shows that as the number of processors increase, the computational time decreases.

Table 4.1. Computational time for different number of processors in QueenBee

Grid size (no. of cells and blocks)	Processors	No. of iterations	Computational time	Computational time for a single iteration /processor/cell (sec)
3.1 million cells, 2088 Blocks	320 (40 x 8)	9200	48 hrs	1.893×10^{-8}
4.2 million cells, 3552 Blocks	320 (40 x 8)	5760	48 hrs	2.232×10^{-8}
4.2 million cells, 3552 Blocks	800 (100 x 8)	12820	48 hrs	3.76×10^{-9}

Scalability is plotted on Figure 4.2. It is seen that the computational speed increases as the number of processors increase, suggesting an almost linear relationship.

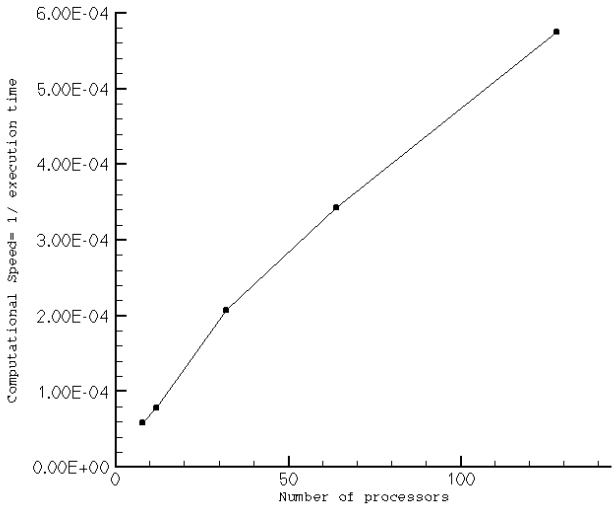

Figure 4.2. Scalability of Chem3D

4.5 Large eddy simulation

Turbulence is a phenomena which involves many length scales in a fluid flow. As other fluid flows, turbulence is also governed by Navier -Stokes equations. Due to presence of length scales, ranging from largest energetic scales to smallest Kolmogorov scales, mathematical modeling of turbulent flows are a challenge. Several models to resolve turbulence have been evolved. In models such as Reynolds Averaged Navier Stokes (RANS), the averaged equations are solved and the turbulent stresses are modeled by different physical arguments. These models possess limitations in accuracy of predictions (Acharya et al., 2001). In Direct Numerical Simulations (DNS), all the scales are simulated directly using a very fine grid. Due to finer grid requirement, DNS is limited to simple flows with low Reynolds number range. To gain a leverage between the highly accurate DNS and easy model of RANS, Large Eddy Simulation (LES) have been developed. LES attempts to simulate larger energetic scales and model smaller scales. Since smaller scales are more universal, LES solutions for turbulence are more accurate than RANS and even

comparable to DNS but with smaller grid requirement. The details of LES for practical simulations can be found in work by (Tyagi & Acharya, 2003, 2005).

4.5.1 Filtering

Mathematically, the scales to be simulated and the scaled to be modeled are separated by a filtering operation, which was introduced by Leonardo in 1974. A filter is chosen and convolution is conducted to apply the filter to different parameters.

$$\overline{(u(x,t))} = \int_D u(x_i')G(x_i - x_i')dx_i'$$

Where G is the filter function and D is the entire domain of simulation.

Different filters can be used. A common top hat filter is given as:

$$G(x - x_i') = \begin{cases} \frac{1}{2\Delta_i} & if\ |x_i - x_i'| < \Delta_i \\ 0 & otherwise \end{cases}$$

Where Δ_i is the filter width. For practical simulations, the filter width is taken as the grid spacing itself. Hence, the scales which are filtered out are known as sub-grid scales, those which are resolved are known as resolved scales. Application of above filter terms to Navier Stokes equations yield the filtered equations. In curvilinear formulation, the governing equations become:

$$\frac{\partial}{\partial \xi_i}\left(\sqrt{g}\overline{U}_i\right) = 0$$

$$\frac{\partial}{\partial t}\left(\sqrt{g}\overline{u_\imath}\right) + \frac{\partial}{\partial \xi_j}\left(\sqrt{g}\overline{U}^j\overline{u_\imath}\right) = -\frac{\partial}{\partial \xi_j}\left(\sqrt{g}\left(a^j\right)_i\overline{p}\right) + \frac{\partial}{\partial \xi_j}\left(\left(\frac{1}{Re} + \frac{1}{Re_t}\right)\sqrt{g}g^{ik}\frac{\partial u_i}{\partial \xi_k}\right)$$

$$\frac{1}{Re_t} = C_s^2\left(\sqrt{g}\right)^{2/3}|\bar{S}|$$

$$\bar{S}_{ik} = \frac{1}{2}\left((a^m)_k \frac{\partial \overline{u_\iota}}{\partial \xi_m} + (a^m)_j \frac{\partial \overline{u_k}}{\partial \xi_m}\right)$$

Where $\sqrt{g}$ is the jacobian of the transformation, $\sqrt{g}\overline{U}^j = \sqrt{g}\left(a^j\right)_k \bar{u}_k \; with \; \left(a^j\right)_k = \frac{\partial \xi_j}{\partial x_k}$ are the contravariant velocity components and g^{ik} are the elements of contravariant metric tensor. $|\bar{S}|$ is the magnitude of the strain rate tensor.

An extra filter called test filter is used to determine the Smagorinsky constant dynamically (Germano et al., 1991). Based on model by Smagorinsky, developed in 1963, sub-grid (-) and sub-test (~) stresses are related to the strain rate tensor as:

$$\tilde{\tau}_{ij}^a = -2C_s^2\left(\sqrt{g}\right)^{2/3}\widetilde{|\bar{S}|\bar{S}_{\iota J}}$$

$$T_{ij}^a = -2C_s^2\alpha\left(\sqrt{g}\right)^{2/3}|\tilde{\bar{S}}|\tilde{\bar{S}}_{ij}$$

The Germano Identity relates the sub-grid and subtest stresses to the filtered quantities as:

$$T_{ij} = \widetilde{\overline{u_\iota u_J}} - \tilde{\bar{u}}_\iota \tilde{\bar{u}}_j$$

$$\tau_{ij} = \overline{u_\iota u_J} - \bar{u}_\iota \bar{u}_j$$

The Leonard stress is the difference between these two stresses:

$$L_{ij} = T_{ij} - \tilde{\tau}_{ij}$$

Anisotropic Leonard stress is given by:

$$L_{ij}^a = L_{ij} - \frac{1}{3}\delta_{ij}L_{kk}$$

So combining the SGS model and Germano identity we get:

$$L_{ij}^{a} = -2C_s^2\left(\sqrt{g}\right)^{2/3}\left(\alpha|\tilde{\bar{S}}|\tilde{\bar{S}}_{ij} - \widetilde{|\bar{S}|\bar{S}_{ij}}\right)$$

Or

$$L_{ij}^{a} \overset{\Delta}{=} -2C_s^2\left(\sqrt{g}\right)^{2/3} M_{ij}$$

Finally the Smagorinsky constant can be determined by following the least square modification done by Lilly (1992)

$$C_s^2 = -\frac{1}{2}\frac{1}{\left(\sqrt{g}\right)^{2/3}}\frac{L_{ij}^{a}.M_{ij}}{M_{ij}.M_{ij}}$$

To prevent backscattering of energy from smaller length scales to larger length scales, Cs is limited to positive values, and under a certain maximum. The model constant is further volume weighted averaged over neighboring cells for smooth distribution. The details of the implementation can be found in Tyagi and Acharya (2005). Application of the above formulation for film cooling can be found in Kalghatgi and Acharya (2014).

CHAPTER 5. EFFECT OF JET GEOMETRY ON TRANSVERSE JETS

Jets in crossflow are studied numerically using LES. The velocity ratio is 5.7 and the jet Reynolds number is 5000. Parabolic profile is used for the jet inlet. There are four specific cases- one of which is with cylindrical pipe inlet, and three with rectangular pipe inlet, having the same mass flow rate of the jet, which are compared in this chapter.

5.1 Background

Detailed past work relevant to this study can be found in Chapter 2.

5.2 Section 2- Numerical details

Numerical methods and algorithms, used for simulation and analysis, are discussed in this section.

5.2.1 Numerical methodology

The numerical methodology used has been described in Chapter 4.

5.2.2 DMD algorithm

The concept of DMD lies in mapping subsequent samples of data (generally velocity fields in fluid flows) in a linear manner and representing final sample using the linear combination of earlier samples. The residual error associated with this combination, is minimized using different techniques. The eigenvalues and eigenvectors of the array obtained, after linearization, gives the information about dynamics of the system. The details of the algorithm can be found in Schmid (2010) and Rowley (2009). The algorithm discussed on Schmid (2010) is followed closely for the current work.

Let N be the total number snapshots collected at regular time intervals. The samples are arranged into two matrices- one containing snapshots from first to (N-1)th interval and the other containing data from second to Nth interval.

$$V_1^{N-1} = \{v_1, v_2, \dots, v_{n-1}\}$$

And

$$V_2^N = \{v_2, v_3, \dots, v_n\}$$

where v= single snapshot of flow field (Velocity fields in fluid flows)

A linear mapping operator 'A' is assumed which connects the flow field to subsequent flow field as:

$v_{i+1} = Av_i$

Now using these linear operators, it can be defined that:

$$V_2^N = AV_1^{N-1} = \{Av_1, A^2v_1, \dots., A^{N-1}v_1\}$$

The dynamic modes in the system are represented by the eigenvalues and eigenvectors of A. The linear dependability can be assumed to hold, and the dominant features can be understood from the above formulation, after a critical number of snapshots is reached. Beyond that, addition of more snapshots would not change the information obtained. When this limit is reached, the last snapshot can be represented by the combination of previous snapshots as

$$v_N = a_1v_1 + a_2v_2 + \cdots + a_{N-1}v_{N-1} + r$$

where $a^T = \{a_1, a_2, \dots., a_{N-1}\}$ and r is the residual vector. The coefficients 'a' are obtained by minimizing the above residual by using least squares method.

It can further written as:

$$V_2^N = AV_1^{N-1} = V_1^{N-1}S + re_{N-1}^T$$

where $e_{N-1}^T = (0,0,\dots,1)$ and matrix S is the companion matrix with

$$S = \begin{bmatrix} 0 & & & & a_1 \\ 1 & 0 & & & a_2 \\ & \ddots & \ddots & & \vdots \\ & & 1 & 0 & a_{N-2} \\ & & & 1 & a_{N-1} \end{bmatrix}$$

The eigenvalues of S then approximates some eigenvalues of A. The only unknowns are the coefficients 'a' which can be solved by least squares minimization.

There are two popular methods to perform the minimization of the linear equation above to find the values of a. The first one is using a QR decomposition. Mathematically, 'a' is solved by

$$a = R^{-1}Q^H v_N$$

with $QR = V_1^{N-1}$ is the economy-size QR-decomposition of the data sequence V_1^{N-1}. The vector 'a' then is used to form the companion matrix S. As per Schmid (2010), a practical implementation of the above decomposition yields an ill-conditioned algorithm that is often not capable of extracting more than first, or first two, dominant dynamic modes. Hence, another method is generally used for decomposition, to finally extract the dynamic modes. This method involves performing a singular value decomposition of the data sequence V_1^{N-1}.

$$V_1^{N-1} = U\Sigma W^H$$

where W^H is the complex conjugate transpose of W.

Using this formulation in equations described above,

$$U^H A U = U^H V_2^N W \Sigma^{-1} \equiv \tilde{S}$$

The modal structures are then extracted from the matrix $\tilde{S}$ by using eigenvalue decomposition as:

$$\tilde{S} y_i = \mu_i y_i$$

Finally the dynamic modes are evaluated as

$$\Phi_i = U y_i$$

The growth rate and frequency for each dynamic mode are calculated using the eigenvalues as:

$$\lambda_i = \ln(\mu_i) / \Delta t$$

The growth rate is given by the real part of λ_i and the frequency is given by the imaginary part. In literature, the eigenvalues evaluated from DMD are often called as Ritz values and the corresponding eigenvectors as Ritz vectors.

For the amplitudes, the expression used is $a = 1/\|A\|$ where $A = V\Sigma^{-1}X$

5.2.3 Problem description

To model the JICF problem, a geometry consisting of a box is used. The dimensions are shown in Fig 5.1. Inlet is provided at two positions- for the jet and for the crossflow. Crossflow inlet lies in the x-min plane, and jet inlet lies in the y-min plane of the pipe. Outlet is at the x-max plane and the top y-max plane. On the spanwise (z) direction, periodic boundary conditions are used. After several trials, the current domain size is chosen, such that the boundaries would not constrain the jet in any manner. For simplicity, jet has a parabolic velocity profile making a laminar flow at

the inlet. The velocity ratio between jet and crossflow is maintained as 5.7, and the jet Reynolds number is around 5000.

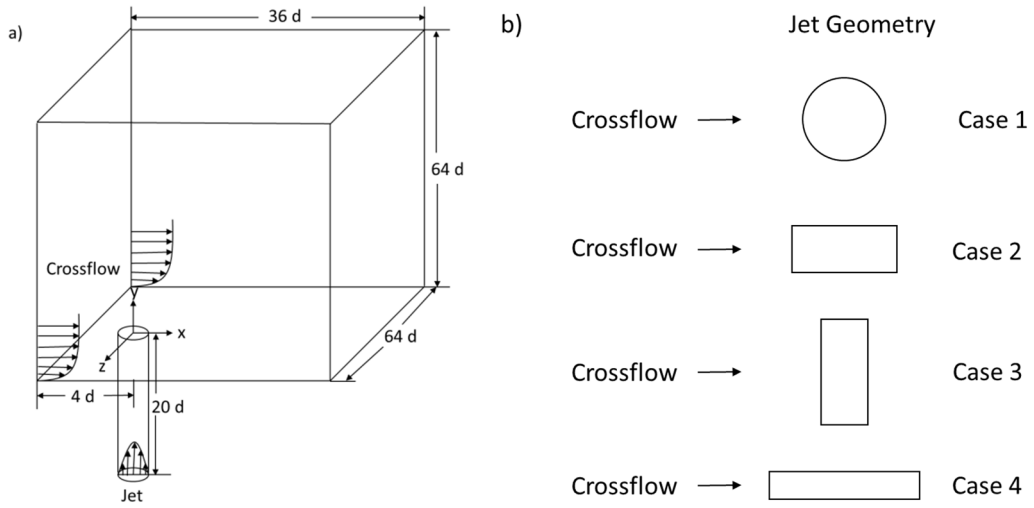

Figure 5.1. Geometry used for simulation

Double O-grid strategy is used to mesh the curvilinear multi-block geometry. Pipe of the jet is first connected to the domain by an O-grid and the pipe itself is meshed inside using another O-grid. Any specific wall modeling is not used. Thus, for LES, stretching is required at the wall regions to resolve steep gradients. Wall resolution for crossflow wall is (y^+=0.1) and the pipe wall is (r^+=0.4). Total mesh size for the simulation is about 15 millions. For the rectangular duct jet, same cross sectional area was maintained as of the pipe. The mean velocity was also same and an empirical parabolic profile was specified for laminar flows (Shah and London, 1978). This was done to maintain the same mass flow rate of the jet. Mesh resolutions and other boundaries are kept same as that of pipe flow. The different cases simulated are listed in table 5.1.

Table 5.1: List of simulated cases

Case	Type of jet	Aspect Ratio	Orientation
1	Circular	N/A	N/A
2	Rectangular	2	Long edge in x-direction
3	Rectangular	2	Long edge in z-direction
4	Rectangular	3	Long edge in x-direction

The timestep was chosen to simulate within Kolmogorov time scales. In non-dimensional units (using jet diameter and jet mean velocity), the timestep is 8.14×10^{-3}. Based on jet mean velocity and the streamwise length after the jet enters the domain, approximately 5 flow through times was simulated for the transients to exit the domain. Averaging was done for 10 additional flow through time periods. It was seen that the statistics did not change after this, and hence, the data was considered for analysis.

5.2.4 Grid independence

Before selecting the above mesh as final mesh, several coarser meshes were simulated. Grid independence was decided on the basis of prediction of time averaged jet trajectory. It was observed that the grid of 8 million was enough to predict the time averaged jet trajectory correctly. However in that grid, the upstream vortical shear layer structures were not resolved completely. Our main purpose is to study turbulent phenomena. Hence, for better capturing of such coherent structures, the mesh size of 12.3 million was finalized. Even in 12.3 million mesh, other parameters are visualized in a reasonable manner, but the flow structures and the wake

region were not resolved well. Hence, the mesh was further refined to the current size where the structures and wake were resolved.

5.2.5 Crossflow boundary

For crossflow profile, a flat plate boundary layer is applied in such a manner that the 80% boundary layer thickness is at y=1.32 d, at the point where the jet meets the crossflow, but in absence of jet. This condition was measured by Su and Mungal (2004) in their experiments and also applied in numerical studies. This specification of boundary layer is achieved by using the following equation:

$$\frac{u}{u_\infty} = 2\left(\frac{y}{\delta}\right) - \left(\frac{y}{\delta}\right)^2$$

For validation of crossflow profile, a separate simulation was carried out on a coarse mesh, without the presence of the jet. The dimensions for this simulation was (20dX10dX6d). The profile is extracted from x=4d where the jet enters the main domain in Fig 5.2. The boundary profile matches the one used by Muppidi and Mahesh (2005).

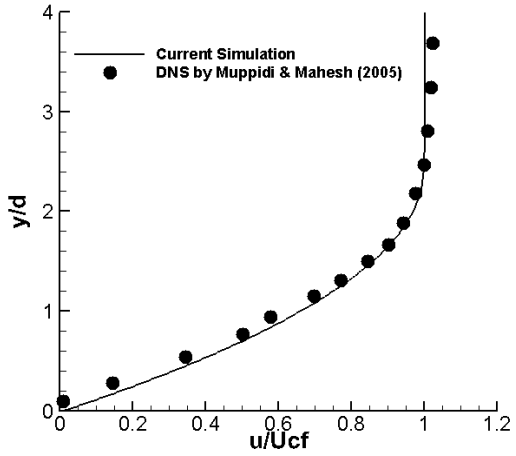

Figure 5.2. Crossflow boundary layer

For laminar JICF, a parabolic profile is used to match the jet exit profile mentioned by Muppidi and Mahesh (2005) in their DNS studies. Outflow boundary condition is used at the streamwise end edge. Spanwise walls have cyclic boundary conditions. The top-wall also has an outflow boundary condition.

5.2.6 Inlet turbulence generation

An inlet turbulence generation method was applied at the jet inlet to simulate turbulent jet in a crossflow using LES. A synthetic turbulence generation method was selected in order to study downstream behavior of JICF with different turbulence kinetic energy at the jet inlet. The advantage of synthetic turbulence generation method is that they take turbulent kinetic energy as an input in some form. Hence, the inlet kinetic energy can be varied and thus studied. Synthetic Eddy Method (SEM) developed by Jarrin et al. (2006) is attractive since it is physically more intuitive and can be implemented easily. The details of the SEM algorithm is discussed in Appendix A.

A separate pipe-only simulation is done to get right parameters for the algorithm to generate fully developed turbulence at the end of pipe. The pipe length used for this simulation is 10d. The mesh sizes used for the simulation are($r_{min}^{+} \approx 0.15, r_{max}^{+} \approx 3.95, r\Delta\theta^{+} \approx 7.85, z^{+} \approx 13.54$). Using the SEM, a good validation is obtained for fully-developed pipe flows. This case was presented by Pokharel (2017).

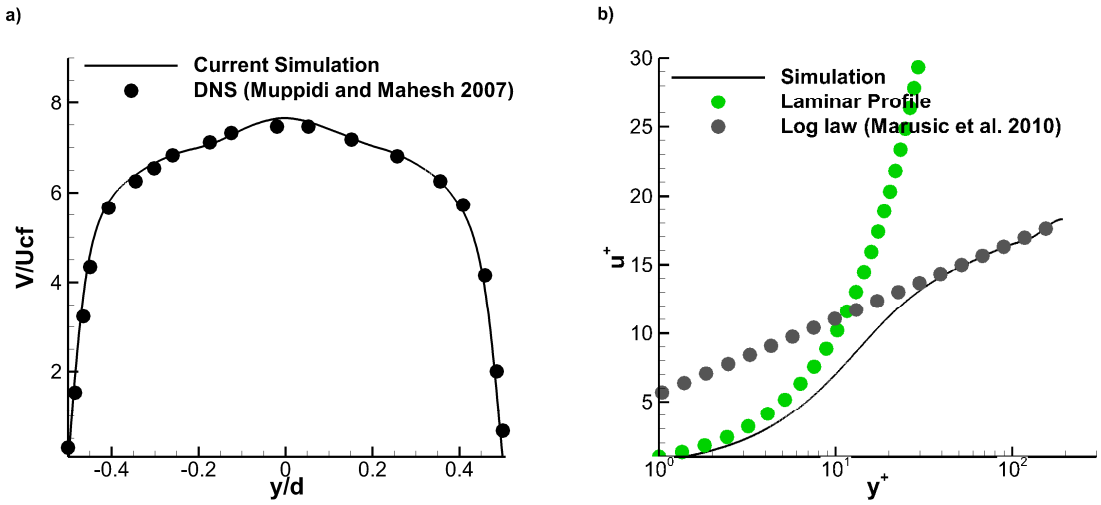

Figure 5.3. Validation of SEM; (a) Mean velocity at jet exit; (b) The log-law of mean profile

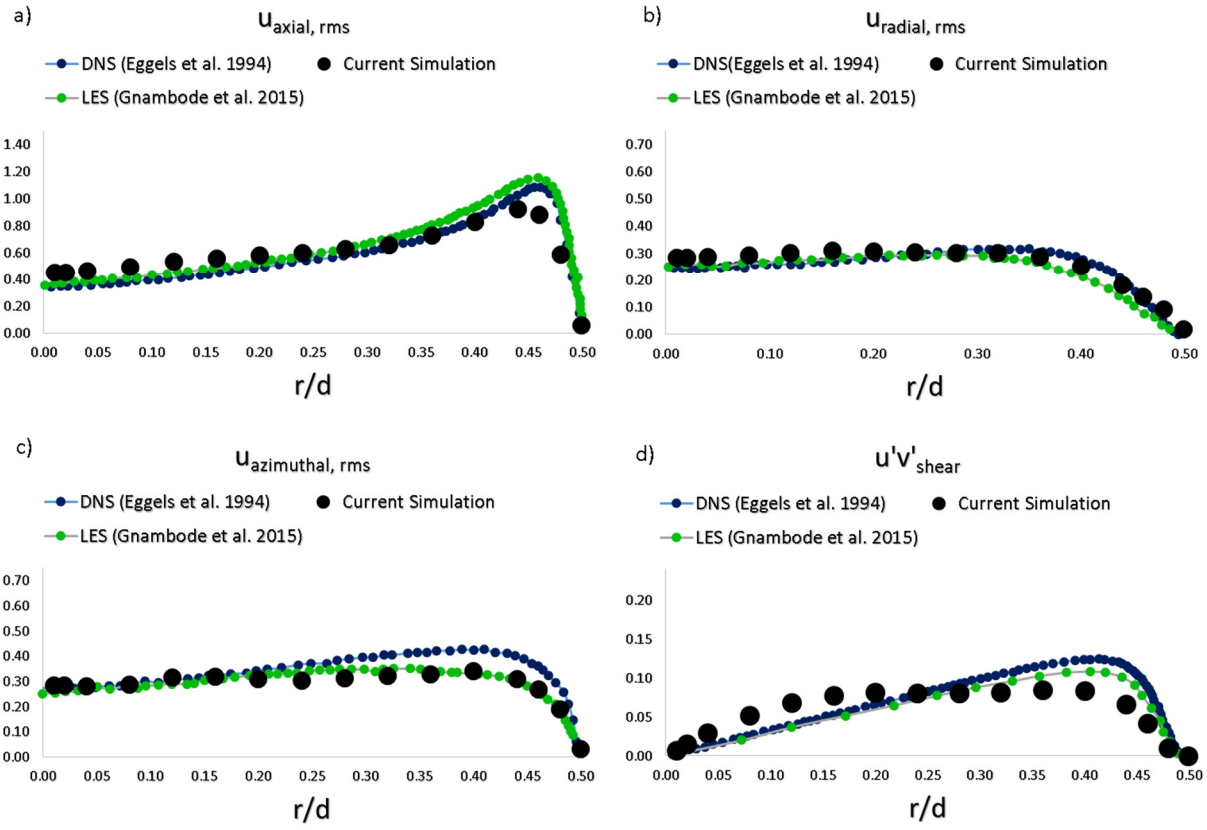

Figure 5.4. Validation of Reynolds stresses; (a), (b), (c) Normal stresses; (d) Shear stress

Fig 5.3 and 5.4 show the validation of SEM method with jet mean profile (Muppidi & Mahesh 2007). The rms profiles are taken from Eggels et al. (1992). The mean is specified in such a manner

that jet exit profiles match inlet profiles used by Muppidi and Mahesh (2007) in their DNS studies. Fig 5 shows some deviation from fully developed pipe flows, especially for shear stress. The integral error (defined by integrating the profile over the radial length) estimates show an underprediction of 12% which is expected for the algorithm at the specified distance. Additional results from the simulation of pipe only flow is discussed in Appendix B.

For rectangular laminar JICF cases, the mean velocity was kept same and an empirical parabolic profile was specified for laminar flows (Shah and London, 1978). For rectangular turbulent JICF cases, SEM was used with the same parameters. For comparison purpose, all other boundaries are kept same as that of pipe flow.

5.3 Section 3- Validations

The current configuration of velocity ratio 5.7 is among the cases simulated by Muppidi and Mahesh (2005). DNS results from the work was used to validate the current LES simulation. Fig. 5.5 (a) shows a good match for time averaged jet centerline trajectory. 5-5(b) also shows a good match with time averaged vertical velocity profile at jet exit. Validations show good predictability of LES to complex interactions happening in JICF. This initial validation was presented by Pokharel et al. (2013).

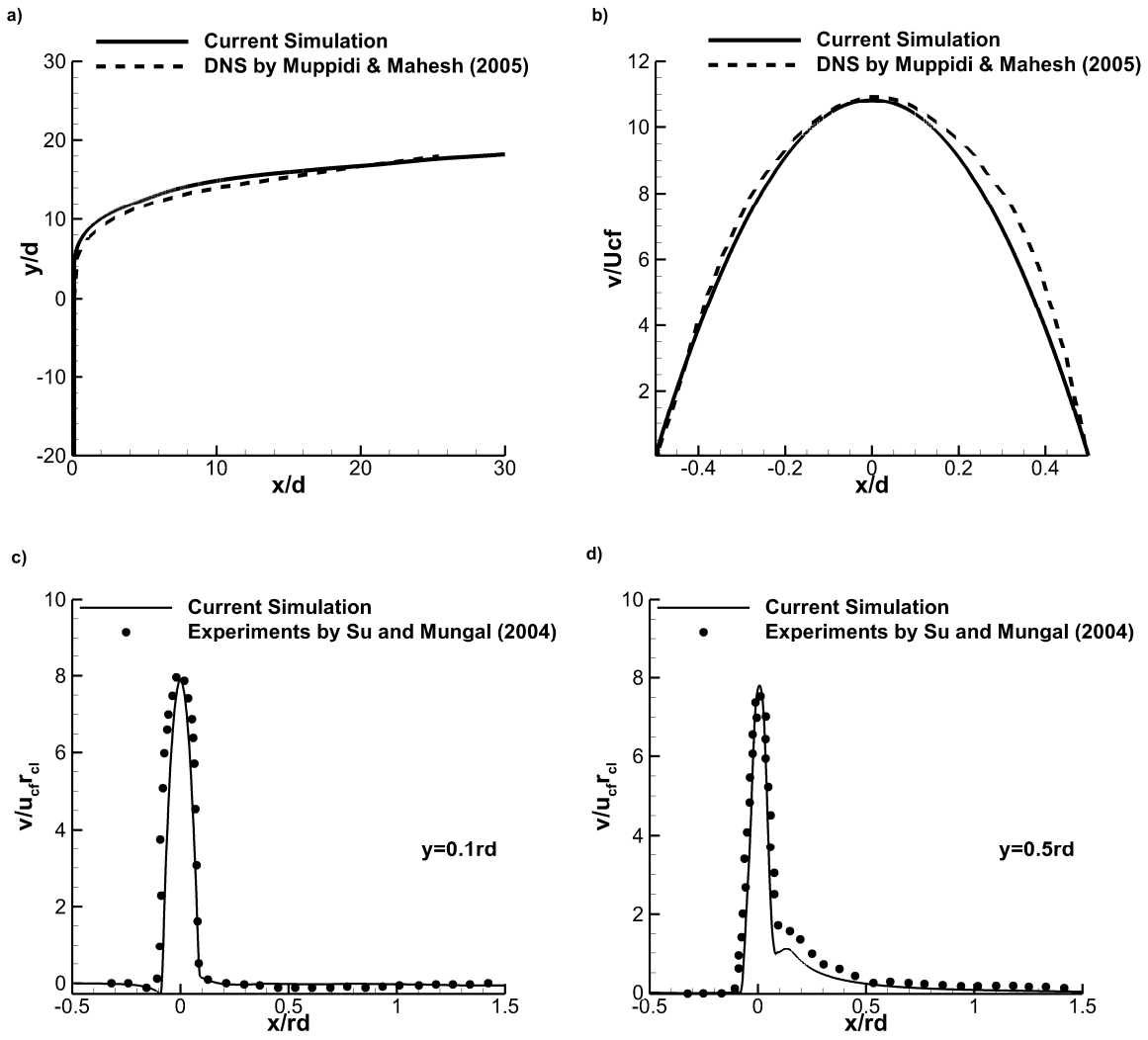

Figure 5.5. (a) Validation of time averaged jet trajectory; (b) Velocity profile at jet exit ; (c) Velocity profile normalized by centerline ratio at near field station (0.1 rd); (d) Velocity profile normalized by centerline ratio at station (0.5 rd);

Comparisons of experiments were done to further illustrate the accuracy of the simulation. In the experiment by Su and Mungal (2004), the velocity ratio of the jet (r) and the Reynolds number of the jet is same as that of the current case. However, the jet flow is a fully developed turbulent pipe flow. In the current case, laminar flow is simulated. For comparison a centerline velocity ratio is defined as

$$r_{cl} = \frac{v_{cl-parabolic}}{v_{cl-turbulent}} = 1.3677$$

The centerline velocity for the turbulent profile is taken from near-field velocity profile (0.1 rd) from the experiment. When this ratio is used for the current case, in the near field, it takes the effect of turbulence in the mean flow field. Same approach was undertaken for rectangular jet study by Yu and Girimaji (2005). At the far field, significant effects of turbulent flow is seen which makes the cases incomparable. For two near field stations (y=0.1 rd and y=0.5 rd) the velocity profiles show a good match (Fig 5.5 (c) and 5.5 (d)). In Fig 5.5 (d), it can be seen that a secondary peak is higher in the experiment compared to the simulation. This is the effect of inherent turbulence of the jet. Overall, a good match indicates that the near field flow is correctly predicted by the current simulation.

5.4 Section 4-Flow structures

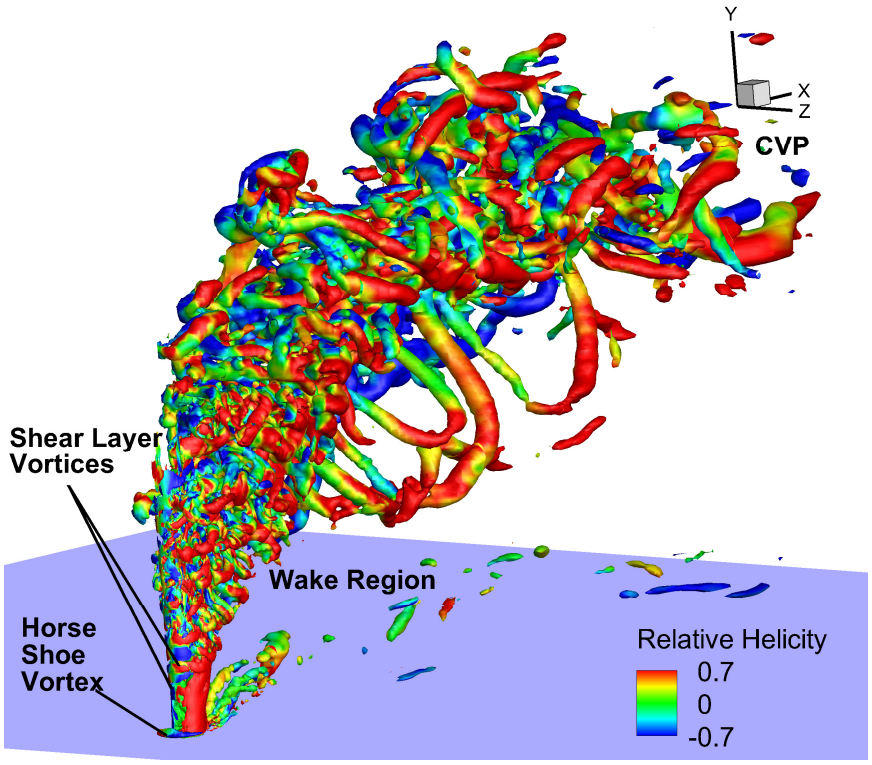

Figure 5.6. Flow features of JICF using Q-criteria for Case 1

Coherent structures are plotted in Fig. 5.6 using the iso-surfaces of Q criteria (Haller 2005) for case 1. The contours are plotted using relative helicity. All major structures were studied extensively in the past. Only a brief discussion is provided here with emphasis on the current cases. Horseshoe vortices are captured clearly for cases 1 and 3. Case 1 is circular, and case 3 has a long edge facing the crossflow. Cases 2 and 4, show an incomplete formation of horseshoe system. Shear layer vortices are seen clearly for all the cases. Due to complex interaction of these vortices, periodic breakups and mergers are seen in the shear layer. Change of orientation of these vortices are also evident in the flow field. Counter-rotating vortex pair is a characteristic feature of any JICF. It was clearly captured for all cases in time averaged data. It forms with a kidney like shape in the far field. In instantaneous data, it shows a collection of small structures. Wake vortices are typically formed as upright vortices in the wake region. For the current cases however, due to high Reynolds number of the jet and low crossflow velocity, effective shedding of vortices are suppressed in the wake side. Therefore, a quiescent region with occasional long streamwise vortices are seen in the wake.

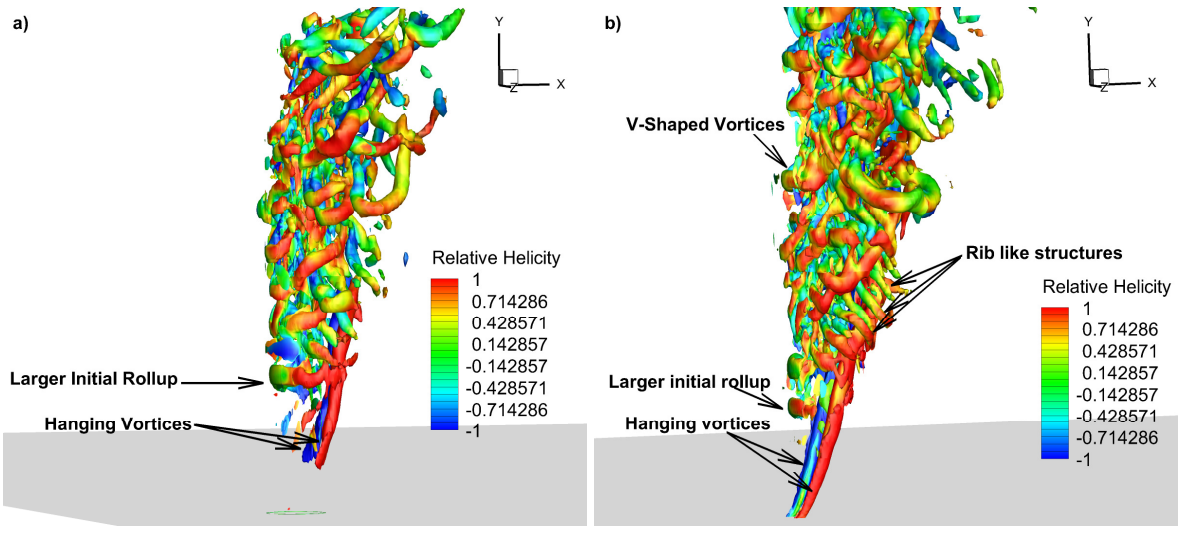

Figure 5.7. Iso-surfaces of larger structures using Q-criteria; (a, b) Case 1 and 2;

Using Q criteria vortical structures having high vorticity can be visualized in the near field (Fig 5.7). This visualization helps identify additional structures. Hanging vortices are evident in the immediate wake of the jet (Fig 5.7(a) and 5.7(b)). Larger initial rollup is formed by the KH instability between the jet and the crossflow fluid (Fig 5.7 (a) and 5.7 (b)). As the jet evolves, wall normal structures are seen with a V-shape (Fig 5.8 (c)). The rotation of these vortices follows exactly that of the CVP. These vortices are also considered to help the formation of the CVP in the near field and they promote mixing between jet and the crossflow fluid. Further down, all these small structures rotate together to create another large overall rollup (Fig 5.8 (d)). After this rollup was observed, jet starts to bend rapidly in the direction of the crossflow, which eventually form the CVP in the far field. For rectangular JICF, rib-like vortices were also seen distinctly in the near field (Fig 5.7 (b)). These vortices are shown to be responsible for axis switching (Gutmark & Grinstein, 1999).

Mixing processes can be qualitatively attributed to the rotation of the vortical structures of jet within the crossflow fluid. It is thus evident that larger initial rollup, which encompasses around the jet and meets the hanging vortex, enhances mixing around the jet. The smaller structures (wall normal), which form after breakup of this vortex, positively influence mixing in both the streamwise and wall normal directions vigorously. The final rollup downstream further enhances mixing in both the wall normal direction (due to presence of small structures) and streamwise direction around the jet. Furthermore, the rib like vortices in rectangular JICF enhances mixing for such jets. This supports the evidence that rectangular jets show better mixing than circular jets (Gutmark & Grinstein, 1999).

Evolution of vorticity in the shear layer of JICF happen due to few universal mechanisms. Large initial counterclockwise rollup is formed in the early stages (Fig 5.7 a), due to the mechanism of KH instability. Once the rollup is seen, stretching occurs in the core of the vortex and the core elongates. After reaching a critical length of elongation, the vortex splits into multiple cores. These smaller vortices behave differently in the shear layer (Fig 5.8 a).

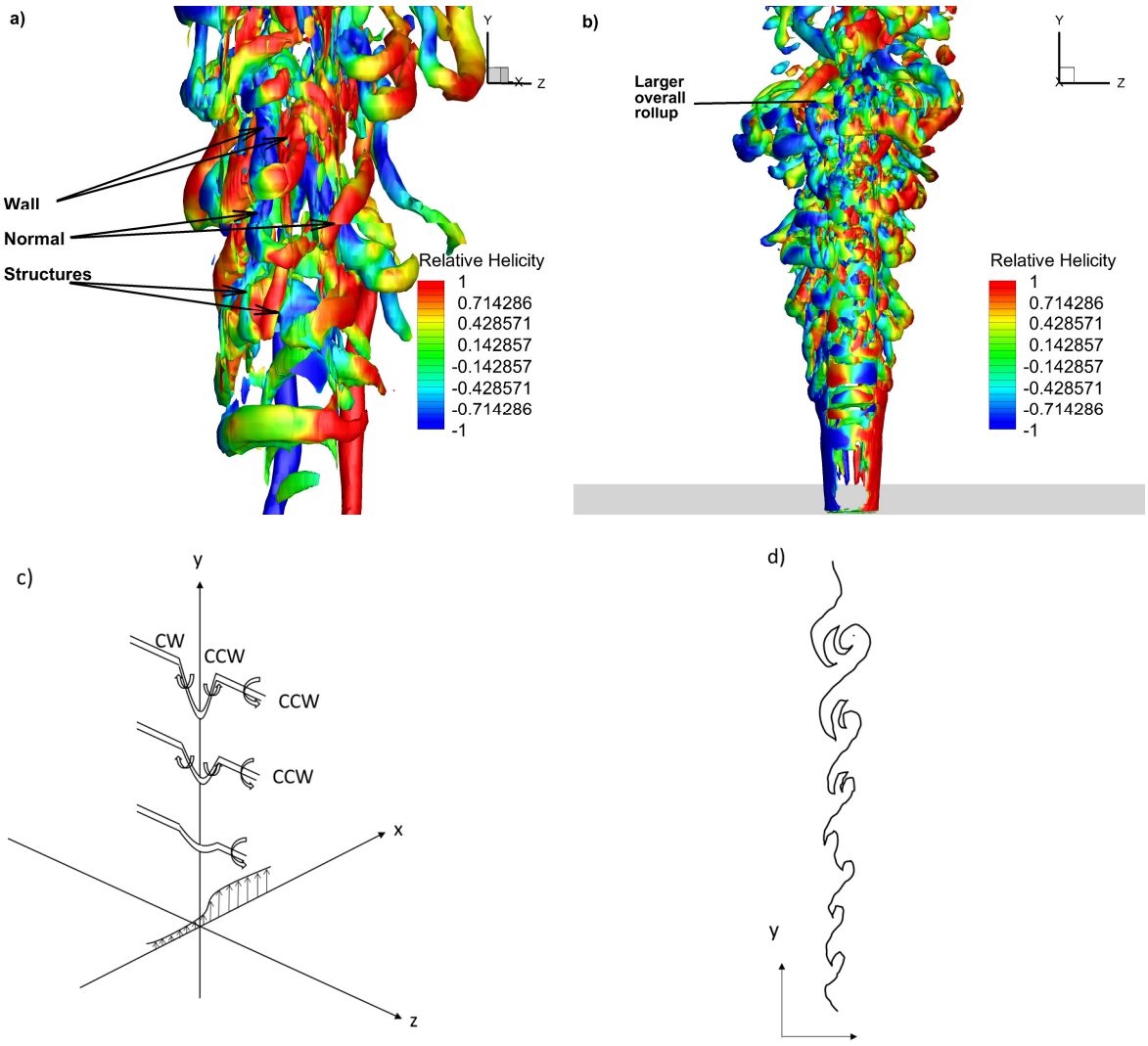

Figure 5.8. (a) Case 1- Zoomed and seen from different direction; (b) Case 1- Seen from spanwise direction; (c) Mechanism of formation of wall normal vortices; (d) Rollup of spanwise vortices;

Fig 5.8 (c) depicts the change of orientation of vorticity as the vortex evolves in the shear layer conceptually. The split part from the initial rollup slightly raises in the region of crossflow (negative x direction in Fig 5.8 (c)). This creates uneven velocity along the length of the vortex. The part of the vortex in the jet region travels much faster than the part in the crossflow region. This creates a stretching which will align the vorticity in wall normal direction. One leg of the aligned vortex has clockwise wall normal rotation, and the other leg counterclockwise. This is the same alignment of the CVP. This vortex therefore is of importance in the formation of CVP as it moves around the jet.

Mechanism of pairing of vortices in the shear layer (Fig 5.8 b) is well understood (Wu et al., 2005). It is depicted conceptually in Fig 5.8 (d). As the vortices move along the shear layer, natural pairing occurs between two vortices and they overlap to create a larger rollup as seen in the JICF. One can note that the rotation of the rollup is same as that of the individual vortices.

5.4.1 Axis switching

Axis switching is a phenomena that is seen on jets having unequal length in two axes. In the cases studied, only rectangular JICF (Case 2, 3 and 4) exhibit axis switching. Axis switching phenomena has been studied in detail and mechanisms have been identified to explain it (Zaman, 1996; Gutmark & Grinstein, 1999; Chen & Yu, 2014). The evolution of primary vortex ring formed for jets undergoes stretching on one side and shrinking on the other side, and hence, switches the axis (Grinstein, 2001). Wall normal vortices surrounding the edges are responsible for creating the appropriate push and pull on the edges of the jet, which eventually creates axis switching (Zaman, 1996; Chen & Yu, 2014).It is also established that rectangular jets exhibit 90° axis switching. (Gutmark & Grinstein, 1999).

While the vortex ring deformation takes place, the corner regions of rectangular and square jets, deform and intermingle with other vortices to create rib-like vortices. These vortices are depicted in fig 5.7 (b). Due to absence of corners, these vortices are not distinct in Case 1. The presence of these vortices enable rectangular jets to exhibit higher mixing than cylindrical jets.

5.5 Section 5- Effect of geometry in flow features

The mass flow rate of the JICF and Reynolds number, based on equivalent length, is the same for all the cases. This enables a comparison between them. Furthermore, the boundary conditions and the mesh resolutions are the same. Any differences, therefore, observed on the flow field are solely due to the effect of geometry.

In this chapter, comparison is conducted in detail for four aspects of the flows- Effect on the instantaneous flow field, effect on the mean flow field, second order (turbulence) effects and effect on the frequencies and modes of the JICF system. Relevant flow physics are identified to explain the differences. The comparisons yield insight of three aspects – geometry (cylindrical vs rectangular), aspect ratio of rectangular JICF, and edge length facing the crossflow.

5.5.1 Effect on instantaneous flow field

Muppidi and Mahesh (2005, 2007, 2008) have discussed that major dynamics of JICF is dictated by the activities in the near field. In the current study, near field is focused more to extract the effect of geometry and physics leading to the deflection of the jet.

5.5.1.1 Shear layer rollups

Initial effect when jet enters the domain is seen in the formation of shear layer rollup, due to KH instability. Four cases are plotted in Fig 5.9 to show the streamlines in the symmetry plane. In these cases, the initial rollup has a small core. It can also effectively be gauged by the turning of

the streamlines above and below the first stagnation. At y=1.5 d, the rollup is formed earliest for case 1. For case 2 and 4, they are seen at similar depths of about y=1.7 d. For case 3, the rollup forms the deepest at y= 2 d. Cylindrical JICF, provides a larger smooth circumference of the jet surface to initiate KH instability. The perturbation provided from the crossflow, thus, has an opportunity to generate instability the earliest among the cases. From Fig 5.7 (a) it can be seen that the larger rollup is formed around the jet circumference for case 1. For cases 2 and 4, the initial rollup is not seen to be fully formed around the jet (Fig 5.7 (b)). Shorter edge facing the crossflow provides lesser length to generate the instability, and hence, delay is seen. In contrast, case 3, which has the largest edge facing the crossflow, also does not provide ample opportunity for the KH instability to kick in, which may be linked to a straight length in the spanwise direction. It is conclusive that cylindrical geometry favors the initial rollup more than rectangular counterparts. Among the rectangular JICF, edge length facing the crossflow (i.e. orientation of the jet) plays a role in affecting the rollup inversely. Aspect ratio effects is not pronounced significantly in the initial rollup formation.

Interesting observation can be made for horseshoe vortex. Case 1 and 3 display horseshoe vortex upstream of the jet. Case 2 and 4, on the other hand, display only jumps in the crossflow boundary layer. It is clear from literature that horseshoe vortex is formed primarily due to the adverse pressure gradient imposed by the jet on the upstream crossflow. This pressure gradient forces the crossflow fluid to turn downwards to the jet and then deflect backwards to form a vortex. Strong intensity of the gradient favors the formation of a full vortex, whereas weak intensity is not able to deflect the crossflow fluid to form a full vortex. In the current cases, it is observed that the edge length facing the crossflow has a high influence on the formation of the

horseshoe vortex system. Larger edge lengths tends to produce more prominent vortices compared to smaller edge length. This effect is observed not to be highly affected by the geometry type, or aspect ratios (>1). Details of pressure gradient will be discussed in a farther section.

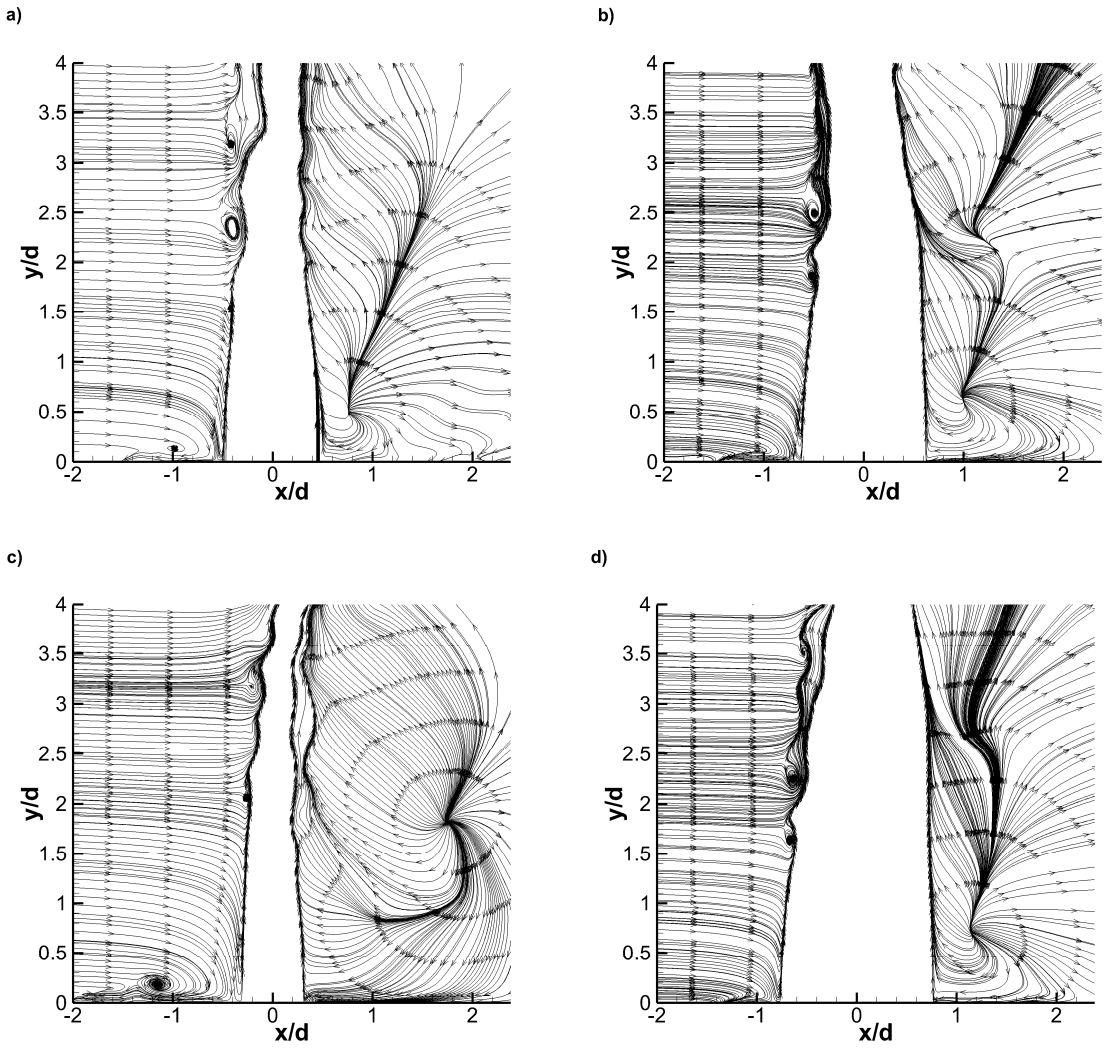

Figure 5.9. Instantaneous streamlines in the symmetry plate; (a-d) Case 1- 4

On the wake of the jet, a straight edge acting like a source flow is observed. This is formed by the crossflow fluid which wraps around the jet and meets in the wake region. The orientation of this edge is different for the cases. For case 1, as expected, a simple straight edge is formed. For all

the rectangular JICF cases, an edge is formed, which dips inwards and again protrudes outwards. This reflects the change in shape of the jet, which is changed periodically by axis switching. For case 2 and 4, the jet becomes thinner in the streamwise direction as axis switches. For case 3, the jet becomes large in streamwise direction as axis switching happens, so the edge on the wake does not narrow down, but bulge outward.

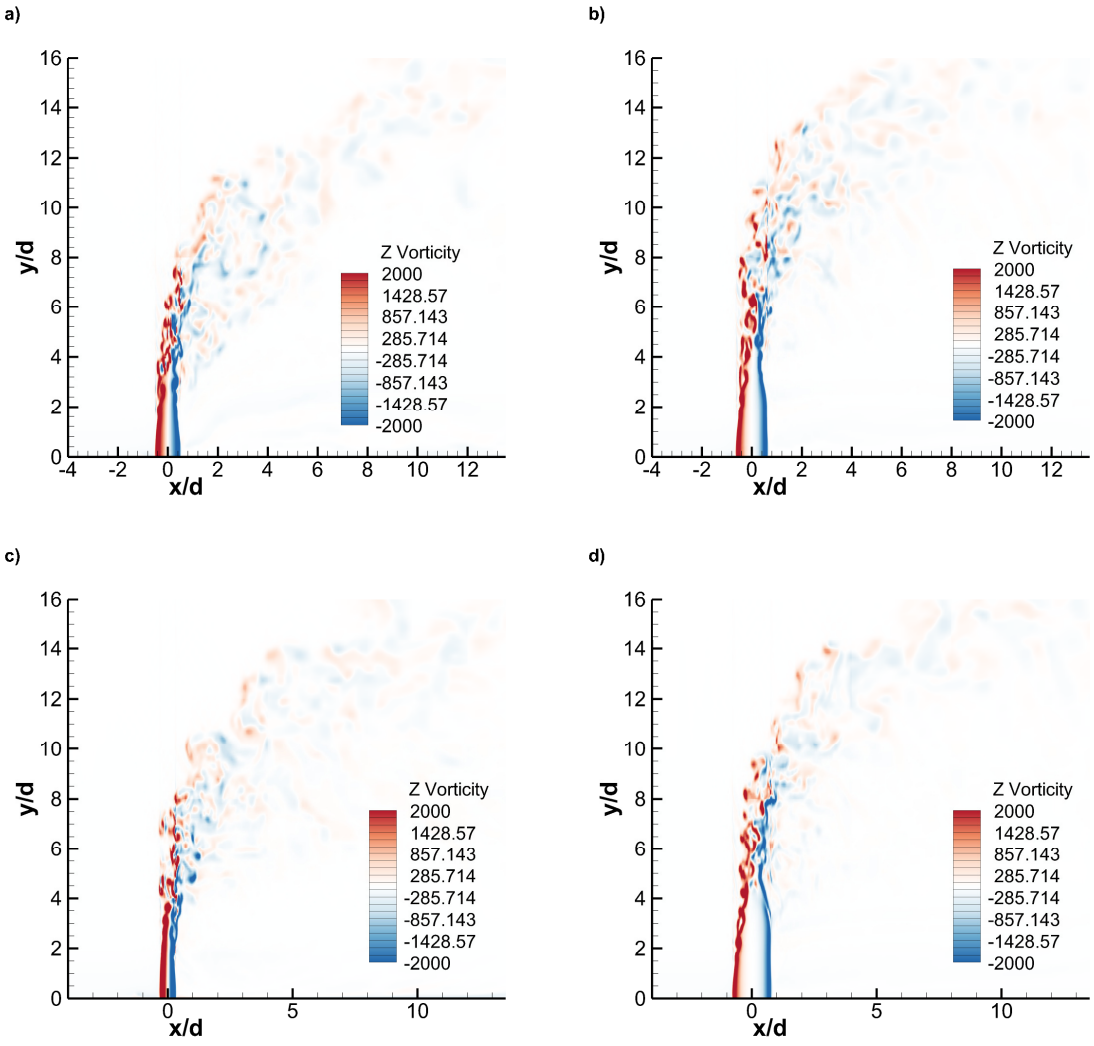

Figure 5.10. Spanwise Vorticity contours in the symmetry plane; (a-d) Case 1- 4

Spanwise vorticity plots on the symmetry plane (Fig 5.10) reveal additional information. For the cases, the trailing edge vortices initiate differently in the domain. For case 1, the initiation of

trailing edge vortex forms simultaneously, as with leading edge. For case 3, the trailing edge has a clearer vortex formation somewhat earlier than leading edge. For case 2 and 4, the trailing edge rollup happens later than the leading edge. Here, the effect of geometry type is less pronounced. As the edge length that faces the crossflow increases, trailing edge vortices form earlier. In case 1, followed by case 3, the flow of crossflow in the streamwise direction has to travel shorter distance downstream progressively, creating the vortices earlier. As the aspect ratio increases for rectangular JICF, the delay in formation of trailing vortices also increase. This is due to the fact that instability in the leading edge has to travel a larger distance in the streamwise direction to create vortices in the trailing edge.

5.5.1.2 Pressure behavior

Fig 5.11 shows the instantaneous coefficient of pressure for case 1 and 2 in the symmetry plane. The type of geometry show minor effects in the pressure field. The pressure minima, which represent the vortex cores, are seen at locations where the shear layer vortices are present. For case 1, uniform alternating cores are evident whereas for case 2, this uniformity is disturbed at a certain distance downstream (about y=4 d), possibly reflecting the effect of axis switching on rectangular JICF.

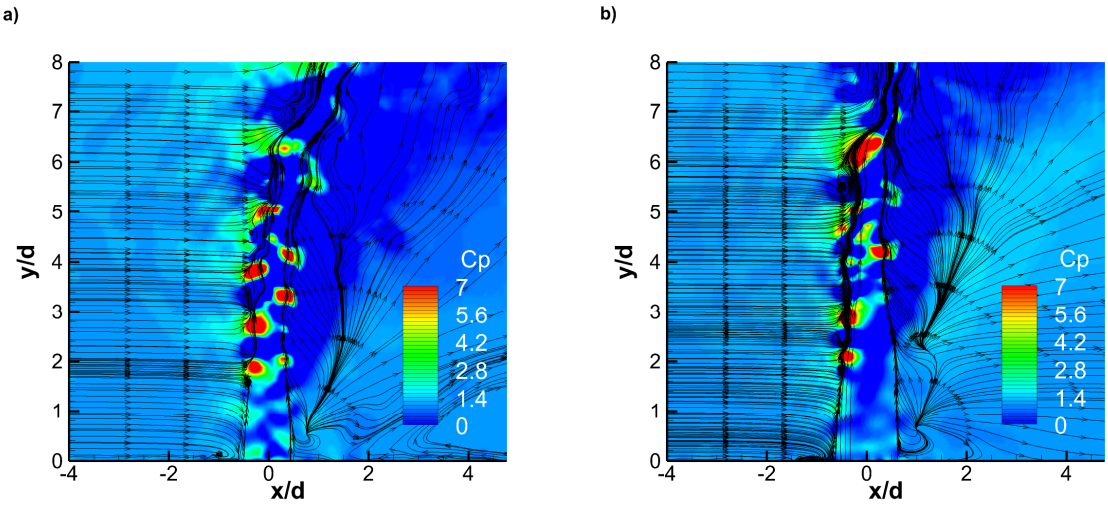

Figure 5.11. Instantaneous coefficient of pressure in the symmetry plane for (a) Case 1; (b) Case 2

5.5.1.3 Hanging vortices

Hanging vortices are observed in the immediate wake of the jet (Fig 5.7). For the cases, the hanging vortex cores are not exactly on the symmetry planes but at a spanwise distance from the center. Hanging vortices come as counter rotating pair because the crossflow fluid wraps around the jet and create opposite vortices when they tend to meet together. Hanging vortices only stand a certain length and after that a vortex breakdown occurs (Yuan et al., 1999). After the vortex breakdown occurs, the orientation of these vortices is captured and the jet bends rapidly creating a CVP like structure. These vortices are thus considered important structures to generate CVP in the near field. The behavior of these vortices, which have a direct effect on the pressure field, will be explored in detail in another section. For the cases, the vortices are plotted in positive spanwise (z=0.39 d) plane.

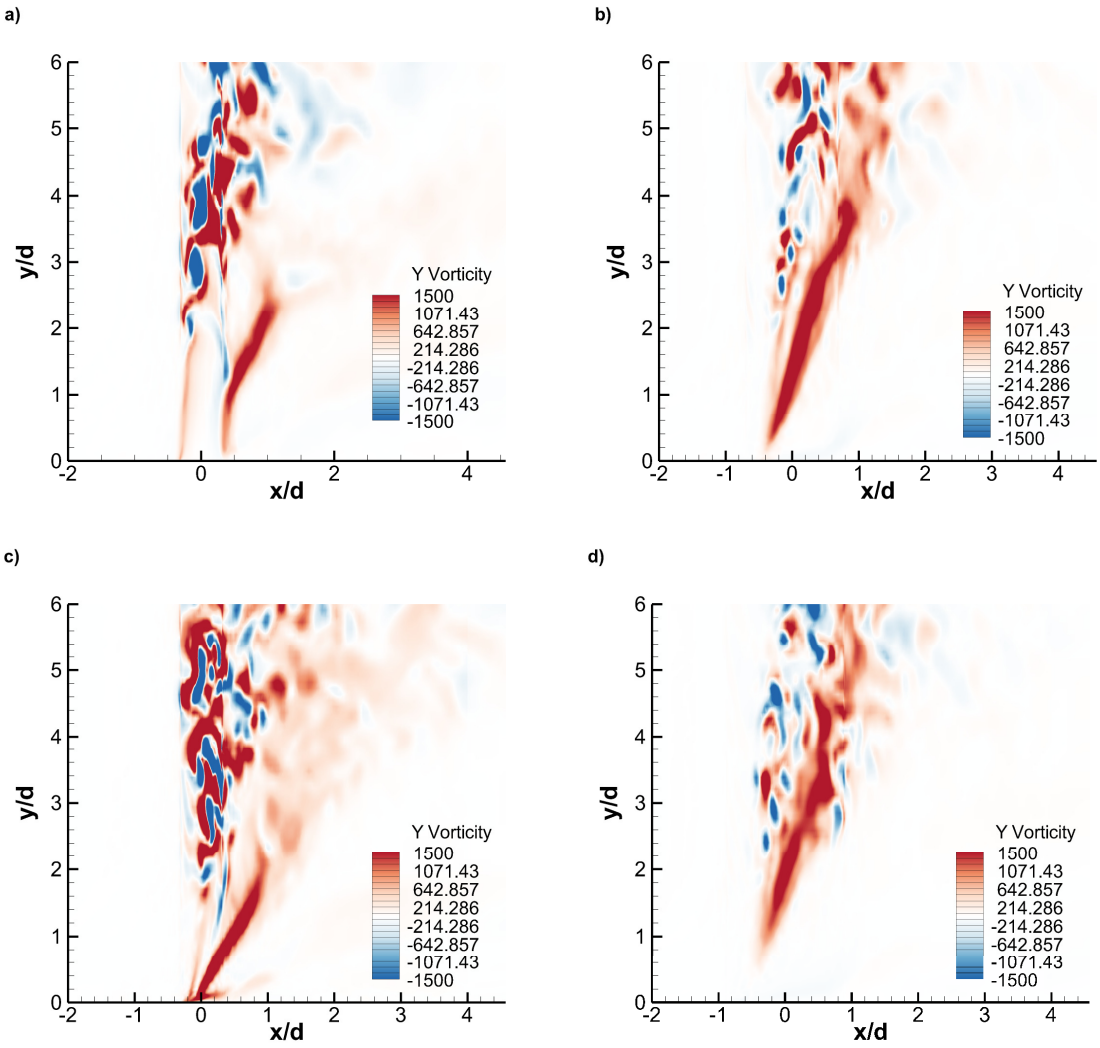

Figure 5.12. Wall normal vorticity contour at z=0.39d plane; (a-d) Case 1-4

The hanging vortices are longer for rectangular JICF, compared to cylindrical JICF (Fig. 5.12). These vortices penetrate until y=4d for case 2, and until y=2.8d for case 1. Case 3, shows shorter life of hanging vortex until y=2.2 d. Case 4, shows later initiation and lasts till y=5d before breakdown. Case 3 has earlier initiation, because the crossflow fluid wraps the fastest around the jet to form the vortices in the wake. This also explains the deepest initiation for case 4, which has the largest distance of edge in the streamwise direction. The edge of streamline, in the wake discussed

before, mimics the orientation of hanging vortex because these vortices are on immediate spanwise sides of the symmetry plane.

Cylindrical JICF has the shortest hanging vortex, compared to others. The longer existence of hanging vortices in rectangular JICF hint at the phenomena of axis switching. Before the breakdown of vorticity, these vortices play a role in initiating axis switching, which is not the case for case 1. Among the rectangular JICF, aspect ratio tends to increase the length of these vortices. In other words, aspect ratio delays the breakdown of vortices before the jet bends. There is a possibility of axis switching also playing a role in delay of jet bending.

5.5.2 Mean flow field

The near field was observed to be significantly affected by the change in geometry. This, in fact, tends to alter the jet behavior as a whole, which is discussed by analyzing the mean flow field. Jet-centerline trajectory is a good indicator of the path taken by the jet, as discussed by Muppidi and Mahesh (2005). The time average jet centerline trajectory on the symmetry plane is compared for the cases to understand the path of the jet.

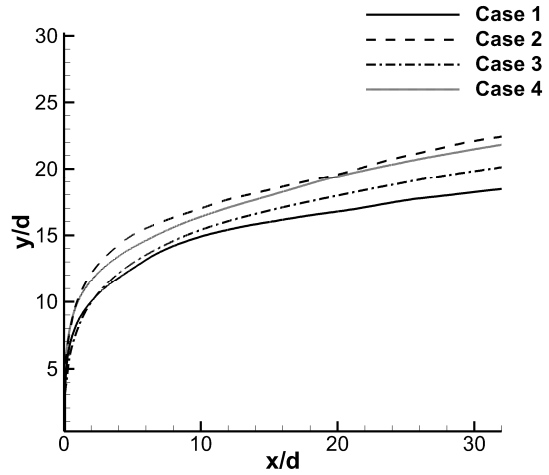

Figure 5.13. Time averaged jet centerline trajectory for all cases

Deepest penetration is observed for Case 2. This is followed by case 4, 3, and 1. The effect of geometry is reflected in the penetration of jet. For the current shapes (Case 1, 3, and 4) of the jet, low velocity ratios were studied by Haven and Kurosaka (1997), Tyagi (2003) and it was concluded that jet penetration increased from case 3, 1, and then 4. The vorticity of the spanwise edges create the appropriate lift off for different shapes of the jet (Haven & Kurosaka, 1997). Current simulation is of high velocity ratio (5.7). Below about y=10 d, similar pattern is observed. However, after y=10 d, a crossover is observed between case 1 and 3, and downstream, case 3 penetrates more than case 1. This effect is due to axis switching. Although axis switching has not been touched in detail in the above studies, current analysis shows that axis switching is significantly important in high velocity ratio JICF. For case 2 and 4, case 4 is more penetrating earlier till about y=9 d. After that, case 2 overtakes and penetrates more. Thus, aspect ratios (>1) inversely influence jet penetration in the near field. In the far field, the penetration is almost similar. This is an important conclusion because it paves a way of flow control. In situations where the JICF configuration is limited by mass flow rate and velocity ratio, different geometries and aspects can be changed to alter the jet path as desired.

To compare the evolution of mean flow in the domain, in detail, in the near field, three stations are picked for analysis. The location of these stations were inspired by the study of Su and Mungal (2004) and Muppidi and Mahesh (2007). The first location is at y=0.1 rd, second is y=0.5 rd in the symmetry plane, and the third location is y=1.0 rd in the symmetry plane. Mean vertical velocity is plotted on these locations from x=-0.5 rd to 1.5 rd (Fig 5.14). The mean vertical velocity is normalized by the velocity ratio and crossflow velocity. A widening of the jet in JICF is observed as the flow evolves. One peak in the first stage and consequently a formation of a secondary peak

in the third stage, is observed. Pressure gradient imposed by the jet on crossflow favors entrainment of the crossflow in the jet on the wake region (Muppidi & Mahesh, 2008). This entrainment is the main cause in widening of the jet as the flow moves downstream. Axis-switching effect is also reflected for cases 2, 3, and 4. A wider profile is seen, for the earlier 2 stations of case 2 and 4, compared to case 1. In contrast, a narrower profile in the third station suggests the shape of the axis has been inverted. Opposite behavior reflecting the same trend is seen for case 3. In the third station, deeper penetration of case 2 and 4 reflects the jet trajectory described.

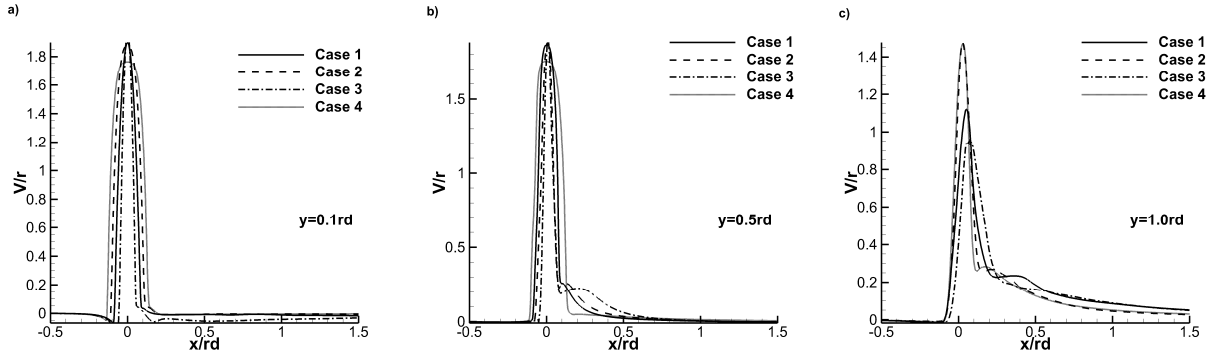

Figure 5.14. Time averaged vertical velocity (normalized by velocity ratio) at 3 stations in the domain

Analysis of horizontal velocity profile at the location, where majority of the jet is in horizontal position, gives us an understanding of far field conditions attained by different cases. Fig 5.15 shows time averaged horizontal velocity profile at a station of x=2.0 rd.

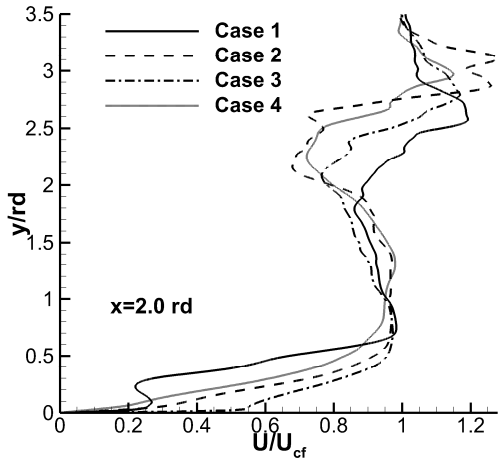

Figure 5.15. Time averaged streamwise velocity (normalized by crossflow velocity) at a horizontal station for all cases

It is seen that rectangular jet - case 2, penetrates more at this station than others. The overall higher penetration of rectangular jets in the near field, is observed on the far field as well. The smoother the velocity profile at this station, the far field conditions are realized earlier. Depth of the dip after the first peak suggests that case 1, reaches far field conditions earlier, followed by case 3, and further by case 4 and 2. Edge length facing the crossflow, thus, inversely affects the reaching of far field conditions. If the width of the largest peak is measured, case 2 spans 0.6898 rd, whereas case 1 spans 0.5062 rd. Case 3 spans 0.8046 rd, and case 4 spans 0.5725 rd. Among the rectangular JICF, the streamwise jet penetration (evidenced by span of the peak) is hence affected inversely by aspect ratio for the same mass flow rate.

The velocity field observed, is primarily driven by the pressure field of the JICF system. In the near field, analyzing the pressure dynamics will thus reveal some important physical insights. It is known that the jet exerts a pressure gradient onto the crossflow as a solid object. Fric and Roshko (1994) compared wake of the JICF with wake behind the cylinder and found some contrasting behavior between the two. Muppidi and Mahesh (2005, 2007, 2008) shed some more light on

the pressure gradients formed in the near field. This was further added to by Iyer and Mahesh (2016). For a careful analysis, mean coefficient of pressure is plotted in the symmetry plane for the cases in Fig 5.16.

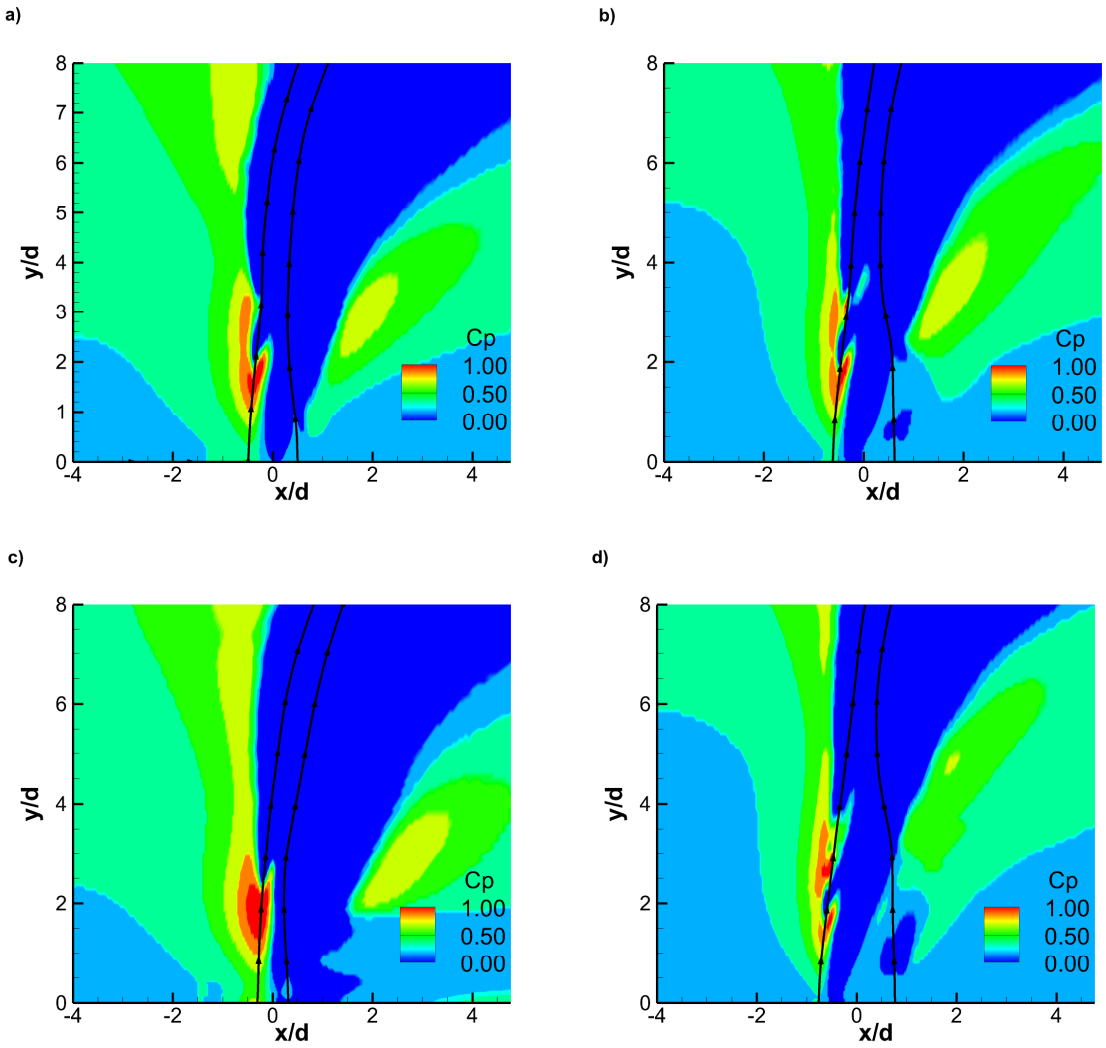

Figure 5.16. Time averaged Coefficient of Pressure (Cp) contours for; (a-d) Case 1-4

The general pressure field shows a consistent pattern for all the JICF cases. The jet exerts an adverse pressure gradient on the crossflow. This will push the crossflow fluid downwards and further backwards to create the horseshoe vortex. A larger pressure minima region in the jet core

is responsible for pulling the fluid from the wake in the jet, and thereby widening the jet, and eventually bending the jet in crossflow direction.

Between the cases, contrasting features are seen as well. Case 3 exhibits the strongest intensity of the adverse gradient. This explains the formation of a prominent horseshoe vortex for case 3, followed by case 1. Because the intensity is low for cases 2 and 4, the horseshoe is not formed completely, as observed before. The pressure minima core is also large near the jet inlet for case 3, this draws more fluid in the trailing edge, which will eventually help bend the jet earlier in the near field.

5.5.2.1 Explanation of bending of jet due to the effect of geometry

Hanging vortices were noted to be affected by different geometries of the jet. The behavior of hanging vortices has major effect on bending of the jet. The physics involved can be described in three states- (i) The initiation of hanging vortices, (ii) The enlarging and merging of the cores of hanging vortices (breakdowns), and (iii) Eventual penetration of these vortices to the jet core, after which the jet bending happens in the domain. To better visualize the physics, mean pressure field is studied at different wall normal locations. The pressure minima depicts a vortical structure- which in this case is the hanging vortex.

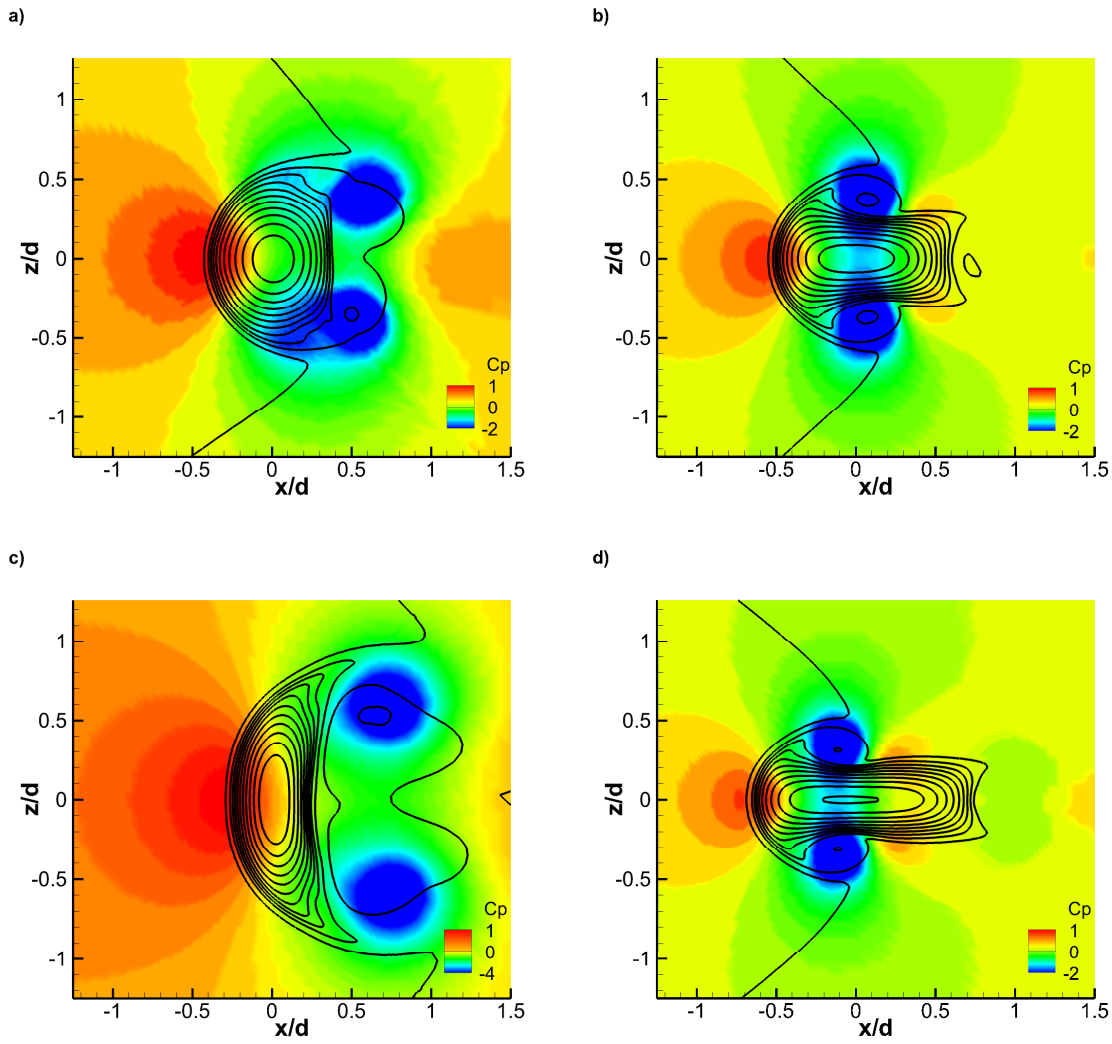

Figure 5.17. Time Averaged Coefficient of pressure in Y=1.5 d plane; (a-d) Case 1-4

The wall normal plane (Y-plane) for the cases are extracted at a location where the near field high pressure gradient is seen for the cases (y=1.5 d) (Fig 5.17). Contours of coefficient of pressure (Cp) are plotted, and contour lines of the vertical velocity field are plotted. When the crossflow fluid wraps around the jet, and meets in the wake region, a recirculation region is created where the flow reverses and a vortex is formed. Change in geometry will have a direct effect on the location of formation of these negative pressure cores. In Case 1, having a circular edge makes it easy for crossflow to wrap around and create vortices in the wake. In cases 2 and 4, the straight

edge makes the fluid flow around the jet more abrupt. This makes the crossflow to flow outwards at an angle to create vortex cores immediately. For case 3, the formation of these vortices is almost immediate after the crossflow wraps around the larger edge. This makes the cores to be seen little farther apart. If the Cp values are noted, case 3 has a larger core which is conducive to earlier bending.

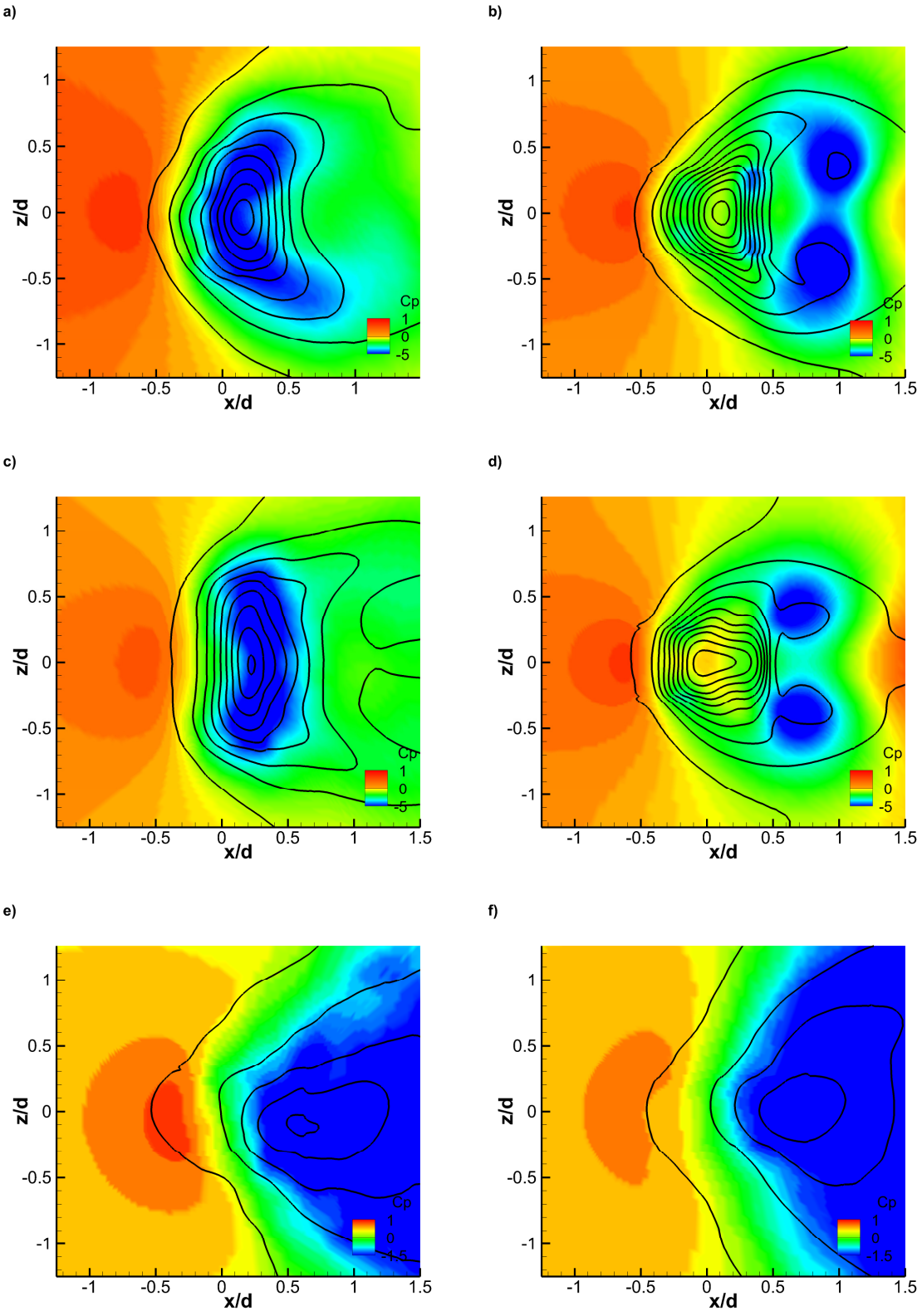

Figure 5.18. Time averaged Coefficient of Pressure on Y=4.5d plane; (a-d) Case 1-4; (e) Y=9.0 d Case 2; (f) Y=9.0 d Case 4

The pressure minima core helps to rapidly entrain fluid from the surrounding. As it entrains more fluid, the core becomes larger and at a point, eventually merge together. After merger of the pressure cores, they penetrate the jet core itself. Further downstream, the pressure cores which is within the jet core, draws more fluid from all around aligning the jet in direction of crossflow. Thus, the jet bends rapidly. For the cases, planes at y=4.5 d is plotted. Case 3 has already penetrated the jet core and is in the process of rapid bending. Case 1, also has penetrated in the jet core but not fully as case 3- making it bend slightly later. Case 2 and 4, still have distinct cores. Case 2, is beginning to merge the cores earlier than case 4, which explains earlier bending seen in the near field. Overall, the geometric effect of the jet is directly responsible for determining the penetration of the JICF system. Fig 5.18 (e,f) depicts cases 2 and 4 in y=9.0 d plane. At this station, case 2 shows that pressure core has not fully encompassed the jet, but case 4 already has achieved this and is in the process of bending of the jet. This further explains the switch between cases 2 and 4 after y=9.0 d. This effect is due to the wake forming closer to the jet core initially in case 4.

5.5.2.2 Turbulence kinetic energy

In this section, effect of jet geometry on second order flow features is studied. Turbulence Kinetic Energy is plotted on the symmetry plane for both the cases is in Fig. 5.19. The turbulence kinetic energy is calculated as:

$$TKE = \langle u_i u_i \rangle / 2$$

TKE is customarily normalized by square of velocity ratio and crossflow velocity. The <>brackets represents time averaging.

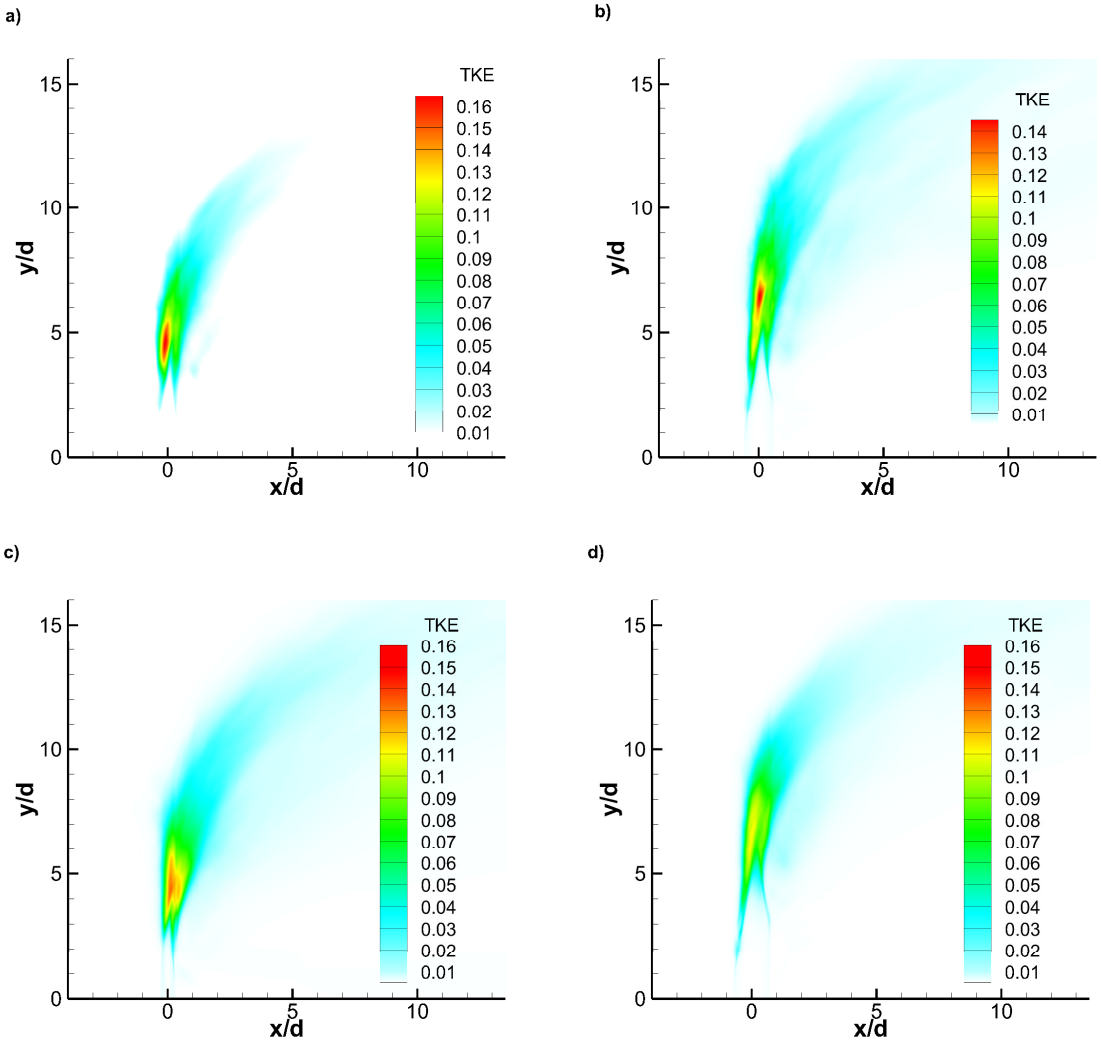

Figure 5.19. Mean TKE in the symmetry plane; (a-d) Case 1-4

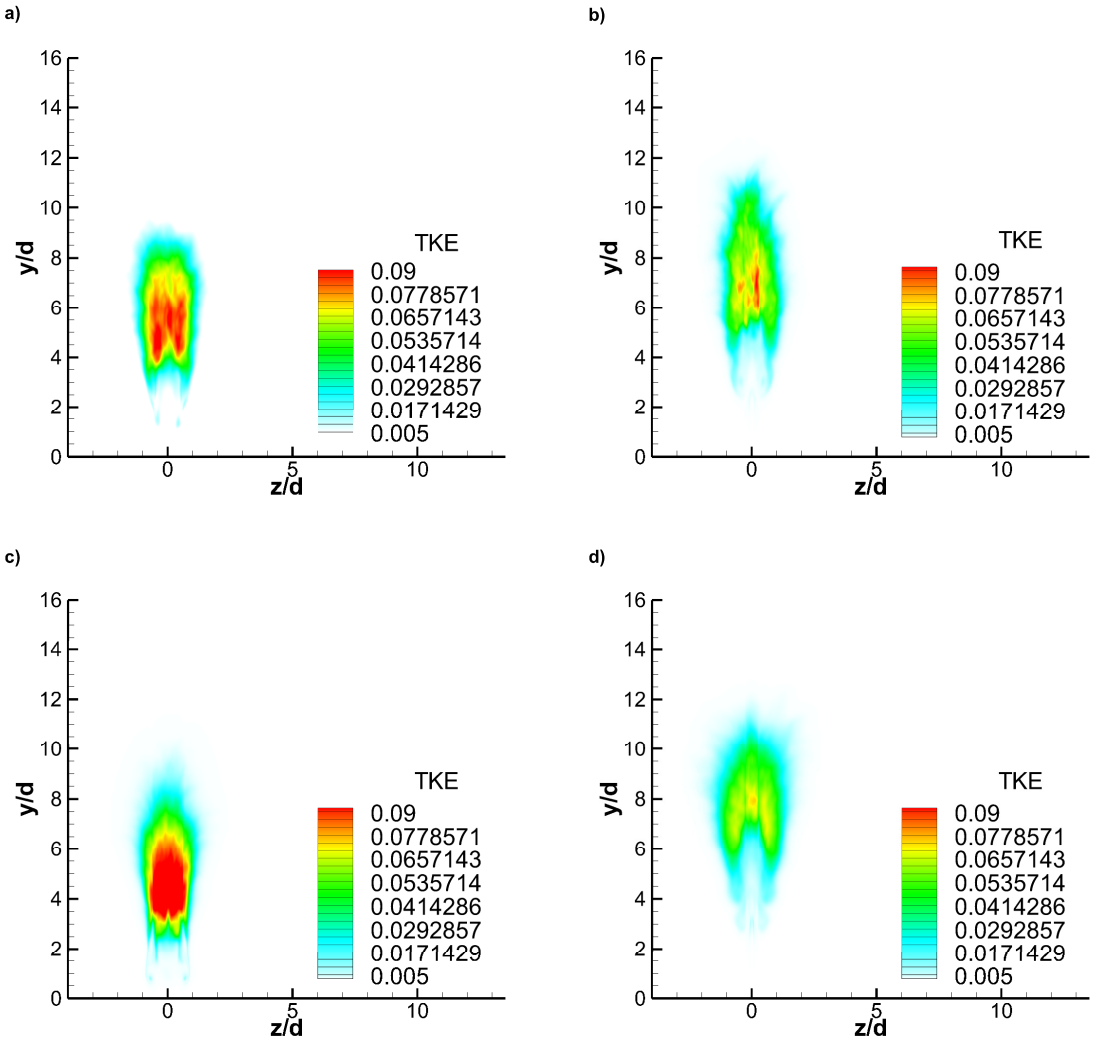

Figure 5.20. Mean TKE for both cases on spanwise plane at immediate wake (trailing edge); (a-d) Case 1- 4

For the four cases, TKE behavior were observed to be different. A common behavior of TKE for all the cases is that it starts at the shear layer and then propagates to the jet core as the flow evolves. Instability, which happens in the shear layer, are the first to trigger turbulence of JICF system. On the shear layers, TKE reflects the instability generated in leading and trailing edges. For case 1 and 3, both edges show TKE but for cases 2 and 4, TKE in the trailing edge is seen later compared to leading edges. Another behavior is the prevalence of high TKE in the leading edge

even after the TKE penetrates to the jet core. This reflects that generation of shear layer vortices are still extant in the shear layer even after penetration of vortices to the jet core.

Merging of TKE in the jet core happens in two stages- initial merging, when the TKE starts to penetrate in the jet core and final merging, after which a uniform TKE field is seen in the jet core. Initial merging for case 1, is seen at (0.05d, 3.5d) and final merging at (0.3d, 6d). For case 2, initial merging starts at (0.1d, 4.5d) and final at (0.7d, 8.7d). Case 3, shows initial merging at (0.04d, 2.8d) and final merging at (0.4d, 6d) and case 4, shows initial merging at (0.02d, 4.5d) and final merging at (0.98d, 10d). This phenomena is often called turbulence breakdown, and the point at which final merging completes is referred as Turbulence Breakdown Point (TBP) (Ruiz et al., 2015). Rectangular JICF delays the TBP to occur further in the domain. In case 3, thin jet on the streamwise direction favors earlier core penetration, and hence, TBP is enhanced compared to others. In general, increasing aspect ratio of rectangular JICF delays the breakdown of turbulence.

The magnitude of maximum non-dimensionalized TKE is 0.163 for case 1, 0.147 for case 2, 0.132 for case 3 and 0.110 for case 4. This is a decrease in maximum TKE for rectangular JICF compared to cylindrical JICF. Among rectangular JICF, aspect ratio inversely affects the maximum TKE in the domain. Kinetic energy persists longer in the shear layer for rectangular JICF, possibly due to the activities involved in axis switching. It is thus described, that rectangular JICF initiates turbulence later in the domain, but spreads it longer in the shear layer with a lower maximum value. Cylindrical JICF initiates turbulence earlier with a higher maximum value, but dissipates it quickly along the shear layer. This effect of change in geometry to local turbulence values are favorable in mixing purposes.

Immediate wake of the jet (which is the plane immediately after trailing edge of the jet) also show the effect of geometry on turbulence (Fig 5.20). Turbulence field is nearest to the jet exit for case 3. Larger edge length, facing the crossflow, generates TKE nearer to the jet in the wake due to earlier wrapping of the crossflow fluid. Higher TKE is seen in the core region for case 3 and 1. Uniform cores suggests further that the TKE has penetrated core and distributed earlier. This observation supports that case 1 and 3 reaches far field condition earlier than case 2 and 4. Large aspect ratio also delays the penetration of TKE in the core region. Mixing in the wake, which is significantly affected by turbulence, is therefore seen to be altered by geometry of the jet.

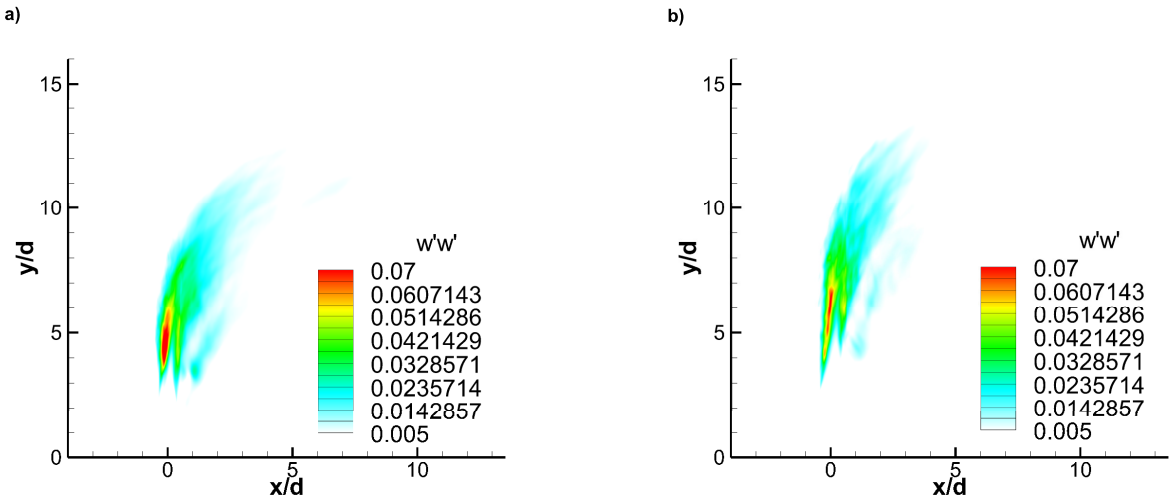

Figure 5.21. Spanwise variance on the symmetry plane; (a-d) Case 1-4 (Figure cont'd)

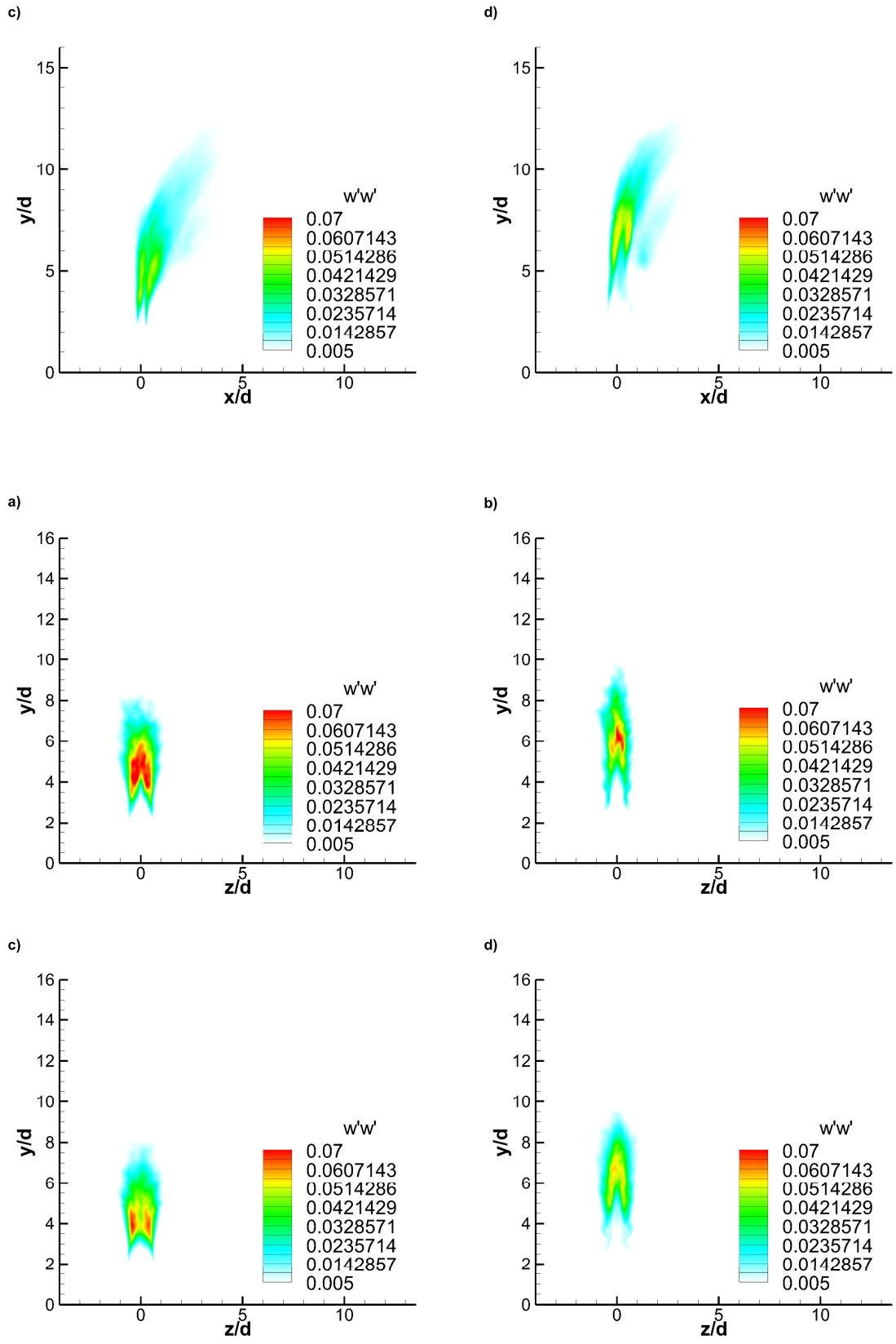

Figure 5.22. Spanwise variance on (x=0 d) spanwise planes; (a-d) Case 1-4

Second order behavior in the spanwise direction, reflective of spanwise mixing can be studied by Fig 5.21 and 5.22. Spanwise variance, which is normalized by square of velocity ratio and crossflow velocity, is plotted. Contours are plotted on the symmetry plane (z=0) and on the spanwise plane (x=0) for the cases (Fig 5.21 and Fig 5.22).

On the symmetry plane, the effect of geometry in spanwise variance mimics the effect on the TKE. High variance region is present in leading edge of case 1, which is short-lived. Comparatively, smaller region is seen in leading edge of case 2, which is long lived. Case 3 and 4, show similar levels on both edges of the jet and both are at higher depth. Case 4, has the deepest initiation of spanwise variance and case 2, has the longest affected area. Increasing aspect ratio (case 3, 2 and 4) initiates the merging of spanwise variance deeper in the domain. Area of spanwise variance can be useful to locate areas favorable to mixing in the spanwise direction. Case 1, has larger length in the streamwise direction compared to case 2, which has narrower length in streamwise direction but larger length in wall normal direction.

Largest edge length facing the crossflow has the earliest generation of spanwise variance. Streamlines traveling around the jet, which is different due to geometry, affects the turbulence in the spanwise plane. High intensity fluctuation is present on case 1, but overall, larger depth downstream is seen for case 3 and 4. This is one of the factors that make rectangular JICF to help more mixing as it moves downstream. Larger aspect ratio tends to push the variance deeper in the domain.

5.5.3 Axis switching

It was observed that axis switching plays an important role in determining the path of the jet, as well as second order Reynolds stresses. From literature, it is known that rectangular JICF exhibit

90° axis switching. However, effect of crossflow on rectangular jets has not been studied for axis switching. Here cases 2, 3, and 4 are compared. Normally, axis switching is determined by crossover of lengths of half centerline velocity.

Different planes are depicted with time averaged velocity (normalized with crossflow velocity) contour lines for the rectangular JICF cases in Fig 5.23. The initial planes are at (y=0d), which show the initial orientation of the jets. Second planes are chosen such that the initiation of axis switching is seen by enlargement of one side of the edges. For case 2, this is seen at y=2.5d. For cases 3 and 4, these are seen at y=4 d. The third plane show the location at which the official axis switching is seen which is rotated by 90°. For case 2, it lies at y=5d, for case 3, at y=6d, for case 4, at y=5.7d. It can be seen that axis switching is affected both by the edge which faces the crossflow, and the aspect ratio of rectangular JICF. This is a novel conclusion found by the current study. If the long edge faces the crossflow, axis switching is delayed, and if the short edge faces the crossflow, axis switching is enhanced. This is due to the enlargement of the axis happening from the edge facing the crossflow. Aspect ratio of rectangular JICF is also seen to delay axis switching, which is consistent with literature for jets in a quiescent flow. For cases 2 and 4, second axis switching is also observed during the study at about y=9.0 d and y=9.3 d which is consistent with the current behavior.

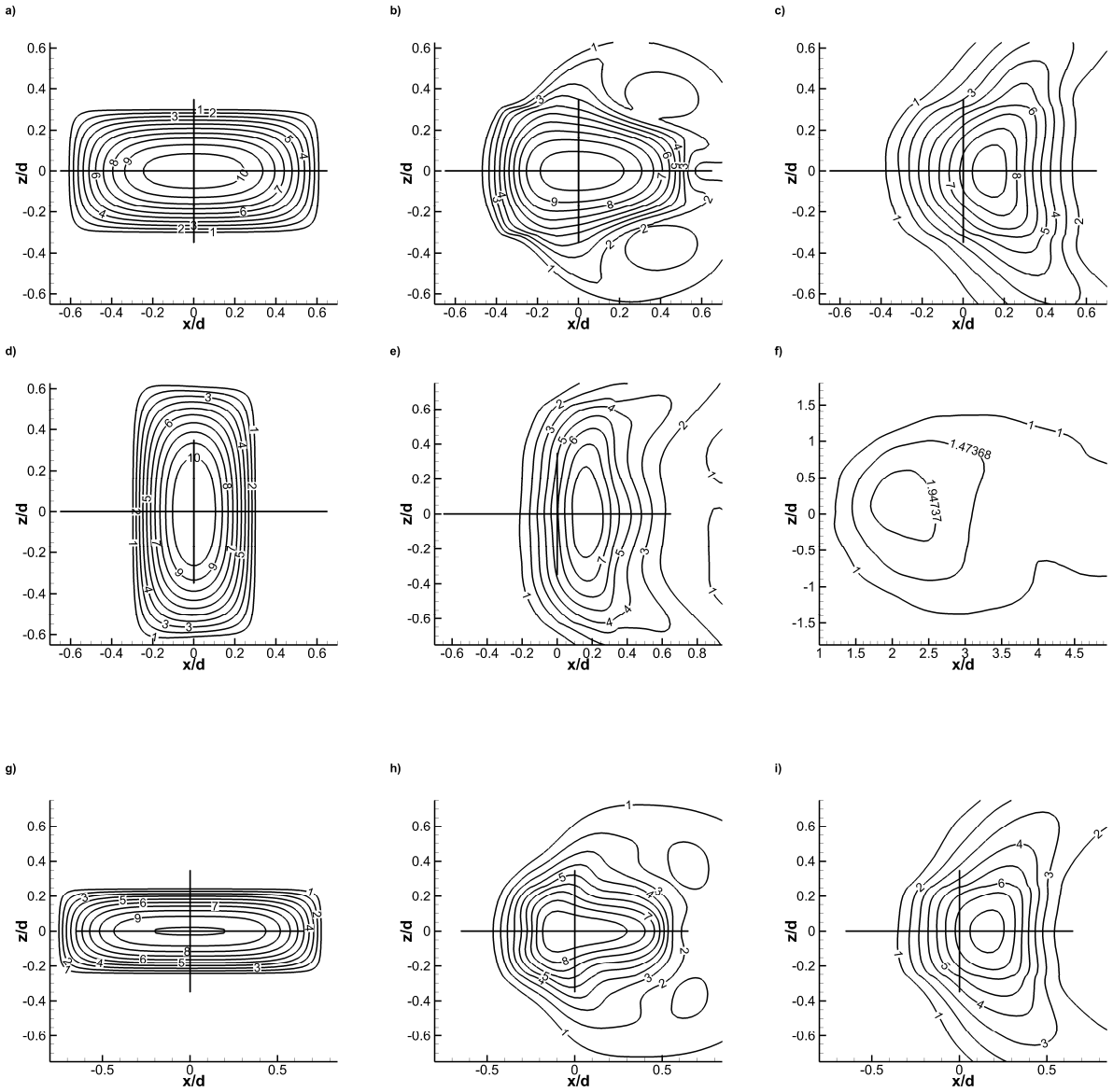

Figure 5.23. Time averaged velocity contour lines of spanwise planes; (a, b, c) Case 2; (d, e, f) Case 3; (g, h, i) Case 4

5.6 Section 6- Stability

5.6.1 Spectral analysis

For convectively unstable shear layer, multiple dominant frequencies are observed by Megerian et al. (2007). To observe and confirm the same behavior, 5 points in the shear layer are picked (s/d =2.0, 3.0, 4.0, 5.0, 6.0). The points in the current simulation are picked at a higher depth than

conventional to account for the laminar jet simulated. For laminar jets, shear layer instability happens at the higher depth compared to turbulent jets of the experiments.

Spectral analysis is done for vertical velocity in the domain normalized by the mean jet velocity. For Power Spectral Density (PSD), the velocity field is stored at each instant of the simulation. The timestep of the simulation is 2.0e-5 s. Hence, the sampling frequency is 50 kHz. So based on the Nyquist criteria, the maximum frequency that can be captured is 25 kHz. The frequency resolution of the PSD (the minimum frequency that can be captured) is about St=0.02. This is below the frequencies that are expected to be observed by orders of magnitude. For the current results, 12 blocks are averaged. A “Hamming” window is used for the signal, and 50% overlapping is done to get a smooth transition between blocks.

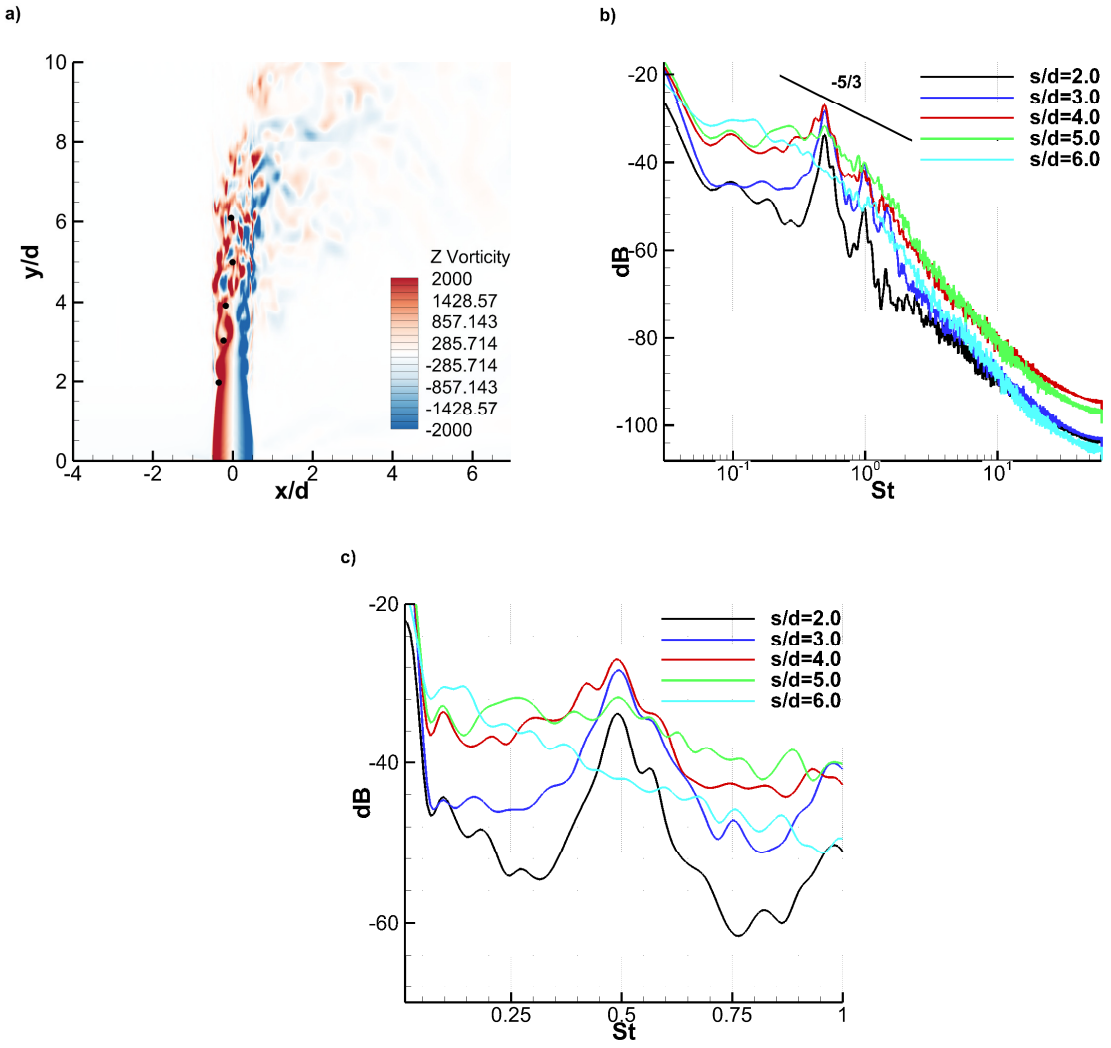

Figure 5.24. (a) Points selected for PSD; (b) PSD of vertical velocity for the selected points- semilog plot; (c) PSD of vertical velocity-initial frequencies

The PSD plot with logarithmic axis (Fig 5.24 (b)), in the x-direction, indicates that the frequencies in the initial regions are most dominant with higher energy in the flow. Furthermore, transition to turbulence is seen in the slope of decay, which is (-5/3). This slope represents characteristic decay of turbulence in the inertial subrange. This indicates that the instability of shear layer region transitions to turbulence, as the jet evolves. Zooming in the initial region (Fig 5.24 (c)), the dominant frequencies and their behavior can be quantified.

The first point lies at a depth where the breakdown of large initial rollup happens. Two frequencies are strong in the shear layer- The dominant is St=0.49 and another strong peak is St=0.1. The 3 points above it have the smaller spanwise and wall normal vortices. The dominant frequency seen from the PSD plots is (St=0.49). The last point shows the initial frequencies around St=0.1 as the dominant one. This point corresponds to the collective rollup of vorticity in the shear layer. Due to presence of much vortical structures, a noisy signal is obtained at this point. PSD plots show less decibels for higher frequencies due to presence of low intensity vortices. The presence of multiple dominant frequencies in the shear layer provides proof of convective unstable jets (Megerian et al., 2007; Iyer & Mahesh, 2016).

5.6.2 Modal analysis

Modal analysis is conducted for the cases using DMD technique. The details of the algorithm are outlined in section 2. A shorter domain (36 d X 29 d X 24 d), from within the main geometry, is selected for analysis owing to its relevance. Total 190 snapshots are taken for DMD. It was observed that by taking 150 snapshots and 180 snapshots, there were no significant difference between the dominant eigenvalues of the problem.

The temporal spacing for the snapshots is considered based on the PSD data and the Nyquist criterion. The non-dimensional time step for each snapshot is 0.325. For validation, 2D flow over a cylinder data was taken from Kutz et al. (2016) and the DMD algorithm was designed from the same. The Strouhal number calculated for the most energetic mode from DMD (St=0.16) is equal to the same as obtained from experiments.

The eigenvalues obtained from DMD analysis are complex in nature. The real part gives the growth rate of the mode, and the imaginary part gives the angular frequency of the mode. The

second norm of the computed amplitudes gives the amplitude associated with each mode. As a consequence, the high amplitude modes are the most dominant in the system.

The amplitude spectrum is plotted in Fig. 5.25. Prominent peaks of amplitude is present for Strouhal numbers (St=0.1 and St=0.496) for cylindrical JICF- case 1. These are exactly the same frequencies observed in the shear layer, as seen from the spectral analysis. Hence, the shear layer modes are most dominant in the system. Other high amplitude modes are also seen for the case. Existence of multiple high amplitude modes are due to rapid breakdown of turbulence in the domain for generating more different sized structures.

For case 2, the significant amplitudes are seen for St=0.178 and St=0.788. Case 3 also shows multiple significant modes and two major significant amplitudes are seen for St=0.082 And St=0.819. For case 4, significant amplitudes are seen for St=0.172 and St=0.713. Unlike case 1 and 3, only two modes are seen to have a high amplitudes in the overall domain for case 2 and 4. Here it is seen that the high amplitude Strouhal numbers are at a higher frequency for rectangular JICF than the cylindrical JICF. Iyer and Mahesh (2016) have seen different dominant frequencies for velocity ratio 4.1 turbulent jet issued from a nozzle (St=0.39 and St=0.78). Also, for velocity ratio 5.7 jet for turbulent pipe flow, Ruiz et al. (2015) report different frequencies along the shear layer (St=0.2, 0.3 and 0.5). Hence, it can be concluded that geometry and inlet conditions play a significant role in altering the dominant frequencies in the shear layer.

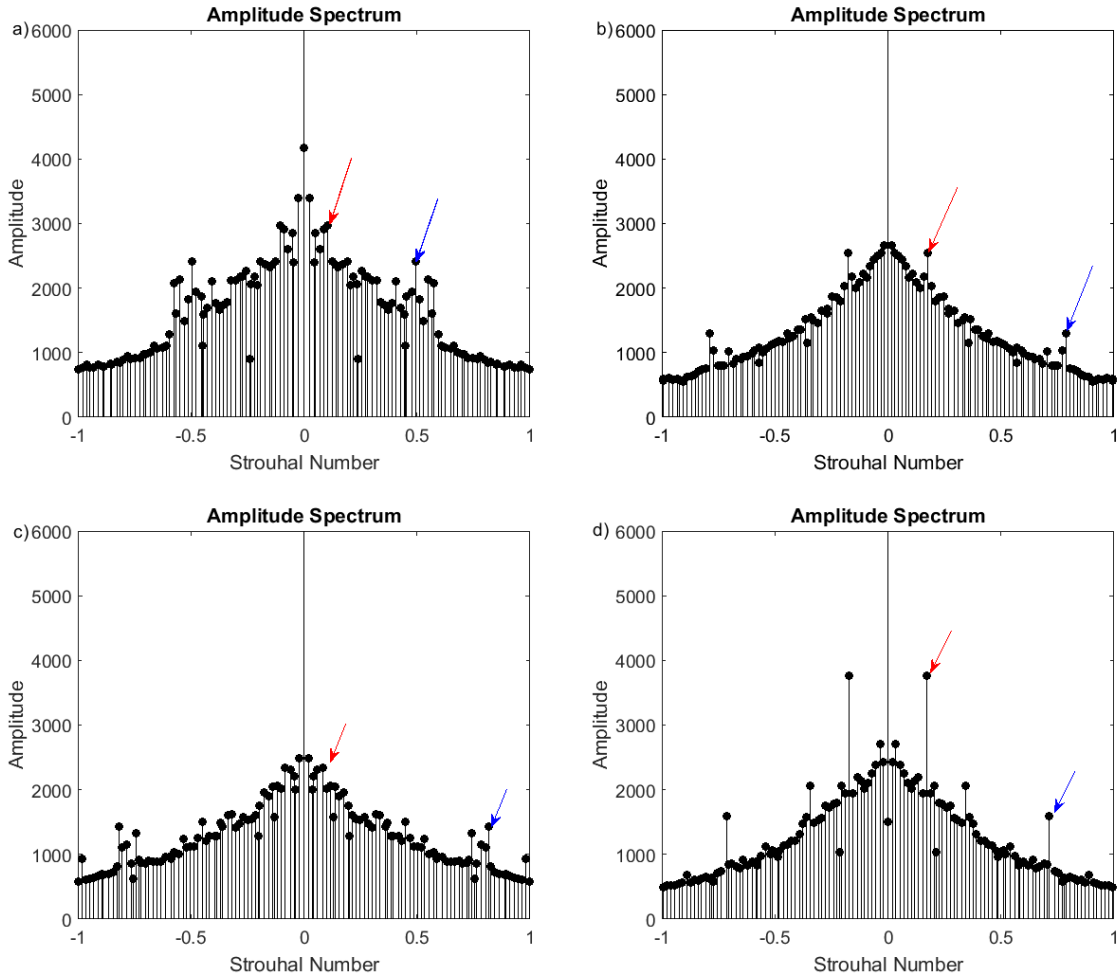

Figure 5.25. Amplitude of Dynamic Modes; (a-d) Case 1-4

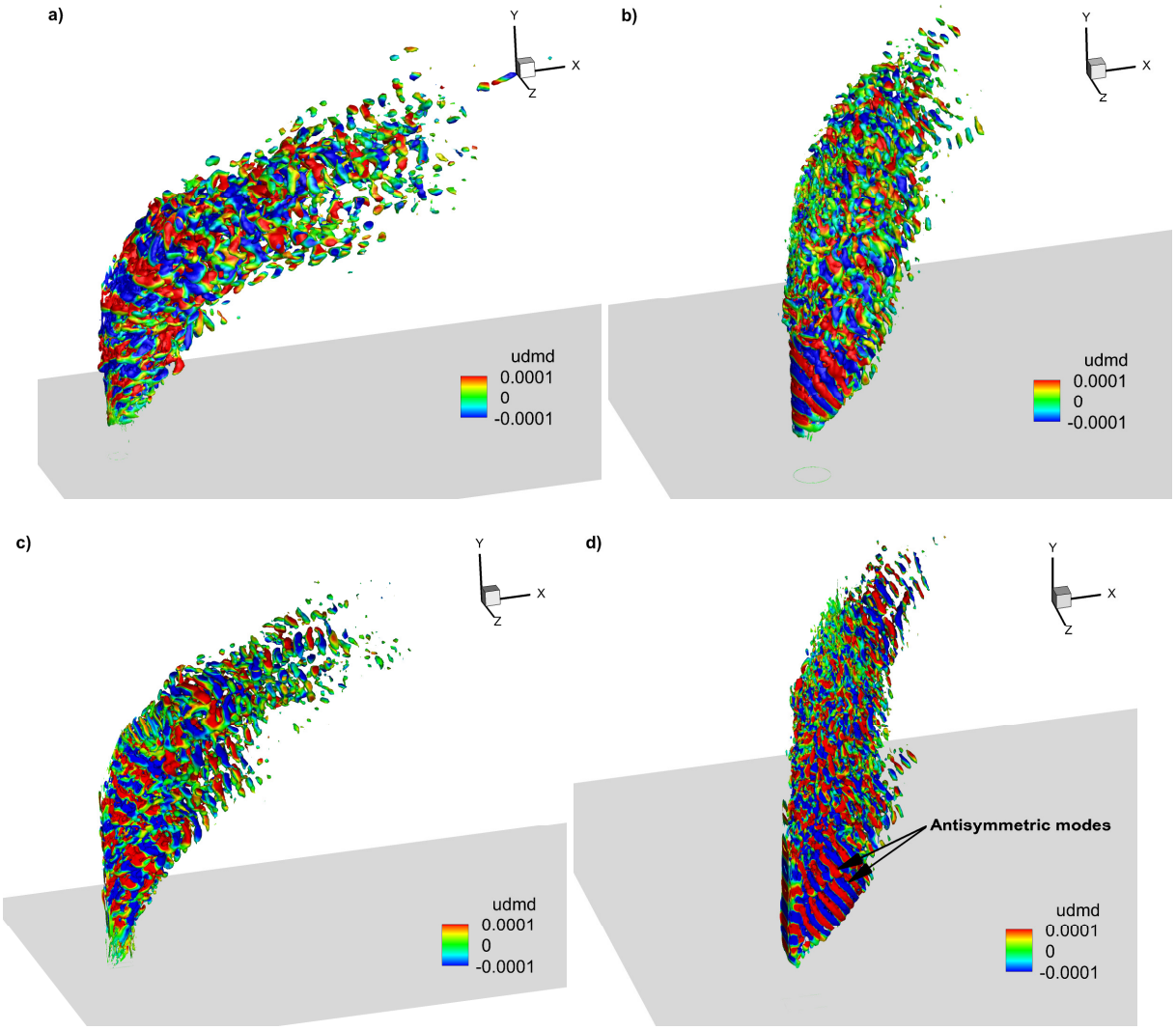

Figure 5.26. Iso surface of Q-criteria calculated for spatial dynamic modes; (a, b) For case 1; (c, d) For case 2; (a) For St=0.1; (b) For St=0.49; (c) For St=0.178; (d) For St=0.788

To understand the effect of these two particular modes in the domain, the iso-surfaces obtained from Q criteria of the real part of the spatial DMD modes are plotted (Fig. 5.26). The contours are colored by the streamwise velocity of the dynamic modes. It can be seen that the lower frequency mode spans larger distance and covers most of the shear layer of the flow. The structures show a larger rollups in the system being of a low frequency. It can be noted that this mode only starts in the domain at a certain depth. Therefore, this mode corresponds to the shear layer rollup observed physically in the domain. In contrast, the high frequency mode corresponds to smaller

rollups and initial split of vorticity on the shear layer. It is further observed that high frequency mode spans lesser depth of the domain, and breakdown into smaller structures also happen early. The depth of the high frequency mode starts at earlier location than that of low frequency mode. As the flow evolves, low frequency mode becomes dominant.

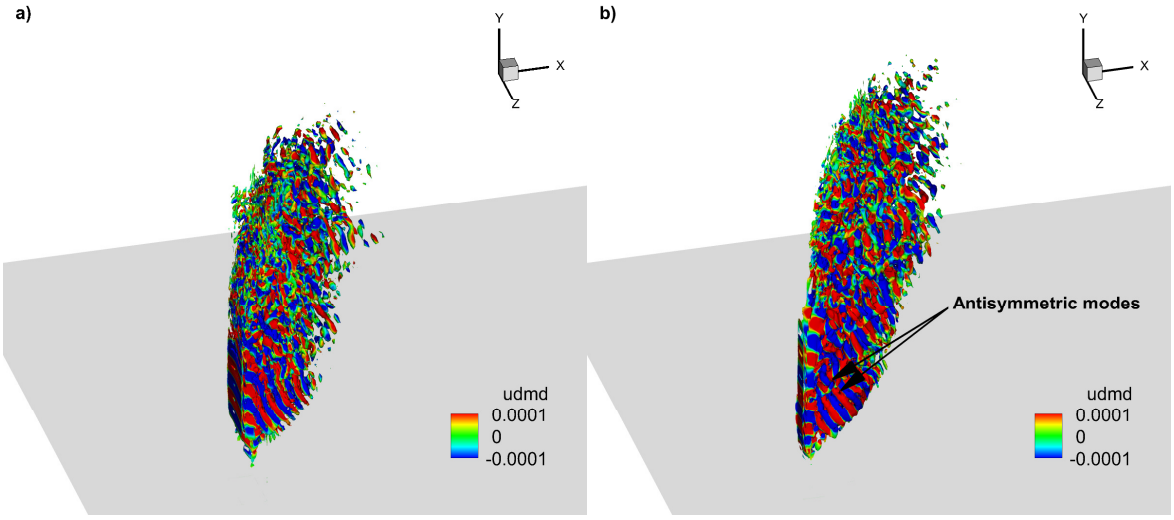

Figure 5.27. Iso surface of Q-criteria calculated for spatial dynamic modes; (a) Case 3- St=0.819; (b) Case 4- St=0.713

For both the modes, breakdown into smaller structures are more present in case 1 compared to case 2. Earlier breakdown of structures drives this behavior for case 1. It is evident that the significant modes are in the shear layer, indicated by the clear geometric shape of the modes, especially for rectangular JICF. For case 3 and 4, only high frequency iso-surfaces are plotted in Fig 5.27. As in the previous plots, it is seen that rectangular JICF shows instability capturing the shape of the leading edge of the jet. On rectangular JICF (case 2 and 4), anti-symmetric modes can be seen for high frequency. These modes are in the location where rollup is in the leading edge, but not seen in the trailing edge. Prominent ribbed-like structures are seen in this distance, which is present during axis switching. Hence axis switching also effects the modes in the nearby the trailing edge shear layer. This behavior is not seen for case 1 and 3.

The significant modes show instability on shear layer of the jet. Vorticity magnitude on the symmetry plane is plotted for the four cases in Fig 5.28.

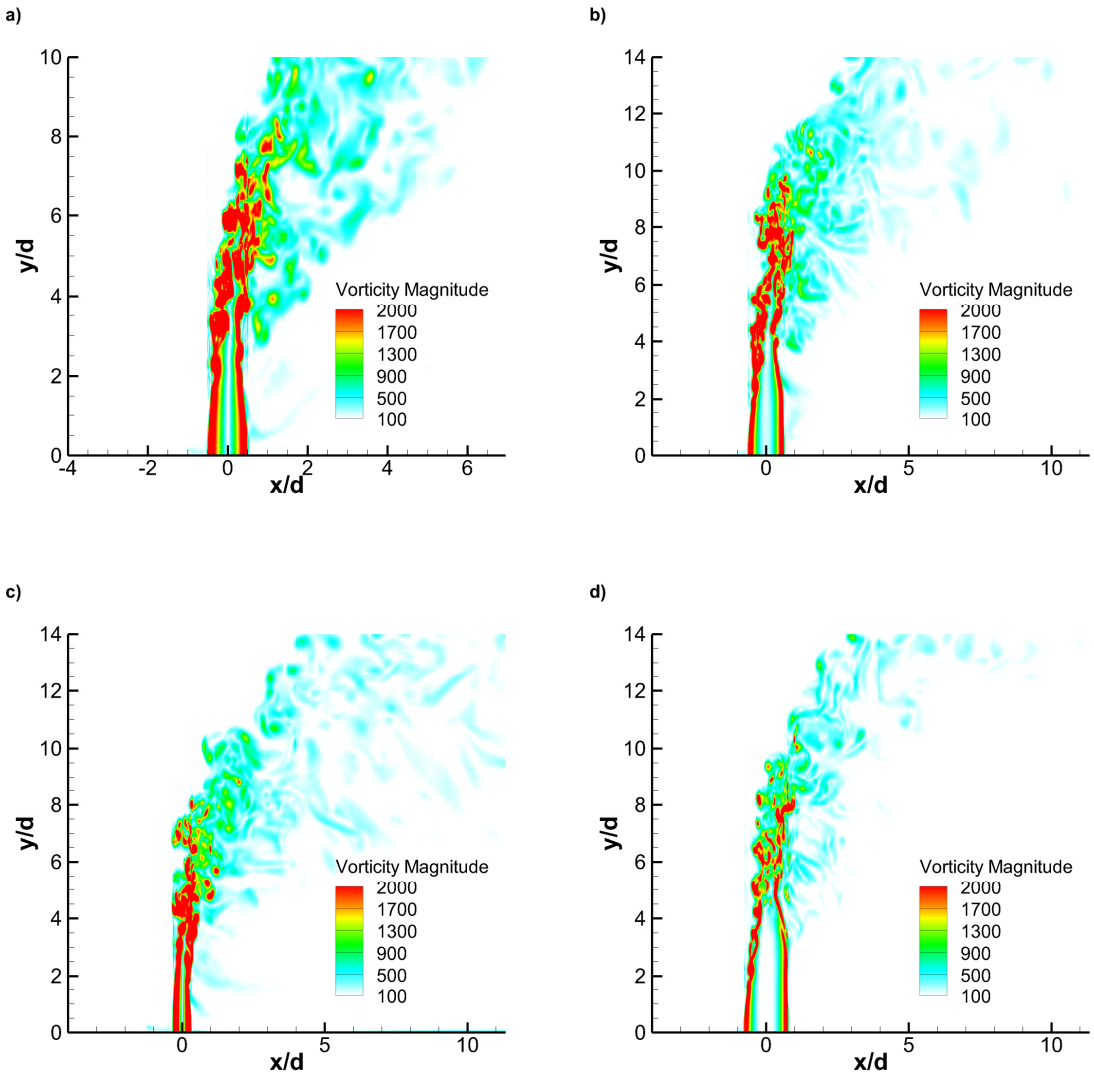

Figure 5.28. Vorticity Magnitude for the 4 cases; (a-d) Case 1-4

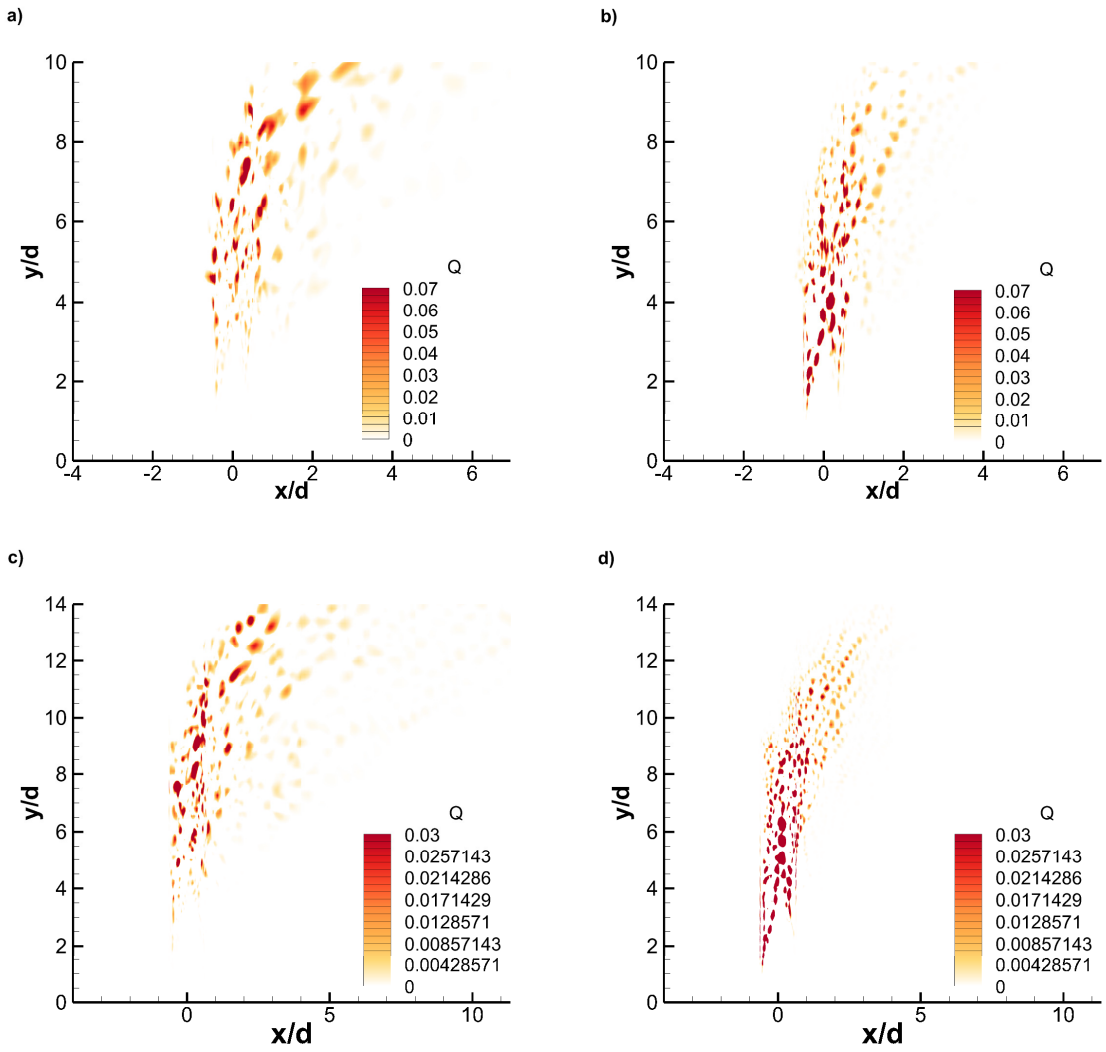

Figure 5.29. Contours of q-criteria of dynamic modes on the symmetry plane; (a, b) For Case 1; (c, d) For Case 2; (a) St=0.1; (b) St=0.496; (c) St=0.178; (d) St=0.788

Q criteria of the dynamic modes on the symmetry plane (Fig. 5.29) gives a clearer picture of the spatial dominance of the multiple modes. Both the modes for case 1 and case 2, are plotted. As before, high frequency mode dominates earlier and then low frequency modes dominate. Comparing with Fig 5.28, the high frequency starts at the place where initial vortex rollup starts to break in the shear layer. The low frequency mode starts where the vorticity from the shear layer moves to the jet core and combine to form larger vortices. High frequency structures begin on the shear layer and then propagate towards the jet core. For high frequency, a breakdown

into smaller intensity is seen after approximately y=6.0 d to 8.0 d (case 1). This corresponds to the switch seen on the PSD plots. Similar behavior is seen for case 2, but at a higher depth. For case 2, the vortices are also smaller compared to case 1 and hence the frequency is higher.

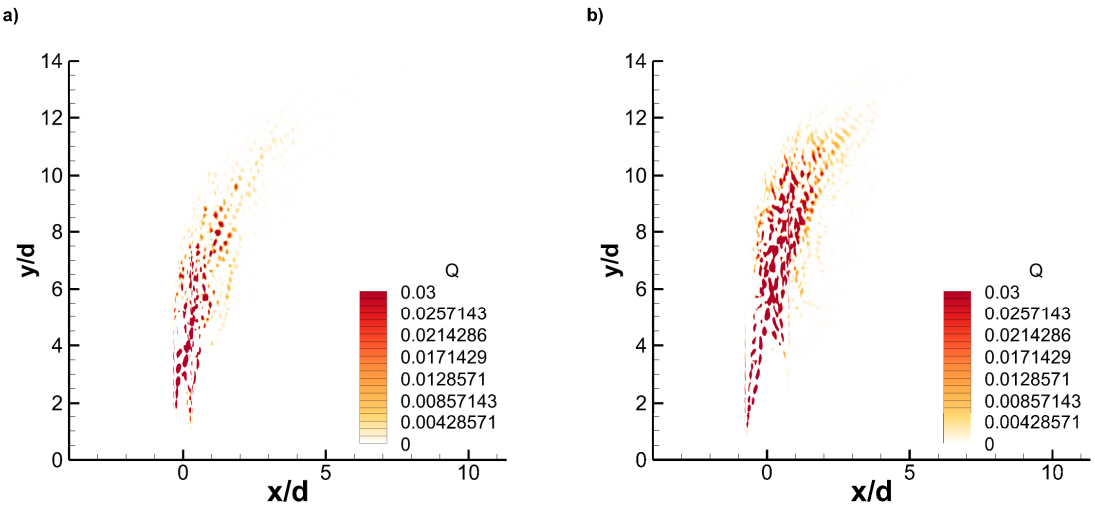

Figure 5.30. Contours of q-criteria of dynamic modes on the symmetry plane; (a) Case 3- St=0.819; (b) Case 4- St=0.713

High frequency modes are plotted on the symmetry plane, for cases 3 and 4 in Fig 5.30. Modes in leading edge and trailing edge closely follows with the vortical structures seen in Fig 5.28. It is further interesting to see the dominance of high frequency mode earlier for case 3 than all other cases. This correlates with the earliest bending before switchover for case 3 because breakdown happens early. Cases 2 and 4 show a deeper penetration compared to cases 1 and 3. This correlates well with the jet penetration in the main domain. Once overall turbulence breakdown occurs, high frequency modes stop dominance and low frequency mode takes over possibly continuing along the domain.

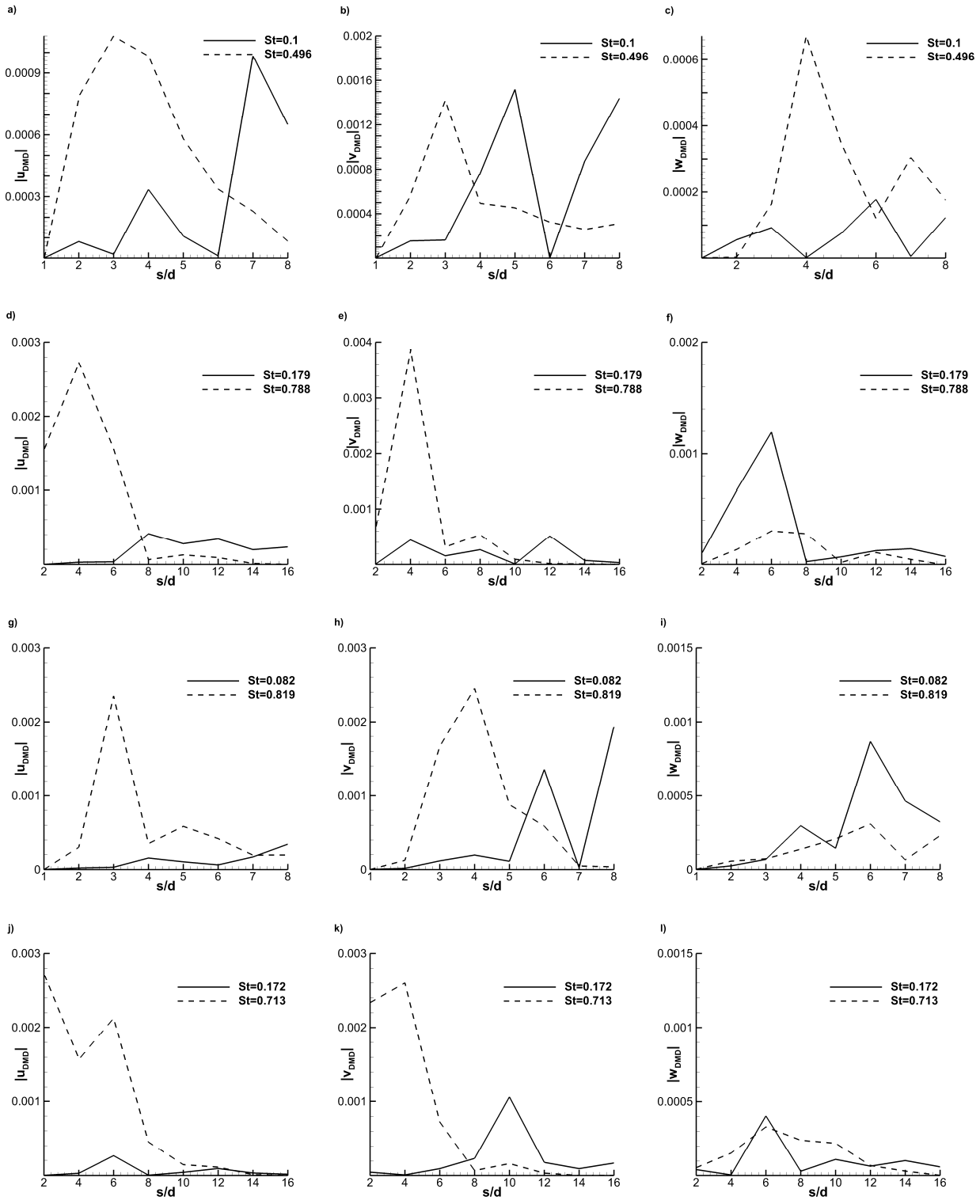

Figure 5.31. Magnitude of Velocity of dynamic modes for both frequencies for (a, b, c) case 1; (d, e, f) Case 2; (g, h, i) Case 3; (j, k, l) Case 4; (a, d) Streamwise velocity; (b, e) Vertical velocity; (c, f) Spanwise velocity

Isolating the fluctuations of three principle directions obtained from DMD gives us deeper insight of the modes in three directions. The magnitudes of the DMD velocity data are plotted (Fig. 5.31) along the shear layer, for the two frequencies for the four cases. For cases 1 and 3, due to earlier bending of the jet, points are picked at same locations of the PSD plots. For cases 2 and 4, the points picked are till double the depth. For all the cases, streamwise mode and vertical mode both show an earlier dominance of high frequency mode and later dominance of low frequency mode. However, contrasting behavior is seen for spanwise mode. This behavior is noted by Iyer and Mahesh (2016) for VR=4 nozzle flow. Case 1 shows full dominance of high frequency mode. On the other hand, cases 2, 3, and 4 show a dominance of low frequency mode in most locations. This also shows that geometry change (from circular to rectangular) affects the instabilities in the spanwise direction. Corner regions play a role in promoting low frequency mode and suppressing high frequency mode, by the abrupt disturbance in the flow itself. Different aspect ratios (cases 2 and 4) show similar qualitative behavior of modes but only the magnitudes of instabilities are different- larger aspect ratio showing lesser magnitude.

5.6.2.1 Modal contribution to velocity field

Once the eigenvalues and the dynamics modes are calculated, the velocity field can be reconstructed using the modal information. The equation used for reconstruction is taken from Kutz et al. (2016). The reconstructed velocity field is given by:

$$\boldsymbol{u}(x,y,z,t) \approx \sum_{i=1}^{N} \phi_i \exp(\lambda_i t) b_i$$

Where vector of initial amplitude of each mode $\boldsymbol{b} = \boldsymbol{\phi}^{\dagger}\boldsymbol{u_1}$ where † denotes pseudo-inverse.

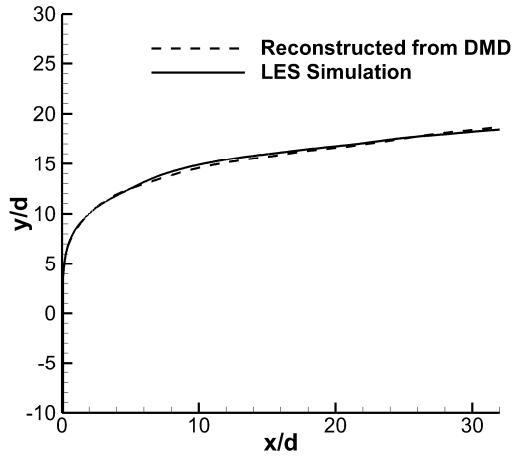

Figure 5.32. Validation of velocity reconstruction procedure

All modes were used to construct velocity field at all 190 time instants. The velocity instants were then averaged and the center streamline from this averaged data was compared with the time average of the original simulation data. It is seen from Fig. 5.32 that a close match is obtained. An important feature of DMD is illustrated by this validation. By adding only significant modes, time averaged data can be predicted with near accuracy with very less number of snapshots. This is useful when dealing with limited data sets. Using the above procedure, velocity contribution of individual modes can be extracted separately. Fig 5.33 depicts the reconstructed velocity field for three modes of case 1 (Mean mode, St=0.1 mode, St=0.49 mode) on the symmetry plane. The velocity field is normalized by the crossflow velocity. Contour levels are adjusted for clarity.

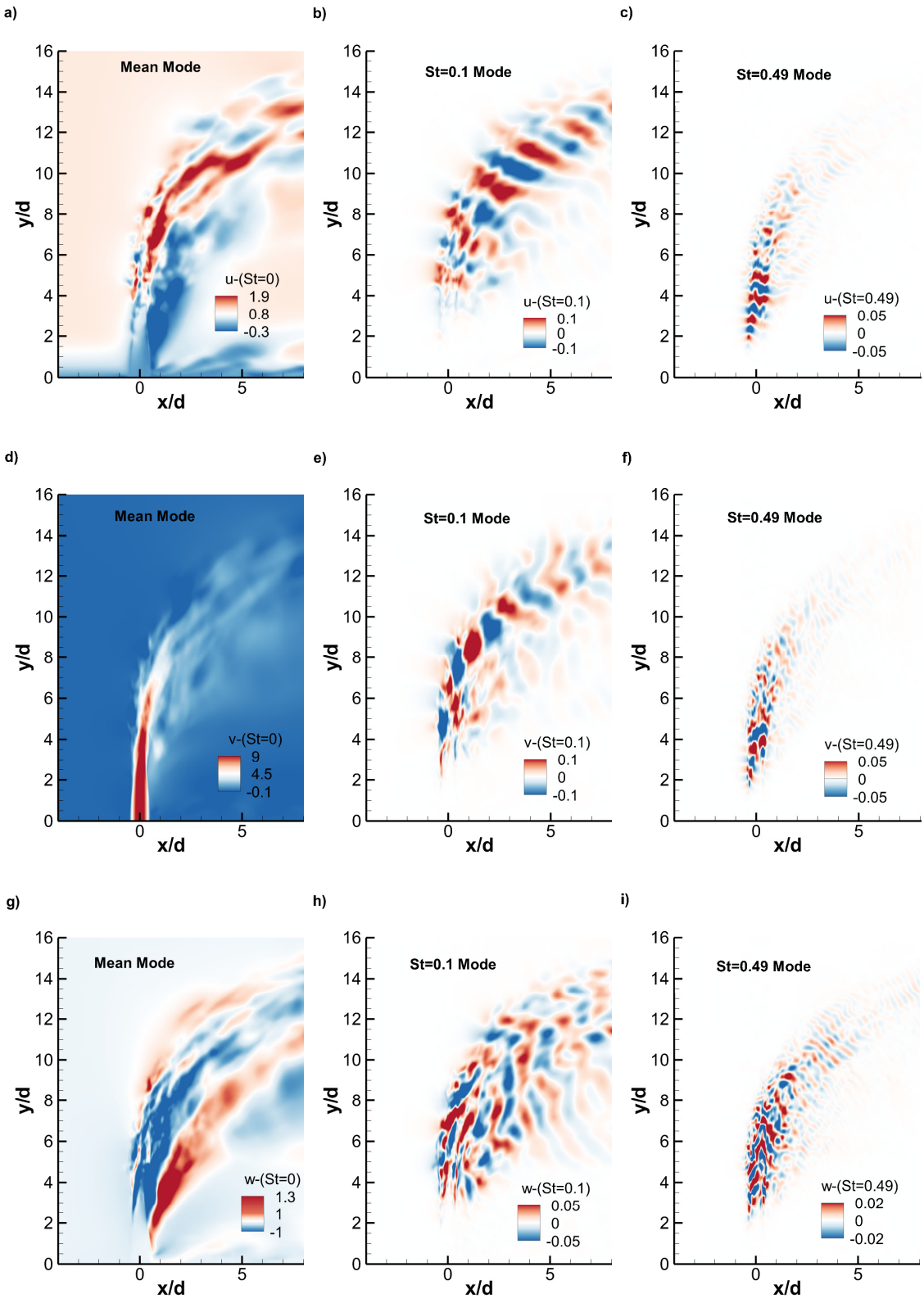

Figure 5.33. Contribution of different modes to the velocity field of cylindrical JICF; (a, d, g) Mean mode; (b, e, h) St=0.1 mode; (c ,f, i) St=0.49 mode

Same reconstruction procedure was used for rectangular JICF- case 2 and the three modes (Mean mode, mode- St=0.179, mode- St=0.788) are plotted on the symmetry plane in Fig. 5.34. The contour levels are adjusted for clarity as before.

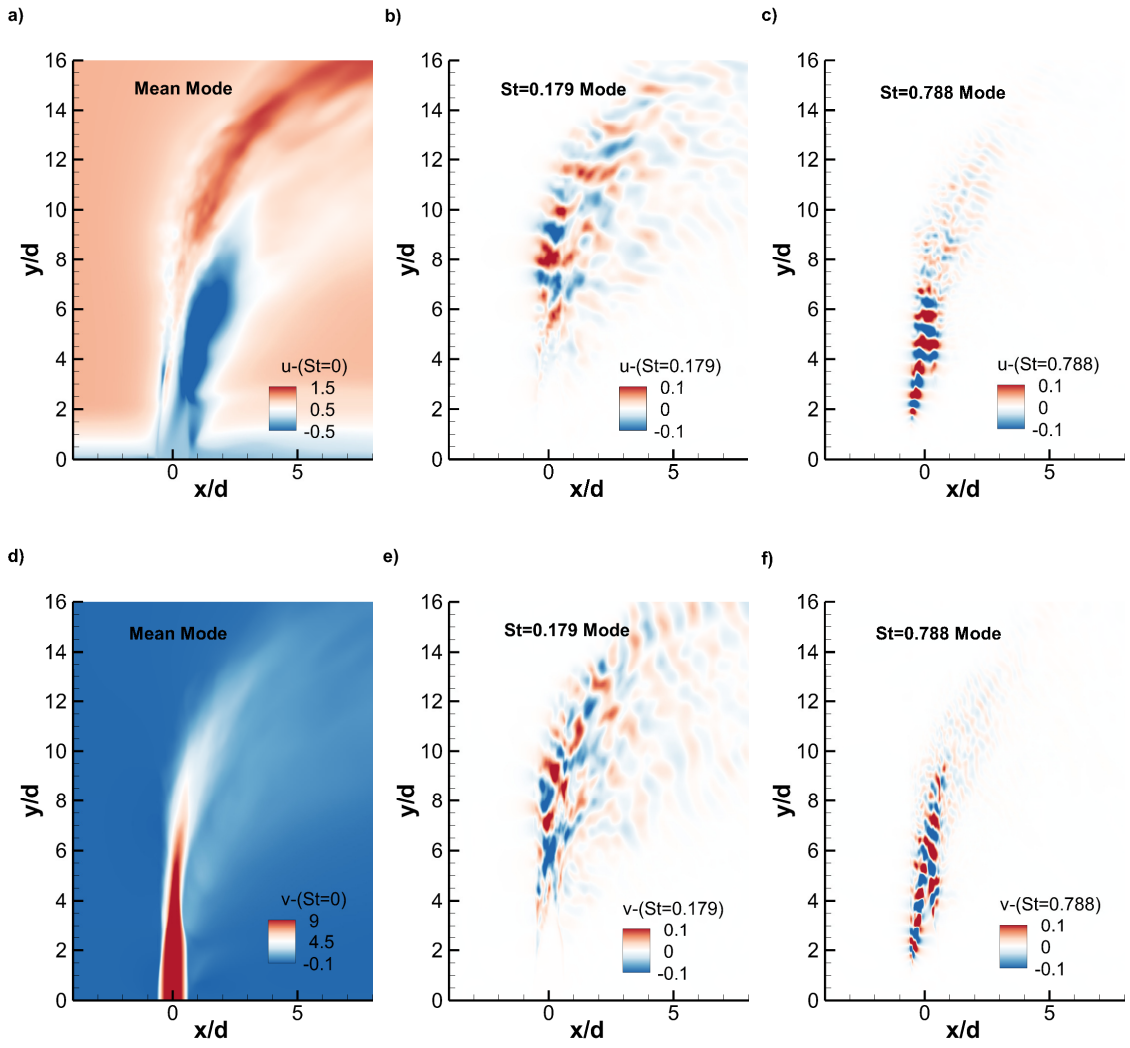

Figure 5.34. Contribution of different modes to the velocity field of rectangular JICF; (a, d, g) Mean mode; (b, e, h) St=0.179 mode; (c, f, i) St=0.788 mode (Figure cont'd)

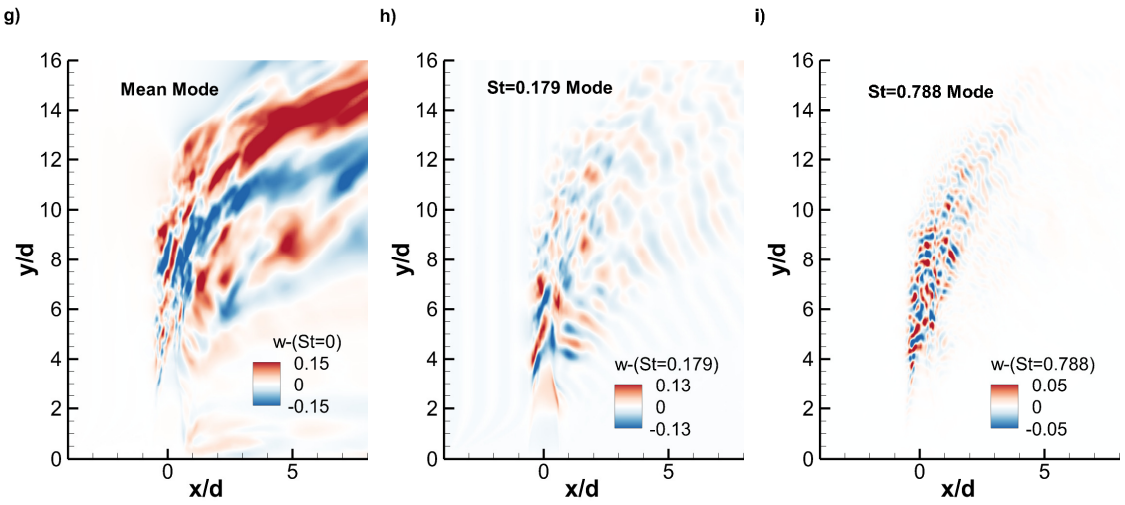

The mean mode from DMD analysis agrees well with the mean flow of the simulation (Fig 5.33 and 5.34). The vertical velocity shows expected magnitudes, as that of LES simulations, for both case 1 and 2. The contributions from each dominant mode is plotted as well. For streamwise and vertical velocity, the modes show high frequency contribution in the near field and then low frequency contribution. This agrees with the previous analysis. Spanwise velocity of the modes show both frequencies dominating from earlier depth. Additionally, a complimentary behavior is observed. If low frequency contributes to spanwise velocity in the shear layer, high frequency contributes to the jet core and vice versa.

For low frequency modes of case 1 and case 2, the streamwise velocity show horizontal streaks passing from leading edge to trailing edge. For the magnitudes, case 1 shows similar intensities throughout the streaks of positive and negative velocity contributions. For case 2, on the other hand, high intensity streamwise velocity is seen more in the leading shear layer initially which later becomes uniform with the jet core. This is due to the later breakdown of structures in case 2. Vertical velocity contributions show velocity streaks, which are also vertical in nature.

Spanwise velocity contributions show an inverted V shape suggesting that velocity in the jet core evolves earlier compared to velocity of the shear layers.

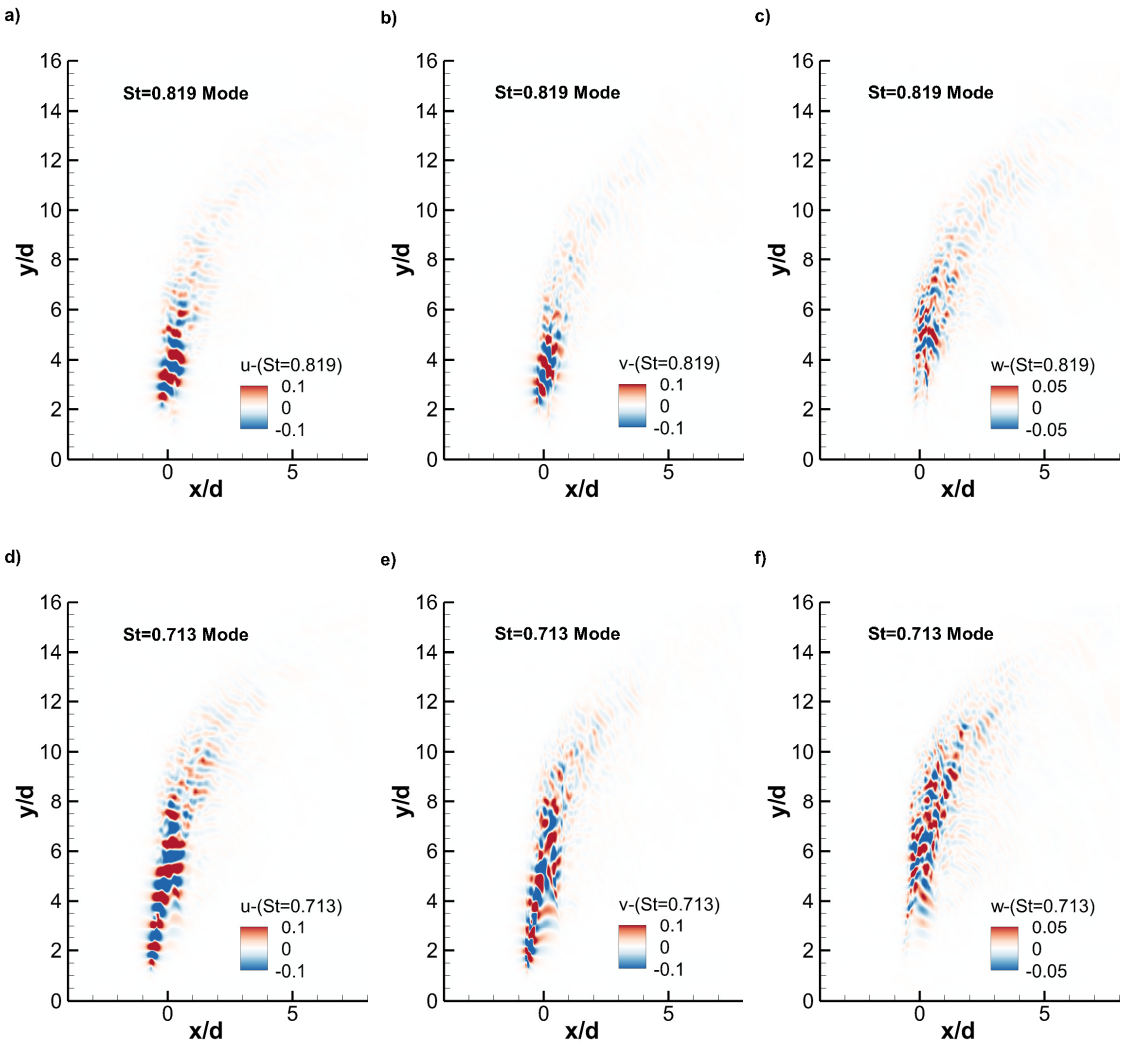

Figure 5.35. Contribution of high frequency mode to the velocity field of rectangular JICF; (a, b, c) Case 3; (d, e, f) Case 4

Considering the maximum of the mean mode, the contribution of low frequency mode is ±4% to streamwise velocity, ±2.3% to vertical velocity, ±5% to the spanwise velocity. Similarly for rectangular JICF- case 2, the low frequency mode has contributions of ±9% to streamwise velocity, ±1.7% to the vertical velocity and ±39.5% to spanwise velocity. The discrepancy in the spanwise velocity contribution in both cases is due to sudden overall instability generated around

circumference of cylindrical jet and less spanwise depth of jet in rectangular JICF (case 2). For the high frequency mode for case 1, velocity contribution is ±3.12% to streamwise velocity, ±1.5% to vertical velocity and ±2.5% to spanwise velocity. For case 2, the contribution is ±19% to streamwise velocity, ±5.6% to vertical velocity and ±30% to spanwise velocity. Except of spanwise velocity for case 2, low frequency mode has higher contribution to the velocity field for case 1. On the other hand, the high frequency mode contributes more to the velocity field overall in rectangular JICF (case 2) compared to cylindrical JICF.

High frequency modes, being more interesting for comparison, are plotted for cases 3 and 4 in Fig 5.35. Case 4 behaves similar to case 2 but with different magnitudes. Case 3 also shows contribution in the shear layer at a similar depth for both leading and trailing edges as case 1. The velocity contribution of case 3 is ±23% to streamwise velocity, ±3.7% to vertical velocity and ±38% to spanwise velocity. For case 4, the contribution is ±32% to streamwise velocity, ±8% to vertical velocity and ±37% to spanwise velocity. Overall, different geometries show dominant modes which have different contributions to the velocity field. Rectangular JICF (cases 2, 3 and 4) has more contribution of high frequency modes to the velocity field (vertical) than cylindrical JICF. Increasing aspect ratio of the jet also increases contribution of high frequency mode to vertical velocity field. Among rectangular JICF, larger edge facing the crossflow (case 3 vs case 2) decreases the contribution of high frequency mode to vertical velocity.

The delay of TBP for rectangular JICF, hints to the variation of the effect of dominant modes to the turbulence of the system. Variance, evaluated from the 190 snapshots and individual velocity field, is plotted on the symmetry plane (Fig. 5.36). All the variance are normalized by the square of the crossflow velocity.

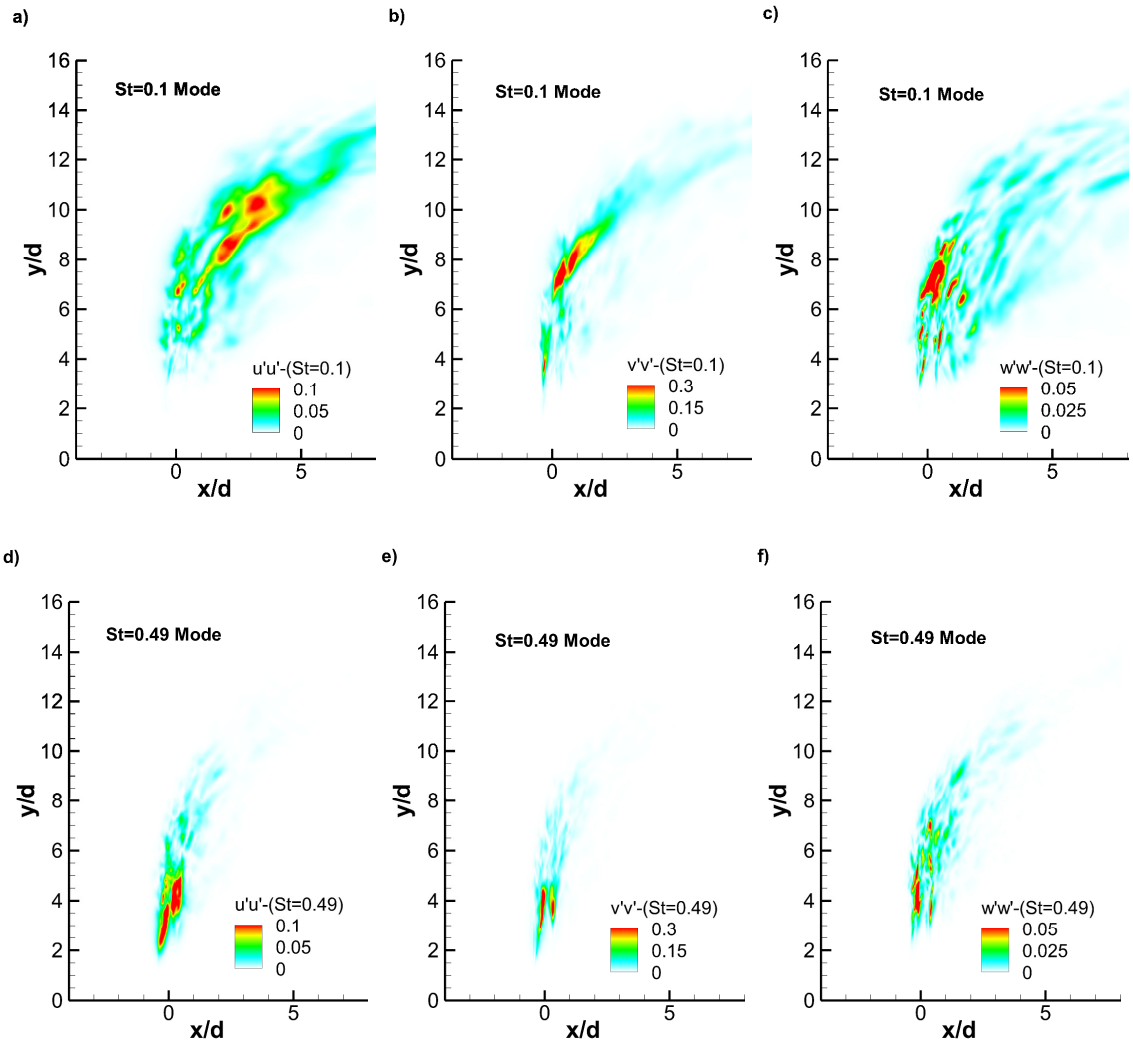

Figure 5.36. Variance of the selected modes in the symmetry plane for case 1; (a, b, c) St=0.1; (d, e, f) St=0.49

Low and high frequencies has higher contribution to the vertical variance of the flow (evidenced by the magnitudes of variance). Larger areas are, however, spanned by streamwise and spanwise variance. High frequency, as before, has higher contribution to turbulence earlier in the domain and low frequency later. Considering the maximum value of mean velocity, the maximum streamwise variance is 3.4%, vertical variance is 5.2%, spanwise variance is 6%.

The streamwise variance of high frequency mode is 5%, vertical is 6%, and spanwise variance is 4.2%, in reference to the maximum value of the mean mode.

Variance is plotted for the modes of case 2 in Fig. 5.37.

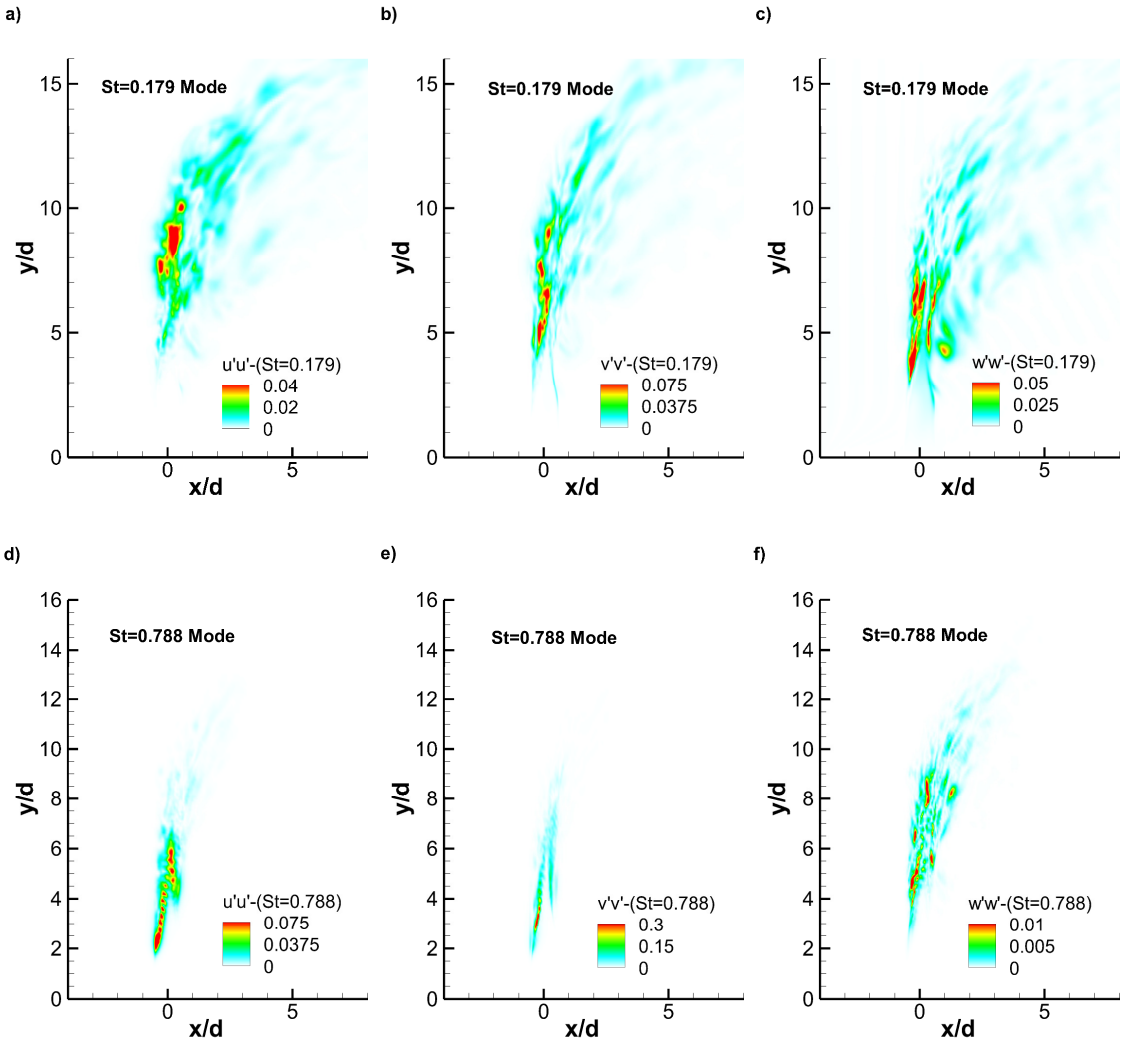

Figure 5.37. Variance of selected modes on the symmetry plane for case 2; (a, b, c) St=0.179; (d, e, f) St=0.788

The trends of the two frequency are same as observed before. For low frequency, streamwise variance is 5.3%, vertical is 1.2%, and spanwise is 30%. For high frequency, streamwise variance is 9.4%, vertical variance is 4.3%, and spanwise variance is 8%.

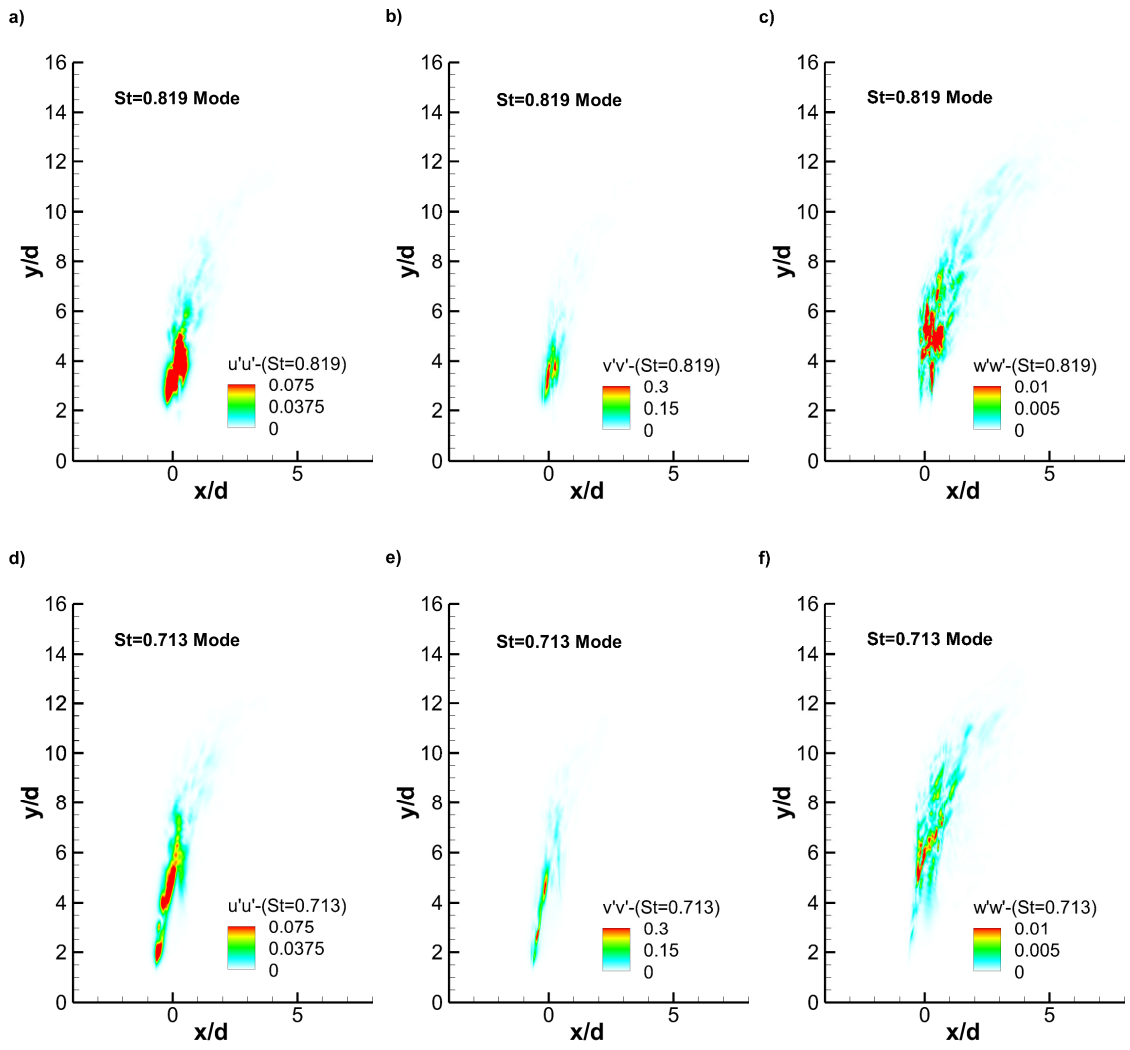

Figure 5.38. Variance of selected modes on the symmetry plane; (a, b, c) Case 3- St=0.819; (d, e, f) Case 4- St=0.713

Only the high frequency contribution to turbulence are plotted for case 3 and 4, in Fig 5.38. For high frequency of case 3, streamwise variance is 19.5%, vertical variance is 4%, and spanwise variance is 12.8%. For case 4, streamwise variance is 12%, vertical variance is 4.3%, and spanwise variance is 5.3%. Except the high spanwise and streamwise direction, rectangular JICF (case 2, 3 and 4) shows a lesser contribution to the vertical variance of the flow compared to case 1. This agrees with the observation of TKE contours for both the cases. Among rectangular JICF, case 3 has highest contribution to streamwise variance. Contribution to spanwise variance also

increases with the length of edge facing the crossflow. High frequency mode of different aspect ratio rectangular JICF is seen to have negligible effect on vertical variance, mixed effect on streamwise variance and inverse effect on spanwise variance. Overall, the contributions of high frequency modes on the shear layer to turbulence is affected by change in geometry and aspect ratios.

Application to JICF control by jet excitation can be aided from the current study. Firstly, the geometry choices for the same mass flow rate governs the frequencies to be picked for excitation of the jet. If rectangular JICF is being used, high frequencies are needed to excite the dominant frequencies compared to cylindrical JICF. Secondly, exciting the jet using dominant frequencies of different geometries of jet gives control over different aspects of the flow field. Rectangular JICF, when excited, would exercise more control over the velocity field (jet path) compared to turbulent field. Cylindrical JICF, when excited, would exercise enhancement of the turbulence field (helpful in mixing) compared to the jet velocity field. Thus DMD analysis provides an important insight to govern the choices of geometry and frequencies as desired for jet control.

5.7 Section 7- Conclusions

Simulations of JICF with same density fluids and a velocity ratio of 5.7 was conducted successfully. For simplicity, laminar jet was used at inlet at a Reynolds number of 5000. Two different jets- one issued from a pipe, and other from a rectangular duct (with an aspect ratio of 2:1) were simulated. In both the cases, the mass flow rate of the jets were maintained same for studying only the geometric effects. Successful validation was obtained for cylindrical JICF, comparing with published literature. The current JICF were observed to be convectively unstable in the shear

layer which also agrees with published literature. For all the rectangular JICF, 90° axis switching was observed. Following are some of the important conclusions obtained from the work.

1) Overall deeper penetration of jet was observed in rectangular JICF compared to cylindrical JICF. As aspect ratio (>1) increases, jet penetration decreases. Shallower jet trajectory is further observed for 0.5 aspect ratio JICF compared to other rectangular JICF configurations.
2) In rectangular JICF having shorter edge, large shear layer rollup initiated deeper into the domain due to having a short edge in the spanwise direction. On the other hand, longer edge facing the crossflow, in rectangular JICF, initiated shear layer rollups earlier in the domain. Increasing aspect ratio was seen to delay the rollups.
3) Direct effect of geometry in the formation of the pressure minima cores was observed, which finally led to different depths of bending for jets with different geometry.
4) The trailing edge instability was seen later than the leading edge in rectangular JICF, while they were simultaneous in the cylindrical JICF, and rectangular JICF having longer edge facing the crossflow. As the aspect ratio increased, the trailing edge rollups started at more depth in the domain.
5) The hanging vortices were initiated earlier in the streamwise direction for rectangular JICF and sustained longer compared to cylindrical JICF.
6) It was seen that cylindrical jets achieve rapid mixing earlier in the domain, and hence, reached far field conditions earlier compared to rectangular jets. This delay of rapid mixing was related to the phenomena of axis switching in rectangular JICF, which was observed.

7) Axis switching was delayed in rectangular JICF as aspect ratio increased. When the longer edge of rectangular jet was facing the crossflow, compared to shorter edge for same aspect ratio, axis switching was delayed as well.
8) Pressure fields also formed consistent with the delayed rollups of the shear layer in rectangular JICF.
9) Turbulence breakdown was delayed in the rectangular JICF compared to cylindrical JICF. Longer spanwise edge of rectangular JICF, in the other hand enhanced the turbulence breakdown. Aspect ratio also seemed to delay this breakdown among rectangular JICF. Also, it was seen that maximum TKE was higher in the cylindrical JICF due to achievement of rapid breakdown. However, due to axis switching, the shear layer sustained high TKE values longer in the domain for rectangular JICF. Geometric effect was also seen in the spanwise distributions of turbulence in the domain. Rectangular JICF with short spanwise edge were seen more prone to initiate spanwise turbulence at a later depth.

Modal analysis was also conducted for both the cases using DMD. The important conclusions obtained from modal analysis were:

1) From spectral analysis, different frequencies were observed to be dominant at different depths in the leading edge shear layer for cylindrical JICF, which agreed well with literature (for convectively unstable JICF).
2) DMD was successful in predicting convectively unstable phenomena on the shear layer and was consistent with the spectral analysis. Most significant modes were found on the shear layer of the flow.

3) It was seen that cylindrical JICF and long spanwise edged rectangular JICF had multiple energetic modes, at different frequencies, due to early rapid mixing in the shear layer. Other rectangular JICF had a comparatively lesser high amplitude modes in the domain.
4) Rectangular JICF had an effect on delaying the frequencies of the modes indicating overall smaller structures dominant in the shear layer, compared to cylindrical JICF.
5) Successful reconstruction of the velocity field was done using the dynamic modes. Rectangular JICF had significant effect on the spanwise velocity field of the flow. Also, higher frequency mode in rectangular JICF had higher contributions to vertical velocity fields, compared to higher frequency mode in cylindrical JICF.
6) The variance evaluated for each modes from DMD analysis showed that rectangular JICF had a little lesser contribution to the vertical turbulence of the flow field, compared to cylindrical JICF.

Overall, from this study it can be concluded that changing geometry has significant effect on flow features and modes of the JICF system. Thus, selecting appropriate geometry based on localized mixing requirements, jet path requirements, frequency excitation requirements for jet control and other JICF flow requirements will be aided by the current study.

CHAPTER 6. EFFECT OF JET TURBULENCE ON CYLINDRICAL AND RECTANGULAR TRANSVERSE JETS

Simulations are carried out for transverse jets issuing from cylindrical pipe and rectangular duct for a velocity ratio of 5.7 and jet Reynolds number of 5000. Numerical algorithm uses LES for turbulence modeling, and inlet turbulent conditions are provided by using SEM. Different levels of turbulent kinetic energy are generated at the jet inlet and compared for cylindrical and rectangular the geometries in this chapter.

6.1 Section 1- Background

Detailed review on the past work can be found in Chapter 2.

6.2 Section 2- Numerical details

6.2.1 Computational domain

The computational domain for jet in a crossflow is shown in the Fig 6.1 below. The origin lies in the center of the pipe where the jet meets the crossflow. In Cartesian coordinates x is the streamwise direction of the crossflow, y is the wall normal direction, and z is the spanwise direction.

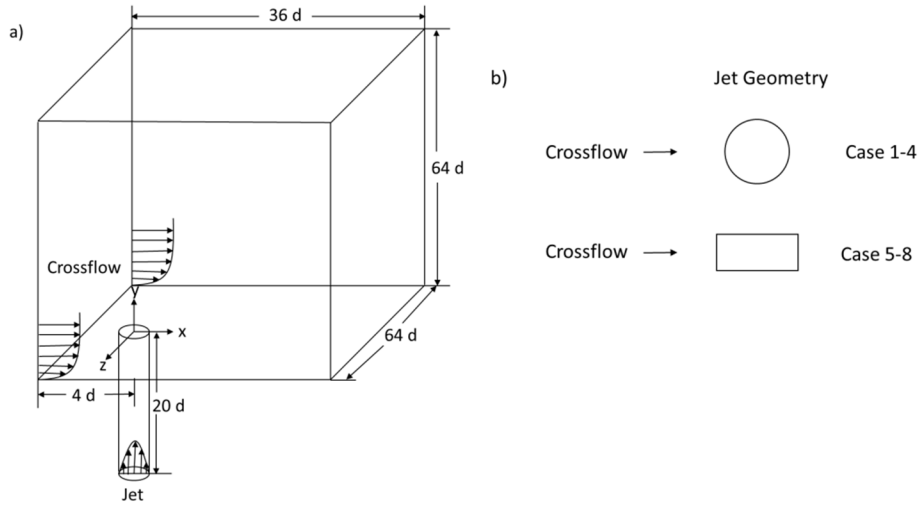

Figure 6.1. Geometry of simulation

The total domain in terms of jet diameter “d” is 36d X 64 d X 64 d. The crossflow inlet is 4 d upstream of the jet. The jet is issued from a pipe. The pipe length used for simulation is 20 d for parabolic inlets and 10 d for turbulent jet inlets. Different lengths of pipe had been tried but it was found out that 20 d and 10 d is required for getting good development of flow inside the pipe, which provides right conditions at the jet exit. For the rectangular duct jet, same cross sectional area is maintained for the duct. The aspect ratio of the duct is 2. Fig 6.1 (b) shows the top view of the domain for rectangular domain.

The current configuration is JICF with a velocity ratio of 5.7. The jet Reynolds number is approximately 5000. This configuration has been studied extensively previously by Su and Mungal (2004), Muppidi and Mahesh (2005, 2007, 2008) and Ruiz et al. (2015). New insights on the configuration adds to the existing understanding of the flow.

6.2.2 Meshing details

For a curvilinear geometry using structured mesh, a careful consideration is needed in meshing the geometry. Meshing is done using Ansys ICEM CFD. The output is then converted to read the mesh in Grid Pro format (input to Chem3D) by using an in-house code developed in FORTRAN. Since the pipe is cylindrical in this case, it is connected to the main domain (which is rectangular) by means of O-grid. The pipe also needs to be meshed to simulate the jet fluid. For that purpose, another O-grid is created for structured mesh inside the pipe. Hence, the geometry has two O-grids. The central block of the outer O-grid is split as inner O-grid which continues throughout the domain.

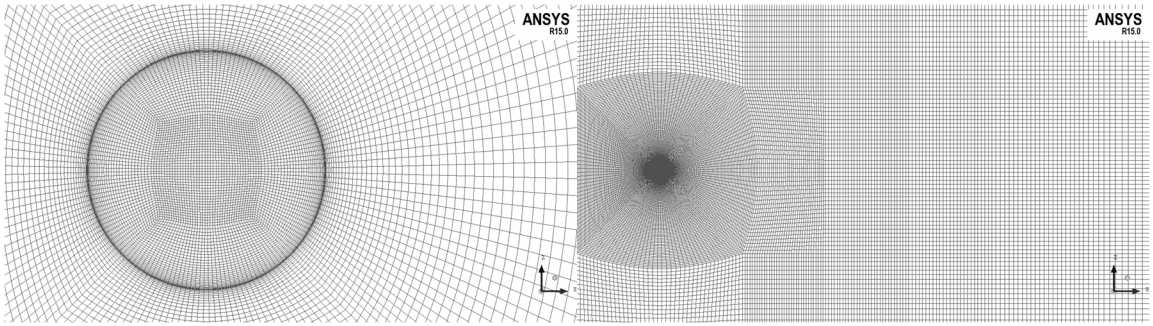

Figure 6.2. Meshing used for simulation (Figure cont'd)

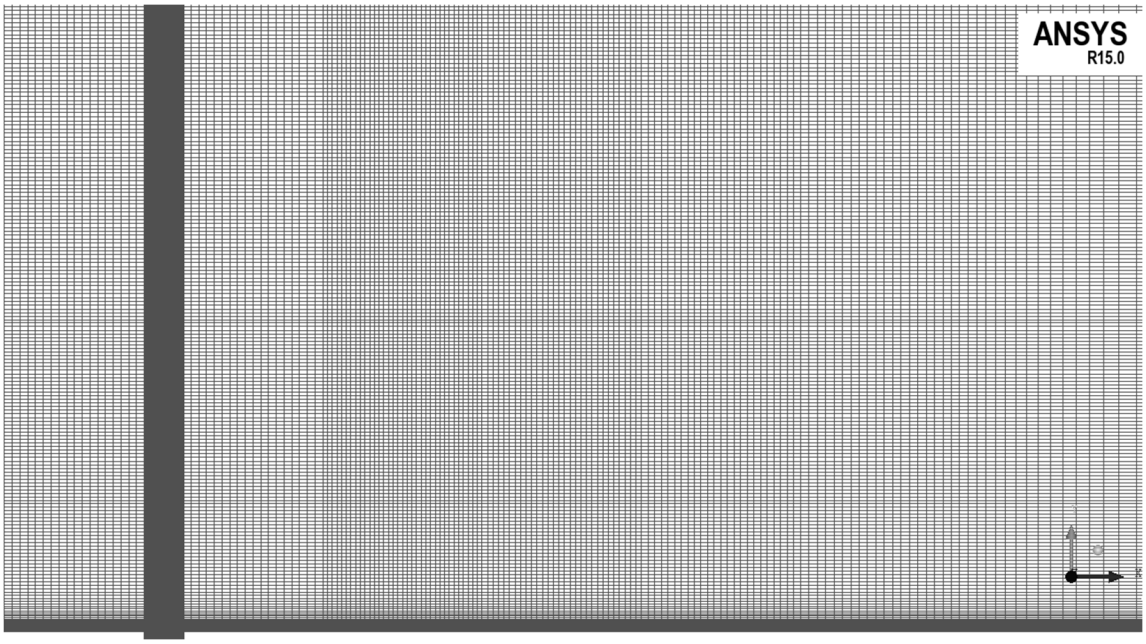

For this study using LES, wall resolution is a crucial part. Hence, careful stretching is needed to mesh the wall regions. The walls of the pipe are meshed first. The radial resolution is 0.4 for laminar jets and 1.42e-3 d (approximately r+ of 0.15) for turbulent jets. Since it is an O-grid, the azimuthal mesh is applied on a square of 1 d side. The azimuthal mesh size is 0.025d. The streamwise direction of the pipe is meshed uniformly at a size of 0.04d. Stretching is only done near the region where pipe meets the main domain, to match the mesh at the bottom wall of the main domain. In order to resolve the crossflow boundary layer effectively, y+ of 0.1 is maintained on the bottom wall of the domain. Geometric stretching is done in the y normal direction till the mesh size reaches about 0.08d. Slanted edges of larger O- grid are meshed with and stretching is done maintaining a ratio of about 1.11. The outer edge of the O-grid is matched in the streamwise direction after about x=5d. After that, the mesh is reduced slowly in the streamwise direction until it reaches 0.4d. Finally, the spanwise direction is maintained a bit coarser after the fineness of larger O-grid. This is allowed since the spanwise domain of the jet was observed to be well

within the O-grid region. All of these resolution makes a total mesh size in the domain (including length of pipe) about 15 million for laminar JICF and about 16.5 million for turbulent JICF cases.

6.2.3 Boundary conditions

The boundary conditions are described in detail in Chapter 5.

6.2.4 Inlet turbulence generation

The inlet turbulence generation has been described in detail in Chapter 5.

6.2.5 Numerical method

The numerical algorithm has been described in detail in Chapter 4.

6.2.6 Simulation details

The timestep was chosen resolving Kolmogorov time scales. In non-dimensional units (using jet diameter and jet mean velocity), the timestep is 8.14×10^{-3}. Based on jet mean velocity, and the streamwise length after the jet enters the domain, approximately 5 flow through times was simulated for the transients to exit the domain. Then, time averaged data was stored for 10 additional flow through time periods. It was seen that the statistics did not change after this, and thus the data was considered for analysis.

6.3 Section 3- Validation studies

For validation of laminar JICF configuration, comparison was done with DNS study by Muppidi and Mahesh (2005). In that particular work, pipe flows were simulated without any turbulence in the pipe (i.e. laminar flow inside the pipe), even though the Reynolds number of the jet was 5000.

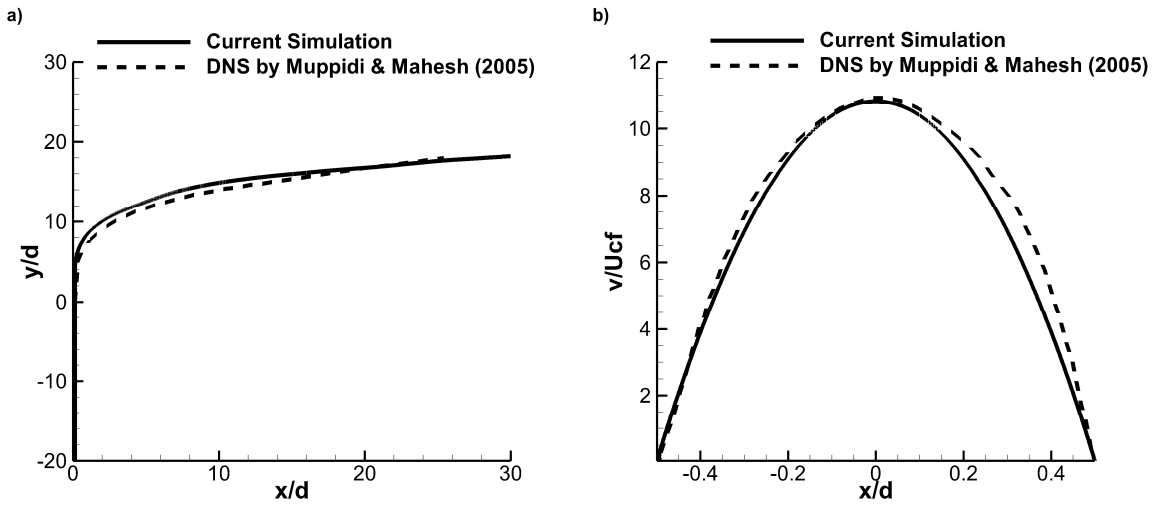

Figure 6.3. Validation of parabolic JICF with DNS studies; (a) Mean jet trajectory; (b) Velocity at jet exit

Fig 6.3 (a) shows the validation of the current simulation, with the time averaged jet trajectory reported by Muppidi and Mahesh (2005). The jet trajectory as defined in Muppidi and Mahesh (2005) is the streamline which originates in the pipe origin (center streamline). Reasonable match is seen with small deviations. These deviations are attributed to mesh stretching in the particular regions. The bending of the jet is affected by the interaction of crossflow fluid and the jet. This interaction results instability in the edges of the jet, which further creates vortical structures, known as shear layer vortices (details will be discussed later). So a reasonable match indicates the physics involving these structures are predicted correctly using LES.

Fig 6.3 (b) shows the comparison of jet exit velocity, with the DNS studies. Overall, a reasonable match is seen. The stretching of the jet in the right lateral direction is not captured by current LES simulation. However, the perfect match of peak velocity indicates the pipe flow simulation produced correct laminar flow at prescribed Reynolds number. A number of studies (Yuan et al., 1999; Muppidi & Mahesh, 2007; Iyer & Mahesh, 2016) stress the importance of simulating pipe flows to predict correct physics at the jet and crossflow interaction plane.

6.3.1 Validation of turbulent JICF

To quantify the effects of the intensity levels, SEM algorithm for turbulent pipe flow was used to generate jet inlet conditions for full JICF, and compared. Initially, validation is sought with the experiments by Su and Mungal (2004) for the same configuration:

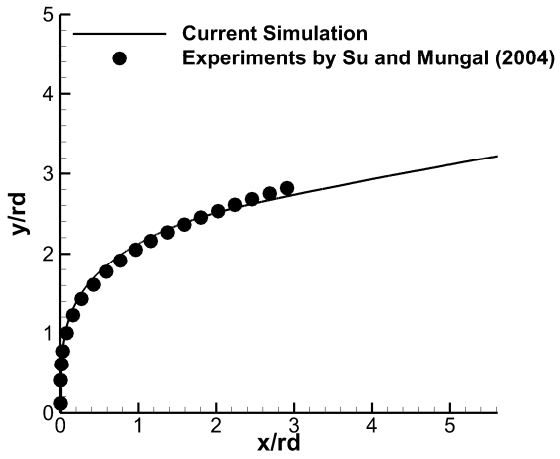

Figure 6.4. Validation of mean jet trajectory of turbulent JICF with experiment

Fig 6.4 shows the validation of time averaged jet trajectory, with experiments done by Su and Mungal (2004). It is seen that a close match is obtained. This validation also reflects that the dynamics responsible for jet bending in crossflow is captured correctly by the simulation. The mean trajectory shows a better validation, compared to DNS done by (Muppidi & Mahesh, 2007) and LES done by Ruiz et al. (2015).

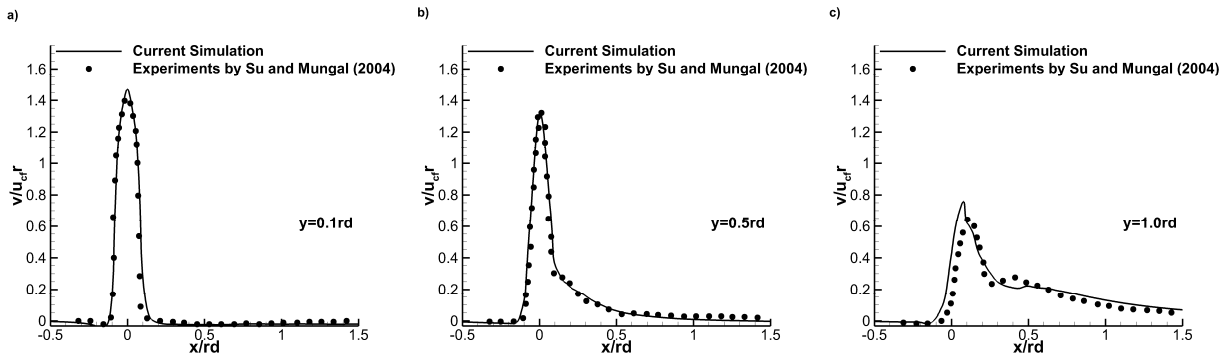

Figure 6.5: Validation of mean vertical velocity with experiments

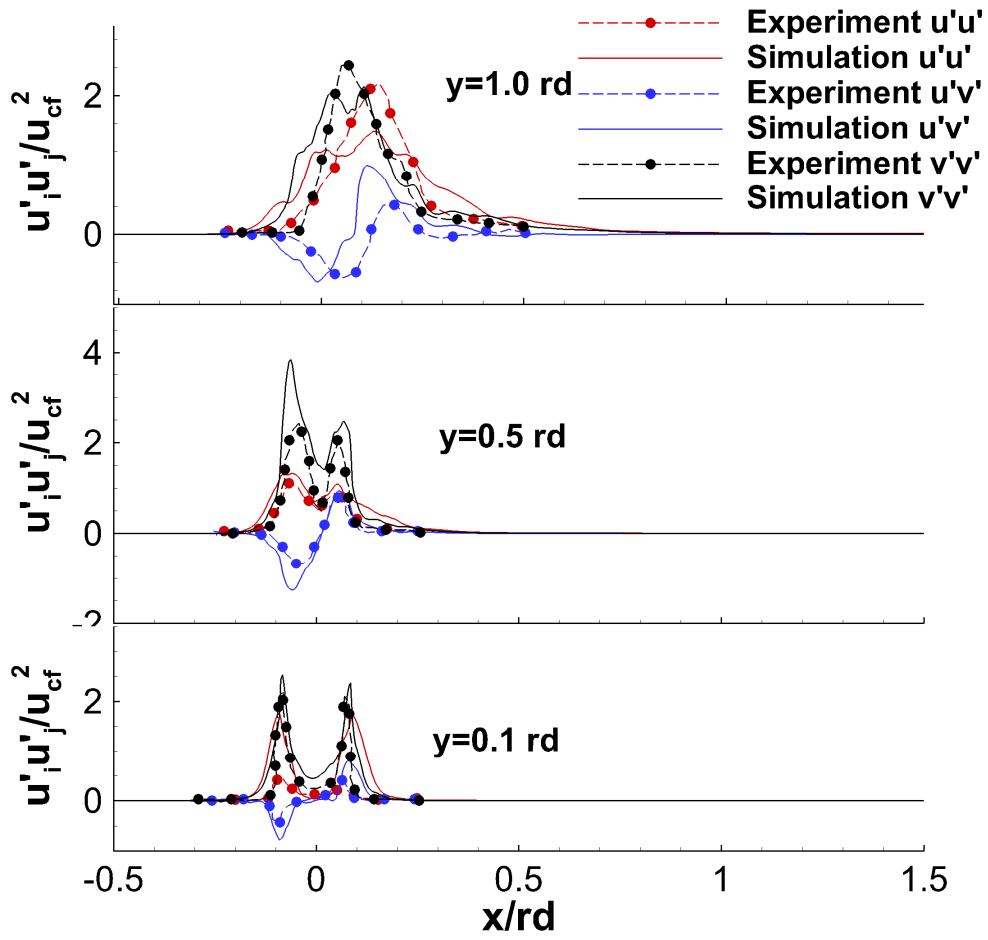

Figure 6.6. Validation of Reynolds stresses at three stations, with experiments

Fig 6.5 and Fig 6.6 show validation of first order and second order correlations, compared to experiments by Su and Mungal (2004). Fig 6.5 shows comparison of mean vertical jet velocity

compared to experiments at 3 stations in the downstream. It is seen that immediately after jet exit, the velocity matches closely with data by experiments. Further downstream, the peak shows a small deviation from the observed experiments. The final station shows a good match, in terms of magnitude, but shows a smaller leftward shift due to the small shift in trajectory.

Second order correlations, however show mixed results (Fig 6.6). The streamwise correlations and shear stresses show a high prediction in the first station just as jet hits the crossflow. However, the vertical correlation shows a reasonable match. On the second station, a wider region of correlations were observed, but the magnitudes show a good match except at the leading edge. On the third station, a good match is seen for vertical correlation and shear stress, but the magnitude of streamwise correlation is underpredicted.

The maximum over prediction for the streamwise correlation at the peak is about 3.6 times at the first station. The maximum under prediction is 1.5 times at the third station. For shear stress, maximum over prediction seen, is 2 times, at the first station. For vertical correlation, maximum over prediction is 1.5 times in the second station.

It is seen that most over predictions are in the first station. In farther station, the errors become less. Similar behavior was also seen in high-resolution LES by Ruiz et al. (2015). The above noted discrepancy is partly due to larger overall mesh used, and partly due to inlet conditions. Same density was assumed for both the fluids in the simulation. However, in the experiments, acetone seeding in the jet had been reported to increase the inlet fluid density by approximately 10%. Muppidi and Mahesh (2007) also worked on a scaling factor citing the same reasons. Hence, overall prediction of jet path is reasonably validated using LES and SEM.

6.3.2 Different intensity levels

Since the SEM method used takes turbulent intensities as an input, it is straight-forward, to generate different intensity levels for the pipe flow. However, the relation between input intensity levels does not directly correspond to the intensity levels at the exit. Hence, after few simulations different intensity levels are generated for pipe flow which will be used in the main JICF simulation.

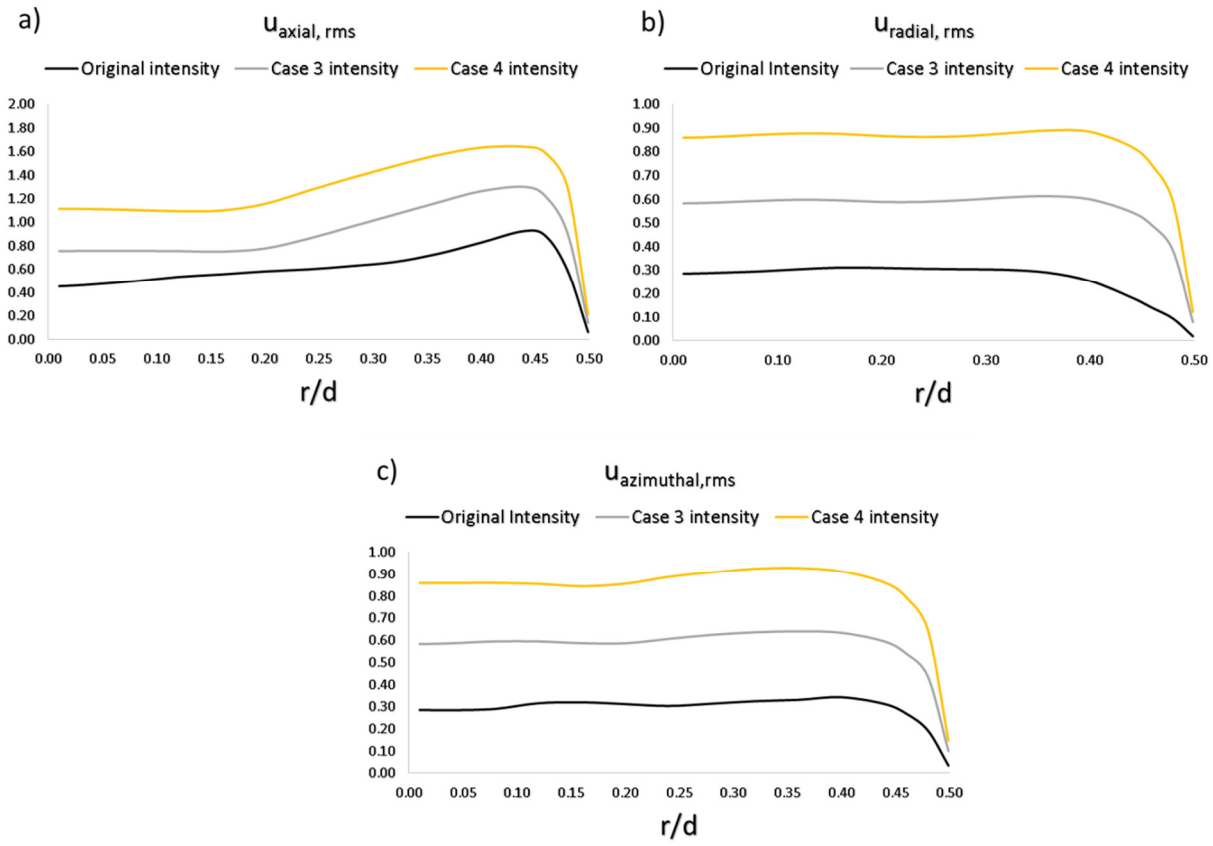

Figure 6.7. Azimuthally averaged rms values for pipe flow with different intensity levels; (a) axial stress; (b) vertical stress; (c) azimuthal stress

Fig 6.7 shows the intensity levels at the exit of the pipe. Since the difference between each intensity level is approximately incremented by the same amount, these levels would be a good way to quantify the effect of intensities on JICF simulations. The cases that are compared in this

work are defined on the basis of inlet turbulent intensity levels, which are quantified on the basis of the above figure.

In this study, the comparison of JICF for eight different cases are conducted and important conclusions are established. The first case is JICF with laminar jet. The second case is fully developed turbulent flow, which was previously validated with experiments. The third case is JICF with higher intensity levels (Case 3 Fig 6.7), and the fourth case is JICF with still higher intensity levels (Case 4 Fig 6.7).

Cases 5 to 8 are similar to cases 1 to 4 but they are for rectangular duct with aspect ratio of 2 and having the same mass flow rates as these cases. Table 1 shows the total list of case simulated.

Different levels are quantified as the ratio of the centerline axial intensity to the original intensity at jet exit. Level ratio

$$L = \frac{v'v'_{cl,current}}{v'v'_{cl,original}} \tag{5}$$

Table 6.1. List of Cases Simulated

Case Number	**Geometry of Jet**	**Vertical rms centerline ratio (L)**
1	Cylindrical Pipe	0
2	Cylindrical Pipe	1.0
3	Cylindrical Pipe	1.66
4	Cylindrical Pipe	2.45

(Table cont'd)

Case Number	Geometry of Jet	Vertical rms centerline ratio (L)
5	Rectangular Duct	0
6	Rectangular Duct	1
7	Rectangular Duct	1.66
8	Rectangular Duct	2.45

6.4 Section 4- Qualitative features

Jet in a crossflow configuration is highly turbulent, having different coherent structures. These coherent structures, and their interplay, create a mechanism that bends the jet in the direction of the crossflow.

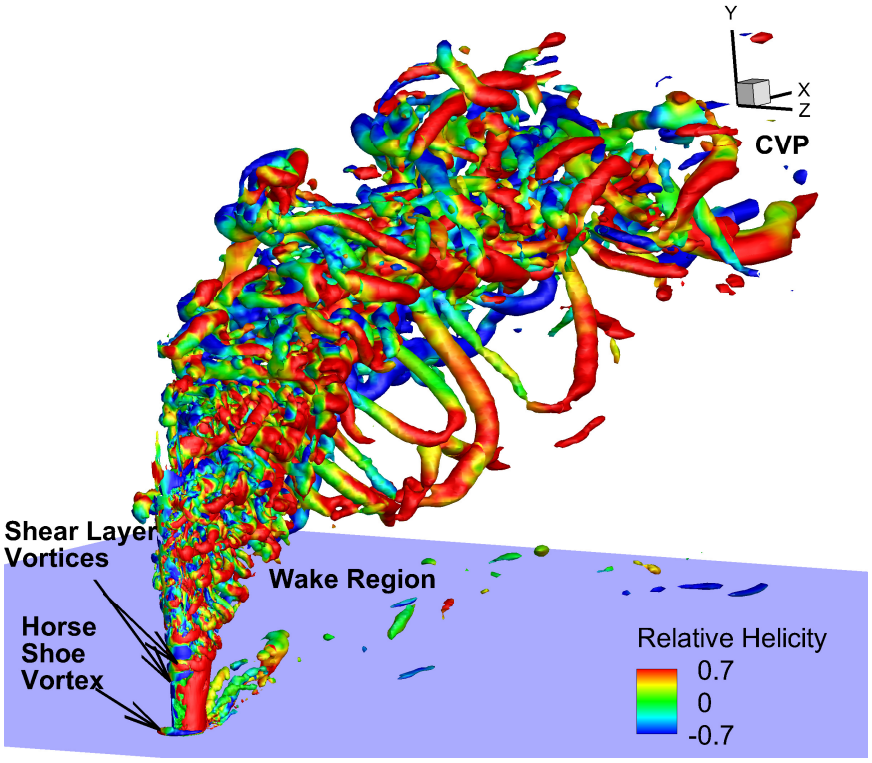

Figure 6.8. Q-criteria of JICF system (Case 1)

Fig 6.8 shows the complex structures that are a feature of JICF visualized using the Q-criterion as defined in Haller (2005). It is seen that the complex structures in the near field break down in the far field of the flow. This phenomenon is called turbulence breakdown and is noted as TBP in Ruiz et al. (2015). To predict the flow in the downstream, and the general behavior of jet, analysis of near field is of paramount importance. Hence, a lot of literature has focused on identifying and studying the behavior of structures in this region.

Several features that are a characteristic of JICF are noted and discussed for the current configuration. Earlier work, such as that by Fric and Roshko (1994), identify four major structures that are a feature of JICF. Those are horseshoe vortices, shear layer or ring vortices, counter-rotating vortex pair (CVP) and wake vortices. Works such as that by Yuan et al. (1999) and Ruiz et al. (2015) identify additional structures in the near field of the jet as 'v' shaped vortex and hanging vortex. Depending on the momentum ratio between the jet and the crossflow, an additional structure would appear on the walls of crossflow downstream of the jet known as hairpin vortices.

6.4.1 Horseshoe vortex

Horseshoe vortex is seen in the upstream side, where the jet meets the crossflow. This vortex is formed by turning of the crossflow toward itself. The physics of formation of horseshoe vortex, and the behavior in near field, is explained by various authors (Krothapalli et al., 1990; Muppidi & Mahesh, 2005).

When the crossflow encounters the jet it sees as an obstacle and forms a stagnation point. And to conserve the mass flow, accelerates around the jet to meet at the downstream side. Due to high pressure gradient in the upstream side, and a pressure gradient from the top as well, the

crossflow fluid on bottom of the stagnation point turns downwards. Since the fluid now encounters boundary layer again and pressure gradient near the obstacle, turns inwards and then encountering the incoming crossflow, forms horseshoe vortex. In high velocity ratio jet, such as in the current configuration, due to high momentum of the jet, the stagnation point lies relatively far from the boundary layer of the crossflow. Hence, sometimes a full formation of horseshoe vortex is seen, but in most cases, semi formation of turning is seen in the simulations. In the current cases, it is seen clearly in case 1. Here, the horseshoe vortex is seen as a system of two coalescing vortices. Two instances of the flow 6 ms apart are plotted in Fig 6.9. In the first instance, two vortices in the horseshoe region is seen and in the second instance they merge into one. This periodic formation of two vortices and then coalescing into one is a type of horseshoe vortex system as explained by Kelso et al. (1995). In time-averaged data, the horseshoe is stably formed.

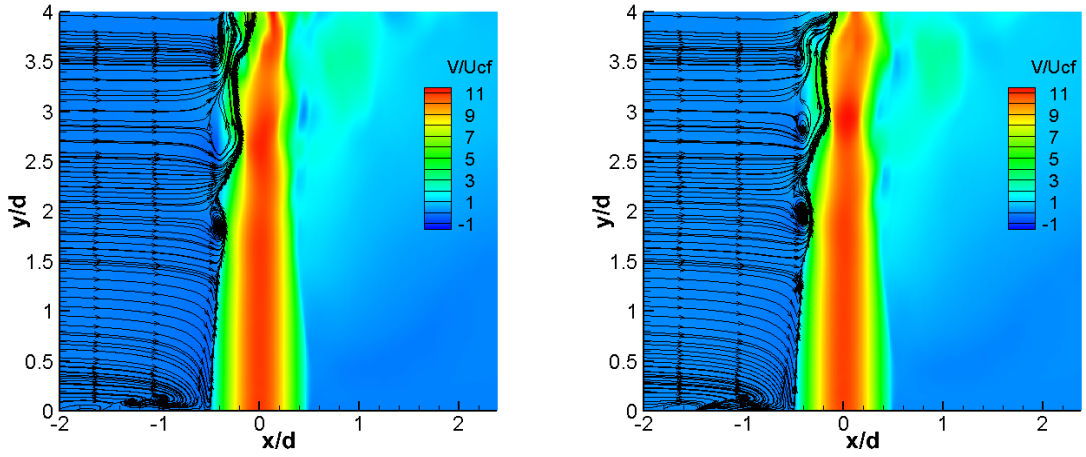

Figure 6.9. Two instances of horseshoe system (case 1)

6.4.2 Shear layer vortices

Shear layer vortices are formed due to the presence of a shear layer of jet fluid in the domain of crossflow fluid. This situation will typically form an unstable surface in the shear layer. This mechanism of instability is known as Kelvin-Helmholtz (K-H) instability. In current case, the surface that surrounds the jet, especially in the windward side (the upstream side of crossflow), is subject to K-H instability. This allows the formation of vortical structures, with spanwise vorticity, along the shear layer. These structures are known as shear layer vortices. It is well researched that these structures mostly contribute to the formation, or strengthening, of Counter-rotating Vortex Pair (CVP) in the downstream region. The mixing phenomena between the jet and crossflow fluid is also initiated by these structures. Hence, an in-depth study of these structures will aid in understanding the downstream evolution of jet.

Fig 6.8 shows the existence of shear layer structures in the near field using Q-criteria. It can be seen that initial shear layer rollup starts at a certain distance, but not immediately when the jet enters the domain. This is seen for laminar JICF. For turbulent JICF, these rollups are more nearer to wall.

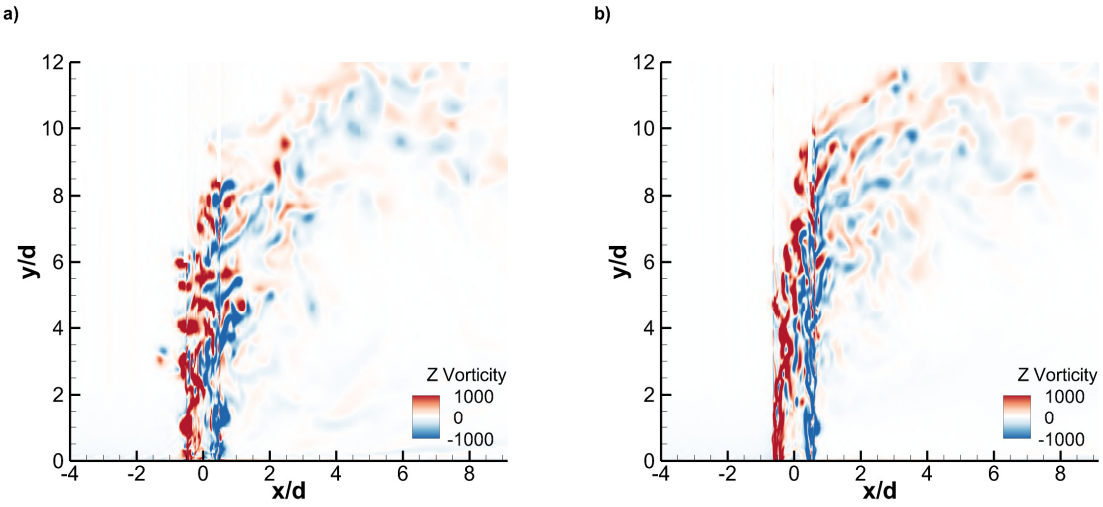

Figure 6.10. Spanwise vorticity in the symmetry plane; (a) Case 2; (b) Case 6

Fig 6.10 shows the spanwise vorticity in the symmetry plane of the domain. In the windward side of the jet we see vortices formed in the shear layer. These are formed due to KH instability, as discussed before. We also see the hovering vortex. Initial vortex rollup is seen at (y=1.0 d) in the shear layer. After that, a lot of small vortical structures are seen, which may be indicative of high activity of small scale fluctuations in that region. Furthermore, as the jet bends, again some larger structures are seen.

6.4.3 Counter rotating vortex pair

One of the characteristic structures, that is a standard feature of JICF, is the counter-rotating vortex pair (CVP). Initially, when the jet enters the domain, it behaves like a free jet flowing perpendicular to crossflow. Due to effect of crossflow, the jet then starts bending in the direction of crossflow, and finally in the downstream, flows in the direction of crossflow. This downstream jet fluid, which is parallel to the crossflow, consists of a pair of vortices which rotate opposite to each other. Hence, this pair is called the CVP. In the far-field, CVP is the dominant mechanism responsible for entrainment and mixing. So a lot of earlier research has focused on this structure

alone. By new numerical tools and high fidelity simulations, formation of CVP is studied in the near field. It is known by now that CVP has a kidney-shaped structure. It is visualized clearly in time averaged data (Muldoon & Acharya, 2010). In instantaneous data, CVP is not a single vortex but a collection of small-scale vortices (Ruiz et al., 2015).

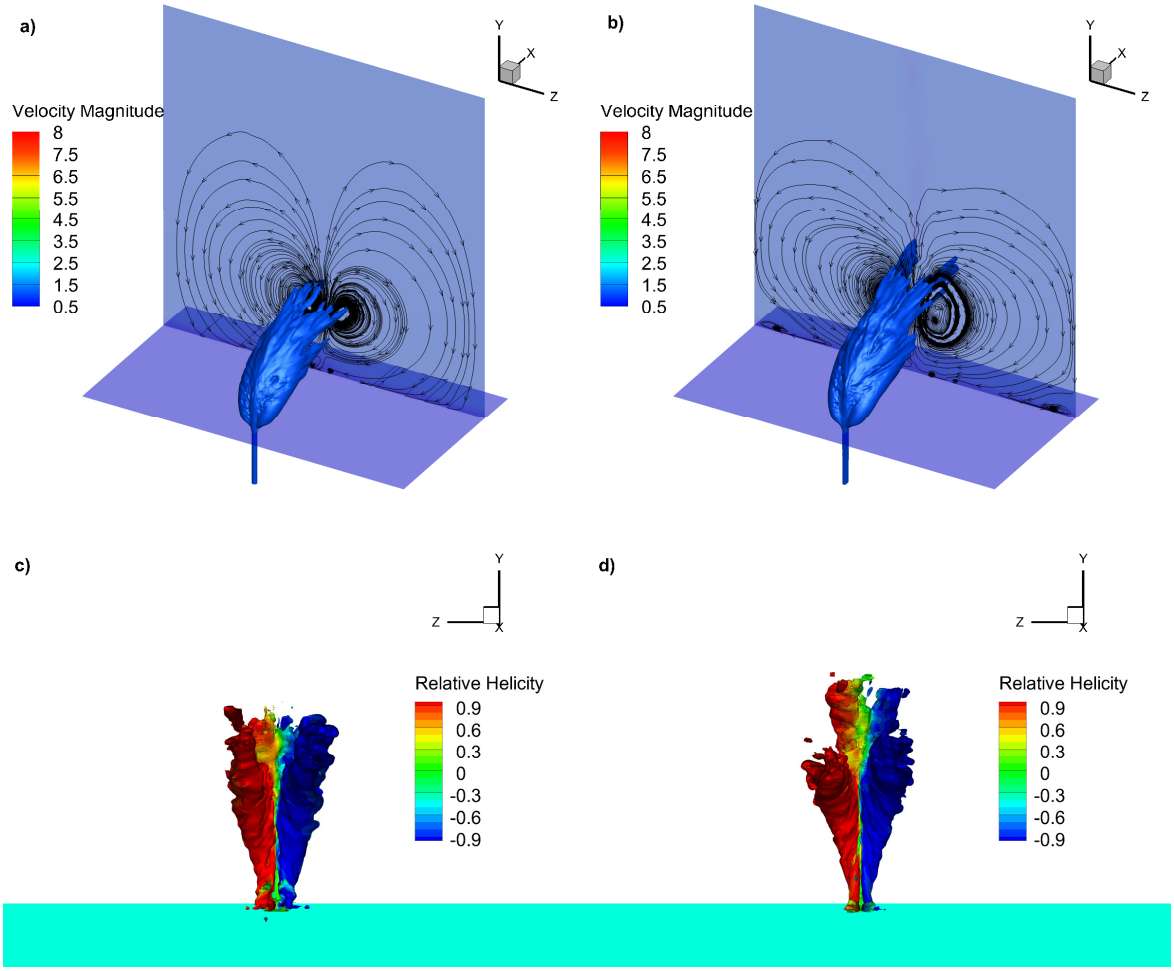

Figure 6.11. (a, b) Time averages streamlines showing CVP; (b, d) Q-criteria of time averaged velocity field seen from the wake side; (a, c) Cylindrical JICF- Case 2; (b, d) Rectangular JICF- Case 6

Fig 6.11 shows CVP in the time-averaged data for case 2 and 5. Relative helicity contours give the information about the rotation of the vortices. Positive values indicate anti-clockwise rotation,

and negative values indicate clockwise rotation. It is seen that the CVP forms in the near field and then extends forming the structure of the jet in the far field. From the Fig 6.11 (a,b) the kidney like shape can also be seen for the CVP. For all the cases discussed in this paper CVP is formed as a kidney like shape. Interestingly, for rectangular JICF, lower and upper CVP are distinctly seen. These vortices have been studied in detail by Haven and Kurosaka (1997).

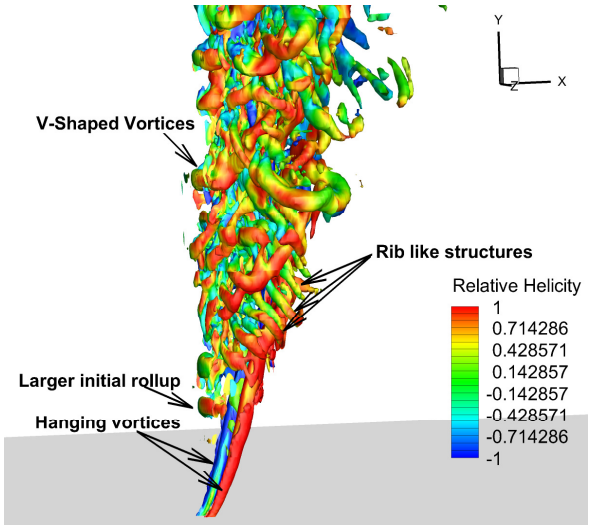

Figure 6.12. Larger values of Q-criteria - Case 5

6.4.4 Near field vortices

Another class of structures recently categorized separately are the v-shaped vortices in the shear layer. Fig 6.12 shows these vortices in the near field for current simulation. These vortices are believed to result from azimuthal instability of shear-layer vortices (Ruiz et al., 2015). These structures are the ones mainly responsible in mixing and eventually forming the basis of CVP downstream. The initial 'v shape' is oriented in the downstream in such a way to form the CVP. Case 5 is represented on Fig 6.12 with larger values of Q-criteria, which reveals near field structures. Another similar structure in the near field was identified as hanging vortex by Yuan et

al. (1999). They also point out this structure to form the initial stages of the CVP. It is seen from the relative helicity contour in the above figure that these structures are also counter-rotating in nature as the CVP. Therefore, this structure may be responsible to initiate the rotational sense of CVP. Furthermore, other instabilities of shear layer build and strengthen the CVP in the near field. In the wake region, important structures exist. If the velocity ratio in the jet is high and Reynolds number of crossflow is also high, tornado like structures exist in the wake. These wake structures are compared to wake behind the cylinder by Fric and Roshko (1994). They find some differences between the two. Experimental study by Smith and Mungal (1994) find the existence of jet fluid in these wake structures for jets above velocity ratio of 10. However, in the current case these structures are not seen owing to low Reynolds number of the crossflow. The wake region has structures which do not interact with the jet (Muppidi & Mahesh, 2007) and if resolved finely will show 'hairpin' like shape (Ruiz et al., 2015). These 'hairpin' structures are characteristic of wall bounded turbulent flows. Fig 6.8 shows the wake region with elongated structures, which do not interact with the jet whatsoever. Complete 'hairpin' is not seen owing to coarse mesh in the far downstream region.

6.5 Section 5-Comparison of JICF with different intensity at the inlet

In this section, different cases listed above are compared to understand the differences.

6.5.1 Effect of jet inlet turbulence on the instantaneous flow field

Initially, the qualitative features are compared for the eight cases. Since most of the dynamics of JICF is directly affected by initiation of shear layer instability, the leading edge shear layer is compared for the cases. The main objective is to isolate the effect of the jet turbulence levels for

both the geometry. For this, four representative cases can be compared. These cases are case 2, case 4, case 6 and case 8.

6.5.1.1 Effect of turbulence intensity on shear layer vortices

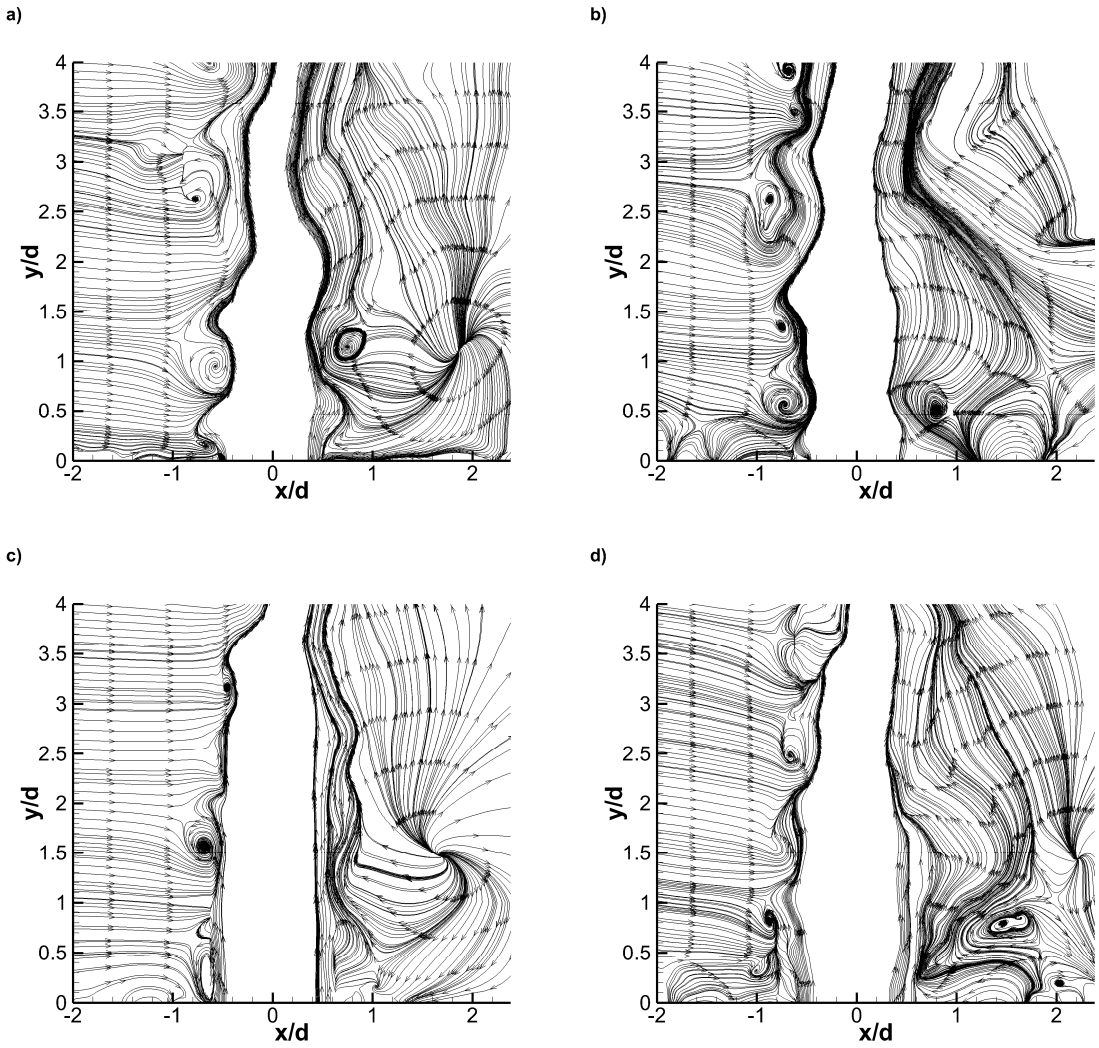

Figure 6.13. Instantaneous streamlines on the symmetry plane; (a) Case 2; (b) Case 4; (c) Case 6; (d) Case 8

Initial effect of different intensity of jet will be when it enters the domain. Hence, shear layer disturbances can be compared to see the effect of turbulence intensity on initiation in the symmetry plane (Fig 6.13). It is seen that for the higher turbulent jet, the instability is nearer to the wall, compared to the jet with lower inlet turbulence levels (Case 2 and 4). This is due to the

fact that turbulent jet provides earlier perturbation for the Kelvin- Helmholtz instability mechanism to develop. Further downstream, more fluctuations are seen in the leading edge shear layer as the intensity is increased.

It is interesting to note that as the turbulence intensity of the jet increases, the immediate wake (consisting of several wall normal vortices) becomes more violent. The edge, which acts like a source flow in the wake, is more displaced towards the downstream region of the wake. The slanting of the edge is also seen to increase from the jet for higher turbulent intensities. These are due to the fact that more violent leading edge shear layer pushes the crossflow fluid around the jet farther to meet later in the wake region. Since wall normal (hanging) vortices in the leeward side also have the same orientation as the edge, the wall normal vortices are also affected.

6.5.1.1.1 Comparison between rectangular and pipe JICF

A longer region of the wake edge flow and longer hanging vortices are seen for all rectangular JICF, compared to the cylindrical counterparts. Also the edge has less slant from the jet. On the shear layer, small vortices are seen to originate earlier, but this rollup does not pass around the jet immediately as seen on the cylindrical JICF. Another larger rollup is seen at a deeper distance in the domain. This delay from smaller to larger rollup spans roughly the same depth as the axis is switched back 90 degrees. In cylindrical JICF, the trailing edge also shows instability at the same location as the leading edge. However, in rectangular JICF, this is not the case. The trailing edge shows rollup only later in the domain, where the major rollup happens in the leading edge. Another reason for this is that the vortices generated during initial rollup of the shear layer play a role in switching the axis instead for propagating through the longer edge.

The horseshoe region in the immediate upstream of the jets, also show some differences. As the turbulence increases, the disruption in the upstream boundary layer is higher. More jumps are seen as the turbulence increases for both pipe and rectangular JICF.

6.5.1.1.2 Comparison of rectangular jets

For shear layer, if only the effect of turbulence are seen in rectangular jets, similar differences are noted as for pipe only cases. In addition to that, the region downstream of trailing edge shows more vortical activity and the source is pushed farther in the rectangular JICF. Due to high turbulence, the rollup in the trailing edge also happens almost at the similar depth as that of the leading edge.

6.5.1.2 Comparison of wall normal vortices

Wall normal vortices result as a feature of JICF, while the crossflow surrounds the jet and meet on the downstream side. The high crossflow shears along the jet surface in the azimuthal direction. This shearing causes wall normal structures around the jet. Also, wall normal structures are formed from the shear layer dynamics that happen in the shear layers. The details will be discussed in a later section. In cases 1 and 4, where there is no inherent turbulence in the jet, clear hanging vortices are seen in the trailing edge side of the jet. However, in the turbulent cases, these structures are not seen, which may be attributed to the rapid disturbance in the leading and trailing edges due to turbulence. Once they are formed, a vortex breakdown occurs downstream, which will later on bend the jet, and CVP initiates with the orientation of these vortices and shear layer vortices rolling in from the sides (Yuan et al., 1999). Hence, these structures play an important role in near field to dictate the dynamics of the JICF. Since they

mostly wrap around the jets on either side of the symmetry plane, the vortices are most clearly seen in z=±0.44 d spanwise planes for cylindrical JICF and z=± 0.39 d for rectangular JICF.

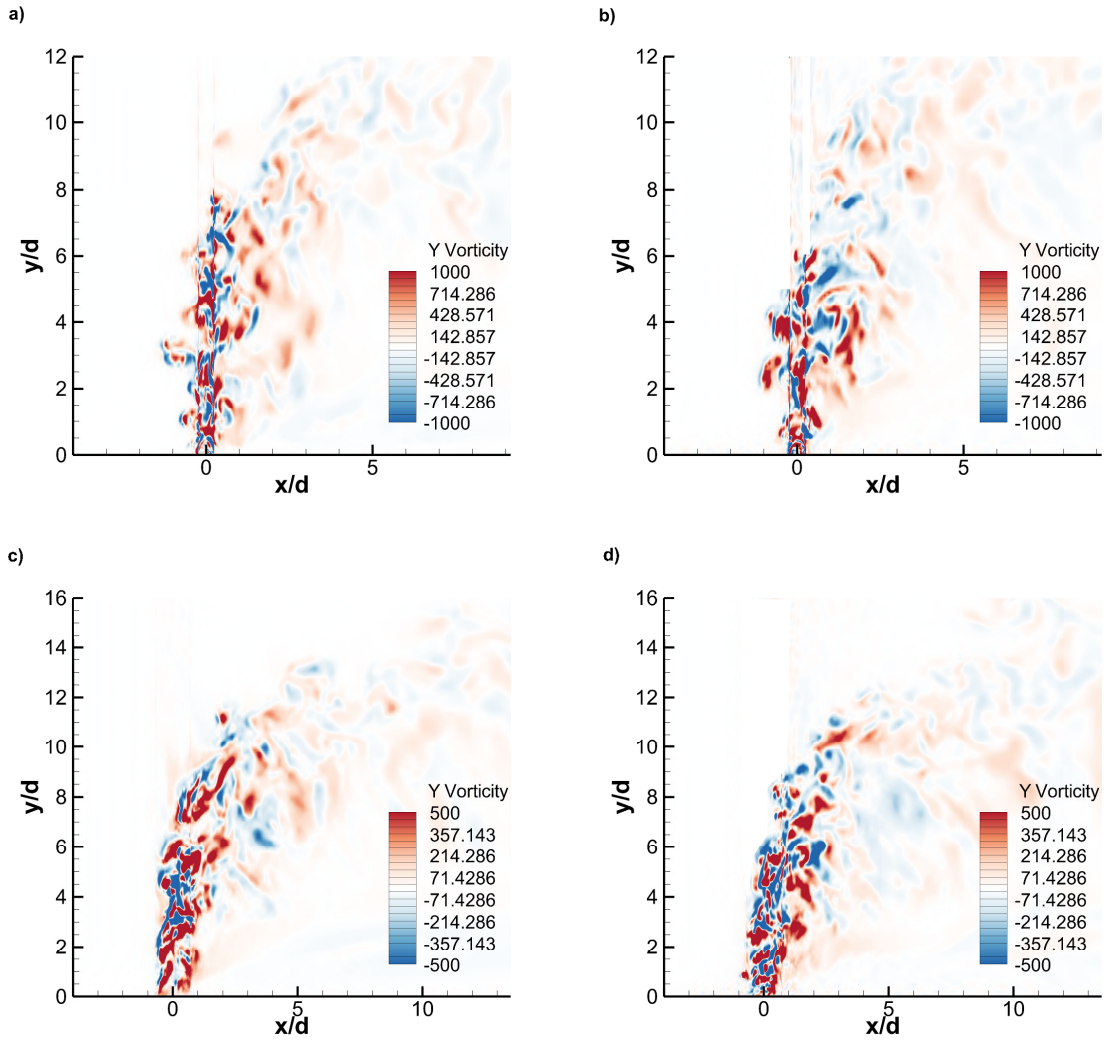

Figure 6.14. Wall normal vorticity contours; (a) Case 2 – Plane z= 0.44 d; (b) Case 4- Plane z=0.44 d; (c) Case 6- Plane z=0.39 d; (d) Case 8- Plane z=0.39 d

The cylindrical JICF (Fig 6.14 (a), (b))shows earlier large scale distribution of wall normal vorticity in the leewad side of the jet (y= 1.5 d and y=1 d). The rectangular JICF (Fig 6.14 (c), (d)) shows this at a deeper depth (y= 4 d and y=3 d). This shows that the rectangular JICF delays the large scale breakdown of structures, which may be due to features such as axis switching. Comparing the inlet turbulence intensities at the jet inlet, higher turbulence increases the disturbance which

enhances the large scale distribution of vorticity, i.e. causes it to happen earlier. In addition, it was observed that increased turbulence at the inlet increases the formation of wall normal vortices. This is likely due to the crossflow shearing across the spanwise edges of the jets and creating wall normal structures which is more favored by turbulence of the jet. Also, the wall normal vortices are thicker and more intense in the high turbulence cases, indicating that inlet turbulence levels affect the formation of wall normal vortices (increases in quantity and intensity).

6.5.1.3 Comparison of spanwise extent

Another interesting aspect is the shedding of the vorticity in the wake of the JICF. As we have seen that the cylindrical JICF bends earlier than the rectangular JICF, the planes selected to study this wake behavior of vorticity are y=7 d for cylindrical JICF and y=7.5 d for rectangular JICF.

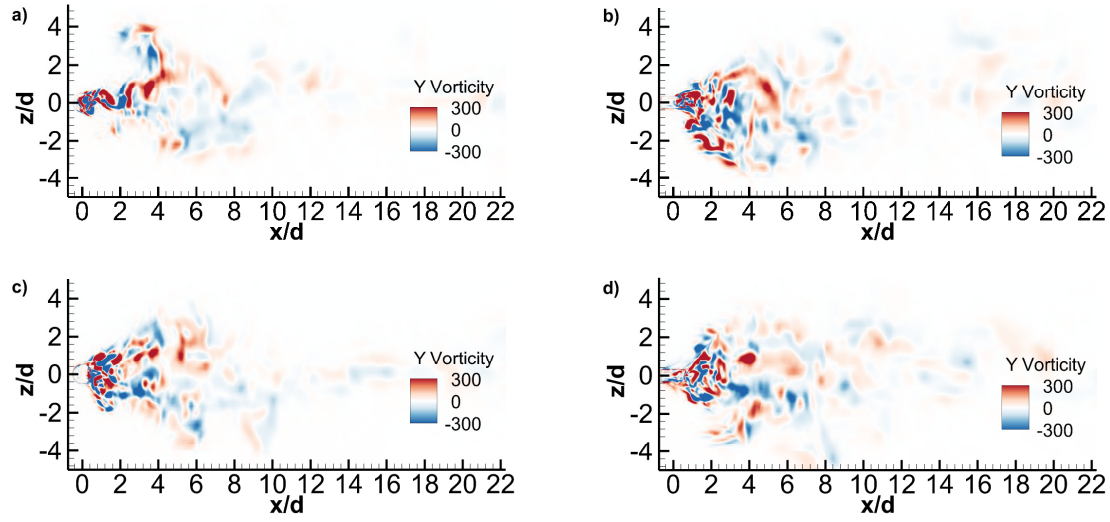

Figure 6.15. Wall normal velocity contours on wall normal planes; (a) Case 2; (c) Case 3; (e) Case 4; (b) Case 6; (d) Case 7; (e) Case 8; (a,c,e) Plane at y=7.0 d; (b,d,f) Plane at y=7.5 d (Figure cont'd)

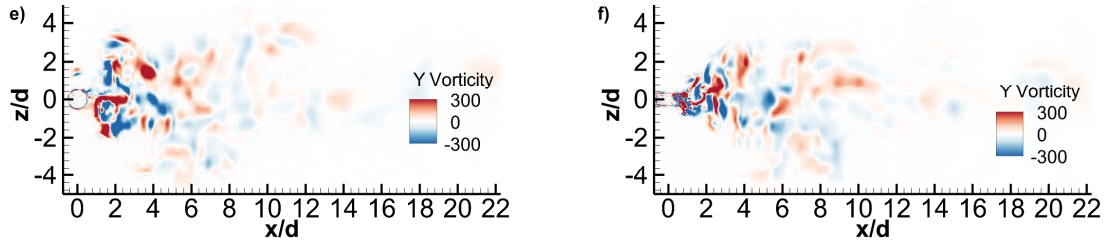

All six turbulent jet cases (2, 3, 4, 5, 6 and 8) are plotted in Fig 6.15 and compared. The initial shedding is similar to the shedding of vortices in the wake of a cylinder. This can be seen clearly in Fig 6.15 (a). After that a breakup of vortices are seen as it travels in the crossflow streamwise direction. As the inlet turbulence intensity increases, more structures are dispersed in the spanwise direction. This phenomena may be linked to the increased activity as the turbulence of the jet increases. Also, it can be noted that the shedding happens earlier for higher turbulence levels. It can be observed by the vortices which are more inside the pipe/ duct for regular intensity and outside for higher intensity. Comparing rectangular and cylindrical JICF, it can be observed that the vortices are still clustered in the central region for longer streamwise length in rectangular JICF. This is likely due to the effect of earlier breakdown for cylindrical JICF as discussed before. The shedding pattern in the both cases are similar indicating similar nature of wake.

6.5.2 Comparison of time averaged velocity fields

6.5.2.1 Mean flow field

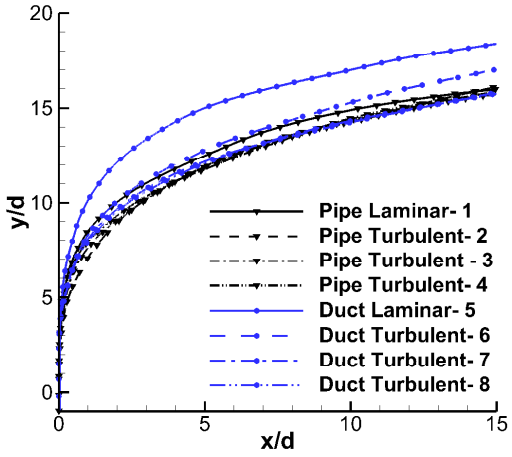

Figure 6.16. Time averaged jet trajectory for all the cases

Fig 6.16 shows the comparison of time averaged jet trajectory for all the eight cases. It is seen that the jet penetrates the deepest when the jet is laminar, i.e. when there is no turbulence in the jet when it enters in the domain. The fully turbulent jet penetrates less into the domain. This conclusion have already been discussed by Muppidi and Mahesh (2005). However, the effect of turbulent intensities have not been studied. It is seen that for all the turbulent jet cases, there is no significant difference. Slight difference that is observed is due to the fact that the level of turbulence in the jet is responsible for earlier initiation of turbulence in the main domain which in turn creates the dynamics that bend the jet differently in the near field.

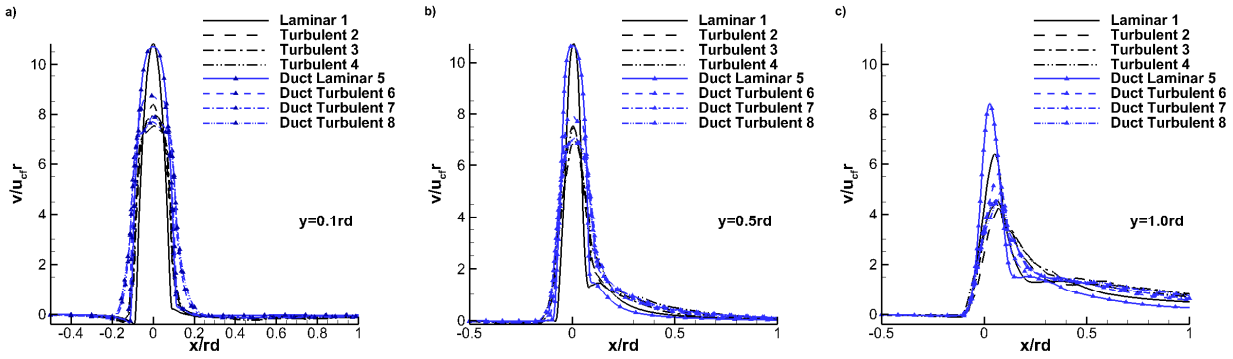

Figure 6.17. Mean velocity profiles at three stations for all cases; (a) At station y=0.1 rd; (b) At station y=0.5 rd; (c) At station y=1.0 rd

For detailed comparison, mean vertical velocity (normalized by crossflow velocity) for all eight cases is compared for three stations in the near field in Fig 6.17. These stations, as above, are inspired by the work of Su and Mungal (2004) and a consequent work by Muppidi and Mahesh (2007). Same behavior is seen as reflected in the trajectory. The mean vertical velocity penetrates deeper for the laminar jet case than the turbulent cases. For the turbulent cases, intensity levels does not significantly change the mean flow. An interesting fact to note is that the jet widens earlier for turbulent cases than laminar cases. This is from the fact that high turbulence incorporates higher fluctuations along the edges of the jet, which widens the overall mean jet area. This also means that higher entrainment and mixing would occur for turbulent jets compared to laminar jet which is physically intuitive.

Comparing rectangular JICF and cylindrical JICF, the extra width is expected because the streamwise edge is longer in the rectangular JICF. The near-field stations (y=0.1 rd and 0.5 rd) behave the same. However in the far field, the rectangular JICF is seen to be more penetrating than the cylindrical JICF. This is indicative of more penetration of rectangular JICF and less dispersion in the surrounding.

6.5.2.2 Far field behavior

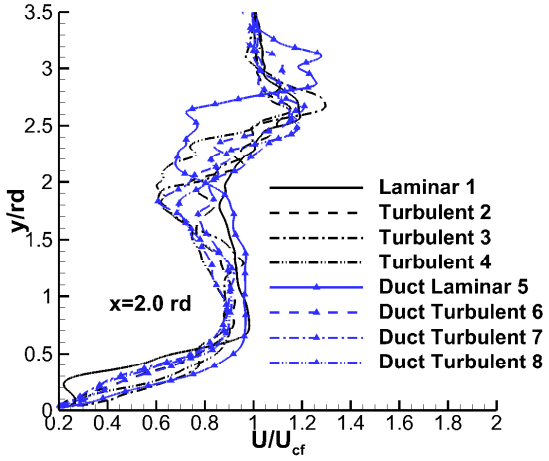

Figure 6.18. Time averaged horizontal velocity for all cases at x=2.0 rd

Jet width in the far field is of concern due to its mixing and entrainment properties. In the far field, CVP is the dominant mechanism of JICF for mixing. Larger jet width means larger area for mixing, and smaller jet width means smaller area for mixing. In order to compare the jet width in the far field (when the jet essentially have turned in the crossflow direction), time averaged streamwise velocity is compared at the station (x=2.0 rd) in Fig 6.18. Flatter profiles are seen when the turbulence is lower and more fluctuating profiles are seen as the turbulence level increases. This indicates that the increase in turbulence delays the JICF to reach the far field conditions. Compared to cylindrical JICF, more increase and decrease of velocity is seen for rectangular JICF which further adds to the previous observation of delay of rectangular JICF to reach far field conditions.

It has been observed above that the instantaneous flow field has notable differences. These differences arise mainly due to the differences in the near field dynamics. The near field dynamics

is established by the pressure gradient of the system. To understand the pressure behavior, mean coefficient of pressure can be studied in the symmetry plane for the cases.

6.5.2.3 Mean pressure field

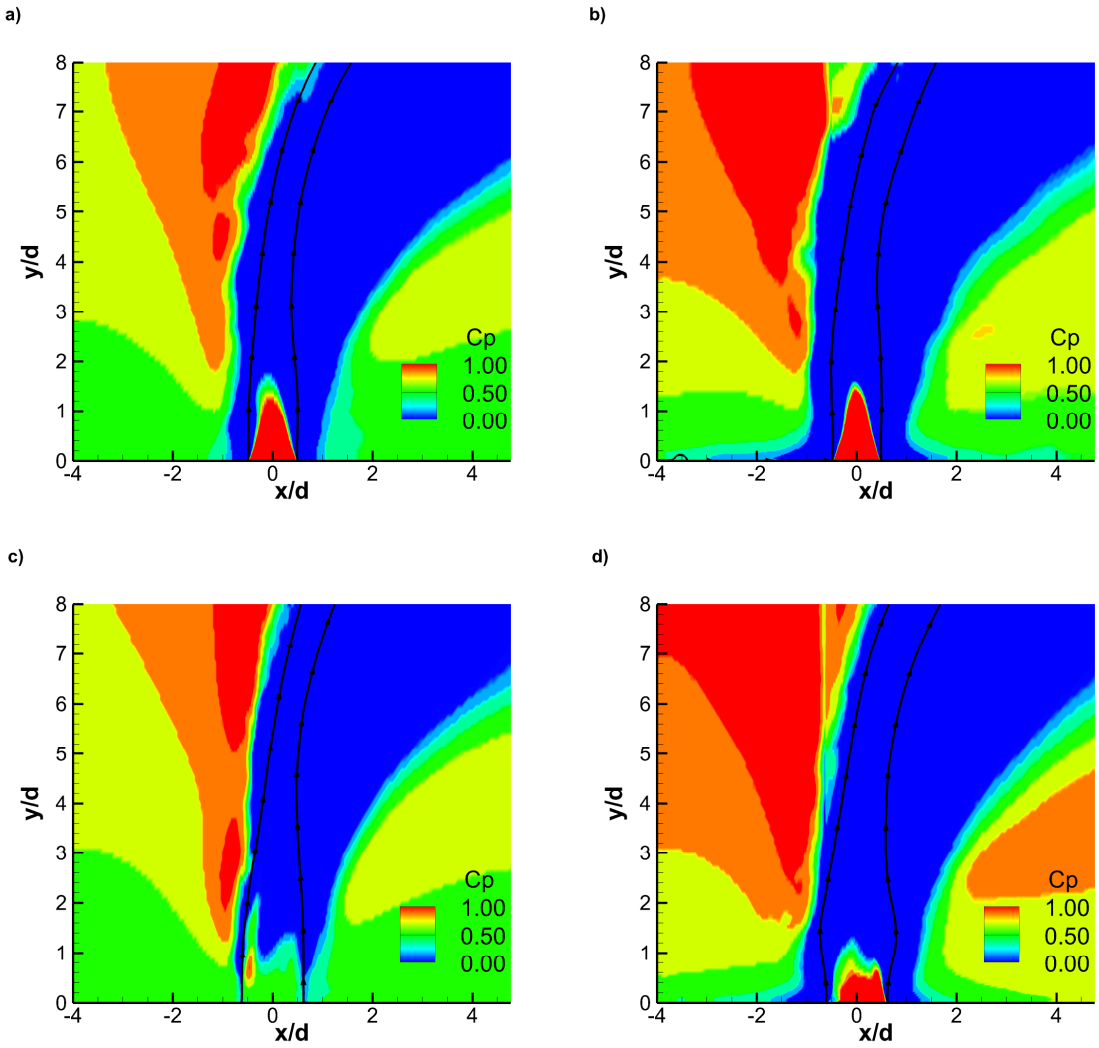

Figure 6.19. Mean Coefficient of Pressure on the symmetry plane; (a) Case 2; (b) Case 4; (c) Case 6; (d) Case 8

The mean coefficient of pressure is plotted in the symmetry plane for the four representative cases in Fig 6.19. This is helpful in analyzing the pressure dynamics in the near field, especially the leading edge. The pressure dynamics in the leading edge are primarily responsible for the formation of spanwise vortex. This has been explained in detail by Muppidi and Mahesh (2005).

Hence, a comparison of this region will provide meaningful insight. It can be clearly seen for both the geometries that there is a large region of coefficient of pressure in the leading edge. This region is larger as the turbulence in the jet increases. This behavior is seen for both the geometries. An interesting fact that had been noted earlier is also reflected by the mean pressure behavior. The region of trailing edge Cp also increases as inlet turbulence levels increase. This will in turn create earlier instability in the trailing edge. The increase in jet turbulence also enhances the large minimum gradient region in the central region around the jet periphery. This enhances the fluids from the around the jet to propagate towards the core region which affects mixing favorably and also increase the width of the jet.

6.5.2.3.1 Jet Bending due to pressure gradient

Effect of geometry is directly seen on the bending of the jet. This is explained clearly from the mean pressure field. Crossflow fluid, while trying to bend around the jet, forms a recirculation region in the wake. For cylindrical geometry, the wake (represented by pressure minima) forms near the immediate wake of the jet. However, due to corner in the rectangular jet, the crossflow fluid travels slightly slanted and forms the wake earlier due to recirculation. This pressure minima wake, enlarges as the jet evolves due to intake of fluid from the ambient. When the pressure minima region merges and then penetrates the core, rapid jet bending takes place, which orients the jet in the direction of the crossflow. At the depth where maximum pressure is encountered in the leading edge (y=1.9 d), the spanwise planes are plotted for the four representative cases in Fig 6.20. In addition to geometric effect, turbulence level in the jet also affects the bending. The pressure minima region is clearly larger for high turbulence levels indicating the formation due to more disturbed jet.

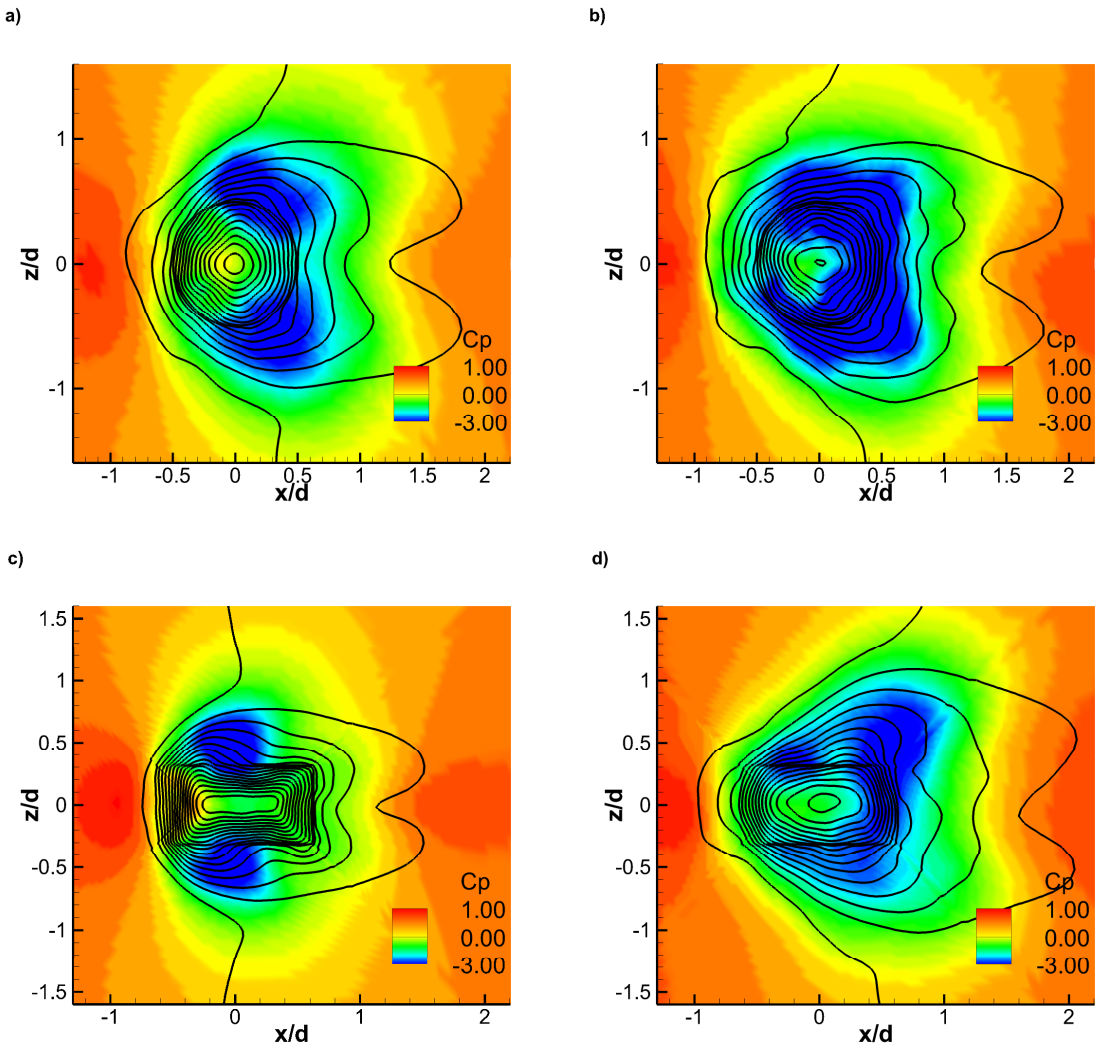

Figure 6.20. Mean coefficient of pressure at plane of y=1.9 d; (a) Case 2; (b) Case 4; (c) Case 6; (d) Case 8

At a higher plane (y = 4 d), the merging of the pressure minima region can be seen, and this is directly correlated to the bending of the jet. For both circular JICF, pressure minima region already has penetrated to the core and for rectangular JICF, they have not yet penetrated to the core. This indicates rectangular JICF, due to direct effect of geometry, penetrates deeper in the domain. Turbulence levels also play a role as can be seen in Fig 6.21. The higher turbulence jet has a deeper penetration in the jet core compared to lower turbulence jet for both geometries which also indicates earlier bending.

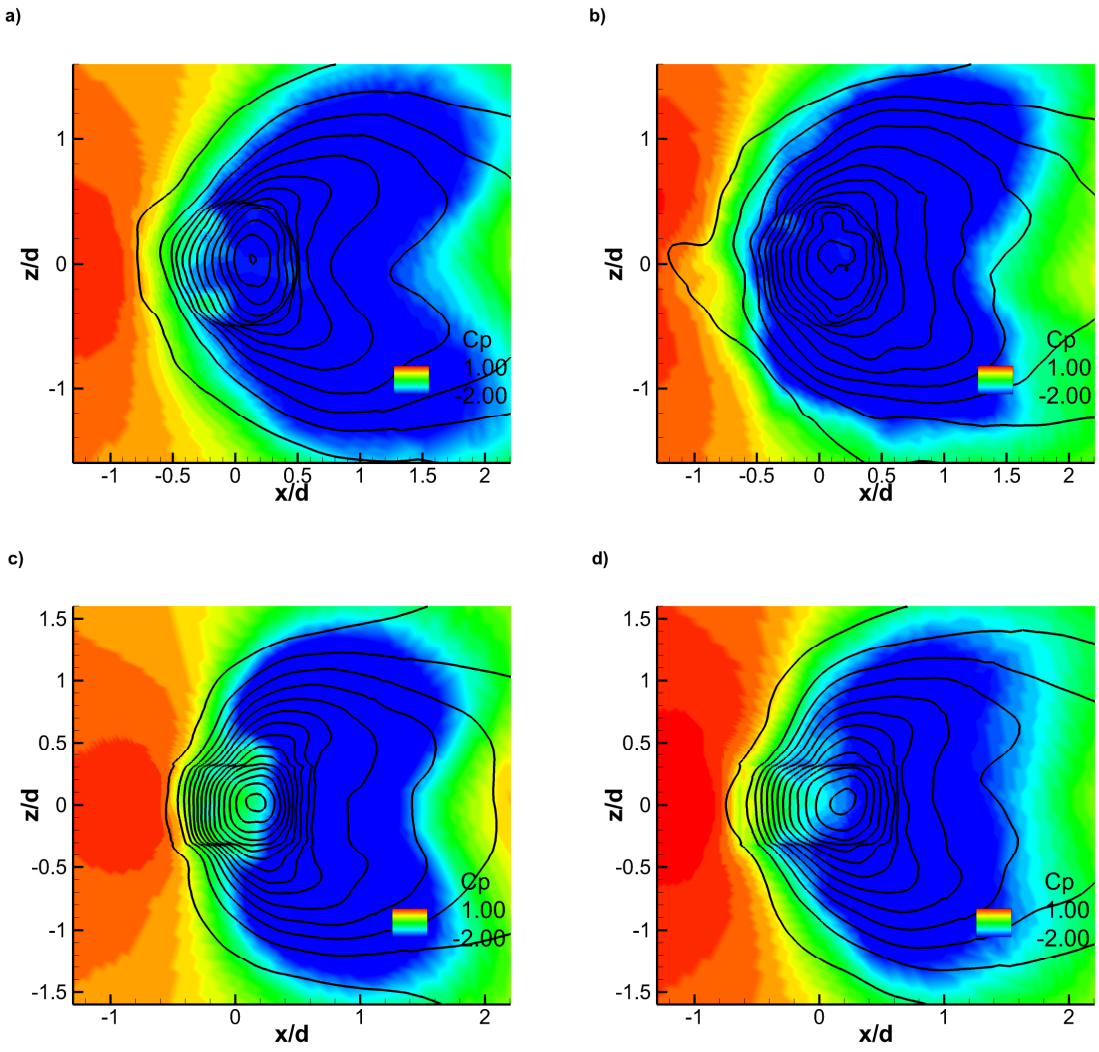

Figure 6.21. Mean coefficient of pressure at plane of y=4.0 d; (a) Case 2; (b) Case 4; (c) Case 6; (d) Case 8

6.5.2.4 Analysis of effect of turbulence intensity on shear layer

It is seen from the previous analysis that jet inlet turbulence plays a significant role in the initial rollup happening on the leading edge shear layer. The location of the rollup moves near to the wall as the turbulence intensity increases in jet. But does the size of the rollup change as well? We will be able to analyze that if we study the dynamic evolution of the shear layer. To isolate the effect of jet turbulence only, it is reasonable to study case 2, 3, and 4 for pipe JICF only. Four

instances of flow for each case are plotted which are 2 ms apart (Fig 6.22, 6.23, 6.24).

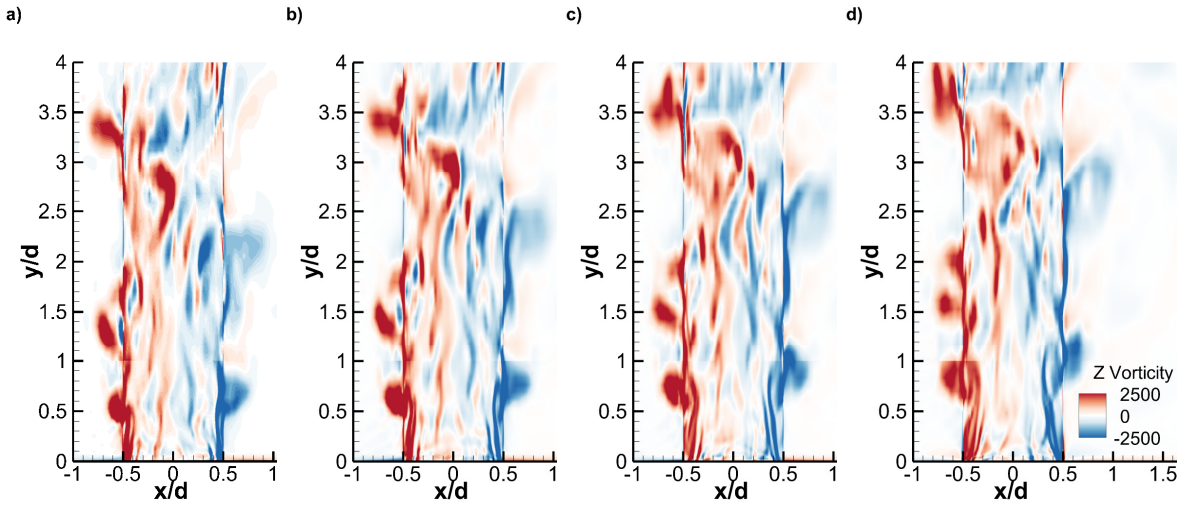

Figure 6.22. Four instances of spanwise vorticity in the symmetry plane for Case 2

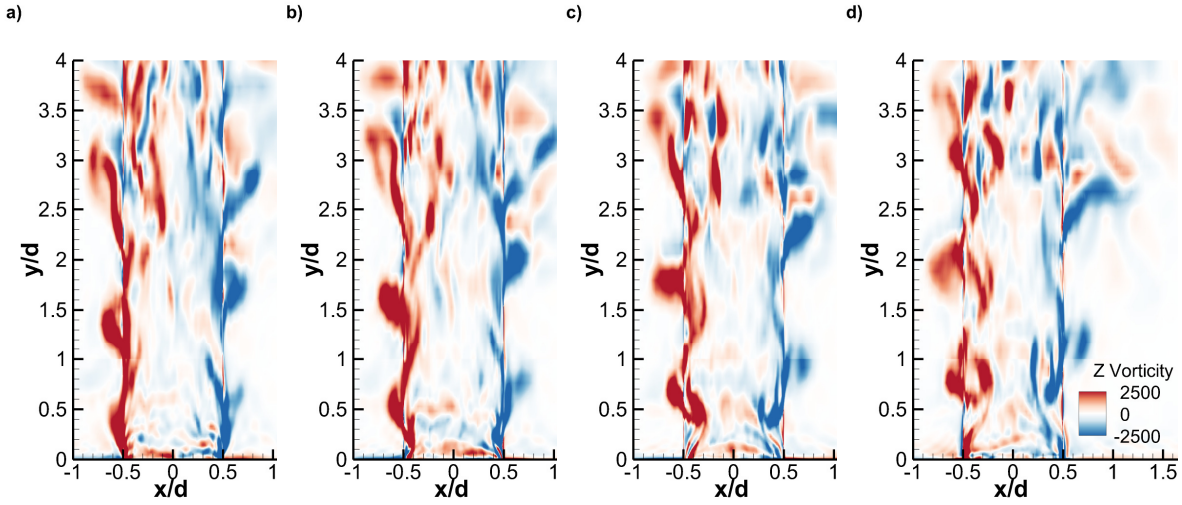

Figure 6.23. Four instances of spanwise vorticty in the symmetry plane for Case 3

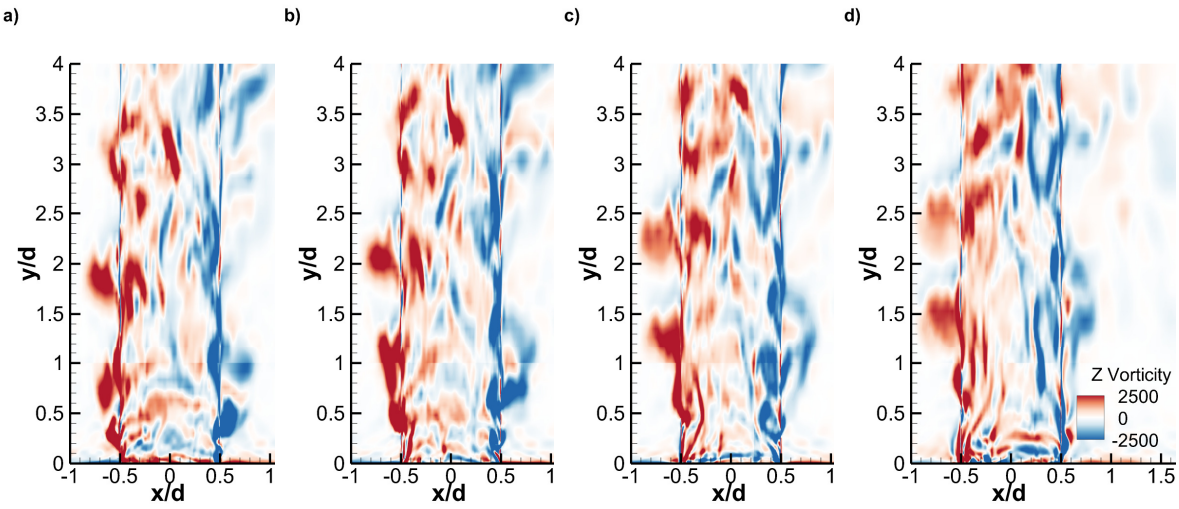

Figure 6.24. Four instances of spanwise vorticty in the symmetry plane for Case 4

It is seen that the size does not vary significantly with the increase in the intensity levels at the inlet. However, the split of the initial rollup happens progressively earlier as the turbulence intensity increases at the inlet. All the above cases are 2 ms apart. It can be seen that for the regular intensity levels, after formation of the initial rollup in the leading edge shear layer, split of vorticity and subsequent shedding happens after about 6 ms. For case 3 (Fig 6.23), it happens within about 4 ms and for case 4 (Fig 6.24), it happens within 2 ms. It has been seen that after this split, the wall normal vortices are generated easily from streamwise vortices in the leading edge shear layer.

6.5.2.5 Comparison of second order correlations

We have discussed the effects of inlet turbulence on the mean pressure field. Since the turbulence intensity has direct effect on the second-order correlations, it is necessary to understand the behavior on the second-order correlations on the domain. For that, second order correlations of pressure are compared for all eight cases at three stations of the symmetry plane.

The pressure variance are normalized by the square of dynamic pressure (based on the mean jet velocity).

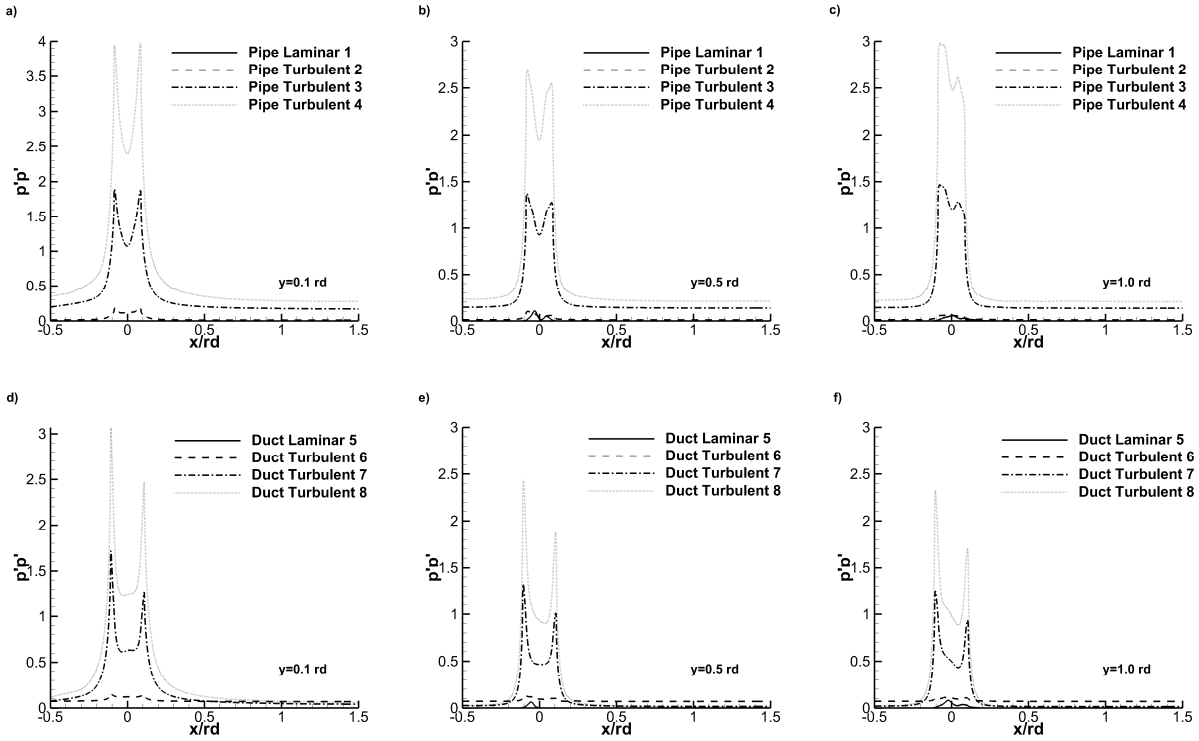

Figure 6.25. Second order pressure variance at three stations; (a, d) At y=0.1 rd; (b, e) At y=0.5 rd; (d, f) At y=1.0 rd; (a, b, c) Cylindrical JICF; (d, e, f) Rectangular JICF

Significant differences can be observed for different turbulent intensity levels in Fig 6.25. For cylindrical pipe flows (Fig 6.25 (a), (b), (c)) initially, a symmetric profile is seen. It is expected to be asymmetric. This may be due to high streamwise fluctuation in the inlet station, as discussed before. The asymmetry is seen in the second and the third station. For rectangular duct flows (Fig 6.25 (d), (e), (f)), the asymmetry is captured earlier and then continues downstream. It is seen for all the stations and both cases that as the inlet turbulence levels increase the pressure variance also increases. Comparing the centerline values, as the turbulence level ratio (L) increases by 1.66, the centerline pressure variance increases by 9.06 times the regular variance and if L increases by 2.45 times, the centerline pressure variance increases by around 20 times.

For rectangular JICF, the increase in centerline pressure variance near jet exit is about 5.16 times regular value for L of 1.66 and 10.2 times for L of 2.45. In the far field (y=1.0 rd), same trend is seen. Hence, the pressure field in pipe JICF are more sensitive to the change in inlet turbulence than in rectangular JICF.

6.5.2.5.1 Comparison of turbulent stresses

For understanding the effect of turbulence intensity of jet, a detailed analysis is done comparing the turbulent stresses for all the eight cases. Turbulent stresses are extracted along the same three stations in the domain.

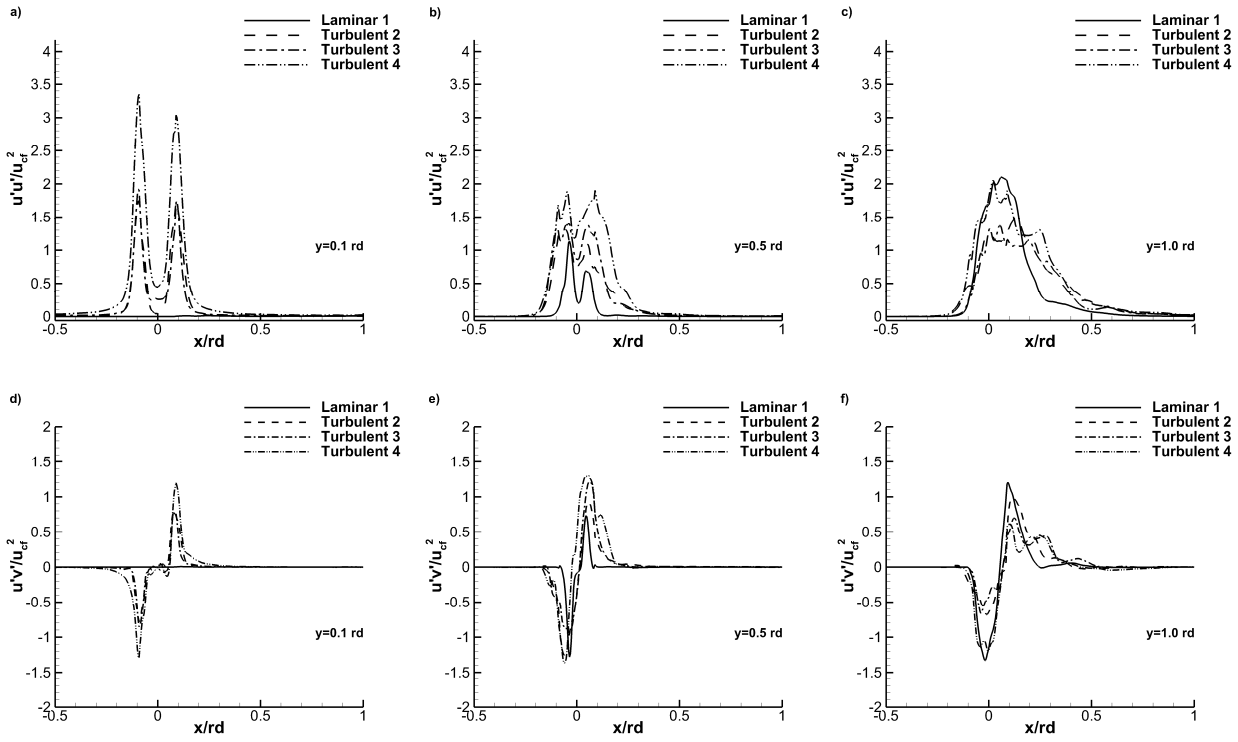

Figure 6.26. Second order Reynolds stresses for Cylindrical JICF; (Top to Bottom) Three stresses; (Left to Right) Three stations (Figure cont'd)

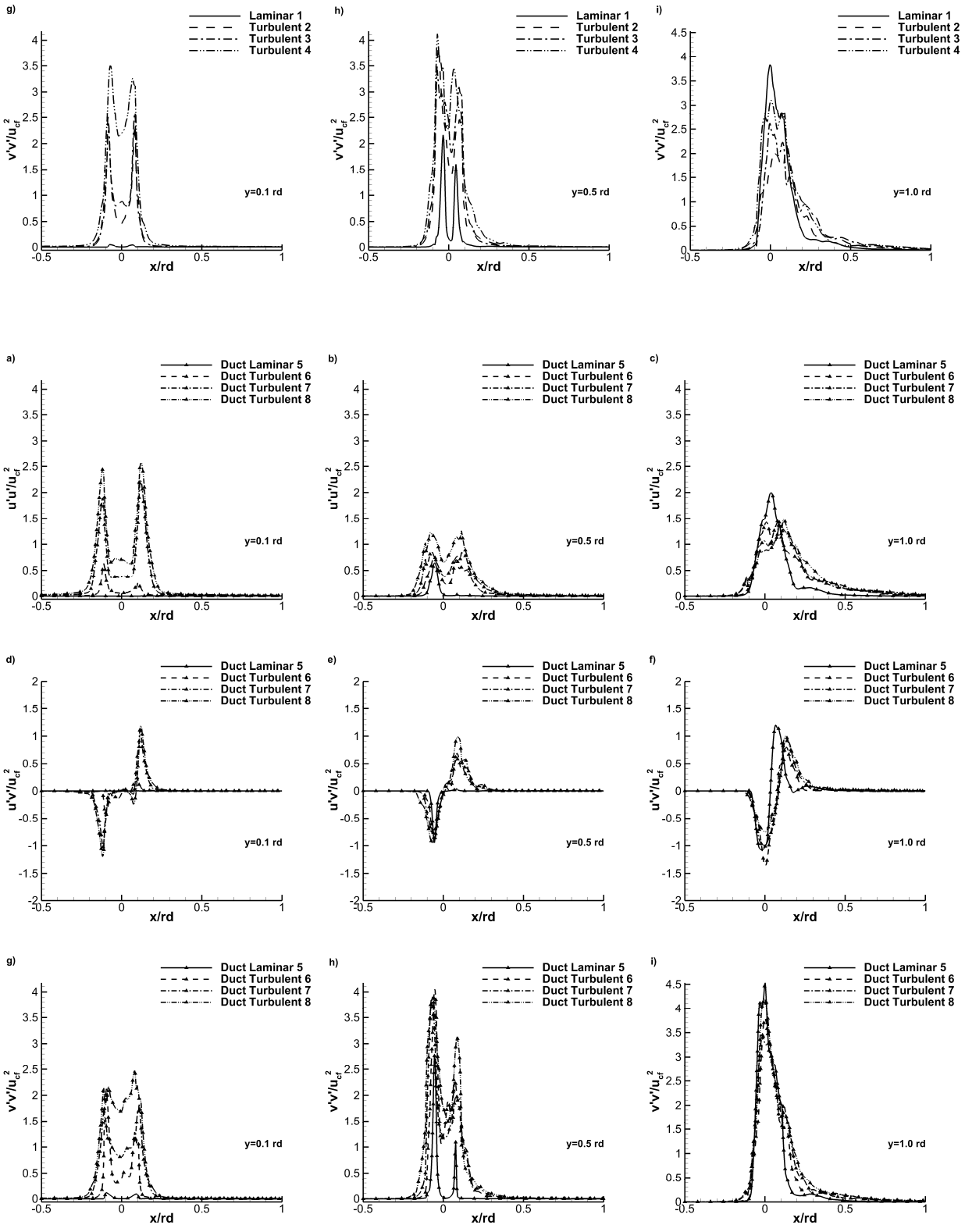

Figure 6.27. Second order Reynolds stresses for Rectangular JICF; (Top to Bottom) Three stresses; (Left to Right) Three stations

Fig 6.26 and 6.27 compares the three principal Reynolds stresses, at three stations respectively, for all the eight cases. In the initial station, the laminar jet cases (Case 1 and Case 4) have no turbulence activity whatsoever. Other cases show activity from the initial station itself. At the initial station, two distinct peaks which are almost equal are seen on the edges of the jet. Then in the second station, the peak at the leading edge becomes higher. At the third station however, the two peaks have merged and the fluctuations now show a single peak. For the shear stress also, the third stations shows symmetric behavior. This phenomenon of turbulence transferring from the edges of the jet to the core of the jet is called turbulence breakdown.

The effect of inlet turbulence levels on the stresses can also be discussed from the plots. It is obvious that as the turbulence level increase higher stresses for all the components are seen in the first station. The most notable change is in the jet streamwise velocity variance. As the flow moves downstream the difference between different turbulence levels is less. Interestingly, at the higher stations of the JICF, a larger width of fluctuations are seen for higher turbulence levels. This is especially notable in the third station where for the turbulence level (L) of 2.45, the width is 1.375 times for (u'u'=1), 1.337 times for (u'v'=0.3) and 1.4 times for (v'v'=1.5) compared with regular levels. For rectangular JICF, these values are 1.13 times for (u'u'=0.7), 1.17 times for (u'v'=0.3) and 1.19 times for (v'v'=1.5).

In the initial station, the fluctuations in the pipe are higher than in the rectangular JICF. This is because of the fact that the integral turbulence levels are the same, but the rectangular duct has larger length in the streamwise direction, indicating slightly smaller peaks. Also, since the instabilities in cylindrical JICF are triggered earlier around the circumference of the jet at once, higher turbulence activity can be expected in the edges of the jet. In the mid station, both the

cylindrical JICF and rectangular JICF have a similar behavior showing more activity in the leading edge than the trailing edge. In the last station, higher peak for the vertical variance in rectangular JICF indicates that the jet still has inherent turbulence, which may be due to delay of earlier breakdown by axis switching phenomenon. This in turn delays the rectangular JICF to reach far field conditions as described already.

6.5.2.5.2 Comparison of turbulent kinetic energy

It is seen from the above analysis that at some point, the turbulence activity propagates from shear layers to the core of the jet. To capture this point, turbulent kinetic energy (TKE) contours are plotted in the symmetry plane for all the cases. This point where the turbulent stresses merge from the shear layer to the core of the jet, and the stresses become uniform in magnitude, is referred as Turbulence Breakdown Point (TBP). This is in following the work of Ruiz et al. (2015).

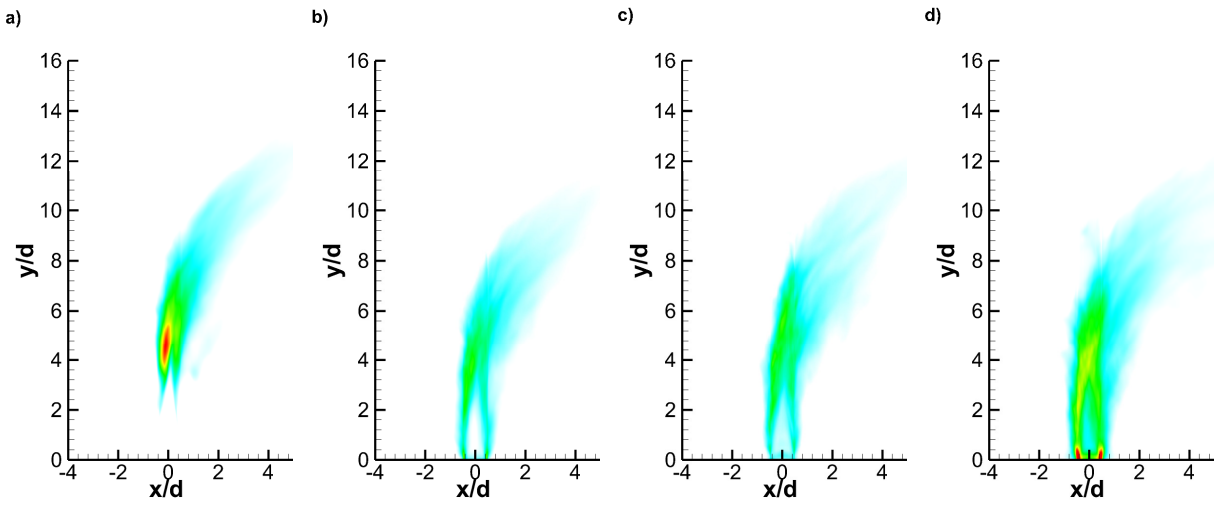

Figure 6.28. Contours of TKE on the symmetry plane for all cases; (a-h) Case 1-8 (Figure cont'd)

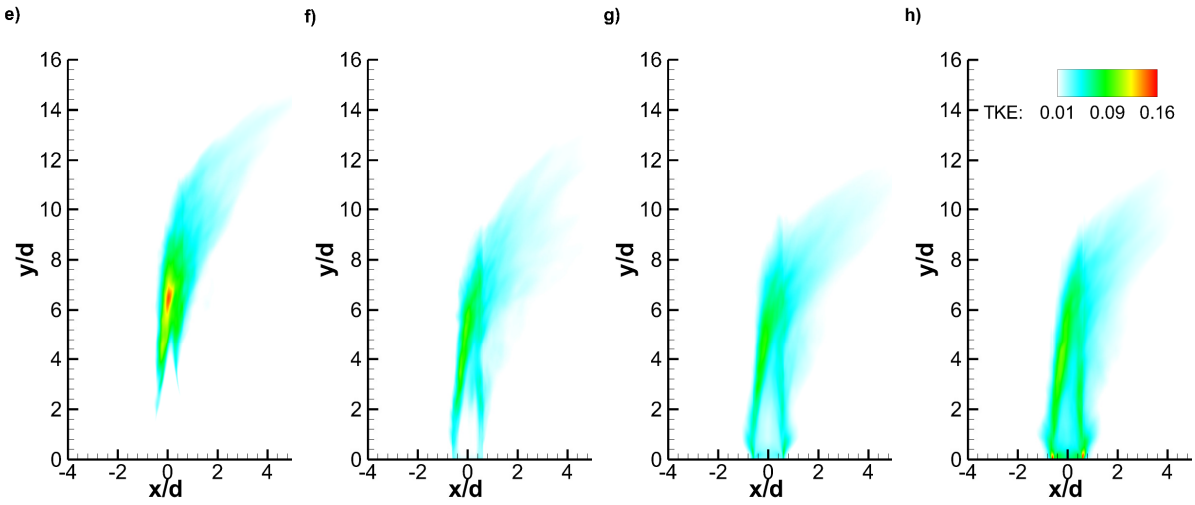

Fig 6.28(a),(e) shows that for the laminar jet cases, turbulence activity starts only after jet has penetrated some distance in the main domain. However, for all the turbulent jet cases, turbulence activity start immediately after jet enters the domain. The turbulence, initially is present in the shear layer, which then collapse to the core of the jet. This collapsing happens in two stages- when the initial shear layer TKE penetrates in the core and when the TKE within the core becomes uniform throughout. In the laminar case, the final collapse is seen sooner after the TKE activity initiates. In all the turbulent cases the final collapse is seen after a longer depth of the initiation of TKE.

There are some significant differences between different turbulence level cases. The initial point where the shear layers merge and turbulence is seen in the core, happens progressively earlier as the turbulence level increases. For high turbulence levels (case 4 and 8), there is inherent turbulence in the jet core when it enters the domain itself. Thus, it can be said that turbulence of the jet plays a significant role in ascertaining the location of the initial penetration of turbulence. The final collapse is also affected by the turbulence levels. Final collapse is defined in this work as the point in the jet centerline where the maximum TKE from the leading edge shear layer

penetrates. The depth of final collapse for each case are – Case 1- y=4.8d, Case 2-y=4.74d, Case 3-y=4.68d, Case 4- y=3.84d, Case 5-y=6.7d, Case 6-y=6.65d, Case 7-y=6.07d, Case 8-y=5.99d. Hence, it is seen that increase of turbulence of the jet enhances the initial collapse significantly but only slightly enhances the final collapse. It is also evident that larger region of high turbulence in the leading edge shear layer is seen for higher turbulence cases. Thus, turbulence in the jet also helps in sustaining higher turbulence in the shear layers in the near field, which is favorable for mixing.

For the cases, rectangular JICF (Fig 6.28 (e)-(h)) shows deeper merging of the shear layers compared to the corresponding cylindrical JICF (Fig 6.28 (a)-(d)). Furthermore, it shows larger region of TKE in the domain. This means change in geometry helps in delaying the onset of turbulence breakdown and further helps in sustaining larger region of turbulence, which is also favorable in mixing in the downstream region.

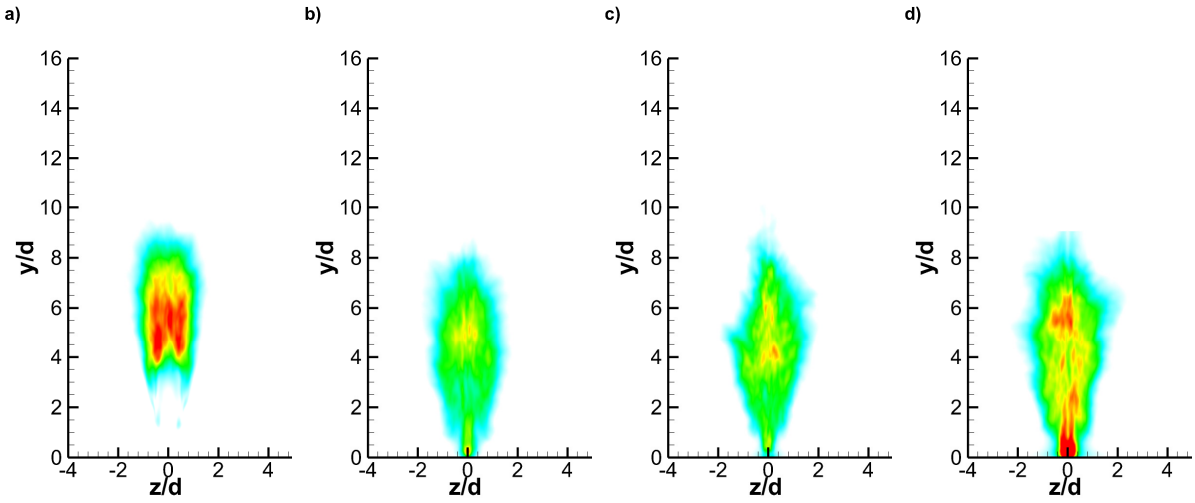

Figure 6.29. Contours of TKE on the wake plane for all cases; (a-h) Case 1-8; (a-d) x=0.5 d plane; (e-h) x=0.63 d plane (Figure cont'd)

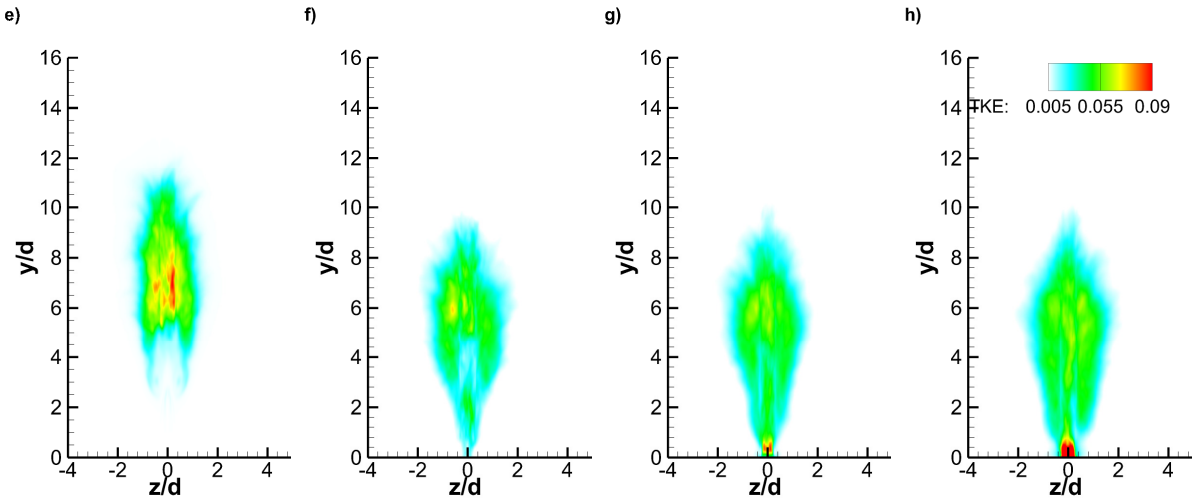

Spanwise plane reveals a detailed effect of geometry and inlet turbulence levels on JICF flow field (Fig 6.29). As the turbulence levels increase, the maximum width of TKE in the spanwise plane also increase. This may be favorable for mixing. Intuitively, as the turbulence increases we can expect increase in the area of TKE, which is confirmed from the above analysis. Furthermore, the TKE effect is nearer and larger to the jet exit as the turbulence level increases. Higher TKE is evident in the core region for high turbulence of the jet. Comparatively, TKE in rectangular JICF spans deeper in the domain and higher TKE in the core is evident for cylindrical counterparts. As discussed before, the effect of wrapping of crossflow fluid around different geometry of the jet is the cause of these differences. In rectangular JICF, the effect of axis switching is also reflected in the spanwise planes. For lower turbulence levels, complete TKE penetration in the core is seen after axis switching is complete. For high turbulence levels, the penetration is earlier compared to lower turbulence levels.

6.5.2.5.3 Comparison of spanwise variance

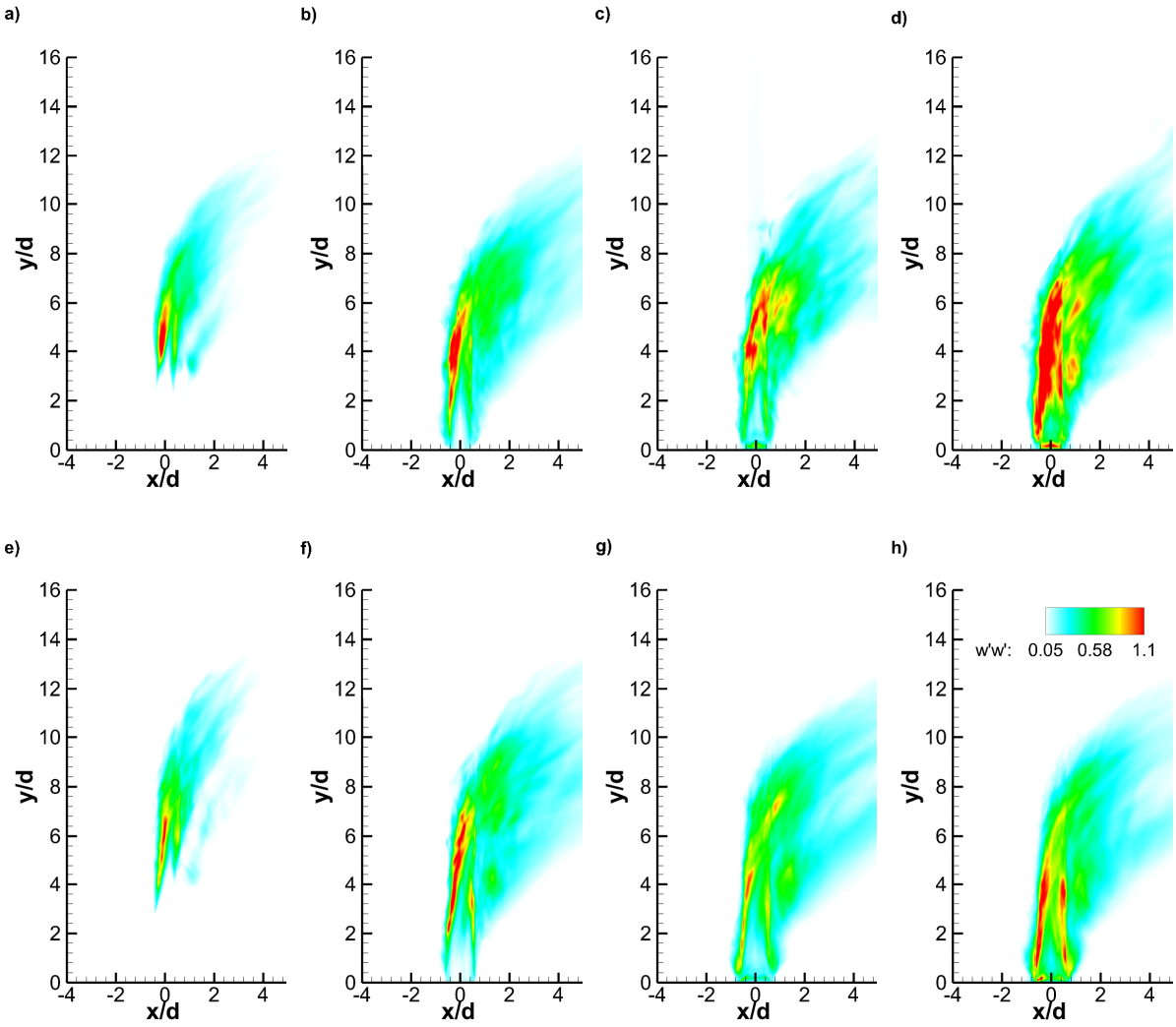

Figure 6.30. Contours of spanwise variance on the symmetry plane for all cases; (a-h) Case 1-8

To understand the nature of variance in the spanwise direction of JICF, the spanwise variance (w'w') is compared for the cases in the symmetry plane (Fig 6.30). This gives us the idea of the three dimensional effects of inlet turbulence in the domain. It is seen that as the turbulence level at the inlet increases, the spanwise variance increases in the leading edge shear layer. This directly correlates to the high disturbance in the shear layers provided by the turbulence. The spanwise variance shows earlier penetration in the jet core for cylindrical JICF. The variance

region in the trailing edge of the jet also increases as the turbulence of the jet increases. This also enhances the local mixing in the trailing edge region.

Compared to cylindrical JICF (Fig 6.30 (a)-(d)), rectangular JICF (Fig 6.30 (e)-(h)) shows thinner region of high spanwise variance. This may be due to the fact that rectangular JICF having smaller spanwise edge compared to the cylindrical.

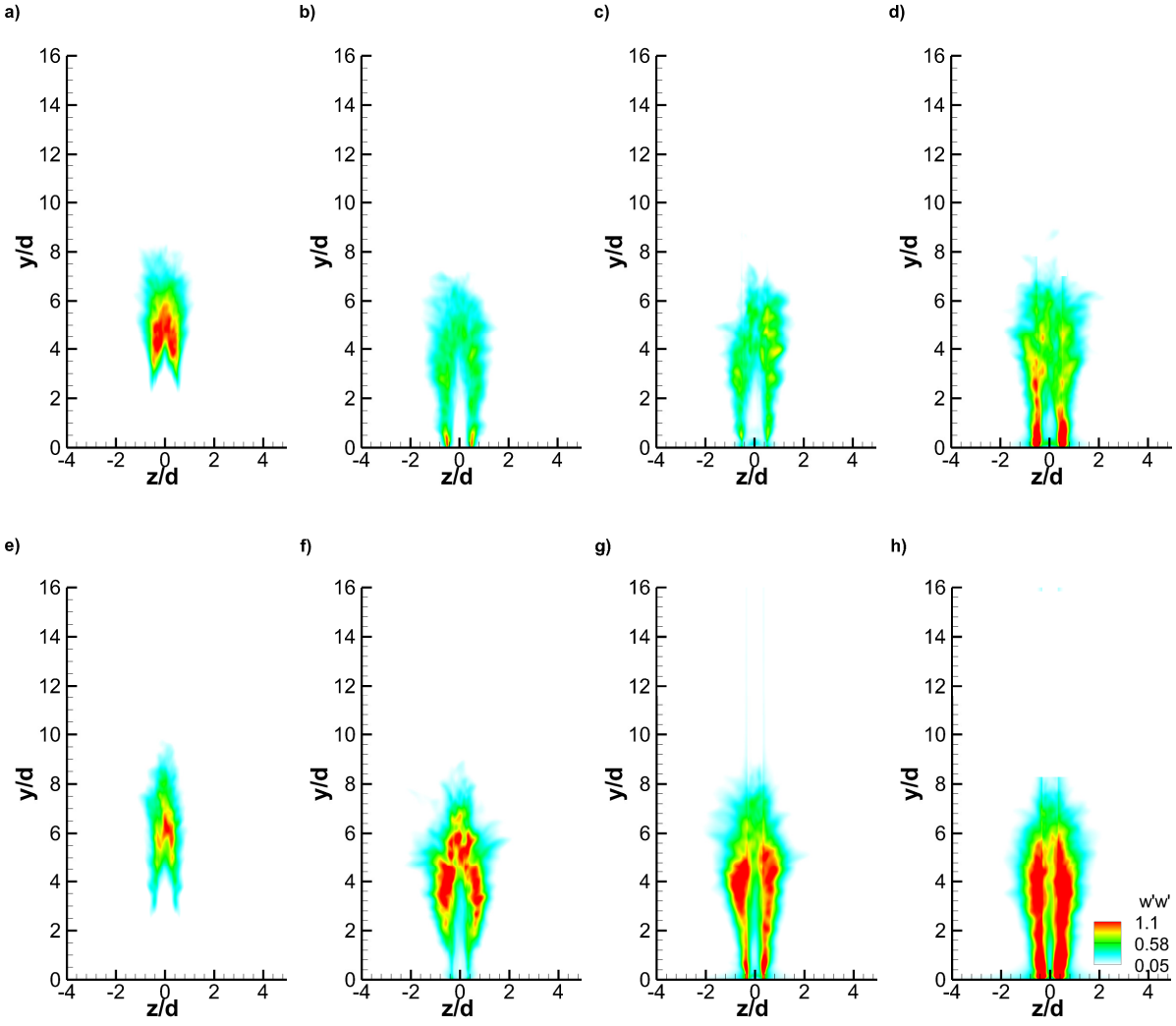

Figure 6.31. Contours of spanwise variance on the spanwise plane (x=0 d) for all cases; (a-h) Case 1-8

Effect of turbulence levels is seen on the spanwise planes as well (Fig 6.31). As the turbulence levels increase, the spanwise intensity on the shear layer region increases. Also the merging of spanwise intensity to the core of the jet happens progressively earlier as the turbulence level increases. Contrary to the behavior of TKE, spanwise intensity for rectangular JICF shows higher intensity in the shear layer than cylindrical JICF for the turbulent cases. Axis switching also has a role for this phenomena. Sudden increase in thickness of the high spanwise intensity in the core of the jet represents the flip of the geometry of the jet, which increases the distance between the shear layers. This may further explain the increase of mixing seen in rectangular jets compared to cylindrical jets.

6.6 Section 6-Comparison of axis switching

Axis switching is seen in the jets that have regular geometric shapes (except circular), and different width in two directions in the cross section. In the cases above, only rectangular jets exhibit 90 degrees axis switching as seen in Fig 6.32. To compare the effect of jet turbulence on axis switching, the latter four cases are compared. All comparisons are made on the basis of planes at which axis switching is seen for rectangular laminar JICF (Fig 6.32). Hence, two planes (y=2.5 d and y=5.0 d) are compared to see the relative stages of axis switching for rectangular JICF cases.

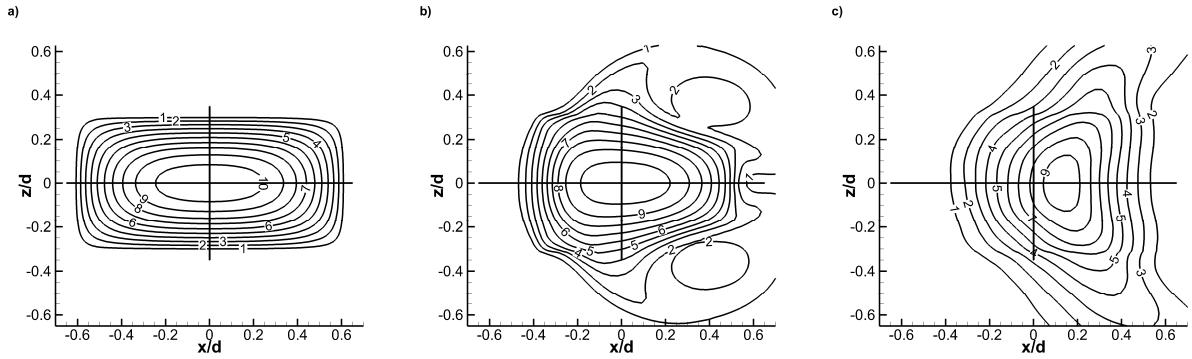

Figure 6.32. Velocity contour lines normalized by crossflow velocity on three different planes for Case 5; (a) Plane y=0 d; (b) Plane y=2.5 d; (c) Plane y=5.0d

6.6.1 Effect of crossflow

In literature, axis-switching has been documented mostly for jets in a quiescent flow. Hence, most profiles of velocity that exhibit axis-switching are symmetric about both the cross-sectional axes. However, the presence of crossflow will have an additional effect on axis-switching. As we have seen previously that in JICF, the primary instability initiates earlier in the leading edge shear layer than the trailing edge. The wall normal vortices also form earlier in the leading edge. These wall-normal vortices are primarily responsible for axis switching. Therefore, the deformation here happens in the leading edge of the JICF earlier than the trailing edge. From Fig 6.32, it can be seen that the jet is symmetric in both the directions initially. As the jet evolves, the deformation to switch the axes starts in the leading edge, and the jet becomes bulged in the leading edge compared to trailing. The same behavior carries further downstream and as the trailing edge has completed switching, the leading edge has deformed further creating a round shape. Hence, the axis switch does not remain symmetric about the x-plane. Thus, crossflow has an effect of switching the axis unevenly between the windward side and the leeward side, which is not seen in jets evolving in the quiescent environment.

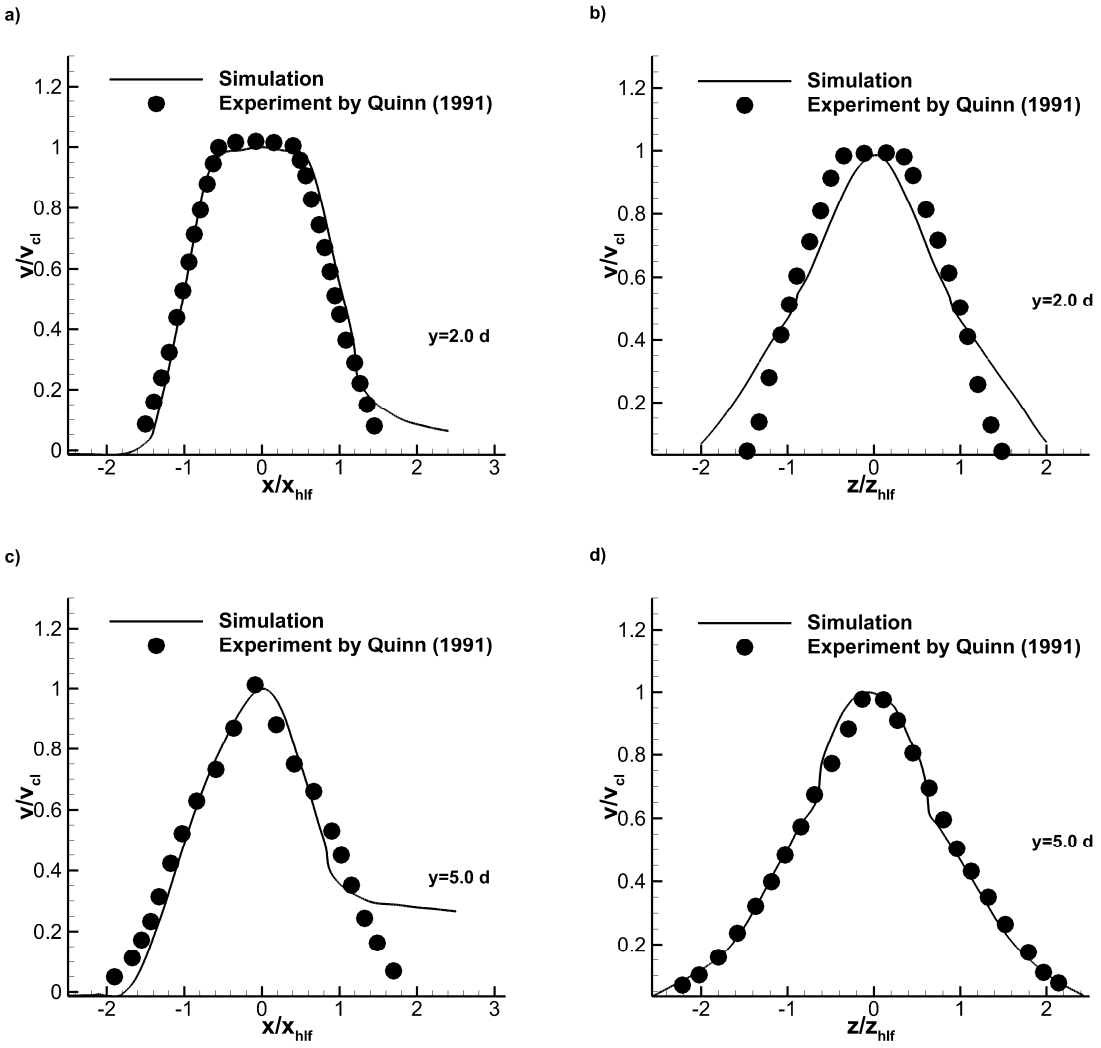

Figure 6.33. Validation of time averaged vertical velocity normalized with centerline velocity for Case 6 and experiments at two stations; (a, c) Symmetry plane profiles; (b, d) Spanwise profiles

To exactly find the effect that crossflow has on rectangular jets, comparison is done with RTJ (Rectangular Turbulent Jets) experiments done by Quinn (1991), in Fig 6.33. The mean velocity normalized with mean centerline velocity, is plotted at two different depths as in the experiment. The half widths in both directions are calculated by the distances at which the mean centerline velocity becomes half. In case the profiles are not symmetric (due to the effect of crossflow), preference was given to leading edge and the top edge. Although in the experiment, three depths are reported, only two depths are considered for comparison since at the third depth (y =10.0 d)

the current JICF is significantly bent to extract comparable vertical velocities. Also, for the depth of y=5.0 d, the streamwise edge profile was offset in the positive x direction. In that case, the offset was corrected for exact comparison with the experiment. However, for spanwise profiles (Fig 6.33 (b), (d)), no offset was encountered.

For the mean velocity, some differences are observed, which are due to effects of crossflow on the jet. For the initial streamwise profile, the leading edge has a good match with the experiments. However, the trailing edge shows larger region of lower magnitude velocity. This is due to the rollups in the leading edge happening earlier and travelling downstream towards the trailing edge. A significant deviation is seen for rectangular jet in a quiescent flow and crossflow on the spanwise edges. Larger region of low magnitude velocity and a shallower peak of high magnitude is seen for JICF. This may be due to the movement of outer fluid on the spanwise edges, which will create additional instability resulting in higher disturbance, and hence extension of velocity region. At a higher depth, the streamwise profile shows larger region of low velocity magnitude in the trailing edge. However, the effect of crossflow on the spanwise edges has stabilized and the JICF behaves as a normal jet. So it can be seen that the effect of crossflow is most in the near field when the structures start to form initially.

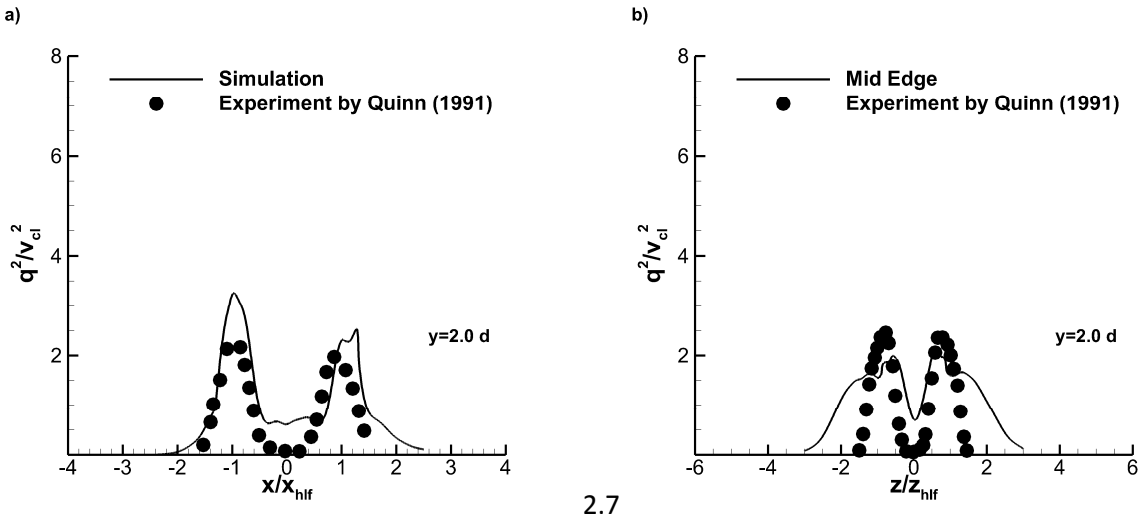

2.7

Figure 6.34. Turbulence Kinetic Energy in: (a) streamwise direction; (b) Spanwise direction

Comparing second-order correlations in the near field, the effect of crossflow on turbulence can be understood. Second-order correlations are compared in the initial station (y=2.0 d) in Fig 6.34. Although the experiment was done from a flow issued from a nozzle and different Reynolds number, the scale of square of centerline velocity makes it comparable. Crossflow aids to provide more perturbations in the leading edge shear layer to trigger the KH instability earlier. This is reflected by the increase in TKE, especially in the leading edge. Turbulence in the core is also evident due to earlier breakdown promoted by earlier rollups in the shear layer. Spanwise direction exhibit turbulence for wider region of jet consistent with the mean velocity field (Fig 6.34 b). The effect of crossflow is thus, to increase TKE in the spanwise direction as the fluid moves around the jet. At this spanwise station as well, higher turbulence than experiment is in the jet core, which has been provided by the earlier formation of instability in the leading-edge shear layer.

Dynamics of the flow field can be analyzed to study the vortex rollups, which aid in axis switching. For rectangular jets without a crossflow, vortex rings are formed around the jet simultaneously

(Grinstein, 2001; Gutmark & Grinstein, 1999). For current cases, 4 instances which are 2 ms apart are visualized in the leading edge to understand the nature of these rollups (Fig 6.35).

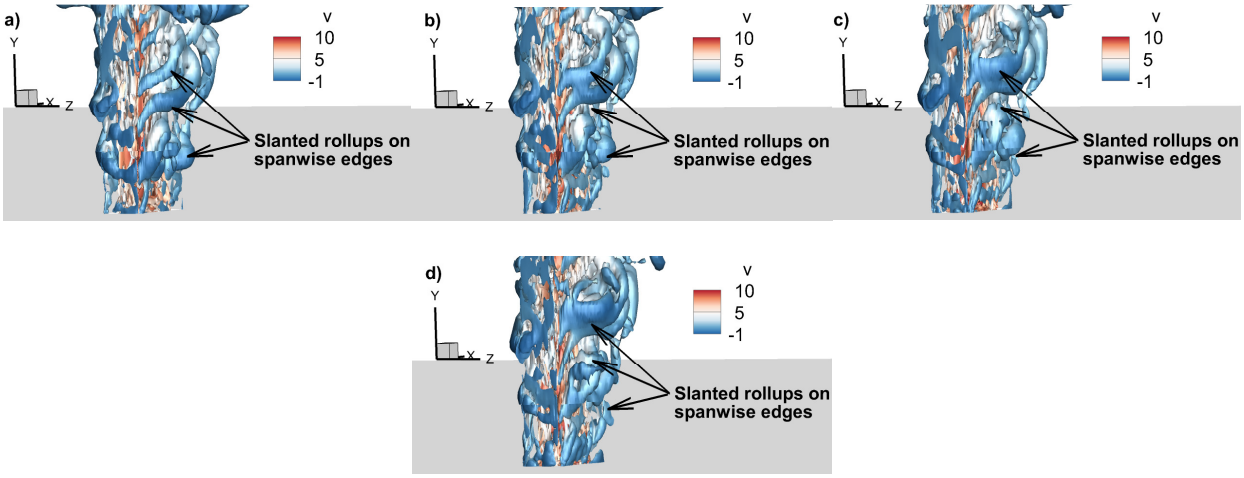

Figure 6.35. Four instances of iso-surfaces of Q which are 2 ms apart

The rollups are not straight around the jet as seen for jets with no crossflow. They are slanted in a way to start early at the leading edge, and then wrapping around to reach the trailing edge at a higher depth. This demonstrates that, in the leading edge where the crossflow hits the jets the earliest, rollups are formed earlier than jets in a quiescent flow. Thus, earlier initiation in the leading edge, compared to trailing and spanwise edges, leads to the slant of the vortices as seen above. The effect of crossflow is to enhance the shear layer rollups, which in turn helps in increasing the turbulence levels. On the spanwise side as well, turbulence level is wider due to crossflow moving around the jet, increasing the perturbations. These elevated turbulence levels are beneficial for mixing applications.

For axis switching, it has been noted in the previous chapter that deformation starts at the leading edge. This is because vortices are generated earlier in the leading edge, which deform earlier to switch the axes.

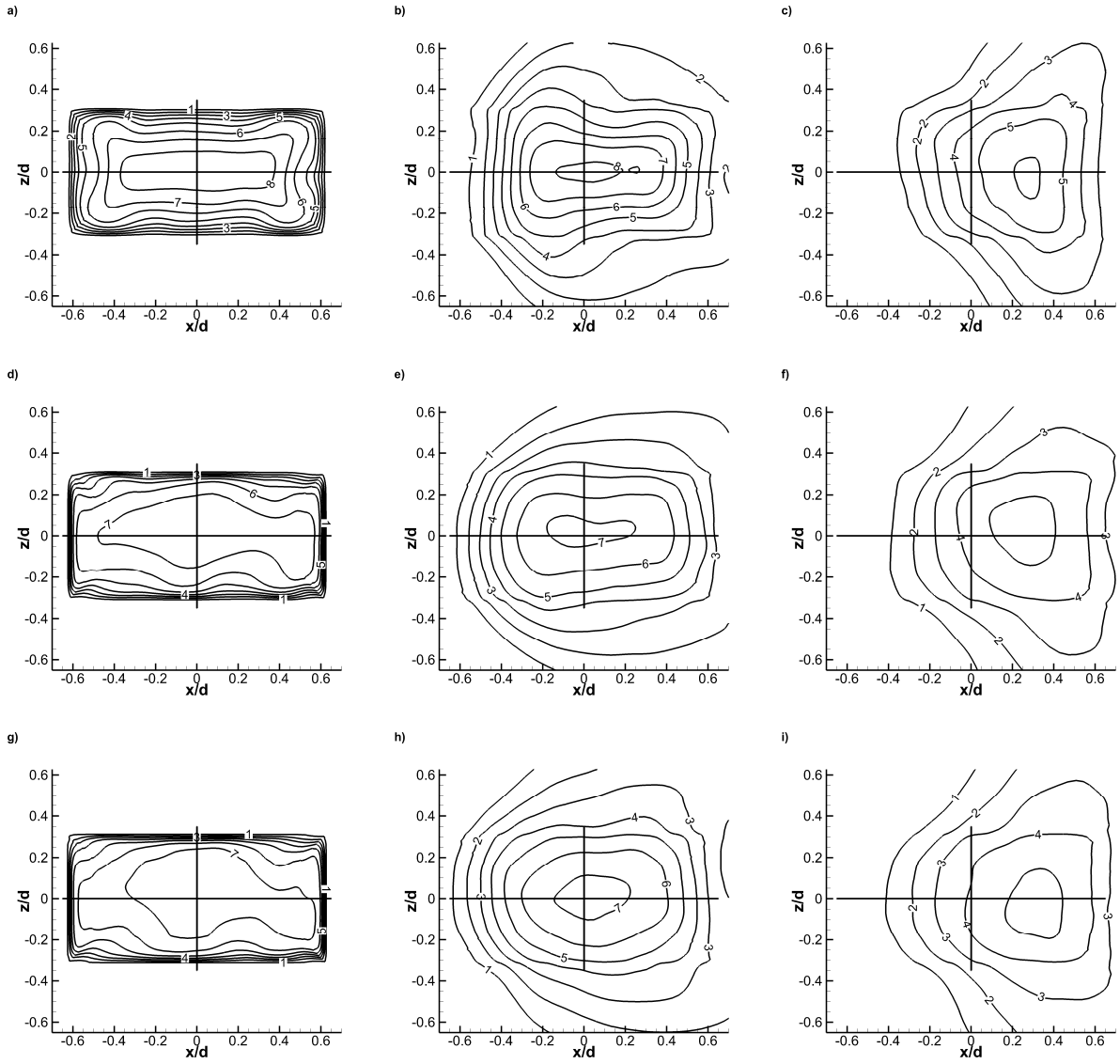

Figure 6.36. Velocity contour lines normalized by crossflow velocity on three different planes for Case 5; (a, d, g) Plane y=0 d; (b, e, h) Plane y=2.5 d; (c, f, i) Plane y=5.0d; (a, b, c) Case 6; (d, e, f) Case 7; (g, h, i) Case 8

It is seen that as the inlet turbulent levels increases, axis switching occurs earlier. This is seen for three turbulent cases (Fig 6.36). It can be judged by the contour levels of the vertical velocity. For the full laminar case (Fig 6.32), the central velocity level is only one level lower when the axis switches. But for all the turbulent cases, at these locations there is a bigger drop of velocity levels. This shows that axis switching happens earlier in turbulent cases.

In literature, axis-switching is visualized by finding the crossover of half-width of velocity. If the half-width of velocity is larger in a perpendicular direction than initial orientation, axis switching occurs and the point is noted (Fig 6.37). For the turbulent cases, the exact location of the axis switching gets nearer to the jet exit as the inlet turbulence levels increase. For the regular turbulent case, the first axis switch is seen at a depth of y=3.4 d. For higher intensity level, this is seen at a depth of y=3.33d and for still higher intensity levels, the depth is at y=3.2d. Second axis switching is also seen for the three cases. These are seen at y=6.3 d, y=6.1 d and y=6.0 d. The exact locations at which the full axis switch is seen for the turbulent cases is seen below:

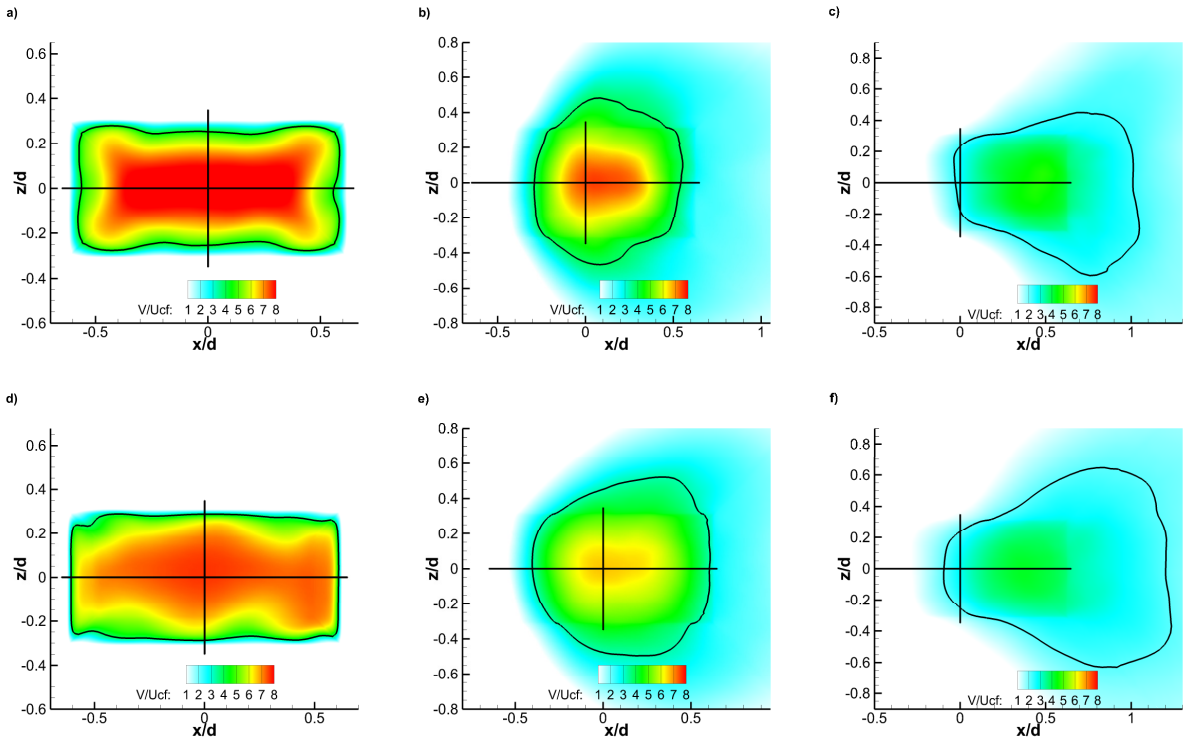

Figure 6.37. Velocity contour lines normalized by crossflow velocity on three different planes; (a, d, g) Plane y=0 d; (b, e, h) Plane y=3.4 d, y=3.33 d, y=3.2 d; (c, f, i) Plane y=6.3d, y=6.1 d, y=6.0 d; (a, b, c) Case 6; (d, e, f) Case 7; (g, h, i) Case 8 (Figure cont'd)

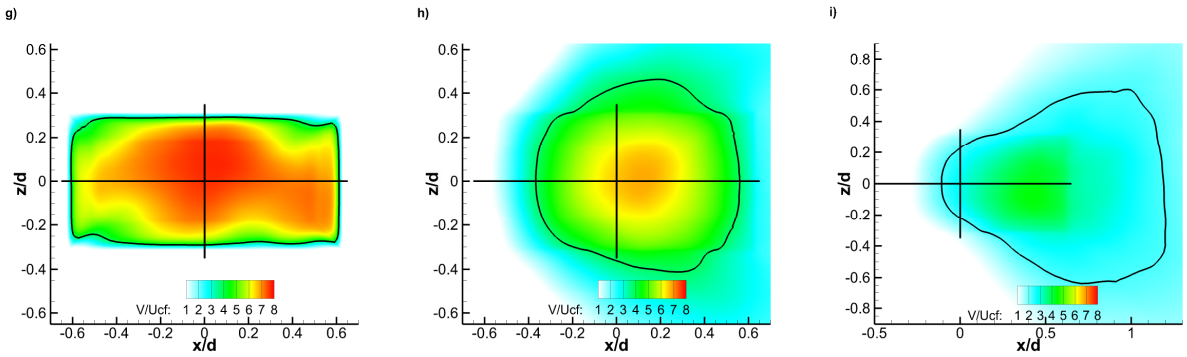

6.6.2 Explanation of effect on axis switching

The mechanism of axis switching can be understood by the wall normal vortices formed around the jet edge. On the leading edge, the pair of counter-clockwise and clockwise vortices tend to push the jet fluid inwards. On the spanwise edges, the vortices form, which tend to pull the fluid outwards. Thus, this mutual pushing and pulling will eventually switch the jet axes as it moves downstream. Then the orientation of the vortices again repeat the process in the opposite direction. This eventually creates another axis switch, which again orients the major jet axis in the initial direction. This mechanism has been studied and confirmed from the works by Chen and Yu (2014), Zaman (1996) to name a few. Vortex ring dynamics also have been documented to explain axis switching in detail by works of Gutmark and Grinstein (1999) and Grinstein (2001).To observe the same mechanism and understand the differences, instances of flow for the three rectangular turbulent JICF cases are analyzed which are 2 ms apart.

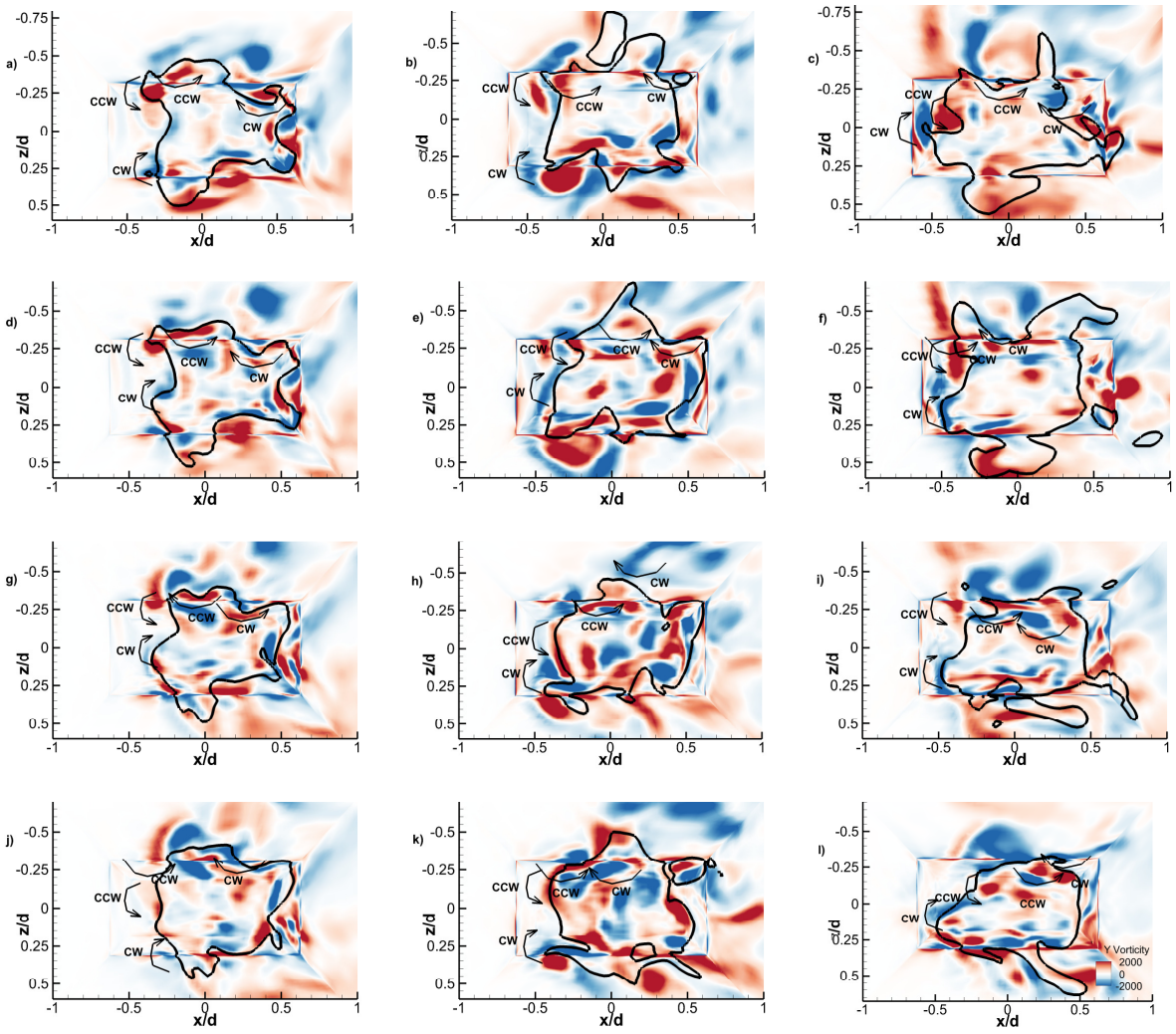

Figure 6.38. Four instances of wall normal vorticity contours for plane y=3.0 d; (a, d, g, j) Case 6; (b, e, h, k) Case 7; (c, f, i, l) Case 8

The plane at y=3.0 d, which is near the jet exit, is analyzed for the three turbulent rectangular JICF (case 6, 7, 8) in Fig 6.38. The edges are taken as the half of the centerline value of the instantaneous velocity. Since these are taken from instantaneous snapshots, many vortices are present in the representative edges of the jet. However, the main vortices which are characteristic for axis switching are identified in the snapshots. Since the deformation starts from the leading edge, the push of the edge is identified in the leading edge and the pull is identified in the top spanwise edge. Comparing the three turbulent cases, it is observed that in case 6, the

vortices are more round and distinct in the leading edge side. Also on the top side, they are small and distinct. However, for case 7 and 8, the leading-edge vortices are sometimes larger and sometimes elongated. More vortices are also present in both the top and bottom edges. This makes the velocity field more violent. Among the two, larger/longer and/or more prominent structures are seen in case 8, compared to case 7. The larger vortices and more activity aids more pushing and pulling of the edges which will create switching earlier. Hence, it can be concluded that as the inlet turbulence intensities increase, the wall normal structures formed increase in size and quantity which will switch the axis faster.

Now it is imperative to know how these wall normal vortices change as the inlet turbulence intensities differ. We have already established in previous section that the increase in turbulence intensity at the jet inlet, the splitting of the vorticity happens earlier. This means that over time, high intensity levels produce more split vortices than less intensity levels. Since the split vortices are smaller, they are subject to shear layer dynamics (Chapter 5), which makes their ends rotate and rise upwards to form wall normal vortices. This may provide explanation for more wall normal structures being present for case 8, compared to case 6 in the leading edge shear layer. On the spanwise edges, crossflow would also have effect on the formation of wall normal vortices. As the crossflow shears across the jet edges, a shear layer is formed on the crossflow fluid (Fig 6.39). This shear layer will roll up the fluid around the edge which forms the wall normal vortex (Fig 6.39 c). As the turbulence in the jet increases, the disturbance in the jet edge makes the formation of wall normal vortex easier, and hence, larger structures are seen in the spanwise edges as well (Fig 6.39 a, b).

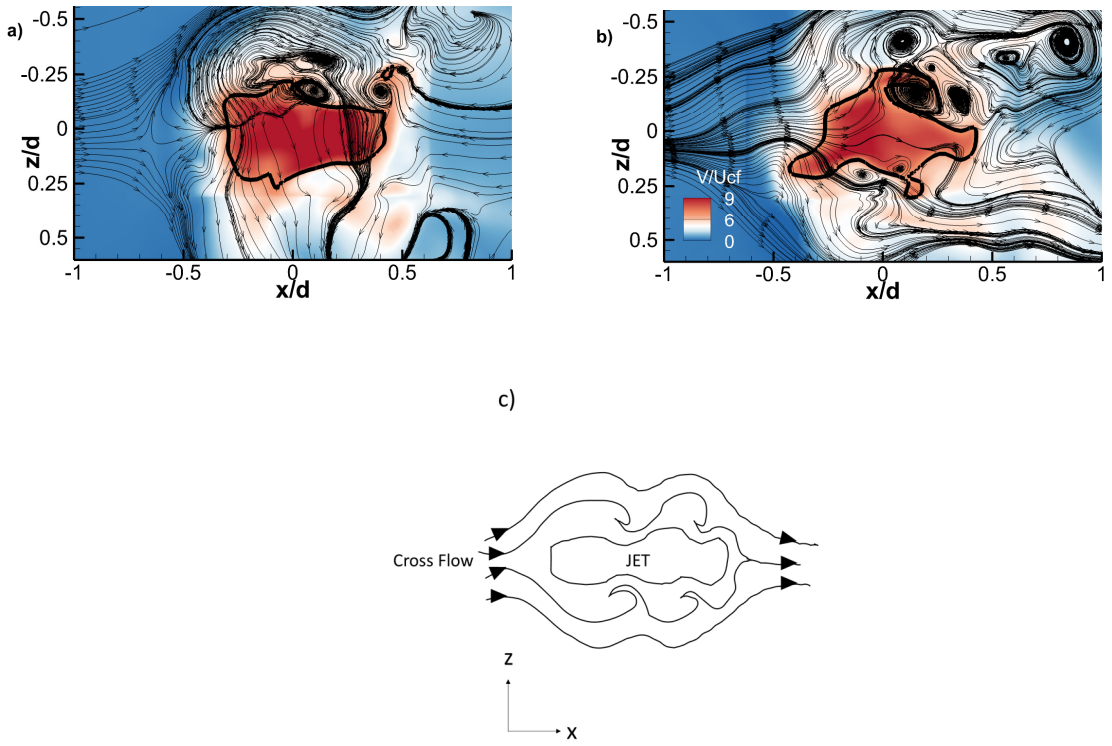

Figure 6.39. Streamtraces of velocity field; (a) Case 6 wall normal plane; (b) Case 8 wall normal plane; (c) Mechanism of shear layer

It can also be understood that since the split happens faster for higher intensity levels, the split vortices, and hence, wall normal vortices have more time to get distorted as they travel downstream. This in turn will provide more opportunity for the vortices to get elongated and sometimes enlarge. Thus, the effect of all these phenomena will aid in making the axis switch faster for case 8, than case 7, and then case 6.

6.7 Section 7- Conclusions

Successful simulation was carried out for cylindrical and rectangular JICF with a velocity ratio of 5.7 and jet Reynolds number of 5000 using LES. For providing turbulent boundary conditions, SEM was used successfully. Validations were sought with experimental studies of Su and Mungal (2004). Excellent agreement was observed for mean flow. Second order correlations also showed good agreement. The overall agreement was improved in some aspects, compared to previous LES and synthetic turbulence studies for the current mesh size. Due to the advantage of SEM, three different turbulence levels (Regular – L=1, Higher- L = 1.66, Highest- L=2.45) for both the geometries were successfully simulated and compared. Some of the important conclusions arrived from the current study were:

1) The crossflow boundary layer upstream of the jet shows more jumps as the turbulence of the jet increases.
2) As the turbulence increases, the initial rollup of shear layer moves nearer towards the jet.
3) Wall normal vortices are increased in quantity and intensity as the turbulence level of the jet increases.
4) Even the shedding of the vortices in the streamwise direction happens earlier as the jet turbulence increases.
5) By the analysis of dynamics for cylindrical JICF, it was revealed that the split of the initial rollup happens earlier respectively as the turbulence increases. This explains the increase of the wall normal vortices in the main domain.

6) From the mean flow analysis, it was seen that the turbulence level of the jet did not change the mean jet trajectory significantly. However, the change in trajectory was significant between cylindrical and rectangular JICF.
7) Jet width also increases due to the effect of increased turbulence.
8) The increase of turbulence also seems to delay the JICF in reaching the far field conditions.
9) The second order Reynolds stresses show a wider profile downstream as the inlet turbulence increases. However, the peak, as expected, gets higher as the turbulence levels increase. This behavior was seen as same for both cylindrical and rectangular JICF.
10) Second order pressure correlations are seen to be highly sensitive to inlet turbulence data. Mean pressure field is also altered from the increase in inlet turbulence.
11) TKE breakdown is seen to be enhanced by the increase of turbulence levels. Also higher TKE is sustained in the leading edge with increasing turbulence levels. On the other hand, rectangular JICF is seen to delay the TBP compared to cylindrical JICF.
12) Higher spanwise activity is also seen as the turbulence levels increase.
13) Comparing with jet experiment, the effect of crossflow on rectangular jets is seen mostly on the spanwise edges – where it increases the width of the jet, and then on the trailing edge.
14) Turbulence is higher, due to crossflow, at the leading edge and on the spanwise edges. This is dictated by the earlier formation of vortices in the leading edge shear layer which propagates around the jet in a slanted manner.
15) An important effect of turbulence levels on the inlet of rectangular jet is to initiate axis switching earlier in the domain.

16) Physics leading to the earlier initiation of axis switching is identified as due to presence of large number and higher intensity wall normal vortices around the edges of the jet. Furthermore, couple of mechanisms – effect of shear layer dynamics and crossflow are identified, which is related to the high turbulence inlet levels and larger number of wall normal vortices which favors earlier axis switching.

Thus, it can be concluded that change in jet inlet turbulence levels can affect the jet in multiple ways, which in some applications, can be utilized to improve localized mixing and in others, to change some flow aspects. Geometry was also seen to affect the JICF system. In rectangular JICF, inlet turbulence levels can be used to alter the axis switching as desired.

CHAPTER 7. CONCLUSIONS

Some of the important conclusions obtained from the above work and its overall contribution to the current understanding of JICF are discussed below. Direct applications, which can benefit from the new understanding developed from this research, are further identified.

Velocity ration 5.7 JICF with jet Reynolds number of 5000 was simulated successfully and validated. Rectangular JICF was also simulated for the same mass flow rate. Three different aspect ratios- 0.5, 2, and 3 were simulated for rectangular JICF and compared. Differences were seen in the instantaneous flow field, mean flow field, and flow dynamics. A new addition to the understanding of these flows is the effect of axis switching. In literature, low velocity ratio JICF (Haven and Kurosaka 1997, Tyagi 2003) had established the jet path taken by these geometries in the presence of crossflow. In these studies, axis switching had not been discussed in detail. The current study also confirmed similar jet path up until a certain depth. However, due to axis switching, a cross-over in the jet path of AR 0.5 rectangular JICF and cylindrical JICF was seen which changed the jet penetration downstream. New understanding gained is that even though axis switching may not have significant effect on low velocity ration JICF, it does play a significant role in high velocity JICF which cannot be neglected. This conclusion has direct effect on jet geometry choices to dictate the path of the jet.

Axis switching specifically has mostly been studied in jets in a quiescent flow. This study is also new to address the effect of crossflow in axis switching. A new finding from this study is that if the short edge faces the crossflow, axis switching is enhanced, but if the long edge faces the crossflow, axis switching is delayed. Other flow physics such as hanging vortices and pressure

behavior were also identified to be directly affected by the jet geometry, which further dictated the path of the jet. Second order analysis also revealed that rectangular jets have an effect to delay the breakdown of turbulence in the domain. Differences were also obtained for spanwise variation of second order statistics, which in some cases were favorable to mixing, and in some cases were unfavorable to mixing. This part of study aids in applications where high mixing is desired or vice versa.

Modal analysis was conducted using DMD. This study was also first of its kind to perform DMD on full rectangular JICF. Higher frequencies were dominant for rectangular JICF compared to its cylindrical counterparts. This was directly correlated to smaller structures in rectangular JICF. Furthermore, the dominant frequencies had lower contribution to turbulence for rectangular JICF and higher contribution to velocity field than cylindrical JICF. Other differences were also seen between different aspect ratios of rectangular JICF. By the conclusions of this area of study, jet control achieved by flow excitation, can be specifically enhanced for pipe and rectangular geometries.

For generation of turbulence in the jet, SEM was used together with LES. The parameters were chosen as to get the correct turbulent statistics at the end of the jet. Initially, pipe only simulation was carried out to validate the statistics and fix the parameters. The same parameters were then used in the full JICF simulation. Good validation was obtained for the first order statistics. Second order statistics also revealed improved validation than previous LES studies in literature. Using the inherent property of synthetic turbulence generation methods, different turbulent kinetic energies of the jet were simulated and compared. This also demonstrates the improvement of numerical algorithms to better predict turbulent flows. Study of different turbulence levels at

same Re of the jet, is also the first of its kind. In practice, different turbulence levels can be generated by careful addition of disturbance to the jet flow.

For cylindrical JICF, different turbulence levels had significant effect on second order pressure and velocity fields. Effect of jet trajectory was minimal. It was observed that as the turbulence levels increase, earlier breakdown of shear layer vortices occur. This, in turn creates more disturbance earlier in the domain. As expected, turbulence breakdown is also enhanced as the inlet turbulence levels increase. These conclusions can have direct impact in mixing enhancement applications such as combustors, mixers etc.

For rectangular JICF, turbulence levels of the jet also had some interesting effects in the flow field. Effect of crossflow is also documented by comparison of flow with rectangular turbulent jets (RTJ) in a quiescent flow. Velocity and turbulence field is observed to be more widespread in the spanwise edges due to instability from crossflow. This study is also new to find out the effect of the turbulence levels of jet on axis switching. It is seen that as the turbulence levels increase, axis switching happens earlier in the domain. Flow physics responsible for this phenomena is identified. Two mechanisms- development of leading edge wall normal vortices and shearing of the jet by the crossflow, are identified that contributes to the phenomena. This part of study aids in precision control of rectangular JICF for different applications.

Overall, the current research realized the objectives successfully and enhanced the understanding of JICF flow field in different aspects.

CHAPTER 8. SCOPE OF FUTURE WORK

In this chapter, some of the ideas to add to the study are discussed.

Using the inlet turbulence generator, turbulence can be added to the crossflow. Effect of turbulence levels of crossflow is an addition to make the study more robust. For cylindrical JICF, this effect can be analyzed by studying the shear layer vortices and their development which will dictate other aspects such as jet trajectory. For rectangular JICF, this effect can also be studied for aspects such as axis switching. For this study, a validation will have to be obtained to get turbulent crossflow at the jet inlet location. In order to do this, the domain needs to be extended upstream for the flow to evolve to realistic turbulence conditions from SEM. Then the study would be completed by varying the turbulence levels and comparing appropriately.

Another dimension would be the analysis of other different geometries, such as elliptical jets. Elliptical JICF also exhibit axis switching. This can be compared to the axis switching exhibited by rectangular JICF. This comparison can isolate the effect of corners and straight edges of jet on the flow field. As we have seen that edge facing the crossflow has effect on the flow field, it would be a good study to include jets at different angles of rotation. This makes the jet edge at an angle facing the crossflow, and hence, the effect of this angle can also be isolated and compared to the JICF system.

Further addition would be modal analysis for the jets with varying jet turbulence levels. This will be a novel study to study the effect of turbulence on the frequencies involved in the JICF system. Particular contributions of the frequencies to mean velocity field and turbulence field can also be understood for these JICF.

APPENDIX A. DETAILS OF SEM ALGORITHM

SEM method employed of inlet turbulence is described in this section. The velocity field that is added to the inflow plane is given by:

$$u_i = \bar{u}_i + a_{ij} u_j'$$

Where a_{ij} is the Cholesky decomposition of Reynolds' stress tensor and is given by

$$\begin{pmatrix} \sqrt{R_{11}} & 0 & 0 \\ R_{21}/a_{11} & \sqrt{R_{22} - a_{21}^2} & 0 \\ R_{31}/a_{11} & (R_{32} - a_{21}a_{31})/a_{22} & \sqrt{R_{33} - a_{31}^2 - a_{32}^2} \end{pmatrix}$$

And u_j' are the synthetic fluctuations discussed by the SEM algorithm

$$u_j'(x,t) = \frac{1}{\sqrt{N}} \sum_{i=1}^{N} \varepsilon_{ij} f_j\big(x - x_i(t)\big)$$

Where the shape function f is a function which has a compact support on prescribed length scale.

$$\frac{1}{\sigma_i} \int_{-\sigma_i/2}^{\frac{\sigma_i}{2}} f_{i\sigma}^2(x)dx = 1$$

In the current case the shape function is taken as a tent function

$$f(x) = \begin{cases} \sqrt{\frac{3}{2}}(1 - |x|) \; if \; x < 1 \\ 0 \qquad otherwise \end{cases}$$

The theoretical basis and subsequent details for this algorithm can be found in Jarrin et al. (2006) and Jarrin (2008).

APPENDIX B. ADDITIONAL RESULTS FROM PIPE-FLOW SIMULATION

A separate, pipe-only simulation, is done to get right parameters for the algorithm to generate reasonable turbulence at the end of pipe. The pipe length used for this simulation is 10d. The total mesh used for the simulation is approximately 2 million. For simulating LES, mesh stretching was used with finer mesh near the walls. The mesh size using wall coordinates are $(r^+{}_{min}\sim 0.15, r^+{}_{max}\sim 3.95, r\Delta\theta^+\sim 7.85\ and\ z^+\sim 13.54)$. The Reynolds' stresses required for the algorithm are taken from the data provided by Eggels et al. (1994). The length scales for the turbulence at the inlet are specified from the two point correlation provided in Eggels et al. (1994) corresponding to the flow in the core region of the pipe. The length scales are taken as the integral of the curve till the point when the correlation is about 0.1 (10%). For wall bounded pipe flows, it is understood that the length scales would be higher in the streamwise direction, compared to spanwise, and wall-normal directions. This fact is considered by choosing different length scales in different directions. Inlet mean velocity is taken from the fully developed turbulent profile specified in Muppidi and Mahesh (2005). Target friction velocity is obtained from the fully developed wall shear stress taken from the following correlation for flat plate (Kempf-Karman):

$$C_f = 0.055 * {Re_x}^{-0.812}$$

The simulation shows a good development of friction velocity compared with the target along the domain.

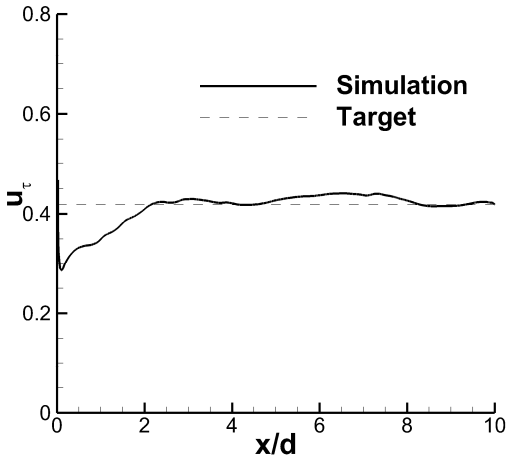

Figure B.1. Development of friction velocity in the domain

Using the SEM, a reasonable validation is obtained for fully-developed pipe flow. The mean flow is compared with the exact flow inside the pipe, as reported by Muppidi and Mahesh (2007). Reynolds stresses are compared with the values provided by Eggels et al. (1994). It is known that LES tends to under predict shear stress, compared with DNS or experiments. This is due to the fact that some of the smallest scales near the wall are modeled using LES. Hence, the simulated stresses may not capture all the phenomena occurring near the wall. Thus, for a better comparison the results from periodic LES by Gnambode et al. (2015) is also included in the comparison of Reynolds stresses. These plots are depicted in the section 2 of Chapter 5.

Instantaneous flow field:

The flow field of the simulation show features that agrees with fully developed pipe flows. Two major structures are long wall vortices and hairpin like vortices.

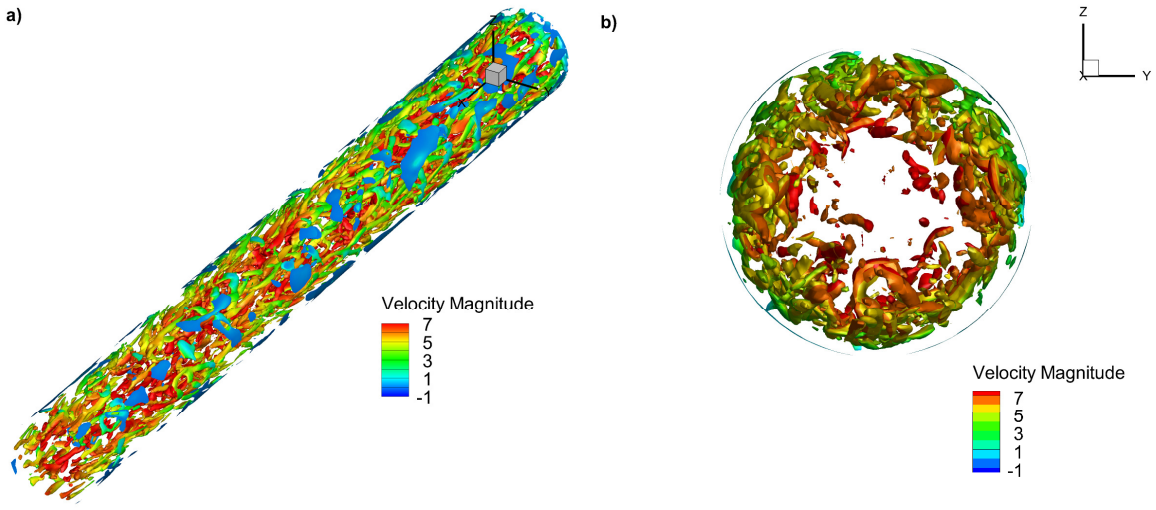

Figure B.2. Structures using Q-criteria for pipe flow; (a) Structures in the full pipe; (b) Structures inside the pipe

Long streaks of vortical structures are present in the wall region (Fig B.2 (a)). This is due to the presence of high velocity gradient provided by the turbulent flow. If some spanwise vortices are present, they elongate along the flow and slightly raise in the wall normal direction appearing like raised 'hairpins' (Fig B.2 (b)). Some of these structures are identified in the wall region for the simulation. These structures confirm the nature of wall bounded turbulent flow. Thus, the application of SEM to pipe flow provide a mechanism of getting fully developed turbulence at the pipe exit.

REFERENCES

Acharya, S., M. Tyagi and A. Hoda (2001). "Flow and heat transfer predictions for film cooling." *Heat Transfer in Gas Turbine Systems* **934**: 110-125.

Alder, M., D. Gonzalez, M. Waindim and D.V. Gaitonde (2015). “Spatially Evolving Equilibrium Turbulent Boundary Layer Profiles for LES.” *Presented at AIAA Comput. Fluid Dyn. Conf.*, 22nd, Dallas, TX, AIAA Pap. 2015-3214

Alves, L. S. de B., R.E. Kelly and A. R. Karagozian (2005). “Linear Stability Analysis of Jets in Crossflow.” 43rd *AIAA Aerospace Sciences Meeting and Exhibit*, 43rd, Reno, NV, AIAA Pap. 2005-1118

Araya, G., L. Castillo, C. Meneveau and K. Jansen (2011). "A dynamic multi-scale approach for turbulent inflow boundary conditions in spatially developing flows." *Journal of Fluid Mechanics* **670**: 581-605.

Arolla, S. K. and P. A. Durbin (2015). "LES of spatially developing turbulent boundary layer over a concave surface." *Journal of Turbulence* **16**(1): 81-99.

Batten, P., S. Palaniswamy, U. Goldberg, O. Peroomian and S. Chakravarthy (2015). “Generating Synthetic Inhomogenous Turbulence from RANS Statistics.” *Presented at AIAA Comput. Fluid Dyn. Conf.*, 22nd, Dallas, TX, AIAA Pap. 2015-3215

Bagheri, S., P. Schlatter, P. J. Schmid and D. S. Henningson (2009). "Global stability of a jet in crossflow." *Journal of Fluid Mechanics* **624**: 33-44.

Broadwell, J. E. and R. E. Breidenthal (1984). "Structure and Mixing of a Transverse Jet in Incompressible-Flow." *Journal of Fluid Mechanics* **148**(Nov): 405-412.

Broze, G. and F. Hussain (1996). "Transitions to chaos in a forced jet: Intermittency, tangent bifurcations and hysteresis." *Journal of Fluid Mechanics* **311**: 37-71.

Camussi, R., G. Guj and A. Stella (2002). "Experimental study of a jet in a crossflow at very low Reynolds number." *Journal of Fluid Mechanics* **454**: 113-144.

Chen, N. and H. D. Yu (2014). "Mechanism of axis switching in low aspect-ratio rectangular jets." *Computers & Mathematics with Applications* **67**(2): 437-444.

Cortelezzi, L. and A. R. Karagozian (2001). "On the formation of the counter-rotating vortex pair in transverse jets." *Journal of Fluid Mechanics* **446**: 347-373.

da Silva, C. B. and O. Metais (2002). "On the influence of coherent structures upon interscale interactions in turbulent plane jets." *Journal of Fluid Mechanics* **473**: 103-145.

Davidson, L. (2007). "Using Isotropic Synthetic Fluctuations as Inlet Boundary Conditions for Unsteady Simulations." *Advances and Applications in Fluid Mechanics* **1**(1): 1-35.

Davitian, J., D. Getsinger, C. Hendrickson and A. R. Karagozian (2010). "Transition to global instability in transverse-jet shear layers." *Journal of Fluid Mechanics* **661**: 294-315.

Dhamankar NS, Blaisdell GA, Lyrintzis AS. (2015). "An overview of turbulent inflow boundary conditions for large eddy simulations." *Presented at AIAA Comput. Fluid Dyn. Conf.*, 22nd, Dallas, TX, AIAA Pap. 2015-3213

Dietzel, D., D. Messig, F. Piscaglia, A. Montorfano, G. Olenik, O. T. Stein, A. Kronenburg, A. Onorati and C. Hasse (2014). "Evaluation of scale resolving turbulence generation methods for Large Eddy Simulation of turbulent flows." *Computers & Fluids* **93**: 116-128.

Druault, P., S. Lardeau, J. P. Bonnet, F. Coiffet, J. Delville, E. Lamballais, J. F. Largeau and L. Perret (2004). "Generation of three-dimensional turbulent inlet conditions for large-eddy simulation." *Aiaa Journal* **42**(3): 447-456.

Eggels, J. G. M., F. Unger, M. H. Weiss, J. Westerweel, R. J. Adrian, R. Friedrich and F. T. M. Nieuwstadt (1994). "Fully-Developed Turbulent Pipe-Flow - a Comparison between Direct Numerical-Simulation and Experiment." *Journal of Fluid Mechanics* **268**: 175-209.

Fric, T. F. and A. Roshko (1994). "Vortical Structure in the Wake of a Transverse Jet." *Journal of Fluid Mechanics* **279**: 1-47.

Fric, T.F. & Gharib, M. (1990). "Wake formation of the transverse jet". *Bull. Am. Phys. Soc.* **35**: 2338.

Fric, T.F. & Roshko, A. (1988). "Views of the transverse jet near field". *Phys. Fluids* **31**: 2390.

Fric, T.F. & Roshko, A. (1991) "Structure in the near field of the transverse jet". In Turbulent Shear Flows 7 (cd. F. Durst et al.). *Springer*.

Germano, M., U. Piomelli, P. Moin and W.H. Cabot (1991). "A dynamic subgrid-scale eddy viscosity model." *Phys. Fluids A* **3**: 1760.

Gnambode, P. S., P. Orlandi, M. Ould-Rouiss and X. Nicolas (2015). "Large-Eddy simulation of turbulent pipe flow of power-law fluids." *International Journal of Heat and Fluid Flow* **54**: 196-210.

Grinstein, F. F. (2001). "Vortex dynamics and entrainment in rectangular free jets." *Journal of Fluid Mechanics* **437**: 69-101.

Gropp, W., E. Lusk, N. Doss and A. Skjellum (1996). "A high-performance, portable implementation of the MPI message passing interface standard." *Parallel Computing* **22**(6): 789-828.

Gutmark, E. J. and F. F. Grinstein (1999). "Flow control with noncircular jets." *Annual Review of Fluid Mechanics* **31**: 239-+.

Haller, G. (2005). "An objective definition of a vortex." *Journal of Fluid Mechanics* **525**: 1-26.

Hasselbrink, E. F. and M. G. Mungal (2001). "Transverse jets and jet flames. Part 1. Scaling laws for strong transverse jets." *Journal of Fluid Mechanics* **443**: 1-25.

Haven, B. A. and M. Kurosaka (1997). "Kidney and anti-kidney vortices in crossflow jets." *Journal of Fluid Mechanics* **352**: 27-64.

Huang, S. H., Q. Li and J. R. Wu (2010). "A general inflow turbulence generator for large eddy simulation." *Journal of Wind Engineering and Industrial Aerodynamics* **98**(10-11): 600-617.

Iyer, P. S. and K. Mahesh (2016). "A numerical study of shear layer characteristics of low-speed transverse jets." *Journal of Fluid Mechanics* **790**.

Jarrin, N. (2008). "Synthetic Inflow Boundary Conditions for the Numerical Simulation of Turbulence." *The University of Manchester*: U.K.

Jarrin, N., S. Benhamadouche, D. Laurence and R. Prosser (2006). "A synthetic-eddy-method for generating inflow conditions for large-eddy simulations." *International Journal of Heat and Fluid Flow* **27**(4): 585-593.

Jewkes, J. W., Y. M. Chung and P. W. Carpenter (2011). "Modification to a Turbulent Inflow Generation Method for Boundary-Layer Flows." *Aiaa Journal* **49**(1): 247-250.

Kalghatgi, P. and S. Acharya (2010). "Investigation of Film-Cooled Rough Surfaces Using Large Eddy Simulation." *Heat Transfer Research* **41**(7): 753-768.

Kalghatgi, P. and S. Acharya (2014). "Modal Analysis of Inclined Film Cooling Jet Flow." *Journal of Turbomachinery-Transactions of the Asme* **136**(8).

Karagozian, A. R. (1986). "The Flame Structure and Vorticity Generated by a Chemically Reacting Transverse Jet." *Aiaa Journal* **24**(9): 1502-1507.

Karagozian, A. R. (2010). "Transverse jets and their control." *Progress in Energy and Combustion Science* **36**(5): 531-553.

Karagozian, A. R. (2014). "The jet in crossflow." *Physics of Fluids* **26**(10).

Karasso, P. S. and M. G. Mungal (1996). "Scalar mixing and reaction in plane liquid shear layers." *Journal of Fluid Mechanics* **323**: 23-63.

Karypis, G. and V. Kumar (1998). "A fast and high quality multilevel scheme for partitioning irregular graphs." *Siam Journal on Scientific Computing* **20**(1): 359-392.

Kataoka, H. (2008). "Numerical simulations of a wind-induced vibrating square cylinder within turbulent boundary layer." *Journal of Wind Engineering and Industrial Aerodynamics* **96**(10-11): 1985-1997.

Keating, A., U. Piomelli, E. Balaras and H. J. Kaltenbach (2004). "A priori and a posteriori tests of inflow conditions for large-eddy simulation." *Physics of Fluids* **16**(12): 4696-4712.

Keffer, J. F. and W. D. Baines (1963). "The Round Turbulent Jet in a Cross-Wind." *Journal of Fluid Mechanics* **15**(4): 481-&.

Kelso, R. M. and A. J. Smits (1995). "Horseshoe Vortex Systems Resulting from the Interaction between a Laminar Boundary-Layer and a Transverse Jet." *Physics of Fluids* **7**(1): 153-158.

Kelso, R. M., T. T. Lim and A. E. Perry (1996). "An experimental study of round jets in cross-flow." *Journal of Fluid Mechanics* **306**: 111-144.

Klein, M., A. Sadiki and J. Janicka (2003). "A digital filter based generation of inflow data for spatially developing direct numerical or large eddy simulations." *Journal of Computational Physics* **186**(2): 652-665.

Kraichnan, R. H. (1970). "Diffusion by a Random Velocity Field." *Physics of Fluids* **13**(1): 22-+.

Krothapalli, A., L. Lourenco and J. M. Buchlin (1990). "Separated Flow Upstream of a Jet in a Cross-Flow." *Aiaa Journal* **28**(3): 414-420.

Kutz, J. Nathan, Steven L. Brunton, Bingni W. Brunton and Joshua L. Proctor (2016) Dynamic Mode Decomposition: Data-Driven Modeling of Complex Systems, *Society for Industrial and Applied Mathematics.*

Lilly D.K. (1992). “A proposed modification of the Germano subgrid-scale closure method.” *Phys. Fluids A* **4**: 633-635.

Lumley, J. L. (1970) Stochastic Tools in Turbulence, *Academic Press.*

Lund, T. S., X. H. Wu and K. D. Squires (1998). "Generation of turbulent inflow data for spatially-developing boundary layer simulations." *Journal of Computational Physics* **140**(2): 233-258.

Mahesh, K. (2013). "The Interaction of Jets with Crossflow." *Annual Review of Fluid Mechanics, Vol 45* **45**: 379-407.

Margason RJ. (1993). “Fifty years of jet in cross flow research”. *Comput. Exp. Assess. Jets Cross Flow,* AGARD-CP 534, Advis. Group Aeronaut. Res. Dev., Washington, DC

Marusic, I., B. J. McKeon, P. A. Monkewitz, H. M. Nagib, A. J. Smits and K. R. Sreenivasan (2010). "Wall-bounded turbulent flows at high Reynolds numbers: Recent advances and key issues." *Physics of Fluids* **22**(6).

Mayor, S. D., P. R. Spalart and G. J. Tripoli (2002). "Application of a perturbation recycling method in the large-eddy simulation of a mesoscale convective internal boundary layer." *Journal of the Atmospheric Sciences* **59**(15): 2385-2395.

Megerian, S., J. Davitian, L. S. D. B. Alves and A. R. Karagozian (2007). "Transverse-jet shear-layer instabilities. Part 1. Experimental studies." *Journal of Fluid Mechanics* **593**: 93-129.

Morgan, B., J. Larsson, S. Kawai and S. K. Lele (2011). "Improving Low-Frequency Characteristics of Recycling/Rescaling Inflow Turbulence Generation." *Aiaa Journal* **49**(3): 582-597.

Morgan, B., K. Duraisamy and S. K. Lele (2014). "Large-Eddy Simulations of a Normal Shock Train in a Constant-Area Isolator." *Aiaa Journal* **52**(3): 539-558.

Muldoon, F. and S. Acharya (2010). "Direct Numerical Simulation of pulsed jets-in-crossflow." *Computers & Fluids* **39**(10): 1745-1773.

Muppidi, S. and K. Mahesh (2005). "Study of trajectories of jets in crossflow using direct numerical simulations." *Journal of Fluid Mechanics* **530**: 81-100.

Muppidi, S. and K. Mahesh (2006). "Two-dimensional model problem to explain counter-rotating vortex pair formation in a transverse jet." *Physics of Fluids* **18**(8).

Muppidi, S. and K. Mahesh (2007). "Direct numerical simulation of round turbulent jets in crossflow." *Journal of Fluid Mechanics* **574**: 59-84.

Muppidi, S. and K. Mahesh (2008). "Direct numerical simulation of passive scalar transport in transverse jets." *Journal of Fluid Mechanics* **598**: 335-360.

Nakayama, H., T. Takemi and H. Nagai (2012). "Large-eddy simulation of urban boundary-layer flows by generating turbulent inflows from mesoscale meteorological simulations." *Atmospheric Science Letters* **13**(3): 180-186.

Nikitin, N. (2007). "Spatial periodicity of spatially evolving turbulent flow caused by inflow boundary condition." *Physics of Fluids* **19**(9).

Nozawa, K. and T. Tamura (2002). "Large eddy simulation of the flow around a low-rise building immersed in a rough-wall turbulent boundary layer." *Journal of Wind Engineering and Industrial Aerodynamics* **90**(10): 1151-1162.

Pokharel, P., S. Roy, S. Acharya (2013). "Simulation of Oil Plume Trajectory." *Presented on Annual DWH Conference*, 3rd, Baton Rouge, LA

Pokharel, P. (2017). "Turbulence Generation Methods for LES." *Presented on MIE Graduate Student Conference*, 2017, Louisiana State University, Baton Rouge, LA

Pratte, B.D. & Baines, W.D. (1967). "Profiles of the round turbulent jet in a cross flow." *J. Hydronaut. Div. ASCE* **92**: 53-64

Priebe S. and Martin, M.P. (2010). "Low frequency unsteadiness in the DNS of a compression ramp shockwave and turbulent boundary layer interaction." *Presented at AIAA Aerosp. Sci. Meet.*, 48th, Orlando, FL, AIAA Pap: 2010-108

Quinn, W. R. (1991). "Passive near-Field Mixing Enhancement in Rectangular Jet Flows." *Aiaa Journal* **29**(4): 515-519.

Ricou, F. P. and D. B. Spalding (1961). "Measurements of Entrainment by Axisymmetrical Turbulent Jets." *Journal of Fluid Mechanics* **11**(1): 21-32.

Rowley, C. W., I. Mezic, S. Bagheri, P. Schlatter and D. S. Henningson (2009). "Spectral analysis of nonlinear flows." *Journal of Fluid Mechanics* **641**: 115-127.

Roy, S. and S. Acharya (2010). "Microinstability and perturbation in turbulent stirred tank flows." *Louisiana State University*: Baton Rouge LA

Ruiz, A. M., G. Lacaze and J. C. Oefelein (2015). "Flow topologies and turbulence scales in a jet-in-cross-flow." *Physics of Fluids* **27**(4).

Schluter, J. U., H. Pitsch and P. Moin (2004). "Large eddy simulation inflow conditions for coupling with Reynolds-averaged flow solvers." *Aiaa Journal* **42**(3): 478-484.

Schmid, P. J. (2010). "Dynamic mode decomposition of numerical and experimental data." *Journal of Fluid Mechanics* **656**: 5-28.

Shah, R.K. and London A.L. (1978). “Laminar Flow Forced Convection in Ducts.” *Academic Press.*

Shan, J. W. and P. E. Dimotakis (2006). "Reynolds-number effects and anisotropy in transverse-jet mixing." *Journal of Fluid Mechanics* **566**: 47-96.

Smirnov, A., S. Shi and I. Celik (2001). "Random flow generation technique for Large Eddy Simulations and particle-dynamics modeling." *Journal of Fluids Engineering-Transactions of the Asme* **123**(2): 359-371.

Smith, S. H. and M. G. Mungal (1998). "Mixing, structure and scaling of the jet in crossflow." *Journal of Fluid Mechanics* **357**: 83-122.

Spalart, P. R. (1988). "Direct Simulation of a Turbulent Boundary-Layer up to R-Theta=1410." *Journal of Fluid Mechanics* **187**: 61-98.

Spalart, P. R., M. Strelets and A. Travin (2006). "Direct numerical simulation of large-eddy-break-up devices in a boundary layer." *International Journal of Heat and Fluid Flow* **27**(5): 902-910.

Spille-Kohloff A., H.J. Kaltenbach (2001). “Generation of turbulent inflow data with a prescribed shear-stress profile.” *Compil. Part Notice ADP013648*, Def. Tech. Inf. Cent., Fort Belvoir, VA

Su, L. K. and M. G. Mungal (2004). "Simultaneous measurements of scalar and velocity field evolution in turbulent crossflowing jets." *Journal of Fluid Mechanics* **513**: 1-45.

Tabor, G. R. and M. H. Baba-Ahmadi (2010). "Inlet conditions for large eddy simulation: A review." *Computers & Fluids* **39**(4): 553-567.

Tamura, T. (2008). "Towards practical use of LES in wind engineering." *Journal of Wind Engineering and Industrial Aerodynamics* **96**(10-11): 1451-1471.

Tyagi, M. and S. Acharya (2003). "Large eddy simulation of film cooling flow from an inclined cylindrical jet." *Journal of Turbomachinery-Transactions of the Asme* **125**(4): 734-742.

Tyagi, M. and S. Acharya (2003). “Large Eddy simulations of complex turbulent flows.” *Louisiana State University*: Baton Rouge LA

Tyagi, M. and S. Acharya (2005). "Large eddy simulation of turbulent flows in complex and moving rigid geometries using the immersed boundary method." *International Journal for Numerical Methods in Fluids* **48**(7): 691-722.

Urbin, G. and D. Knight (2001). "Large-eddy simulation of a supersonic boundary layer using an unstructured grid." *Aiaa Journal* **39**(7): 1288-1295.

Weiss, J. M. and W. A. Smith (1995). "Preconditioning Applied to Variable and Constant Density Flows." *Aiaa Journal* **33**(11): 2050-2057.

Werle, H. (1968). “Flows with large velocity fluctuations.” Motion picture film no. 575, *ONERA*, Chatillon, France.

Wu, Jie-Zhi, Hui-Yang Ma, Ming-De Zhou (2005) Vorticity and Vortex Dynamics, *Springer*

Wu, X. (2017). "Inflow Turbulence Generation Methods." *Annual Review of Fluid Mechanics*, Vol 49 **49**: 23-49.

Xiong, Z., S. Nagarajan and S. K. Lele (2004). "Simple method for generating inflow turbulence." *Aiaa Journal* **42**(10): 2164-2166.

Yu, H. D. and S. S. Girimaji (2005). "Near-field turbulent simulations of rectangular jets using lattice Boltzmann method." *Physics of Fluids* **17**(12).

Yu, H. and S. S. Girimaji (2008). "Study of axis-switching and stability of laminar rectangular jets using lattice Boltzmann method." *Computers & Mathematics with Applications* **55**(7): 1611-1619.

Yuan, L. L. and R. L. Street (1998). "Trajectory and entrainment of a round jet in crossflow." *Physics of Fluids* **10**(9): 2323-2335.

Yuan, L. L., R. L. Street and J. H. Ferziger (1999). "Large-eddy simulations of a round jet in crossflow." *Journal of Fluid Mechanics* **379**: 71-104.

Zaman, K. B. M. Q. (1996). "Axis switching and spreading of an asymmetric jet: The role of coherent structure dynamics." *Journal of Fluid Mechanics* **316**: 1-27.

Ziefle, J. and L. Kleiser (2009). “Large-Eddy Simulation of Round Jet in Crossflow.” *Aiaa Journal* **47** (5): 1158-1172.

VITA

Pranaya Pokharel was born in Naxal, Kathmandu, Nepal in March 1986 to Mr. Shreeram Pokharel and Mrs. Bina Pokharel. He completed his high school in Kathmandu, Nepal. He completed his undergraduate study from Institute of Engineering (IOE), Pulchowk, Nepal in 2008. Then he came to USA and completed his Master's Degree in Mechanical Engineering from McNeese State University, Lake Charles, Louisiana in 2011. After that he joined Louisiana State University, Baton Rouge, for his doctoral studies. He expects to receive the degree of Doctor of Philosophy at the December 2018 commencement.